METAL-ORGANIC FRAMEWORKS FOR THE TRACE DETECTION OF EXPLOSIVE SUBSTANCES AND RELATED COMPOUNDS

MONIKA JURCIC

University College London

Department of Chemistry
Department of Security and Crime Science

This thesis is submitted in partial fulfilment of the requirements for the Degree of Doctor of Philosophy, 2018

DECLARATION

I, Monika Jurcic, confirm that the work presented in this thesis is my own. Where information has been derived from other sources, I confirm that this has been indicated in the thesis.

Monika Jurcic

ABSTRACT

The threat of terrorism-related explosive attacks is substantial. Thus, the successful detection of explosives, be that on a person, surface or as a vapour, is of great importance.

Despite a number of effective trace detection methods being currently available, there is still a requirement to develop novel materials that demonstrate timely, sensitive, selective, and portable sensing of explosives.

Metal-organic frameworks (MOFs) have emerged in recent years as promising candidates for the fluorescence-based detection of explosives owing to their structural tailor-ability, facile synthesis, variable luminescence properties and high permanent porosities.

This thesis further expands on the relatively limited knowledge of MOFs for the application of trace explosives detection, with a particular focus on probing their potential for real-world applicability.

The first experimental Chapter details a pilot study whereby two novel fluorescent MOFs have been synthesised and characterised for the vapour-phase detection of explosives-related compounds. It was found that porosity is an important consideration for analyte detection.

Chapter three discusses the synthesis and characterisation of another novel fluorescent MOF, which was tested for its ability to detect trace quantities of explosives as both vapours and liquids. This MOF demonstrated flexibility in its structure. Thus, additional techniques were used for its characterisation; included in this was in-depth study of its humidity stability.

Chapter four investigates the use of MOFs in sensory arrays for the discriminative detection of explosives. It was found that MOFs can identify explosives they are exposed to using this approach.

Chapter five explores the potential of MOFs as explosive vapour pre-concentrators; samples of the MOF presented in Chapter three could be used to capture and release 2,4,6-trinitrotoluene vapours.

Ultimately, this thesis combines materials synthesis, crystal engineering, various materials characterisation techniques with fluorescence spectroscopy and mass spectrometry to conclude that MOFs hold promising potential in the application of trace explosives detection.

ACKNOWLEDGMENTS

Primarily I must thank the University College London Security Science Doctoral Training Programme for allowing me the opportunity to pursue a Ph.D. in my chosen subject area. With this said, I must extend this thank you to my primary supervisor Professor Ivan Parkin who has allowed me to drive my own project and has been nothing but supportive; offering guidance whenever necessary. I must also thank my second supervisor Professor Tony Kenyon, whose input into my research alongside Ivan's has been invaluable.

I acknowledge and thank all those who have collaborated with me. Firstly, I must thank the Explosives Detection Group within the Defence Science and Technology Laboratory for giving me the opportunity of a two-year part-time secondment. This secondment facilitated exciting research that would not have been possible to achieve otherwise.

I would also like to thank Dr. Vladimir Martis and Surface Measurement Systems UK for the collaborative dynamic vapour sorption experiments, as well as Dr. David Scanlon and Chris Savory of University College London for all computational calculations. My thanks are also extended to Dr. Huw Marchbank for the PXRD LeBail fitting analyses and Dr. Emily Glover and Dr. Mike Powell for running XPS measurements. I would also like to thank Dr. Steve Firth, Martin Vickers and Dr. Steve Hudziak for training on TGA and SEM, PXRD and TCSPC respectively. Finally, I would like to thank Dr. William Peveler for not only his input in the collaborative array-based sensing work but also for general scientific discussions, proofreading, and for being a great friend. On this topic I would also like to thank Gwyn, Nick, Emily, Mike, Lily, Carlos, Emma and all other UCL chemists for an amazing four years of friendship; may it continue. To my friends outside of UCL, particularly Jessica Marshall and Conor Curtis – thank you for keeping me sane and being the best friends anyone can ask for.

This thesis is dedicated to my wonderful parents Branka and Drazen Jurcic who are the inspiration for everything I do.

CONTENTS

1 INTRODUCTION AND SCOPE 1

2 LITERATURE REVIEW 3

2.1 Explosive materials 3

2.2 Classification of explosives 4

2.2.1 Chemical nature 4

2.2.2 Performance 6

2.2.3 Uses of explosives 7

2.3 Explosives detection 10

2.3.1 Approaches to explosives detection 10

2.3.2 Challenges in trace explosives detection 11

2.3.3 Detector requirements 16

2.4 Current technologies 17

2.4.1 Animal olfaction 17

2.4.2 Separation and ion detection techniques 19

2.4.3 Spectroscopic techniques 23

2.4.4 Sensors 25

2.5 Fluorescence-based explosives detection 28

2.5.1 Fluorescence theory 29

2.5.2 Mechanisms and processes for fluorescence-based explosives detection 31

2.5.3 Previous contributions to fluorescence-based explosives detection 40

2.6 Fluorescent metal-organic frameworks 46

2.6.1 An introduction to metal-organic frameworks 46

2.6.2 The origin of fluorescence in MOFs 62

2.6.3 Advantages of MOFs as fluorescence-based explosives sensors 65

2.6.4 Previous contributions to research on MOFs as explosives sensors 67

2.7 Thesis aims, outline and novelty of research 86

3 A PILOT STUDY INTO TWO NOVEL MOFS FOR VAPOUR-PHASE SENSING 87

3.1 Introduction 87

3.2 Experimental 90

3.2.1 Synthesis of metal-organic frameworks 90

3.2.2 Washing regimes to afford active MOFs 91

3.2.3 Fabrication of the MOF 'thin films' used in sensing 92

3.2.4 Generation of analyte vapours and 'thin film' exposure method 93

3.2.5 Fluorescence sensing methodology 93

3.3 Results and discussion 95

3.3.1 Characterisation of metal-organic frameworks 95
3.3.2 Vapour-phase fluorescence sensing 107
3.4 Conclusions and future work 122
4 A FLEXIBLE MOF SENSOR 127
4.1 Introduction 127
4.2 Experimental 130
4.2.1 Synthesis of linker (H_8L) 130
4.2.2 Synthesis of MOF $Zn_4L(H_2O)_4 \cdot (solvent)]_n$ (**3**) 131
4.2.3 Activation of MOF **3** 132
4.2.4 MOF **3′** water and humidity stability tests 132
4.2.5 Solution-phase sensing procedures 136
4.2.6 Vapour-phase sensing procedures 138
4.2.7 Computational simulations 140
4.3 Results and discussion 141
4.3.1 Characterisation 141
4.3.2 Solution-phase sensing 168
4.3.3 Vapour-phase sensing 187
4.4 Conclusions 194
5 A MOF SENSOR ARRAY FOR SOLUTION-PHASE EXPLOSIVES DETECTION 199
5.1 Introduction 199
5.1.1 Basics of array-based sensing 201
5.1.2 Previous research on array-based sensing for explosives detection 203
5.1.3 Experimental design 204
5.2 Experimental 209
5.2.1 Synthesis and activation of array metal-organic frameworks 209
5.2.2 Solution-phase sensing methodology 211
5.2.3 Linear discrimination analysis (LDA) on sensing array responses 211
5.3 Results and discussion 216
5.3.1 MOF structure confirmation 216
5.3.2 Fluorescence sensing results 217
5.3.3 Results of linear discrimination analysis (LDA) 220
5.4 Conclusions and future work 226
6 A MOF AS AN EXPLOSIVES VAPOUR PRE-CONCENTRATOR 229
6.1 Introduction 229
6.2 Experimental 237
6.2.1 Sample tube preparation 237
6.2.2 Vapour generation and sampling 238
6.2.3 Sample tube analysis 244
6.2.4 Chemical analyses on MOF **3′** samples after pre-concentration experiments 248
6.3 Results and discussion 249
6.3.1 Initial proof-of-concept experiment 249

6.3.2 An attempt to identify optimal MOF **3′** degas conditions 251
6.3.3 Secondary degassing and reuse of MOF **3′** samples 260
6.3.4 High temperature degassing 262
6.3.5 A chemical investigation into the varied preconcentration capabilities of differently degassed MOF **3′** samples 266
6.4 Conclusions and future work 279
7 CONCLUSIONS AND FUTURE WORK 283
7.1 Overview of results 283
7.2 Future work 289
8 GENERAL EXPERIMENTAL MATERIALS AND INSTRUMENTATION 293
8.1 Chemicals 293
8.2 Instrumentation 293

I APPENDIX 299
A CHAPTER THREE ADDITIONAL DATA 301
B CHAPTER FOUR ADDITIONAL DATA 303
C CHAPTER FIVE ADDITIONAL DATA 305
D CHAPTER SIX ADDITIONAL DATA 307

BIBLIOGRAPHY 309

LIST OF FIGURES

Figure 2.1 Molecular structures of common explosive substances 8
Figure 2.2 Molecular structures of detectable explosives related compounds 13
Figure 2.3 Jablonski diagram 29
Figure 2.4 Molecular orbital schematic detailing the photo-induced electron transfer (PIET) mechanism 33
Figure 2.5 Molecular orbital schematic detailing the Förster-resonance energy transfer mechanism 34
Figure 2.6 Molecular orbital schematic detailing the Dexter electron exchange mechanism 36
Figure 2.7 Amplifying fluorescent conjugate polymer examples 41
Figure 2.8 Metal-organic frameworks and their constituting components 47
Figure 2.9 The isoreticular MOF concept 48
Figure 2.10 Schematic overview of flexible MOFs 49
Figure 2.11 Conventional solvothermal synthesis of MOF structures 50
Figure 2.12 Microwave-assisted solvothermal synthesis of MOF structures 51
Figure 2.13 IUPAC classification of sorption isotherms 56
Figure 2.14 The origin of fluorescence in MOFs 62
Figure 2.15 Pioneering MOF for explosives detection 68
Figure 2.16 Structure of MOF $Zn_2(oba)_2(bpy)$ 70
Figure 2.17 PIET mechanism proposed for fluorescence changes in MOFs 72
Figure 2.18 Illustration of the 2D Cartesian coordinate MOF sensing projections 75
Figure 2.19 Illustration of the fluorescence emission profile of a MOF after a solution phase sensing titration with TNT 79
Figure 2.20 Illustrative example of MOF-analyte spectral overlap that leads to FRET 82
Figure 2.21 Examples of linkers used to synthesis highly fluorescent MOFs 83
Figure 3.1 Molecular structure of 2,2′-bipyridine-4,4′-dicarboxylate (H_2dcbpy) 88
Figure 3.2 SEM image showing a side on view of a representative MOF **1′** 'thin film' used in vapour-phase sensing experiments 92

Figure 3.3 Illustration of the vapour-phase sensing methodology employed for MOF 'thin films' 93
Figure 3.4 MOF **1** asymmetric unit 95
Figure 3.5 MOF **1** secondary building unit 96
Figure 3.6 Representations of the three-dimensional structure of MOF **1** with and without the present of solvent guest DMF molecules 97
Figure 3.7 MOF **2** asymmetric unit 98
Figure 3.8 MOF **2** secondary building unit 99
Figure 3.9 MOF **2** three-dimensional structure 99
Figure 3.10 PXRD patterns of MOFs **1** (simulated and as-synthesised), **1M**, **1'**, **1M'**, **2** (simulated and as-synthesised) and **2'** 102
Figure 3.11 SEM images of MOFs **1**, **1M** and **2** 104
Figure 3.12 SEM image of active MOF **1'** 105
Figure 3.13 Results of the TGA analyses conducted on MOFs **1'** and **2'** 106
Figure 3.14 Fluorescence emission spectra of MOF **1'** and free linker H_2dcbpyin the solid-state 108
Figure 3.15 Fluorescence emission profile of MOF **1'** upon exposure to DMNB vapours 109
Figure 3.16 Summary of the fluorescence quenching of MOF **1'** upon exposure to DMNB, NB, *p*-NT and 2,4-DNT 109
Figure 3.17 Schematic of the calculated valence band maximum (VBM) and conduction band maximum (CBM) positions for **1'**. As well as the ionization potentials (IPs) and electron affinities (EAs) for the explosive TNT and 5 explosive related analytes 112
Figure 3.18 MOF **1'** regeneration results 114
Figure 3.19 MOF **1'** interferents study results 116
Figure 3.20 Fluorescence quenching percentages demonstrated by 'thin films' of **1M'** upon exposure to explosive related analytes DMNB, NB, *p*-NT and 2,4-DNT 118
Figure 3.21 Fluorescence emission profile of MOF **1M'** upon exposure to DMNB vapours 119
Figure 3.22 Fluorescence emission spectrum of MOF **2'** in the solid-state 121
Figure 3.23 Fluorescence quenching percentages demonstrated by 'thin films' of **2'** upon exposure to explosive related analytes NB and *p*-NT 122
Figure 4.1 Illustration of the **tbo** framework topology of MOF HKUST-1 and the isoreticular Cu MOF as synthesised by Eddaoudi *et al.* 129

Figure 4.2 'DVS Vacuum' analyser instrument 134
Figure 4.3 Example of a MOF **3′** suspension in acetonitrile (MeCN) 136
Figure 4.4 Experimental set up for the prolonged exposure of MOF **3′** to the saturated vapours of 2,4-DNT 140
Figure 4.5 NMR spectrum of linker H_8L 141
Figure 4.6 MOF **3** ASU 144
Figure 4.7 Unit cell and dual-pore representation for MOF **3** 145
Figure 4.8 Three dimensional representations of the over topology of metal-organic framework **3** 146
Figure 4.9 TNT molecular dimensions 147
Figure 4.10 PXRD patterns confirming the phase purity of synthesised MOF **3** 148
Figure 4.11 SEM images of MOF **3** crystals 148
Figure 4.12 PXRD patterns of MOF **3** after each stage of activation 149
Figure 4.13 SEM images of the activated MOF **3′** crystals 150
Figure 4.14 The proposed nature of active MOF **3′** 153
Figure 4.15 PXRD patterns showing the restoration of long-range order in MOF **3′** upon immersion in MeCN 154
Figure 4.16 Graph illustrating the results of the thermogravimetic analysis of MOFs **3** and **3′** 155
Figure 4.17 PXRD patterns of MOF **3′** pre and post- exposure to ambient air conditions 158
Figure 4.18 PXRD pattern of MOF **3′** pre and post-degassing to afford MOF **3″** 160
Figure 4.19 Kinetics of uptake in MOF **3″** upon exposure to 0-90% relative pressure of water vapour as a function of time 161
Figure 4.20 The water vapour sorption and desorption isotherms for MOF **3″** at 25 °C 162
Figure 4.21 HKUST-1 water sorption and desorption isotherms at various temperatures 164
Figure 4.22 Averaged results of three repeated water sorption isotherms of MOF **3″** 165
Figure 4.23 Graph comparing the water sorption isotherms of MOF **3″** obtained at different temperatures 166
Figure 4.24 Explosive substances and related compounds used in MOF **3′** solution-phase sensing 168
Figure 4.25 Fluorescence excitation and emission spectra of MOF **3′** suspended in MeCN. 169
Figure 4.26 Fluorescence emission spectra of MOF **3′** suspended in MeCN and Linker H_8L (dissolved in DMF) 170

Figure 4.27 Graph illustrating the effects of particle settling in MOF **3′** suspensions 171
Figure 4.28 Vortexing steps to establish stable baseline fluorescence emissions of MOF **3′** in MeCN 172
Figure 4.29 The effect of dilution by MeCN addition on the fluorescence of a MOF **3** suspension 173
Figure 4.30 Fluorescence emission spectrum of MOF **3′** upon the incremental addition of a 1 mM solution of Tetryl 175
Figure 4.31 Fluorescence emission spectra of MOF **3′** upon the addition of 1 mM solutions of TNT, 2,4-DNT, RDX and PETN 176
Figure 4.32 Magnitudes of quenching of MOF **3′** upon exposure to Tetryl, TNT, 2,4-DNT, RDX and PETN. 177
Figure 4.33 Computational band gap simulations of MOF **3′** and the ionization potentials and electron affinities of a range of explosives and related analytes 179
Figure 4.34 Partial charge density calculations of the lowest energy unoccupied state of nitrobenzene in the MOF 180
Figure 4.35 Stern-Volmer plots of MOF **3′** after the addition of Tetryl, TNT, 2,4-DNT, PETN and RDX 181
Figure 4.36 Stern-volmer plots and absorption/emission spectra of MOF UiO-68@NH_2 and eight explosive substances and related compounds in water 183
Figure 4.37 Comparison of the emission spectrum of **3′** and the absorption spectra of Tetryl, 2,4-DNT, PETN, RDX and TNT 184
Figure 4.38 PXRD patterns of MOF **3′** confirming stability after solution-phase sensing 186
Figure 4.39 Fluorescence of MOF **3′** upon exposure to saturated 2,4-DNT vapours 188
Figure 4.40 Fluorescence emission spectrum of MOF **3′** after exposure to 2,4-DNT vapours repeated experiment 188
Figure 4.41 PXRD patter of a MOF **3′** thin film pre- and post- 2,4-DNT exposure 189
Figure 4.42 Examples of previously reported MOFs that demonstrate fluoresce emission increases due to the rigidification of framework structures 192
Figure 5.1 General overview of the array-based sensing process 201
Figure 5.2 Metal-organic framework array experimental design 205

Figure 5.3 Three-dimensional crystal structures of the three MOFs used in the MOF sensing array 206
Figure 5.4 Synthesis of MOF $Zn_2(oba)_2(bpy)\cdot DMA$ (**AM2**). 209
Figure 5.5 Synthesis of MOF $Eu(BTC)(H_2O)\cdot 1.5H_2O$ (**AM3**). 210
Figure 5.6 Illustrative example of canonical plots generated from LDA 214
Figure 5.7 PXRD patterns of the MOFs used in the MOF sensing array 217
Figure 5.8 Stern-Volmer quenching plot of the MOF array responses to the explosives (and related compounds) tested 219
Figure 5.9 MOF array response pattern presented used in LDA 221
Figure 5.10 Canonical plot detailing the results of the LDA on the MOF array upon exposure to the tested analytes in the 62.5 μM - 38.5 μM concentration range 222
Figure 5.11 Canonical plot showing the classification results of the LDA on the MOF array sensing responses to the analytes in the 62.5 μM - 26.0 μM concentration range 224
Figure 6.1 Schematic detailing the principles of explosive vapour pre-concentration 230
Figure 6.2 Molecular structure of one repeat unit of Tenax® TA 231
Figure 6.3 Details of the Experimental design probing the capability of MOF **3′** as a TNT explosive vapour pre-concentrator 234
Figure 6.4 Representative MOF **3′**-containing glass sample tube used for TNT pre-concentration experiments 237
Figure 6.5 Markes International Ltd. tube conditioner used for the degassing of the sorbent sample tubes 238
Figure 6.6 A simplistic schematic of the vapour generator instrument used to produce known quantities of TNT vapours 239
Figure 6.7 The sampling technique employed for the collection of TNT vapours produced from the vapour generator 241
Figure 6.8 A schematic detailing the permeation oven set-up used to generate TNT vapours from solid TNT flake 242
Figure 6.9 Pictures of the permeation oven used to generate TNT vapours from solid TNT flakes 243

Figure 6.10 An example TNT chromatogram generated from the thermal desorption and GC-MS analysis of a 500 ng standard Tenax® TA stainless steel tube 247
Figure 6.11 Pictures comparing the colour of MOF **3′** crystals pre- and post-degassing at 230 °C for 30 minutes 249
Figure 6.12 Amount of TNT vapours quantified from initial proof-of-concept capture and release experiments using MOF **3′** and Tenax® TA sorbents 250
Figure 6.13 Calibration curve for the GC-MS analysis of the sample tubes used to capture TNT vapours produced by the vapour generator TNT source 253
Figure 6.14 Amount of TNT (ng) that was pre-concentrated by different sample tube types sampling TNT produced from the vapour generator 253
Figure 6.15 The amount of TNT quantified by GC-MS from the MOF pre-concentrator samples second desorption study 257
Figure 6.16 The TNT quantities (ng) obtained from GC-MS analysis of four different sample tube types used to sample the TNT vapours produced from the permeation oven 258
Figure 6.17 TNT amounts (in nanograms) obtained from the pre-concentration of TNT vapours after secondary MOF **3′** sample tube degassing 261
Figure 6.18 TNT amounts (ng) obtained from TD and GC-MS analysis of MOF **3′** and Tenax® glass tube samples degassed at different temperatures, used to sample TNT vapours from the permeation oven 263
Figure 6.19 The different amounts of TNT obtained from the TD and GC-MS analysis of four 230 °C degassed MOF **3′** samples 265
Figure 6.20 PXRD patterns of a MOF **3′** sample degassed at 100 °C after pre-concentration experiments, the same MOF **3′** sample as-synthesised and activated 267
Figure 6.21 PXRD pattern of an as synthesis, activated and 230 °C degassed proof-of-concept MOF **3′** pre-concentration sample 269
Figure 6.22 Infra-red analysis of the crystals present in the 230 °C (POC) and 100 °C degassed MOF **3′** pre-concentration samples 271

Figure 6.23 SEM images of the crystals present in the 230 °C (POC) and 100 °C degassed MOF **3′** sample used in TNT pre-concentration experiments 272
Figure 6.24 ^{1}H NMR analysis of the MOF **3′** degassed at 100 °C TNT pre-concentration sample which has been acid digested in DCl in D_2O and dissolved in $DMSO_{d6}$ 275
Figure 6.25 ^{1}H NMR analysis of the MOF **3′** degassed at 230 °C proof-of-concept pre-concentration sample which has been acid digested in DCl in D_2O and dissolved in $DMSO_{d6}$ 275
Figure 6.26 Thermogravimetric analysis on the MOF **3′** samples degassed at 100 °C and 230 °C and used in TNT pre-concentration experiments 277

LIST OF TABLES

Table 2.1 Vapour pressures of some common explosives and related compounds 13
Table 2.2 Possible detection outcomes of a trace explosives detector 15
Table 2.3 Water exposure level 61
Table 2.4 Metric of water stability 61
Table 3.1 Crystal and structure refinement data for MOFs **1** and **2** 100
Table 3.2 Literature reports for DMNB sensing 111
Table 3.3 Molecular dimensions of the tested analytes 112
Table 4.1 Saturated vapour pressures of water used in DVS experiments at different temperatures. 135
Table 4.2 Crystal data and structure refinement comparison 143
Table 4.3 Explosives molecular dimensions 147
Table 4.4 Results of PXRD Le Bail fitting on MOF **3** and **3′** 151
Table 4.5 MOF **3′** BET surface area values as obtained from water sorption experiments 167
Table 4.6 Analyte concentration conversion table 178
Table 4.7 K_{SV} constants of MOF **3′** upon exposure to TNT, 2,4-DNT, RDX, PETN and Tetryl 182
Table 4.8 Limits of detection 185

Table 4.9 Results of PXRD Le Bail fitting on MOF **3′** exposed to 2,4-DNT (**3′**-DNT), atmospheric air (**3′**-cont.) and the as synthesised sample for comparison (**3**) 190
Table 5.1 Example confusion matrix 213
Table 5.2 LDA classification matrix for the MOF array upon addition of the analytes in the 62.5 µM - 38.5 µM concentration range 223
Table 5.3 LDA cross-validation (jackknifed) classification matrix for the MOF array upon addition of the analytes in the 62.5 µM - 38.5 µM concentration range 223
Table 5.4 LDA classification matrix explosives and related analytes in the 62.5 µM - 26.0 µM concentration range 225
Table 5.5 LDA jackknifed classification matrix for analytes in the 62.5 µM - 26.0 µM concentration range 225
Table 6.1 Details of the specific thermal desorption conditions used on the pre-concentration experiments sample tubes 245
Table 6.2 Pre-concentrator efficiencies for the POC MOF **3′** and glass tube Tenax® TA samples used to pre-concentrate the TNT vapours produced from the vapour generator 255
Table 6.3 Pre-concentrator efficiencies for an original POC MOF (third cycle pre-concentration) and Tenax® TA (in glass tubes) after sampling TNT vapours from the permeation oven 263
Table 6.4 Elemental analysis on 100 °C and 230 °C degassed (POC) MOF **3′** samples used in TNT pre-concentration 273

ACRONYMS

1,4-DNB 1,4-dinitrobenzene

2,3-DNT 2,3-dinitrotoluene

2,4-DNT 2,4-dinitrotoluene

2,6-DNT 2,6-dinitrotoluene

3D three-dimensional

AFCP amplifying fluorescent conjugate polymer

AIE aggregation induced emission

ANFO ammonium nitrate fuel oil

ANN artificial neural network

ASU asymmetric unit

BET Brunauer-Emmett-Teller

BTC benzene-1,3,5-tricarboxylate

CB conduction band

DCM dichloromethane

DEE dexter electron exchange

DMA *N*,*N*-dimethylacetamide

DMF *N*,*N*-dimethylformamide

DMMP dimethyl methylphosphonate

DMNB 2,3-dimethyl-2,3-dinitrobutane

DNB dinitrobenzene

Dstl Defence Science and Technology Laboratory

DVS dynamic vapour sorption

EA electron affinity

EA elemental analysis

EI electron ionization

EtOH ethanol

FRET Förster resonance energy transfer

FT-IR Fourier transform-infrared spectroscopy

GC-MS gas chromatography-mass spectrometry

GC gas chromatograph

HCA hiereachical clustering analysis

HME home-made explosive

HMTD hexamethylene triperoxide

HOMO highest occupied molecular orbital

HPLC high-performance liquid chromatography

IC internal conversion

IED improvised explosive device

IMS ion-mobility spectrometer

IP ionisation potential

IPA isopropyl alcohol

IR infrared

ISC intersystem crossing

IUPAC International Union Pure and Applied Chemistry

LC-MS liquid chromatography-mass spectrometry

LDA linear discrimination analysis

LLCT ligand-ligand charge transfer

LMCT ligand-to-metal charge transfer

LOD limits of detection

LUMO lowest unoccupied molecular orbital

MeCN acetonitrile

MeOH methanol

MLCT metal-to-ligand charge transfer

MOF metal-organic framework

MS mass spectrometer

NB nitrobenzene

NG nitroglycerine

ng nanogram

NM nitromethane

NMR nuclear magnetic resonance

ORTEP Oak Ridge thermal-ellipsoid plot

PA picric acid

PCA principle component analysis

PE pre-concentrator efficiency

PETN pentaerythritol tetranitrate

pg picogram

PIET photo-induced electron transfer

POC proof-of-concept

ppb parts per billion

ppm parts per million

PXRD powder X-ray diffraction

QP quench percentage

RDX cyclotrimethylene trinitramine

RH relative humidity

RP relative pressure

rpm repetitions per minute

RT retention time

SAV solvent accessible volume

SBU secondary building unit

SD standard deviation

SEM scanning electron microscopy

SV stern-volmer

SVM support vector machines

SVP saturated vapour pressure

TATP triacetone triperoxide

TCSPC time-correlated single photon counter

TD thermal desorption

Tetryl 2,4,6-trinitrophenylmethylnitramine

TGA thermogravimetric analysis

TNP 2,4,6-trinitrophenol

TNT trinitrotoluene

UMS unsaturated metal sites

VB valence band

VOC volatile organic compound

XPS X-ray photoelectron spectroscopy

1

INTRODUCTION AND SCOPE

The threat of terrorism-related explosives attacks is of global concern. Although recent years have seen terrorists use a wide range of different attack methods, the use of explosives within terrorist incidences is still highly prevalent [1, 2]. Since the start of this doctoral research in September 2014, until the present day (February 2018), a vast number of mass casualties have resulted from the direct use of explosives in terrorist-related assaults around the world. Some of which include:

- Sinai, Egypt, 31st of October 2015 - An improvised explosive device (IED) is believed to have been smuggled onto a Russian Metrojet airliner, causing it to crash, killing **224** people [3].
- Paris, France, 13th of November 2015 - Eight militants carried out coordinated shootings and suicide bombings in the French capital, leaving **129** dead, and hundreds more injured [4].
- Brussels, Belgium, 22nd of March 2016 - Coordinated suicide attacks killed **32** individuals and injured more than 300 in Brussels airport and metro station [5].
- Baghdad, Iraq, 3rd of July 2016 - A suicide truck and roadside bomb targeted a crowded shopping area killing **281** and injuring hundreds more people [6].
- Manchester, United Kingdom, 22nd of May 2017 - A suicide attack on a concert arena killed **23** and injured 250 [7].

As evidenced by the above, the explosives threat is very real. As a consequence of such events, the United Kingdom's international ter-

rorism threat level remains at severe, meaning that a terrorist attack within the UK is highly likely [8]. The UK's strategy for countering terrorism (CONTEST) has defined objectives which aim to mitigate the explosives threat [1]. Under the *protect* stream of CONTEST, targets have been outlined to:

- Strengthen UK border security
- Reduce the vulnerability of the transportation network
- Increase the resilience of infrastructure in the UK
- Improve protective security for crowded places and people at specific risk of terrorism

Therefore, there is a crucial demand for explosives detection methods that can successfully identify explosives on a surface, person or as a vapour, in order to meet the protection objectives outlined above. However, explosives detection is not a trivial task, and many factors exacerbate its difficulty; including the very complex environments in which detection is required, as well as the clever concealment of explosives in an attempt to avoid their detection, to name just a few. Although a number of effective technologies exist and are operationally used, there is a growing scope for research into novel materials and methods to add to the current capabilities so that a multifaceted approach to explosives detection can be used [9, 10].

This thesis endeavours to further explore the potential that metal-organic frameworks may hold as fluorescence-based chemical sensors of explosive substances and related compounds, it also investigates their capabilities as explosive vapour pre-concentrators.

2

LITERATURE REVIEW

2.1 EXPLOSIVE MATERIALS

An explosive material is one that has the potential (upon initiation by an appropriate stimulus) to produce a very rapid exothermic reaction, whereby a small quantity of solid or liquid is converted into a large volume of gas. It is the unprecedented speed of an explosives reaction that distinguishes it from conventional combustion [11–13].

A good approximation for the thermodynamic favourability of an explosive reaction is that of Gibbs Free Energy:

$$\Delta G = \Delta H - T\Delta S \tag{2.1}$$

To achieve a successful explosive reaction (a large and negative ΔG); large heats of formation (negative ΔH) and a large increase in reaction volume (large and positive ΔS) are required. For optimal energy release, the explosive composition should be able to convert all of its constituent atoms into gases [13]. Explosive substances (or mixtures) are typically comprised of oxygen, nitrogen and "fuel" components. While nitrogen content is not paramount, it is highly desired for greater energy release, owing to the formation of stable N_2 gas (yielding a more negative ΔH). Additionally, the evolution of N_2 gas increases the expansion of matter and thus, brings greater disorder to the system (increased ΔS). Nitrogen is generally incorporated into explosives through nitrogroups; NO, NO_2 and NO_3^- [11]. Crucially, for the successful conversion of the fuel elements into gases;

'Fuels' refer to oxidizable elements such as carbon and hydrogen.

sufficient oxygen content must be present within the explosive compounds. Cyclotrimethylene trinitramine, or RDX, is an example of an explosive substance with sufficient oxygen content to convert all of its constituent atoms into stable gases, therefore producing a highly powerful explosion. When RDX is detonated, the nitrogen and oxygen molecules separate and subsequently unite with the fuel components of the system; producing the gases shown in Scheme 2.1 [11, 13].

Scheme 2.1: Reaction scheme detailing the detonation of RDX.

2.2 CLASSIFICATION OF EXPLOSIVES

Explosive materials can be classified in three main ways; by their chemical nature, performance or uses [11]. These classifications are not mutually exclusive, and explosives are often characterised using all three descriptives.

2.2.1 *Chemical nature*

Explosive materials can be primarily divided into two groups depending on their chemical nature; those that are classed as SUBSTANCES which are explosive, such as RDX (Scheme 2.1), and those that are MIXTURES, for example the historical 'black powder' also known as *'gun powder'**[11]. Explosive SUBSTANCES are further categorised de-

* Black powder, also known as gun powder, was most likely the first explosive composition ever discovered. This mixture contains a fuel composition of charcoal and sulphur which is mixed with the oxidiser potassium nitrate [14].

pending on their molecular construction, namely their functional group composition [11]:

- Nitroaromatic compounds (NACs)
- Nitric esters
- Nitramines
- Nitroaliphatics
- Derivatives of chloric and perchloric acids
- Azides
- Peroxides
- Various other explosive compounds such as fulminates, acetylides, and ozonides.

The classification of explosives by their molecular functionality is extremely useful when discussing sensors that target specific functional groups for detection (as will be demonstrated in Section 2.4.4). However, categorising explosives in this manner does not indicate as to their performance. Thus, especially within practical contexts (such as within military settings), the classification of explosives is achieved based on their detonation velocities, sensitivities and their role within the 'explosives train' [11] (defined in Section 2.2.3.1).

2.2.2 *Performance*

Detonation velocities

The velocity at which the chemical reaction proceeds through an explosive material and the amount of heat and gas evolved, will depict its practical effects. An explosive material is categorised as either a DEFLAGRATING (low) explosive or a DETONATING (high) explosive. If the speed of the decomposition is less than or equal to the speed of sound (subsonic); the explosive is regarded as deflagrating. Alternatively, when a reaction wave propagates through an explosive material at a supersonic velocity; the material is classed as a detonating (high) explosive. The majority of explosives used within military and commercial contexts, or even those utilised for terrorist activity; are detonating high explosives, as they produce the greatest explosive effects [13].

Sensitivities

The sensitivity of an explosive is the degree to which it can be initiated by stimuli such as impact, heat or friction. This classifies explosives as either PRIMARY explosives, SECONDARY explosives or as PROPELLANTS [11].

PRIMARY explosives burn to detonation (extremely rapidly) and have the ability to transfer their detonation products (heat or shock) to less sensitive explosives. Primary explosives will detonate when subject to heat, shock, friction or electric spark. Detonation velocities of primary explosives are typically between 3500 - 5500 m/s [11].

SECONDARY explosives are distinguished from primary explosives based on their sensitivity; they cannot be easily detonated by application of heat and shock stimuli. Secondary explosives are initiated to detonation by the shock produced by the explosion of primary ex-

plosives. Secondary explosives are usually much more powerful than primary explosives with typical detonation velocities in the range of 5500 - 9000 m/s [11].

PROPELLANTS are an alternate class of explosive. These are self sustaining combustible materials that deflagrate and not detonate (unless placed under extreme conditions), an example of which is black power [11, 13].

2.2.3 *Uses of explosives*

Explosives can also be classified by their *intended* area of use; COMMERCIALLY used explosives, explosives designed for MILITARY purposes, or HOME-MADE explosives (HMEs); produced for illegal/terrorist activities.

COMMERCIAL explosives encompass those that are to be used for demolition within the construction and mining industries. Fuel oxidizer mixtures such as ammonium nitrate fuel oil (ANFO) are most commonly encountered, as these secondary explosives have relatively slow detonation velocities, for the controlled fragmentation of moving rock and dirt [13].

Fuel oil refers to oil fractions as obtained from petroleum distillation such as diesel.

MILITARY explosives make use of high detonating secondary explosives such as Pentaerythritol tetranitrate (PETN), cyclotrimethylene trinitramine (RDX), 2,4,6-Trinitrophenylmethylnitramine (Tetryl) and 2,4,6-Trinitrotoluene (TNT) (Figure 2.1). Military grade explosives require a high level of stability† to prevent accidental detonation when being used operationally. Thus, explosives like RDX, TNT, Tetryl, PETN that commonly occur in powder (or melt-cast) form are typically combined with plasticisers to impart greater stability

† Stability in this context is referring to both the ability to not decompose at elevated temperatures or over time, as well as to not be initiated to decomposition or detonation by flame, impact, friction or spark.

as well as malleability to these compounds; producing explosive formulations like C4 (or PE-4) and SEMTEX [13, 15].

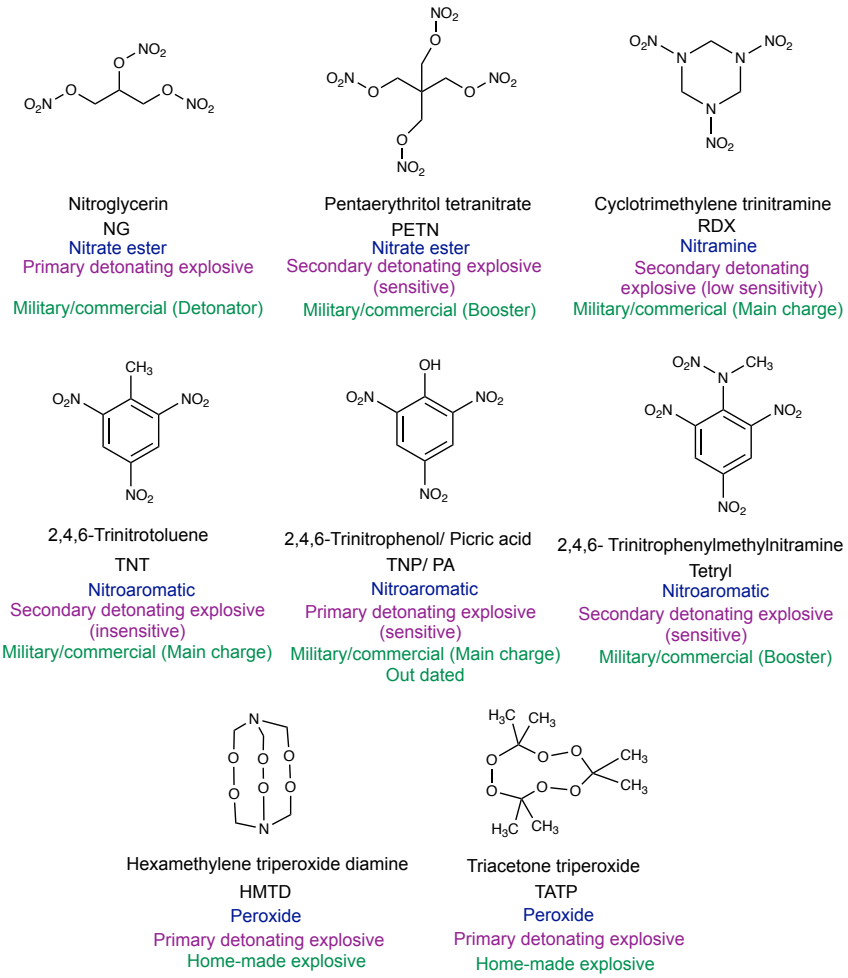

Figure 2.1: Molecular structures of some commonly occurring explosive substances. Detailed underneath each explosive is the chemical nature, performance and use category within which it belongs.

Home-made explosives (HMEs) are defined as those that that can be readily produced through "high street" commercially available chemicals. Examples include fertiliser (ammonium nitrate) used to formulate fuel oxidisers such as ANFO, as well as bleach (sodium hypochlorite), acetone or hydrogen peroxide; used for the synthesis of explosive substances (usually peroxide-based) such as triacetone triperoxide (TATP). Although also used in commercial denotation, home-made ANFO based explosives have featured in a number of terrorist incidences such as the 1995 Oklahoma City bombings [13]. Lately,

the use of peroxide-based explosives such as TATP and hexamethylene triperoxide (HMTD) have gained in popularity, owing to the ease of starting material availability and simple preparatory methods (although despite their ease of synthesis; these materials are often very dangerous to produce) [13]. For reference, peroxide-based explosives (TATP) were used in the Paris and Manchester bombings mentioned in Chapter 1 [16].

2.2.3.1 *The explosives train*

An alternate point to note is that explosive devices (bombs) can be comprised of several substances and/or mixtures. This is mainly due to the fact that in order for an explosive event to occur using secondary explosives; they must be stimulated by the detonation of a primary explosive. For this reason, primary explosives are known as INITIATORS (or DETONATORS) of secondary explosives in what is known as an EXPLOSIVES TRAIN. With this said, secondary explosives with very low sensitivities such as TNT, require greater initial detonating shocks and velocities to be initiated than can be supplied from primary explosives. Thus, to detonate these explosives, BOOSTERS are used. These are secondary explosives with high sensitivity that are used to detonate secondary explosives with low sensitivity (MAIN EXPLOSIVE CHARGE) [13, 17]. The explosive devices fabricated by adversaries engaging in illegal/terrorist activities are typically termed 'improvised explosive devices' (IEDs) and can take various non-traditional forms [18].

2.3 EXPLOSIVES DETECTION

2.3.1 *Approaches to explosives detection*

The detection of explosives involves collecting a sample, processing the sample and deciding whether explosives are present or not [19]. The first decision in explosives detection is which physical form of the explosive is to be detected. Explosives can be detected in either BULK or TRACE form [20]. In BULK detection, macroscopic amounts of explosive materials are detected, most typically through the use of imaging [20]. In essence, bulk detection seeks to locate an entire mass of an explosive within a device [10]. In TRACE explosives detection, non-detonatable microscopic quantities of explosive materials are detected. These are found as either particulates on surfaces or as vapours emitted from bulk devices [21, 22]. Thus, trace explosives detection involves both vapour and particle detection techniques. Although bulk detection is a widely used approach, this thesis focuses on the trace detection of explosives.

Within trace explosives detection, distinctions can also be made between CONTACT and STAND-OFF detection approaches. Both of which are related to the various ways in which explosive materials are sampled for presentation into trace detectors. Contact detection as the name suggests, requires physical contact with the sample under interrogation during the detection procedure. For example the swabbing of a surface, for the detection of explosive particles. ‡ On the other hand, stand-off detection most typically makes use of explosive vapours for detection (although particle stand-off detection is also possible as will be discussed), and is able to place the detection

‡ It is important to note that vapour-phase detectors can be used to analyse particles collected from surfaces, however, their vaporization (within the detector) is required prior to detection [23].

method (and those using it) at some distance away from the explosive being detected. This distance, at present, is typically within one meter of the threat material or screening area [23]. It has been suggested by the explosives detection community that the ideal detection technique would be able to detect trace amounts of explosives from a stand-off distance that ensures personnel safety [24][19]. It can be argued that the direct, stand-off sensing of explosive vapours is of particular importance; as the probability of detecting the main explosive device is high, due to the vapours being emitted directly from the source. In the case of particle detection, information is obtained that the interrogation surface (be that a piece of luggage or a suspects hands) has had some contact with explosive materials (either directly or through contamination), but this does not necessarily mean that the explosive charge is present [25]. However, the trace detection of explosives, especially in the vapour phase, is not a trivial task.

2.3.2 *Challenges in trace explosives detection*

Several factors that exacerbate the difficulty of explosives detection include; the wide range of explosive materials required to be detected, the physical properties of explosives; namely their very low vapour pressures, the dynamic environment in which we need to sense explosives, as well as amongst others; the need for a timely detection response [9, 22, 23].

2.3.2.1 *Wide range of explosive materials*

Trace explosive detection technologies are required to be able to detect a wide range of explosive materials belonging to different chemical classes. For example, trace detectors are required to detect both traditional high explosives such as TNT, as well as chemical used in

IEDs such as ammonium nitrate, TATP and other HME substances or mixtures. The differing chemical nature of these explosives often renders broad-class explosives detection to be quite challenging [9, 10, 22, 26]. For example, some sensors such as optical sensors are effective at detecting nitroaromatic explosive substances, but struggle to detect nitroaliphatic or peroxide based explosives (Section 2.4.4) [26].

2.3.2.2 *Low Vapour Pressures*

A substantial challenge in the vapour-phase detection of explosives is the very low volatility of most explosives at ambient temperature. In addition, explosive vapours are often present in very small sample sizes within large open air environments; which exacerbates the difficulty in their sampling and detection. Moreover, explosives are often concealed within packages by adversaries to prevent their detection, this in turn further reduces the amount of explosive vapours available for presentation into a detector [22]. Kolla *et al.* reported that the wrapping of an explosive can decrease vapour concentrations omitted from the material by a factor of 1000 [27]. As a consequence, many vapour-phase detection platforms detect precursors, breakdown products, or by products of explosives as well as the explosive compounds themselves, as these often give a good indication as to the presence of explosive materials and have much higher vapour pressures than their parent compound [23]. For example, detectable explosives related compounds of TNT include 2,6-dinitrotoluene (2,6-DNT), 2,4-dinitrotoluene (2,4-DNT), *para*-nitrotoluene (*p*-NT) and nitrobenzene (NB), shown in Figure 2.2. Furthermore, regulations state that taggants, such as 2,3-dimethyl-2,3-dinitrobutane (DMNB), must be used in the manufacture of all commercial and military grade plastic explosives in countries such as the United Kingdom and the United States [28, 29]. These highly volatile organic components are

used in explosive compositions such as C4 and SEMTEX to aid detection capabilities owing to their higher vapour pressures [22, 23]. Table 2.1 details the equilibrium (saturated) vapour pressures (SVPs) of some common explosive substances and related compounds at room temperature.

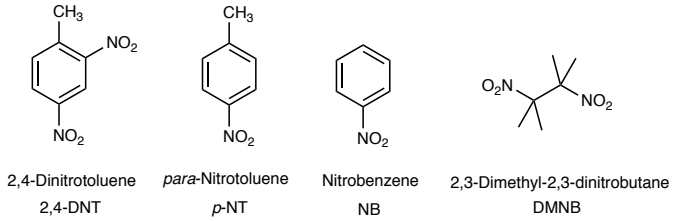

Figure 2.2: Molecular structures of some detectable explosives related compounds.

Table 2.1: Vapour pressures of some common explosives and related compounds[30].[a]

Class	Name	Acronym	$P_{vap.}$ 25°C/Torr[b]
Nitroaromatic	2,4,6-Trinitrotoluene	TNT	5.5 x 10 $^{-6}$
	2,4,6-Trinitrophenylmethylnitramine	Tetryl	6.51 x 10 $^{-9}$
	2,4,6-Trinitrophenol/picric acid	TNP/PA	7.48 x 10 $^{-7}$
Nitramine	Cyclotrimethylene trinitramine	RDX	3.30 x 10 $^{-9}$
Nitrate ester	Nitroglycerine	NG	4.81 x 10 $^{-4}$
	Pentaerythritol tetranitrate	PETN	1.16 x 10 $^{-8}$
Peroxides	Triacetone triperoxide	TATP	4.63 x 10 $^{-2}$
	Hexamethylene triperoxide diamine	HMTD	not reported

Class	Name	Acronym	$P_{vap.}$ 25°C/Torr
Nitroaliphatic	2,3-Dimethyl-2,3-dinitrobutane	DMNB	2.1 x 10 $^{-3}$ [c]
	Nitromethane	NM	36.5
Nitroaromatic	*para*-nitrotoluene	*p*-NT	4.89 x 10 $^{-2}$
	2,4-Dinitrotoluene	2,4-DNT	2.63 x 10 $^{-4}$
	2,6-Dinitrotoluene	2,6-DNT	6.20 x 10 $^{-4}$
	Nitrobenzene	NB	2.4 10 $^{-1}$ [d]

a Vapour pressures have been obtained from Östmark *et al.* [30] unless stated otherwise.

b 1 Torr = 133.322 Pa = 1.3158 x 10 $^{-3}$ atm; 1 Pa = 7.5006 x 10 $^{-3}$ Torr = 9.8692 x 10 $^{-6}$ atm; 1 atm = 760 Torr = 760 mm Hg = 101325 Pa. 1 ppb (in air @ STP) = 101325 x 10 $^{-9}$ = 1.01 x 10 $^{-4}$ Pa.

c Oxley *et al.*[13]

d Li *et al.* [31]

Owing to the low vapour pressure of most explosives, vapour-phase detectors are required to have high levels of sensitivity and low limits of detection (LOD) in order to detect the low levels that may be present in a search environment. However, with increased sensitivity the consideration of selectivity becomes more critical (as discussed in Section 2.3.2.3).

Sensitivity = the probability of the detector identifying an explosive when it is present (the change in measurement signal per unit concentration of target analyte) [32] [19].
LOD = the lowest concentration of analyte able to be detected [32].
Selectivity = the ability of the detector to identify targets only *when they are present. A detector can respond selectively to a group of analytes or specifically to one analyte [32][19].*

The low volatility and very adhesive nature of the majority of explosives does however benefit contact sampling techniques as many explosives are found to adsorb onto surfaces, thus, are available for swab sampling and particle detection [19, 26, 33, 34]. For example, a first generation C4 fingerprint has been reported to yield several micrograms of RDX on a surface which is potentially higher than the amount of RDX that may be present in vapour form in a given scenario, thus, particle sampling is often deemed 'easier' than vapour-phase sampling and is a routinely employed approach to explosives detection within transportation hubs such as airports [19, 22, 35]. Nevertheless, explosive particle contamination requires careful contact sampling methods to be employed in order to effectively retrieve particles from surfaces prior to their detection [35].

2.3.2.3 *Challenging Detection Environments*

An intuitive solution to the challenging vapour pressures of explosives is to produce extremely sensitive detectors (i.e. increase the likelihood of finding the target being sought), however, due to the extremely complex and dynamic environments in which the detection of explosives is required, selectivity becomes increasingly important when detecting ultratrace levels of explosives i.e. the detector responds to explosives and not interferents [10]. Interferents are classed as compounds that may interfere with the detection of explosives; leading to errors in detection known as FALSE ALARMS [36]. In oper-

ational detection environments there are many different compounds that may act as interferents of detectors (both vapour and particle detectors), such as; volatile organic compounds (VOCs), dust and even water molecules (humidity) [23]. During a search for explosives a detector continuously operates within a two-by-two dimension of outcome possibilities (Table 2.2).

Table 2.2: Possible detection outcomes of a trace explosives detector [10].

System Indication	Actual Condition	
	Explosive Present	No Explosive Present
Explosive	True Positive	False Positive
No Explosive	False Negative	True Negative

A system may accurately determine the presence or absence of explosives; TRUE POSITIVES and TRUE NEGATIVES. Alternatively there are two error conditions (false alarms) that may arise, FALSE POSITIVES and FALSE NEGATIVES [10]. A FALSE NEGATIVE is a failure to detect an explosive when it is present; a missed target [19]. These typically arise from the lack of sensitivity of a system, interferents masking the presence of explosives or from user error (i.e. an incorrect interpretation of the detector response) [36, 37]. A FALSE POSITIVE is where a detector suggests the presence of an explosive when explosives are not present. Such outcomes are typical of detectors that lack selectivity and arise due to interferents yielding similar responses of the detector as explosives [19]. Therefore, the sensitivity and selectivity of an explosives detector are frequently in a trade off.

2.3.3 *Detector requirements*

As well as being able to accurately detect the low levels of explosives present within a given environment, in some instances it is also necessary to determine which explosive compound is present and in what quantity, this requirement depends on the situation in which the detector is operating. In fact, many requirements of explosives detectors are dependent on their intended environment of use. For example, a device intended for use in military search operations will have very different requirements to devices used in airport security. A military-used explosives detector will need to have a large dynamic range owing to the high background levels of explosives in military environments. Equally, the portability of the device is also a key requirement for use in military contexts. Whereas a device used in airport security can be fixed; but a high throughput is required [23].

DYNAMIC RANGE = *the analyte concentration from LOD to maximum concentration that can be reliably detected [34].*

THROUGHPUT = *the total time required for an object, person or area to be screened [38].*

Detection = the time required for a detector response from zero concentration to a step change in concentration of analyte (i.e. after sampling has taken place) [32].

Other requirements that necessitate careful consideration when implementing or designing an explosives detector for a particular detection scenario include [9, 23]:

- Real-time sensing *vs.* analysis of different samples
- Detection time
- Size and weight of the device
- Regeneration and reset time before the next measurement
- Operational ease of use (i.e. user friendly)
- Cost (initial investment, maintenance, consumables, lifetime of device)
- Robustness

A commonly held view in the explosives detection community is that whilst there is no single detection system that is perfect and

meets all the requirements for a given scenario (i.e. is capable of direct, stand-off vapour-phase detection at distances that ensures personnel safety, with high sensitivity, selectivity, and is able to identify the explosive that is present in a quick, cost-effective and non-disruptive way), current systems (whilst they do have their limitations) are in general very effective at meeting current threats. This is particularly true when multiple systems are used in conjunction with each other; in a layered or 'orthogonal' detection approach (some of these systems will be briefly discussed in Section 2.4) [39]. Nevertheless, it is acknowledged that the continued improvement of current detectors, and the development of new and emerging technologies, remains important in order to overcome existing and potential new challenges posed by new developments in the field of explosives detection [23].

Orthogonal detectors are those which exploit different physical or chemical properties of targets in their detection [10].

The next section will detail some existing explosives detection technologies with a primary focus on fluorescence-based detectors, before introducing fluorescent metal-organic frameworks and the research completed to date on their potential as explosives sensors; which are the focus materials of this thesis.

2.4 CURRENT TECHNOLOGIES

2.4.1 *Animal olfaction*

The use of sniffer dogs for the stand-off (short-range) detection of explosive vapours are widespread across both military and civilian security settings, and are deemed one of the most effective methods of explosives detection [23, 40]. This is due to their highly sensitive detection capabilities (dogs have been reported to detect down to part-

per-trillion[§] levels of explosives [23]), their ability to detect a broad range of explosives, their good selectivity, as well as their rapid, directional, portable and real-time detection capabilities [23, 40].

During canine olfaction, vapours are very effectively sampled into the dog's nasal cavity where they interact with various receptors. These interactions in turn cause a signal to be sent to the dogs brain where it is interpreted and perceived [41]. However, in order to successfully detect explosives, dogs must be trained to react to smells of interest, in a way that their handler can interpret, for example by sitting or freezing. Dogs are trained to recognise explosives by exposing them to known compounds of interest, as well as to interfering compounds, and rewarding them upon indicating correctly towards a target compound and not an interferent [23].

Whilst canine olfaction is very effective; it is not without its limitations. A significant disadvantage of dogs is the amount of training required for both the dog and handler, which is both lengthy and expensive. In addition, dogs can get tired, they require plentiful maintenance, they can be influenced by handler behaviour and it is difficult to ascertain whether a dog is fully operational in its duties i.e. whether it is 'working' or not. Furthermore, dogs are not able to detail which threat is present of the many they are trained to recognise and they lack the capability to give qualitative information [23, 24, 40].

Other animals have also been explored for explosives detection such as rats [42] and bees [43]. However, they too suffer drawbacks and are not suitable for all detection scenarios [23]. As a result, instrumental techniques are also used and continuously developed to give a further breadth to explosives detection capabilities.

§ 1 part-per-trillion (ppt) is 1 volume of vapour in 10^{-12} volumes of air [13].

2.4.2 *Separation and ion detection techniques*

Some of the most widely used techniques for the trace detection of explosives make use of molecular separation processes to separate different types of molecules (either whole or as fragments) present within a given sample into various fractions, prior to their detection. This allows for the potential isolation of target molecules from those that are interferents; imparting selectivity into the detection process. The most prominent of these technologies include gas chromatography (GC), mass spectrometry (MS) and ion mobility spectrometry (IMS). These techniques can each be used individually or they can be combined (e.g. a GC couple with an MS; GC-MS) for greater efficacy [23].

Common to all three of these techniques is that they require effective sample collection steps (whether that is in either the vapour or solid-state) that deliver adequate amounts of sample into the instrumentation to allow for their detection [10]. Further to this, since the concentrations of explosives available in screening scenarios are often very low (particularly in the vapour-phase) a pre-concentration stage maybe employed during sampling. Pre-concentrators are sorbent materials that enrich analyte concentrations prior to delivering them to a detection system. Therefore, increasing the probability of detecting the analytes [36]. Pre-concentrators can be used in both vapour and particle detection methods [44]. Vapour-phase pre-concentrators will be discussed in further depth in Chapter 6.

2.4.2.1 *Gas chromatography*

Gas chromatography is purely an analyte separation and analysis method. It requires interfacing to a detector for the identification of the separated analytes. Such detectors are generally mass spectrom-

eters (MS), however, electron capture detectors amongst others have also been explored [10, 23]. GC analysis is able to be performed on both direct vapour and particle samples, although vaporization of the particles is required prior to their injection into the GC, however, this does not decompose the compounds within the samples [23].

In gas chromatography, a carrier gas (generally helium or nitrogen) transports the sample vapour through a column that is coated with either a liquid or a polymer; termed the stationary phase. The different constituents of the sample vapour interact with the stationary phase to varying extents. Therefore, they move through the column at different speeds, meaning that they emerge from the column at different 'retention times'. These different retention times are how the materials within the sample are separated. The separated materials are detected by a chosen device that responds with an intensity that is directly proportional to the concentration of that component in the mixture [45].

Gas chromatography is very useful for imparting selectivity in detection and a number of GC-MS explosives detectors are commercially available [23]. However, GC techniques have previously been criticised for their time-consuming procedures that have precluded their applicability to a number of screening scenarios [22]. However, substantial advancements in speed have been achieved and it has been shown that GC in combination with tandem mass spectrometry (two mass spectrometers interfaced with one another) can detect various explosives, at picogram (pg) detection levels, in under three minutes [46].

2.4.2.2 *Mass spectrometry*

In mass spectrometry, analytes are charged and separated according to the mass to charge (m/z) ratio of their parent ions and fragments,

using a magnetic or electric field. A sample (in either vapour or liquid form) is introduced into a sample chamber in one of many ways (for example from the outlet of a GC column), either at atmospheric or reduced (vacuum) pressure. It is then ionised using a specific method, for example; ion impact or electron impact. The resultant ions are then accelerated into the spectrometer (operating under high vacuum) which separates the ions based on their geometric path or time of flight [23, 45].

Mass spectrometry has been deemed a very effective tool for the detection of explosive vapours and particulates [47]. MS offers picogram or better detection sensitivities, high selectivity (on the basis of ion mass generally measured to < 1 Dalton (D)) and rapid instrumental response (some MS analysis times have been reported at around 5 seconds) [21, 23, 47].

Limitations of this technique have often been concerned with its lack of portability (due to the need for a vacuum environment within the spectrometer leading to bulky instrumentation) as well as high costs. However, since the advancements in atmospheric pressure ionisation (API) techniques, plentiful research into the miniaturization of mass spectrometers has been stimulated.

2.4.2.3 *Ion mobility spectrometry*

Ion mobility spectrometry (IMS) is a very prevalent technique used within airport security for the screening of small luggage articles *via* contact swabbing. Although vapour-phase detection is possible with IMS, the low SVP of explosives coupled with the difficulty in vapour sampling; has led to the predominant use of IMS for swab analysis [21].

The explosive particles collected on the swab surfaces are thermally desorbed inside of the IMS instrument. The vapours produced are

subsequently ionised using one of many methods, such as; through the use of radioactive materials (^{63}Ni), electrospray ionization, corona discharge ionization etc. It is important to note that the ionization of the samples (vapours) occurs at atmospheric pressure. The generated ions are then introduced into a drift tube along with a carrier gas (typically purified air), which, upon the application of an electric field; propels the ions through the field at characteristic velocities, which allow for their separation and identification. These velocities are dependent on the mass, charge, and dimensions of the ions [24][23]. The main distinguishing feature between IMS and MS is that the former does not require a vacuum in order to operate. Thus, the size and shape of the ions become important in IMS. This is due to collisions with the drift gas impacting on the movement of the ions through the electric field [48].

IMS has been used to successfully detect picogram (pg, 1 x 10^{-12} g) levels of explosives, with detection times of less than a minute. The popularity of this technique mainly arises from its simplicity [21, 24, 49]. Some reported limitations of the technique include: the fragmentation of explosives during the thermal desorption of the particles present on the collected swabs; leading to issues with selectivity. However, research into atmospheric pressure ionisation/desorption methods are emerging; to avoid the thermal decomposition of fragile explosives. In addition, IMS peaks are relatively broad compared with the total drift time (low resolution), which limits the selectivity of the method. However, combining IMS with GC has been proposed for increased selectivity and false alarm reduction. Further to this, the definitive identification of IMS peaks is often performed by interfacing an IMS instrument with a mass spectrometer [21]. Therefore yielding high selectivity (and sensitivity) in detection.

A common challenge for both IMS and MS is the ability to produce instruments that are compact and portable, whilst still retaining sensitivity as well as ensuring cost-effectiveness. Another significant point to note is that threat materials are typically identified (by both of these techniques) through the matching of the detector outputs (upon exposure to unknown samples) with a pre-defined library of outputs of the threat materials. If the detector outputs match those that are known; the threat is able to be identified. It is therefore imperative that the libraries within these instruments are constantly expanded in line with the constantly evolving threats [9].

2.4.3 *Spectroscopic techniques*

Spectroscopic techniques such as infra-red (IR) and Raman, have attracted ample attention within the explosives detection field. This is primarily due to their ability to perform non-destructive analysis of a wide variety of threat materials, and their potential for stand-off detection (particularly for Raman spectroscopy) [50, 51]. Both of these techniques detect and identify explosives *via* molecular characterisation from their vibrational spectra, adding further breadth to the approaches available for explosives detection [52].

The basic principles of IR spectroscopy are that samples (either solid, liquid or gas) are exposed to an infra-red beam of light and certain functional groups within the materials will absorb the radiation at specific wavelengths that are dependent on the frequency of their molecular vibrations (in the IR spectral range), as well as the change in the dipole moment of a specific molecular vibration [45, 53]. The resultant IR spectra are a reflection of the molecular structure of the interrogated material and can be interpreted in terms of

the functional groups present (or absent), or by pattern matching to a library database of reference spectra [50].

The detection of explosives using IR is especially successful for those containing NO_2 functional groups; owing to the strong infrared absorption signatures of the NO_2 moiety [45]. However, IR is not limited to the detection of just nitro-containing explosives, the detection of peroxides and explosives of other chemical natures are also possible [54]. Various forms of IR instrument have been explored for explosives detection, most of which use Fourier transforms (FT-IR) to allow for the full range scanning of frequencies simultaneously [53]. The most frequently encountered and commercially available instruments are attenuated-total-reflection (ATR) FT-IR instruments that require a trace sample (of between ng to μg mass) to be placed in contact with an ATR prism during detection. The benefit of this approach is that no sample preparation is required and analysis can be completed on solids or liquids. Reported limitations of IR include issues in sensitivity, selectivity, as well as the fact that this technique is very sensitive to the presence of moisture within a system (humidity interferent) [50, 52, 53].

Raman spectroscopy is similar to IR in that it also provides information on molecular vibrations. However, instead of absorbing the incident radiation; Raman relies on the sample scattering the radiation (which is typically a monochromatic laser source). Raman spectra record the inelastic scattering of radiation as a consequence of interaction with the molecular vibrations of a molecule, which require a change in polarisability in order to be Raman active.

Raman and IR spectroscopy are regarded as complementary techniques, this is due to the vibrations that are usually weak in IR spectra being strong in Raman spectra, and vice versa [50, 52]. Portable and commercially available Raman spectrometers have been devel-

oped for trace explosives detection. The main benefit of Raman is that it is able to perform stand-off (short-range at present) detection. In addition, Raman is able to analyse materials present within some containers (typically translucent) which is advantageous owing to the potential hazardous nature of the interrogation materials [50].

Limitations of Raman have included; laser-induced background fluorescence interfering with the detection of fluorescent and coloured compounds. In addition, Raman is frequently criticised for its low sensitivity (it is of lower sensitivity than IR methods). However, plentiful research into surface enhanced Raman spectroscopy (SERS) as well as the use of Raman in conjunction with IR, is aimed at preventing such limitations [50, 52, 53, 55].

2.4.4 *Sensors*

Sensors add another dimension to the explosives detection tool-kit. The advantages of sensors is that they can produce very low-cost, simple-to-use, portable devices, that have the potential for continuous real-time detection and can be economically viable for mass deployment. In addition, sensors have the capability to mimic the canine olfaction system through their incorporation in ELECTRONIC or CHEMICAL NOSES (discussed below). This is of significance as dogs are deemed the most reliable method of explosives detection to date, thus, by mimicking their detection approaches; sensor devices that are both sensitive and selective can potentially be obtained. Whilst only a few sensor-based technologies have been commercialised into devices for real-world explosives detection, a vast amount of research has and continues to lie within this field for the aforementioned reasons [24, 34, 53, 56]. A brief outline of sensors will be given below

with a main focus on fluorescence-based sensors for explosives detection.

Common to any type of sensor are two steps; recognition and transduction. Every sensor must contain an immobilised active species that can recognise a target such as an explosive or class or explosives (either specifically or with some degree of selectivity). It is then the transduction step that converts the recognition of the target by the active species into a measurable change [53]. The active species in a sensor can either be biological or chemical, and transduction can occur as a result of changes in electronic, mass or optical properties of a sensing material; giving many options for sensor design. Consequently, many combinations of active species and transducers have been researched for both the vapour and particle detection of explosives [53, 56, 57].

With the exception of highly specific biosensors (such as immunochemical sensors), a frequent criticism of chemical-based sensors (those that rely on weak chemical interactions between the targets and the receptors for analyte recognition) has been their lack of selectivity towards target analytes, and inability to discriminate between similar target compounds. However, electronic/chemical nose approaches are often employed in such scenarios with aim to overcome selectivity barriers [23, 45, 53, 58].

2.4.4.1 *Electronic/chemical noses*

In essence, electronic (or chemical) noses make use of arrays constructed from semi-selective receptors that each interact with target analytes in different ways and to different extents; depending on the nature of the receptor and the concentration of the analyte present. The collective response of a sensing array towards a target analyte (encompassing each of the different signals yielded by each individual

sensor) is processed using pattern recognition algorithms that generate a unique 'fingerprint' for each analyte the array is exposed to; which is stored in a library of fingerprints. Upon the exposure of the array to an unknown sample; the response produced by the array is processed and the fingerprint produced by the unknown is compared to those that are known. If there is a match between fingerprints; the unknown sample is able to be identified. Array-based sensing approaches are designed with aim to minimise false alarms [53, 58–60]. This concept of electronic/chemical noses will be discussed in substantial depth in Chapter 5.

2.4.4.2 *Chemical sensors for optical-based detection*

Chemical sensors that use optical-based signal transduction are a particularly significant sub-field within the field of sensors for trace explosives detection. Colourimetric and fluorescence-based chemical sensors are amongst the very few sensor systems that have been developed and commercialised for in-field trace explosives detection [21, 23, 61].

COLOURIMETRIC chemical sensors rely on a chemical reaction between the explosive target analyte and an indicator molecule to produce a colour change, which is typically visible to the naked eye. Colourimetric sensors are generally used to identify explosives by their class; based on their different chemical nature. For example, Meisenheimer and Greiss reactions have been used for the detection of nitroromatics and nitramines. In both instances, new chromophores are produced from the chemical reaction between the explosives and the indicator molecules, to yield the observed colour change [21, 61].

Many colourimetric 'kits' based on different chemical indicators targeting different classes of explosives are commercially available

for quick, simple, and easily interpretable in-field diagnostics. Such tools can exist as aerosols that are sprayed onto interrogation surfaces, they can take the form of swipes impregnated with chemicals, reagent drops added to sample swipes or simple small-scale liquid solutions into which particles are added. Generally, colourimetric-based techniques are used for the contact-based detection of explosive particles, with limits of detection of less than miligram (mg) amounts [21]. More recent research has explored the use of colourimetric sensors in chemical noses for the vapour-phase detection of explosives. For example Suslick *et al.* reported the successful detection of TATP vapours using a colourimetric array with an LOD of < 2 parts-per-billion (ppb), which is around 0.02% of the saturated vapour pressure of this peroxide-based explosive [21, 62, 63].

Current limitations of colourimetric-based sensing approaches include the need for hazardous chemicals in some of the liquid reagent based test kits, therefore subjecting those operating these kits to various levels of toxic exposure [63]. In addition, many of these colourimetric approaches are single-use only systems, incurring costs to replace the sensor after each use. Furthermore, in comparison with fluorescence-based optical detection, colourimetric approaches are one to three orders of magnitude less sensitive [26]. Consequently, fluorescence-based explosives detection methods have also been extensively researched.

2.5 FLUORESCENCE-BASED EXPLOSIVES DETECTION

Before discussing the contributions to trace explosives detection using fluorescence-based methods, it is important to define what exactly fluorescence is and how this phenomenon can be exploited for sensing.

2.5.1 *Fluorescence theory*

Luminescence refers to the process of light emission by the absorption of energy, and occurs from electronically excited states. The excitation energy of this process is most typically in the form of photons and so is often termed as PHOTOLUMINESCENCE. Luminescence is formally divided into two categories; fluorescence and phosphorescence, depending on the nature of the excited states. Fluorescence arises form the emission of light between energy states of the same spin multiplicity (spin allowed) and phosphorescence occurs when light is emitted from transitions between states of different spin multiplicity (spin forbidden). Fluorescence is a rapid emission and generally lasts around 10 ns (10 x 10^{-9} s), whereas a phosphorescent emission is approximately in the range of a microsecond to a second in duration [64–66]. These light emitting process are illustrated through use of a Jablonski diagram; Figure 2.3.

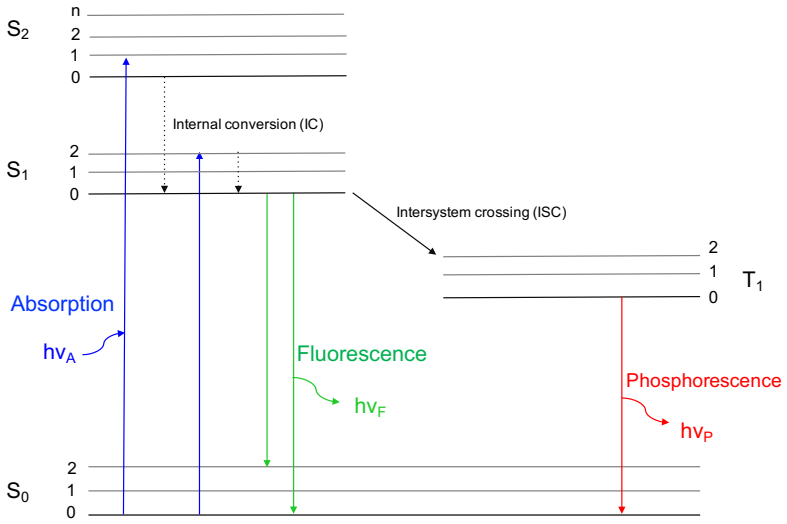

Figure 2.3: Schematic illustration of one form of a Jablonski diagram detailing the electronic (S_0, S_1, S_2) and vibrational states (0, 1, 2) involved in the luminescence phenomena, as well as the transitions between them. Adapted from [67] with permission of the The Royal Society of Chemistry.

In Figure 2.3, the singlet ground state, the first electronic excited state, and second electronic excited state are represented by S_0, S_1, and S_2 respectively. Within each of these electronic energy levels, fluorophores (fluorescent chemical compounds) can exist in a number of vibrational energy levels; 0, 1, 2 *etc.* [64].

Following the absorption of light energy (photons), a fluorophore is excited to some higher vibrational energy level of an excited state (such as S_1). With a few rare exceptions, fluorophores subsequently rapidly relax to the lowest vibrational state of S_1. This process is a non-radiative process (does not emit a photon) and is termed INTERNAL CONVERSION (IC). IC lasts approximately 10^{-12} s or less. As fluorescence lifetimes are $\sim 1 \times 10^{-8}$ s, internal conversion generally occurs prior to emission. Upon the return of the excited state fluorophore (from the thermally equilibrated excited state, that is, the lowest vibrational energy level of S_1) to the ground state; a photon is emitted and fluorescence is observed. Return to the ground state most typically occurs to a higher excited vibrational ground state level, which then reaches thermal equilibrium in approximately 10^{-12} s (returning to the lowest vibrational energy level). It is the return to the an excited vibrational level at the S_0 ground state that generates a mirror image in most fluorophore absorption and emission spectra, as this causes the energy of emission to be lower than that of absorption; this effect is known as the STOKES SHIFT.

Alternatively, excited molecules in the S_1 state may also undergo a spin conversion to the first triplet state, T_1. Emission from this excited state takes the form of phosphorescence. Conversion to the T_1 state from S_1 is termed INTERSYSTEM CROSSING (ISC). Owing to the transition from T_1 to S_1 being forbidden (spin selection rule); the lifetime of phosphoresence emission is several orders of magnitude longer than that of fluorescence [64].

2.5.1.1 *Characterisation of fluorescence properties*

The fluorescence properties of materials are generally characterised by three parameters [64]:

1. FLUORESCENCE EMISSION SPECTRA - which is defined as the fluorescence intensity of a material as a function of a wavelength.
2. THE QUANTUM YIELD - this denotes the efficiency of the fluroescence process for a material, and is determined by the number of photons emitted during fluorescence compared to the number of photons absorbed.
3. THE FLUORESCENCE LIFETIME - the average time a fluorophore stays in its excited state prior to emitting a photon.

2.5.2 *Mechanisms and processes for fluorescence-based explosives detection*

As explosive compounds are non-fluorescent, fluorescence-based sensors offer an indirect approach to explosives detection. In such approach, fluorophores are used to interact with target explosive materials to yield a measurable change in their fluorescence emissions. Alterations in fluorescence intensity (quenching or enhancement), wavelength, anisotropy or lifetime of the material may be exploited for the indication as to the presence (or absence) of explosives. The most common measurable transformation of a fluorescent sensor upon contact with an explosive is that of FLUORESCENCE QUENCHING which is a decrease in the fluorescence intensity of the fluorophore upon interaction with the target analyte. Explosives detection sensors based on fluorescence enhancements or 'turn-on' are also observed, however, they less frequently encountered [26].

There are various mechanism that can lead to the quenching of a fluorescent system upon interaction with an explosive, the most

significant of which are: PHOTO-INDUCED ELECTRON TRANSFER (PIET), FÖRSTER RESONANCE ENERGY TRANSFER (FRET) and DEXTER ELECTRON EXCHANGE (DEE); the mechanisms of which are briefly outlined below.

2.5.2.1 *Photo-induced electron transfer mechanism*

Many explosive substances are highly nitrated organic compounds, as a consequence they are very electron-deficient. This attribute gives them potential to bind to electron-rich fluorophores through DONOR (D) - ACCEPTOR (A) interactions. In photo-induced electron transfer (PIET), the excited state, electron-rich donor analytes (excited state fluorophores) give an electron to the ground state acceptor analytes (electron-poor explosives); forming a complex between the electron donor and acceptor (as demonstrated in Figure 2.4). This charge transfer complex most typically then returns to the ground state without the emission of a photon, thus, causing a quenching of the excited state fluorophore. In some instances, the donor-acceptor complexion yields exciplex formation, in which case exciplex emissions are observed as opposed to a fluorescence quench (which is still a useful and detectable change of the fluorophore emission). Upon returning to the ground state in either case, charge recombination and the regeneration of the ground state donor/acceptor species occurs, with the excess energy released as heat [26, 67].

Exiplexes (excited complexes) = molecular complexes that are formed in the excited state, which dissociate in the ground state. Exiplex emissions are typically characterised by the broadening and loss of features in fluorescence spectra [68].

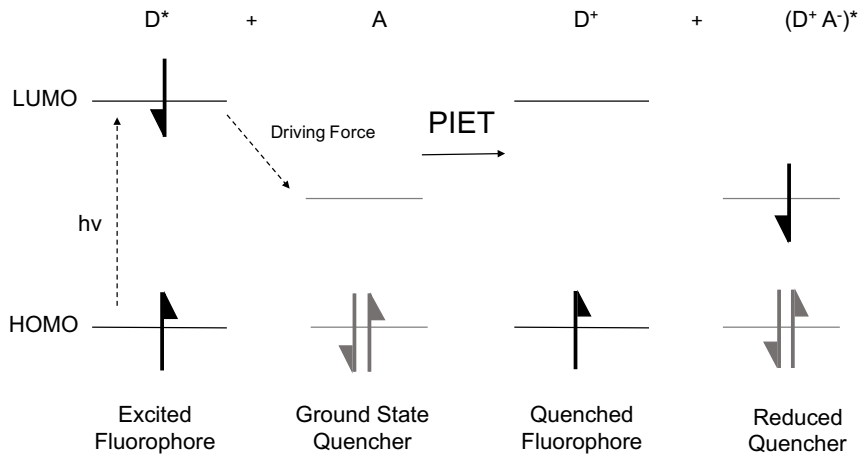

Figure 2.4: Molecular orbital schematic detailing the photo-induced electron transfer (PIET) mechanism [64].

For the PIET mechanism, it is the energy gap between the lowest unoccupied molecular orbital (LUMO) of the electron donor fluorophore and the LUMO of the acceptor (explosive), that is approximately the driving force for this redox process (as shown in Figure 2.4). Further to this, the quenching efficiency of a system is directly proportional to that of the electron transfer and can be analysed using Marcus theory [26, 69, 70].

$$K_{et} = A_{exp}\left(-\frac{\Delta G^*}{kT}\right) = \frac{2\pi^{\frac{3}{2}}}{h\sqrt{\lambda kT}}V^2\left[-\frac{(\Delta G^\circ + \lambda)^2}{4\lambda kT}\right] \tag{2.2}$$

where

K_{et}	Electron transfer rate
h	Planck's constant
k	Boltzmann constant
T	Temperature (Kelvin)
ΔG°	Standard Gibbs free energy difference of the electron transfer reaction
V	Electron coupling between the initial (D^*) and final state (D^+A^-)
λ	Relaxation energy adjusting the molecular structure of the new stable state

Through the use of quantum calculation methods the energy gap between the LUMO of the acceptor and donor may be obtained and thus ΔG for the electron transfer process may be determined. This allows for an approximate evaluation of the quenching efficiency between a donor and an acceptor to be made [70].

2.5.2.2 *Förster-resonance energy transfer mechanism*

An alternate mechanism that can result in the fluorescence attenuation of a fluorophore is FÖRSTER RESONANCE ENERGY TRANSFER (FRET). FRET is a distance-dependent interaction in which energy (not an electron) is transferred from the donor fluorophore to the acceptor (through dipole-dipole interactions), *via* a non-radiative process, which in turn causes a decrease in the fluorescence intensity of the donor [64, 71]. This process is illustrated by Figure 2.5.

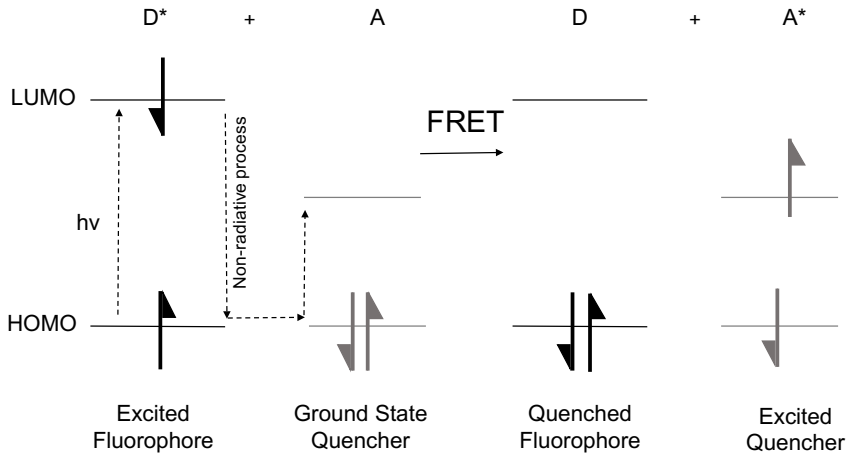

Figure 2.5: Molecular orbital schematic detailing the Förster-resonance energy transfer mechanism [26, 64].

As demonstrated by Figure 2.5 the donor is excited by a photon, after which, it relaxes to the lowest vibrational state of the excited level S_1. If the acceptor (explosive) is in close proximity to the donor fluorophore, the energy released when the excited electron returns to the ground state (S_0) may excite the acceptor. After excitation, the acceptor returns to the ground state typically through the emission

of a photon (providing that no other quenching states exist). However, in the case of explosives, owing to their non-emissive nature, no fluorescence is observed upon the relaxation of the excited state explosive. This transfer of energy from the donor to the acceptor, without the emission of light, causes the fluorescence quenching of the fluorophore.

The FRET quenching mechanism requires the close interaction of the donor and acceptor (typically 10 - 100 Å). In addition, this process relies on equal transitions being possible in both donor and acceptor species and thus, requires spectral overlap between the donor species' emission spectrum and the acceptor species' absorption spectrum [67, 71]. The greater the spectral overlaps the more efficient the energy transfer from donor to acceptor. FRET type interactions have been known to dramatically enhance the fluorescence-quenching efficiencies and thus improve the sensitivities of fluorescent sensors. This has consequently led to the rational design of numerous materials that are able to interact with target analytes using this resonance process (by careful consideration of donor-acceptor spectral overlaps and possibilities for close range molecular interactions). However, owing to the strict requirements for this process to occur, FRET is only commonly observed for fluorophore interactions with some explosive analytes (such as Picric Acid), that are able to demonstrate good absorption spectral overlap with donor emission spectra and where close spacial proximities (between donor and acceptor) can be achieved [26].

2.5.2.3 *Dexter electron exchange mechanism*

The Dexter electron exchange (DEE) mechanism, as the name suggests, involves the exchange of electrons between donors (in their excited state) and acceptors (in their ground state). In this process, the excited state donor transfers an electron present within its LUMO excited state orbital to the acceptor (in the ground state), and the acceptor then transfers an electron back to the donor. The electron from the acceptor comes from its HOMO, and therefore the acceptor is left in the excited state [64]. This process can occur in a concerted process (illustrated in Figure 2.6) or a two step process (where by electron donation from the donor precedes electron donation from the acceptor).

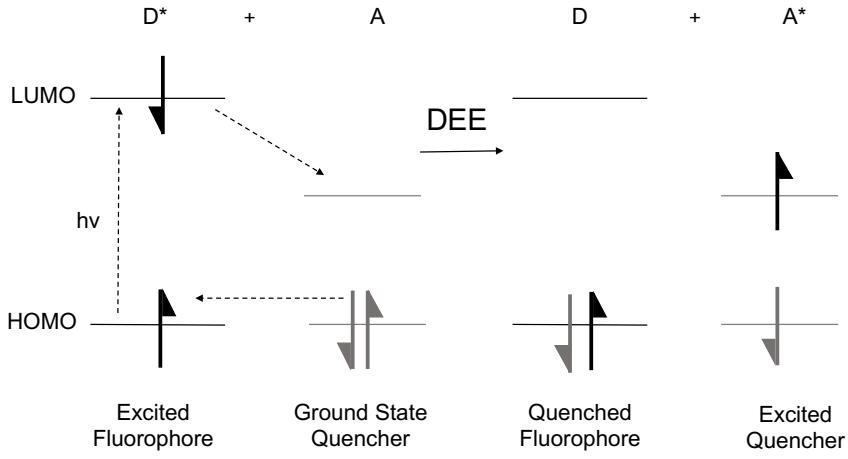

Figure 2.6: Molecular orbital schematic detailing the Dexter electron exchange (DEE) mechanism [64].

DEE is a short-range mechanism (the distances required for this process are shorter than those for FRET, typically less than 10 Å) and like FRET relies on orbital overlap between the donor and the acceptor. However, spectral overlap is less important for DEE. Typically, if spectral overlap is present between a donor and an acceptor, FRET will be the more important interaction. However, where spectral overlap is small, and where interaction ranges are very short; DEE will be the dominant mechanism. Much like FRET, dexter electron exchange

can results in either the quenching or enhancement of the fluorophore in the presence of explosives (or related compounds). However, as aforementioned, quenching is much more common [64].

2.5.2.4 *Quenching rates*

The rate at which a fluorophore is quenched by an analyte (by any of the previously mentioned mechanisms) is determined through steady-state quenching experiments and an evaluation of the Stern-Volmer (SV) equation and binding constant (K_{SV}) [72] (Equation 2.3):

There are two types of fluorescence measurements; steady-state and time resolved. In steady-state measurements the sample is constantly illuminated and the intensity of the sample is recorded. In time-resolved measurements the sample is exposed to a pulse of light, where the pulse width is typically shorter than that of the sample decay time, and the intensity of the sample is measured [64].

$$\frac{I_o}{I} = 1 + K_{SV}[Q] \tag{2.3}$$

I_o	Fluorescence intensity in the absence of a quencher
I	Fluorescence intensity in the presence of a quencher
$[Q]$	Quencher concentration
K_{SV}	Stern-Volmer constant

It should be noted that quenching rates can only be estimated accurately if the plot of $\frac{I_o}{I}$ *vs.* [Q] is linear. A linear stern-volmer plot is indicative of only one type of quenching process occurring within the system. There are two types of quenching processes that can exist; STATIC and COLLISIONAL quenching (which will be defined in Section 2.5.2.5). If an SV plot deviates from linearity; quenching rates cannot be accurately determined. In such instance, it is likely that both static and collisional quenching processes are occurring. Steady-state measurements do not provide insight into which type of quenching process is happening within a system; they can only evaluate rates. For quenching processes to be determined, time-resolved measurements must be performed [72].

2.5.2.5 *Types of quenching processes*

For each of the fluorescence quenching mechanisms discussed, the fluorophore and the quencher are required to come into contact. This association between the two molecules can result from a diffusive encounter, which is DYNAMIC QUENCHING or from complex formation; STATIC QUENCHING. These two processes can be distinguished through the analysis of time-resolved fluorescence decay measurements of the fluorophore material.

During STATIC QUENCHING, the fluorescence decay lifetime of a fluorophore will remain unchanged as the concentration of the quencher is increased. The fluorescence quenching in this interaction arises from the formation of non-fluorescent, ground-state fluorophore-quencher complexes, which are formed prior to excitation, and typically result from the rapid electron transfer from fluorophore to quencher upon photo-excitation; eliminating the fluorescence. Thus, any fluorophore molecules not bound to an analyte will decay following their natural lifetime decay pathways. In COLLISIONAL QUENCHING, the fluorophore and quencher must collide, therefore this process is diffusion controlled and results in a decrease in the average fluorescence lifetime of the fluorophore. The fluorophore and the quencher are unbound and quenching occurs when a photo-excited material interacts briefly with a colliding analyte molecule [26, 61, 64, 72].

The determination of whether fluorescence quenching is occurring statically or dynamically can be ascertained by measuring the fluorescence lifetime change of the material in the presence and absence of the explosive quenchers [72]. Typically the ratios of lifetime ($\frac{\tau_0}{\tau}$) are plotted against the quencher concentration ([Q]). For static quenching $\frac{\tau_0}{\tau} = 1$, whereas for collisional quenching; $\frac{\tau_0}{\tau} = \frac{I_0}{I}$.

For collisional quenching, the Stern-Volmer equation can be used to describe the correlation between the lifetime of the fluorophore and the quencher concentration [26]:

$$\frac{I_o}{I} = 1 + k_q \tau_o [Q] = 1 + K_D [Q] \tag{2.4}$$

$$\frac{\tau_o}{\tau} = \frac{I_o}{I} \tag{2.5}$$

I_o Fluorescence intensity in the absence of a quencher

I Fluorescence intensity in the presence of a quencher

τ_o Lifetime of the fluorophore in the absence of a quencher

τ Lifetime of the fluorophore in teh presence of a quencher

k_q Bimolecular quenching constant

K_D Stern-Volmer dynamic quenching constant

$[Q]$ Quencher concentration

For static quenching the Stern-Volmer is derived to consider the association constant for complex formation (K_S is the Stern-Volmer constant for static quenching):

$$\frac{I_o}{I} = 1 + K_S [Q] \tag{2.6}$$

Combination of these two equations for reactions that involve both collisional and static quenching is given by:

$$\begin{aligned} \frac{I_o}{I} &= (1 + K_D[Q])(1 + K_S[Q]) \\ &= 1 + (K_D + K_S)[Q] + K_D K_S [Q]^2 \end{aligned} \tag{2.7}$$

When quencher concentrations are very low, the contribution to $[Q]^2$ is less significant and so a linear plot for the equation is observed. In contrast, at higher quencher concentrations, the plot deviates from linearity demonstrating an upward curvature, concave to the *y*-axis; such plots are characteristic of flurophores in which both static and dynamic quenching processes are simultaneously occurring.

Whilst both of these fluorescence quenching processes are feasible, it is reported that static quenching is much more prominent in explosives detection, as a result of the high association constants between fluorophores and explosives [73].

2.5.3 *Previous contributions to fluorescence-based explosives detection*

A number of fluorescence-based sensors have been explored for the trace detection of explosives. Arguably the most notable contributions to date have been made by Swager *et al.* with the use of AMPLIFYING FLUORESCENT CONJUGATED POLYMERS (AFCP) as sensing materials, some of which have been developed into devices that are used within the security industry [23].

A conjugated polymer is comprised of a number of macromolecule repeating units which are bound together using both saturated and unsaturated bonds. These generate a main chain which is often referred to as a 'molecular wire', due to the repeating units of the chain being electronically coupled. It is this conjugation that allows for the coalescing of individual molecular orbitals, which gives rise to semiconducting type polymers with electrons in their valence bands and devoid conduction bands. This facilitates fluorescence-based explosives detection by fluorescence quenching, most typically *via* the photo-induced electron transfer mechanism [74].

The uniqueness of AFCPs is their ability for signal amplification when a receptor interacts with a target analyte. As a result of the molecular wire effect, an exciton has the ability to migrate through the conjugated polymer backbone, sampling each receptor site that it passes. If during its excited state lifetime, the exciton encounters a bound analyte, its emission will be quenched. Due to the enhanced delocalization of the structure, this one binding event causes the entire system to be quenched (Figure 2.7a). This signal amplification is synonymous to 'the Christmas tree light effect', whereby the extinguishing of one light bulb in series, turns off the entire network [74].

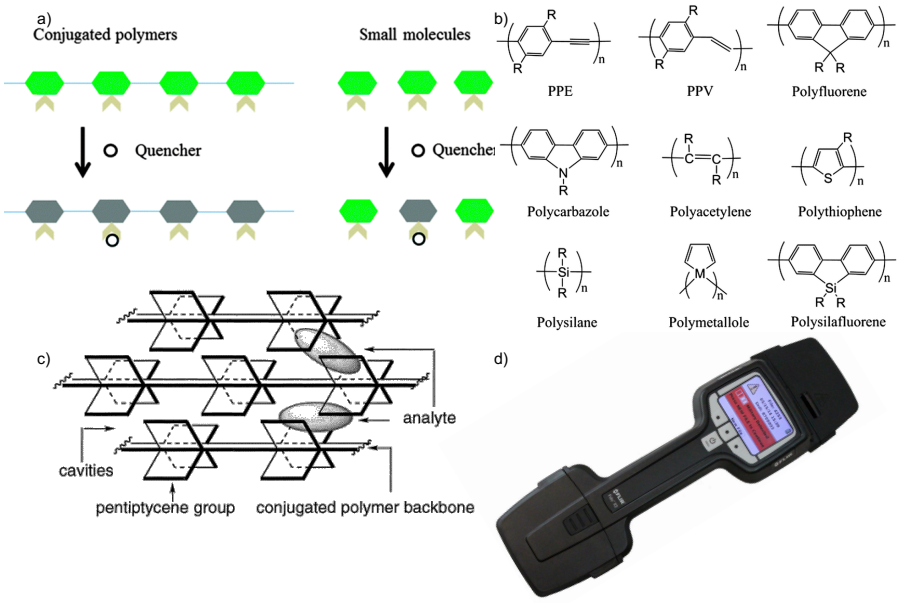

Figure 2.7: a) Schematic illustrating the molecular wire theory. b) Examples of some basic backbone structures of conjugated polymers as synthesised by Swager *et al.*. c) Pentiptycene-derived PPE conjugate polymer structure and a representation of the porosity imparted in this polymer for analyte binding. d) Example of a 'FIDO' amplifying fluorescent conjugate polymer hand held trace explosives vapour detector [75]. Figures a) and b) have been reproduced from [26] with permission from The Royal Society of Chemistry. Figure c) has been reprinted with permission from [76]. Copyright 1998 American Chemical Society.

A number of fluorescent conjugated polymers with varying organic or inorganic basic backbones (some of which are denoted in Figure 2.7b) have been explored for the detection of explosives in either the solution or vapour-phase. Poly(phenylene ethynylene)s (PPEs) and their functionalised derivatives are the most prominent family of conjugated polymers. In the solution state they demonstrate high quantum yields. However, once condensed (when producing thin films for the vapour-phase detection of explosives), PPEs suffer from self-quenching caused by inter-chain aggregation. Thus, spacers must be introduced into these polymers for the efficient separation of PPE backbones to ensure their high fluorescence emission intensity. Swager *et al.* used pentiptycene units for the successful isolation of PPE backbones to prevent the self quenching of the AFCPs, as illustrated by Figure 2.7c. Whilst doing this, the group noted that the porosity that these spacer units imparted into the conjugate polymers thin films, were crucial for the increased sensitivity of vapour-phase explosives detection. The fabricated pores allowed for the diffusion of explosive molecules into polymer films; enhancing interactions between the two.

Thin films of the PPE polymer (shown in Figure 2.7c) demonstrated good quenching upon exposure to the saturated vapours of TNT, with approximately 50% and 70% quenching of the system upon 30 s and 60 s exposure to the analyte respectively. The more volatile derivative 2,4−DNT yielded around a 90% quench of the polymers upon exposure to saturated vapours for 60 s. Demonstrating the effectiveness of these materials for vapour-phase detection. It is important to note that AFCPs are frequently characterised for their sensing capabilities in the solution-phase, prior to fabrication and optimisation of thin films [26, 74, 77].

Significant optimisation attempts have been performed with aim to enhance the sensitivity and selectivity of AFCPs. For example, polymers have been functionalised with highly electron rich moieties (such as pyrene) with aim to enhance the initial fluorescence of the systems and thus, impart a greater driving force for electron transfer. In addition, polymers with different HOMO-LUMO band gaps have been generated. Tailoring the band-gap in order for the PIET driving force to be favourable in the presence of some analytes and not others, can allow for some discrimination in analyte sensing. This is important for preventing the detection of unwanted interferents [26, 74]. Using this strategy AFCP have also been tailored to respond to target analytes that are not nitroaromatic, and are less electron-deficient, such as DMNB, whose interactions with the polymers are less favourable. Through optimisation of the polymers band gap, the detection of this analyte was made successful [78]. Further to this, varying the size of the fabricated pores within AFCP thin films was also observed to impart sensing selectivity. This process is termed the size exclusion principle and is where some analytes are able to diffuse into the pores of the films and some, that are too large, cannot. The included analytes are able to form effective interactions that lead to quenching and those excluded are unable to interact effectively and so do not cause a system quench [74]. Increasing the selectivity of analyte detection has also been attempted through the use of two polymers in tandem, in pseudo-sensing arrays. In such systems two AFCPs are present in different channels, when analytes (in the vapour-phase) are passed over the separate films, the time of response and the different peak shapes are monitored, and ratios between the two polymer responses are obtained. These responses are different for various analytes owing to their different vapour pressures and binding affinities. For example, TNT progresses along the length of tandem polymer films more

slowly than 2,4-DNT, and so it has a different temporal response, inducing some discrimination in the system [74]. Functionalised PPE polymers used in such a process have been successfully incorporated into commercially available devices ("FIDO", FLIR Inc., Figure 2.7d) for the vapour phase detection of nitroaromatic explosives, with sensitivities that have been reported to rival those of sniffer dogs [23, 26, 74]. In addition, some attempts have been made to use AFCPs in electronic noses for the differential discrimination of analytes [58]. However, this area of research appears to be still within its infancy.

Although these chemical sensors have shown very good explosives detection capabilities in particular for nitroaromatic compounds, they are not without their disadvantages [23, 74, 77, 79]. As aforementioned, great importance has been placed on the porosity of these materials for vapour-phase detection; in order to prevent self-quenching and to promote the diffusion of analytes into the sensing material where they can form the most significant interactions. However, this is somewhat a challenging task as conjugated polymers themselves are not inherently porous. Thus, porosity must be imparted with the correct selection of spacer compounds, otherwise the sensitivity of analyte detection is significantly hampered. Further to this, thin film fabrication has proven itself non-trivial. Swager *et al.* found that films with increased thickness led to diminished responses towards target analytes, this was rationalised on the basis of poor diffusion of the analytes into the pores of the film [77]. Furthermore, the synthesis and functionalisation of conjugate polymers is often lengthy, involving complex multi-step routes, that often result in very low yields. Additionally, the control of molecular organisation and structural determination of these polymers is difficult as they are non-crystalline and have poor solubility. This makes it difficult to ascertain whether the correct amounts of binding sites have been incorporated into the

materials and if they are in the correct positions. There is therefore scope to develop new sensory materials that can address these issues whilst still enabling large-exciton migrations ([26])

Other explored fluorescence-based chemical sensors include SMALL MOLECULE FLUOROPHORES. Small molecule fluorophores can be organic or inorganic in nature. Organic polycyclic aromatic hydrocarbons have been extensively researched such as pyrene, anthracene, perylene, naphthalene and have all demonstrated successful detection responses upon exposure to explosive analytes. Inorganic small molecule fluorophores such as oligo-fluorophores have also shown the ability to detect explosives *via* fluorescence quenching. Disadvantages of small molecule fluorophores are their decreased quenching efficiency in comparison to conjugated structures, as they are quenched in a stoichiometric fashion of one analyte per fluorophore and no amplified responses are observed (as illustrated in Figure 2.7a). However, sensing experiments on small molecule fluorophores are useful in the early developmental stages of designing fluorescent sensors such as AFCPs, as they allow for quick and simple proof-of-concept experiments as to which fluorophores interact beneficially with explosives [26, 80].

An alternative approach to creating sensors is through the use of SUPRAMOLECULAR CHEMISTRY; cyclodextrins [81], calix[n]arenes [82, 83], cucurbits[n]urils [84], dendrimers [85], and supramolecular polymers [86] have all been explored. More recently, metal-organic frameworks (MOFs) are emerging as very promising candidates for fluorescence-based explosives detection and will be the focus of this thesis herein.

2.6 FLUORESCENT METAL-ORGANIC FRAMEWORKS

2.6.1 *An introduction to metal-organic frameworks*

A cooordination polymer is defined as a coordination compound continuously extending in 1, 2, or 3-dimensions through coordination bonds [87].

Metal-organic frameworks are defined (following the international union of pure and applied chemistry (IUPAC) recommendations) as coordination polymers with open framework structures that contain potential voids [87]. As the name suggests, MOFs belong to a family of organic-inorganic hybrid compounds. Inorganic metal ions (or aggregates) act as the coordination centres in MOFs for various organic ligands (such as carboxylates or nitrogen donor linkers) to coordinate to, it is the connectivity and geometry of these organic and inorganic components that depict whether one-, two- or three-dimensional infinite structures will be formed [88, 89]. Upon the coordination between one or more inorganic metal ions and the donor atoms of the organic linkers in a MOF, rigid and defined entities are constructed, these are known as secondary building units (SBU), as demonstrated in Figure 2.8. Depending on their varying geometry, these molecular building blocks govern the overall structure a MOF exhibits [90]. Secondary building units are assembled into the overall MOF structures through the linking of multidentate organic ligands (Figure 2.8) [91, 92].

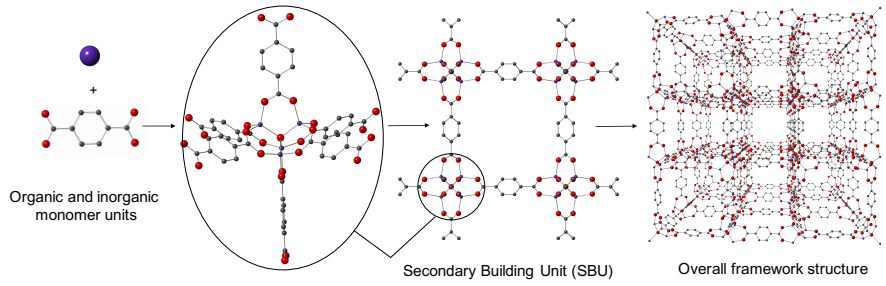

Figure 2.8: Illustration of how metal ions (purple), combine with organic ligands (in this case through the carboxylate moieties) to form the metal aggregates known as secondary building units (circled). The SBUs subsequently link to other SBUs forming the overall three-dimensional MOFs. Oxygen atoms are denoted by the colour red, carbon atoms are grey and the inorganic metal ions are purple. Hydrogen atoms have been omitted for clarity. Adapted with permission from [92]. Copyright (2001) American Chemical Society.

The MOF illustrated in Figure 2.8 is MOF-5, the pioneering and most prevalent metal-organic framework made famous by Yaghi *et al.* [92]. It is important to note that MOFs are sometimes characterised by three letter codes which describe their overall framework (or net) topology, the code that details the structure of MOF-5 is **pcu** and it stands for primitive cubic net. Specific topological nets can often be targeted when designing MOFs [93]. Through the alteration of the individual modular building components, MOFs with the same underlying topology (net) but with different pore size and functionality can be produced; such analogous frameworks are termed 'isoreticular' MOFs. For example, through the use of different organic linkers, sixteen different MOFs based on the **pcu** net of MOF-5 have been produced, all of which have different cavity sizes and environments. An illustrative example can be seen in Figure 2.9.

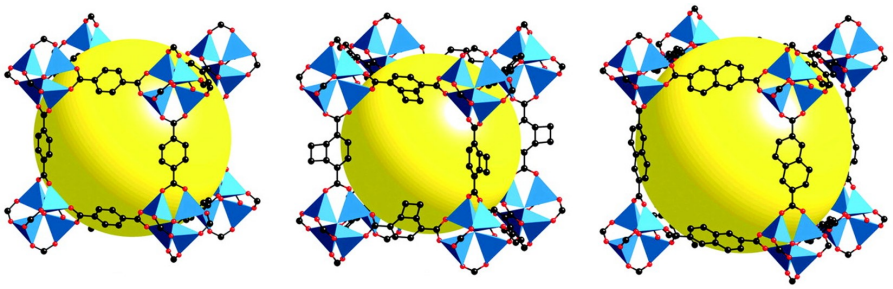

Figure 2.9: Illustration of the isoreticular MOF concept. Each of the three isorteticular **pcu** MOFs are comprised of the same metal (zinc) but vary in their linker composition. As such, three different MOFs with varying cavity size and functionality are produced but still retaining the same net topology. In this representation zinc atoms are represented by blue polyhedron, carbon atoms are black spheres and oxygen atoms are red spheres. The large yellow spheres represent the void space present within the cavities of the MOF. From [94]. Reprinted with permission from AAAS.

Given the almost limitless possibilities of both metal and ligand combinations, metal-organic frameworks prosper in their structural diversity as well as their tunable chemical and physical properties [95]. Such structural tailorability is arguably the most prosperous characteristic of MOFs; owing to its benefit for a number of applications. Other advantageous characteristics of MOFs include their often very porous structures with high surface areas (> 7,000 m^2 g^{-1} and up to 90% free volume); their straightforward synthesis that typically yield highly crystalline materials (that allow for facile characterisation) and their thermal robustness (typically between 250 - 500 °C) [67, 93, 96, 97]. As a result, MOFs have been investigated and have shown promise for use in a number of applications including drug delivery [98], gas storage and separation [99], catalysis [100] and most significantly for this thesis; sensing [31].

2.6.1.1 *Flexible MOFs*

An important sub-category of metal-organic frameworks are flexible MOFs. Despite forming rigid SBUs that contribute to the overall framework structure of these materials; some MOFs (FLEXIBLE MOFs) are able to demonstrate a degree of structural transform-ability upon the application of stimuli. This can include expansion/shrinking of the frameworks (also termed 'breathing'), opening or closing of pores, or some reversible change in the physiochemical properties of the MOF, as demonstrated by Figure 2.10 [101]. These types of frameworks can be very important for sensing as will be discussed in Section 2.6.4.

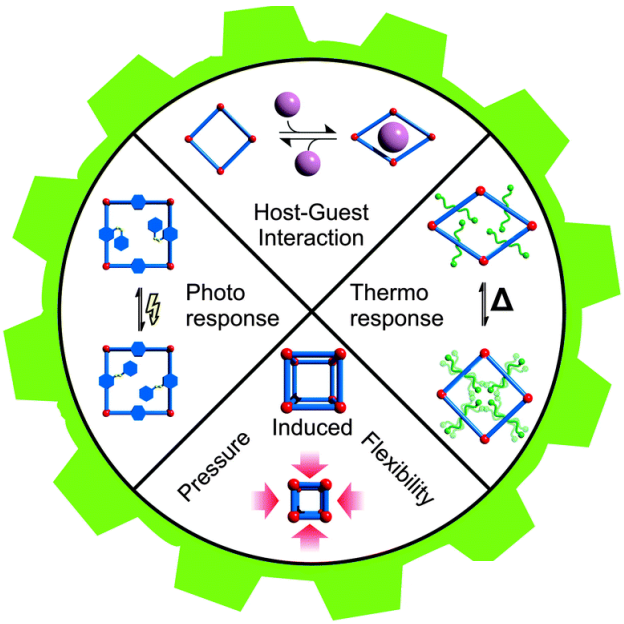

Figure 2.10: Schematic overview of flexible MOFs. Reproduced from [101] - Published The Royal Society of Chemistry.

2.6.1.2 *Synthesis of metal-organic frameworks*

Metal-organic frameworks are generally produced using facile, rapid, one-pot synthetic techniques. The most common approach to MOF synthesis in small-scale laboratories is the SOLVOTHERMAL METHOD. In this approach, reactants and solvents are combined in sealed vessels and raised to elevated temperatures using conventional electric heating, as illustrated by Figure 2.11 [102].

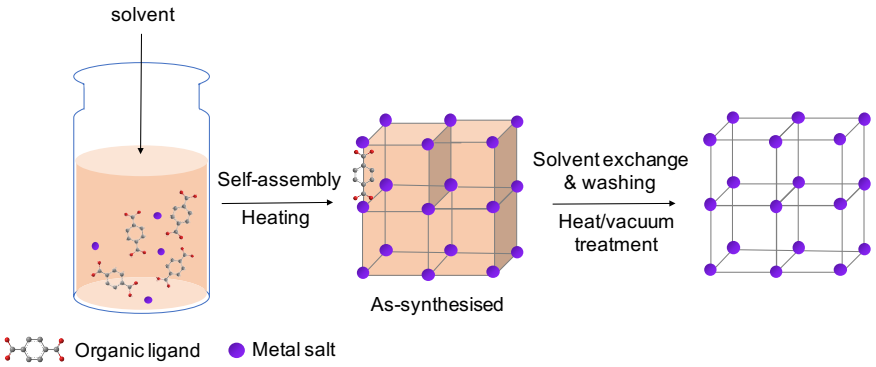

Figure 2.11: Conventional solvothermal synthesis of MOF structures. Reproduced from [102]. With permission from Springer.

For a syntheisis to be classified as SOLVOTHERMAL a reaction must be undertaken in a closed system with autogenous (self-generating) pressure, at a temperature above the boiling point of the solvent used in the system [103] [104]. However, such definition is not always strictly adhered to, as solvothermal syntheses can occur at temperatures below those of the solvent media boiling point. Essentially, MOF syntheses are simply Lewis acid-base reactions, in which metal ions behave as Lewis acids and the organic linkers Lewis bases [105]. The inorganic metal ions used in these reactions are obtained from soluble metal salts such as metal nitrates, sulphates or acetates and the organic ligands are generally carboxylic acids or N-containing compounds. The deprotonation of the carboxylic acid moieties of the organic linkers occurs through addition of bases such as N,N- Dimethylformamide (DMF), which often also act as the solvent for these reac-

tions [105]. The reactants are combined in sealed vessels (glass tubes or Teflon-lined stainless steel autoclaves) in order for autogenous pressure to be reached [106]. Solvothermal synthetic methods often yield good quality three-dimensional and highly crystalline MOFs which can be used for structural analysis using crystallographic techniques. The reaction times for this approach vary from several hours to days.

An Alternative synthetic method that have been explored to shorten these synthetic times and to produce smaller, more uniform crystals is the microwave-assisted solvothermal method (Figure 2.12) [102][107].

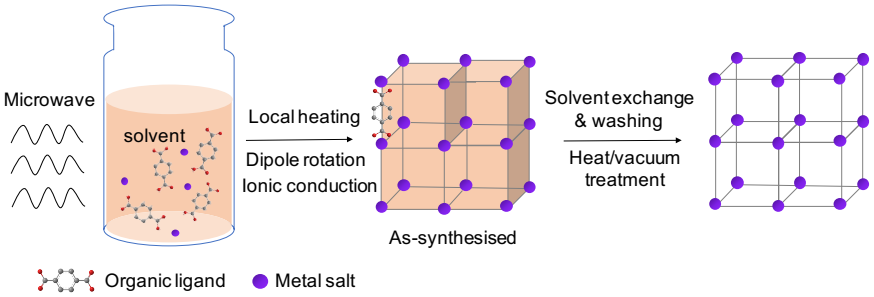

Figure 2.12: Microwave-assisted solvothermal synthesis of MOF structures. Reproduced from [102]. With permission from Springer.

In this method, a reaction mixture in a suitable solvent is transferred into a sealable vessel and placed inside a microwave unit and heated for an appropriate time, at a set temperature. The applied oscillating electric field is coupled with the permanent dipole moment of the molecules in the reaction mixture, inducing molecular rotations that result in the rapid heating of the liquid phase, providing activation energy for the reactions to take place [102]. Reaction times for this approach vary from minutes to hours [104]. As well as fast crystallization, this technique offers phase selectivity, narrow particle size-distributions and simple morphology control [102]. Both conventional solvothermal and microwave-assisted solvothermal synthetic techniques will be demonstrated for the synthesis of novel MOFs within this thesis.

Additional techniques explored for the synthesis of metal-organic frameworks include sonochemical [108], electrochemical [109] and mechanochemical methods [110]. Furthermore, the synthesis of MOF thin films has also been explored through various techniques including: layer-by-layer deposition, liquid phase epitaxial growth and seeded growth on a coated substrate, amongst others [111, 112]. Whilst this sub-field of MOF chemistry is rapidly growing in popularity and importance for various applications; it is still very much in its infancy and proof-of-concept stages. There is no singular method that has been identified that yields the successful production of MOF-films for each framework type [67, 112].

2.6.1.3 *Activation of MOFs*

During the synthesis of metal-organic frameworks solvent molecules are inevitably trapped within their cavities. Therefore, they are required to be removed in order to access the permanent porosities and high surface areas of many MOF structures. This solvent removal process is termed 'activation' and is usually performed prior to the use of a MOF within a given application [111]. The concept of activation is illustrated in both Figure 2.11 and Figure 2.12, and as denoted in these figures; the activation of a MOF is most typically achieved through either vacuum drying (with or without the application of heat) or through a solvent exchange procedure (explained below), or, a mixture of both. It is important to note that MOF activation is not a trivial task, and care is often required when removing solvents from MOF pores as loss of MOF crystallinity (owing to defect and/or disorder formation) and/or porosity can frequently occur (to varying extents) during activation [101, 111, 113–116]. For example, for some MOFs, simply heating the frameworks under vacuum directly after synthesis yields active structures with high crystallinities and porosities.

DEFECTS = *sites that locally break the regular periodic arrangement of atoms or ions in a crystal due to missing or dislocated components.*
DISORDER = *a lack of long-range order [113, 114].*

In most instances, however, this direct application of heat and vacuum post-synthesis yields MOFs with lower surface area (as well as a decrease in crystallinity) than expected, due to framework collapse. Such structural collapse is attributed to the high surface tension and capillary forces inflicted on the framework by the liquid to gas-phase transformations of the trapped solvents. This is most frequently observed for solvents with high boiling points and/or surface tensions [111]. The way that such structural collapse is normally overcome is by exchanging the solvents present within the pores of the MOF with those of a lower boiling point/surface tension, prior to heating under vacuum (termed either 'solvent exchange' or 'washing'). The lower boiling-point solvents have weaker intermolecular interactions and thus, minimise the surface tension and capillary forces acting on the structure during activation.

Solvent exchange is achieved by soaking the as-synthesised MOF crystals in the newly chosen solution for either hours or days; to ensure that the solvent molecules infiltrate the MOF pores. Consecutive solvent exchanges with further decreasing solvent boiling points/-surface tensions can also be employed prior to final vacuum heating. However, while solvent-exchange is a widely and successfully used MOF activation approach, it can still lead to materials exhibiting lower porosities than expected and poorer cyrstallinities, due to the formation of defects, disorder, and some levels of pore collapse. Such findings are most typically observed when incomplete activation occurs (not removing all guest molecules) [111, 114, 116]. It is worthwhile mentioning that activation can often lead to perturbations in the overall structure of a MOF. Solvents in MOF pores often act as templating agents keeping the pores shaped, changing and removing the solvent present in the cavities of the structure may alter these templating effects, thus, altering the shape of the pores [115].

2.6.1.4 *Characterisation of MOFs*

Metal-organic frameworks (particularly newly synthesised MOFs) are rarely characterised using only one technique. Basic MOF characterisation typically includes: Single crystal X-ray diffraction, powder X-ray diffraction (PXRD), absorption and desorption isotherms, scanning electron microscopy (SEM), thermogravimetric analysis (TGA), and nuclear magnetic resonance (NMR) analyses.

Single crystal X-ray diffraction is the best method for the unambiguous structural determination of a MOF. However, as is the case for any material, high quality crystals of the MOF are required for collecting reliable data using this technique; which are not always easy to obtain. Optimisation of synthetic procedures may be required to yield crystals of good enough quality for characterisation using this technique. In general, MOF crystallography is often challenging due to large amounts of disordered solvents present within the pores of as-synthesised MOFs. In addition, activated MOFs are even more difficult and often not possible to characterise using single crystal X-ray diffraction. This is due to their often poorer crystallinity than their non-activated (solvent-containing) parent frameworks (for reasons discussed in Section 2.6.1.3), therefore, other techniques are required for their characterisation [111]. It is important to note that a MOF does not have to be crystalline for it to be useful in its application [114, 117]. Single crystal X-ray diffraction data can also indicate as to the potential porosity of a MOF material through calculation of the solvent accessible volume of a framework. However, the apparent surface area of the activated material should be determined using physisorption isotherms (discussed below) where possible [111].

Powder X-ray diffraction (PXRD) patterns are used to establish bulk crystallinty and phase purity in MOF samples. Once a sample is determined to be crystalline, its PXRD pattern can be used for full struc-

tural determination (although the structure solution process is challenging) or other information such as unit cell size can be extracted (which can indicate as to the presence of flexible MOFs) [101, 118]. The phase purity of a MOF sample can be confirmed through the comparison of the experimentally obtained PXRD pattern with that of the simulated PXRD pattern generated from single crystal X-ray diffraction data or computational modelling [111, 119]. PXRD is also a very useful technique for evaluating the effects of activation on a MOF sample. Shifts in the PXRD pattern peaks, the emergence of new peaks, or the dissaperance of peaks can indicate as to the structural change of a MOF post-activation [115].

Soprtion and desorption isotherms are used to determine the apparent surface areas for MOFs, as well as their pore volumes and pore size distributions. In addition, the shape of a sorption/desorption isotherm (a plot of how much is sorbed/desorbed by a material *vs* the relative pressure of an analyte) can yield valuable information about a MOF material. Generally, physisorption isotherms are classified into one of six categories following IUPAC recommendations, Types I - VI (Figure 2.13) [121]. Each of these isotherm types are generally related to a particular pore structure.

Sorption encompasses both ADSORPTION *(sorbate located on the surface) and* ABSORPTION *(sorbate that penetrates the bulk of the material). Relative pressure (RP, P/P_o) is defined as 'the ratio of the analyte vapour pressure (P) to the measured saturation pressure (P_o) at a given temperature ' [120].*

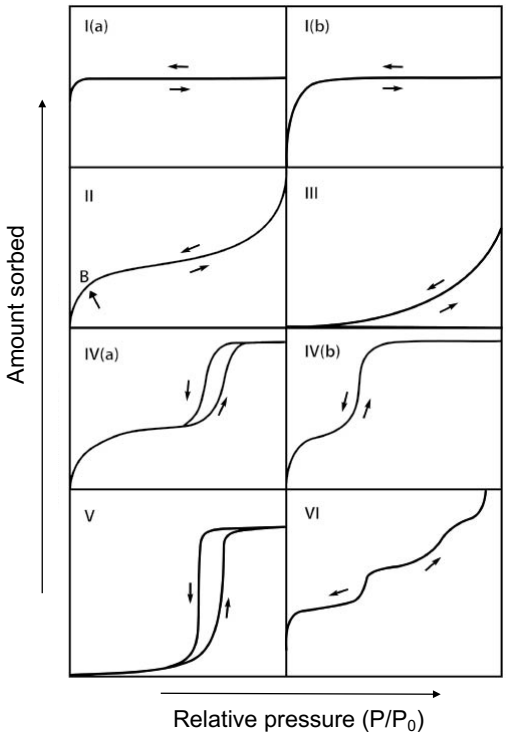

Figure 2.13: IUPAC classification of sorption isotherms [121]. The point labelled 'B' denotes the completion of a monolayer coverage.

The type I isotherm is most generally observed for microporous materials with strong adosrbant-adsorbate interactions, as evidence by the steep uptake of the adsorbate at very low partial pressures [121][122]. The difference between type I(a) and I(b) isotherms are the material pore size; type I(a) have mainly narrow micropores (with widths less that 1 nm or 10 Å) and the materials with I(b) isotherms have pore sizes up to 2.5 nm (25 Å) in width [121]. Type II isotherms are typical of non-porous or macroporous materials with weak adsorbant-adsorbate interactions. The isotherm shape results from unrestricted monolayer-multilayer adsorption. The presence of a sharp bend in isotherm (labelled 'B' in Figure 2.13) indicates that a monolayer coverage has been completed. If a more gradual curve is observed; this indicates that there is a certain amount of overlap between monolayer coverage and the start of multilayer adsorption [121]. Type III isotherms are relatively uncommon and are the direct opposite of

type I isotherms, they occur when adsorbate-adsorbate interactions are much more favourable that adsorbate-adsorbant ones [121]. Type IV isotherms are generally yielded by mesoporous adsorbents (pore widths greater than 2 nm or 20 Å) and often exhibit a hysteresis loop. Sorption follows the same pathway as type II, however, desoprtion is delayed at higher relative pressures owing to capillary condensation (where a liquid-like phase fills the empty space remaining within the pores of the adsorbant after multilayer coverage has been completed)[121]. The difference between type IV(a) and IV(b) isotherms are the size and shape of the mesopores; in IV(b) hysteresis is not observed. Type V isotherms are similar to type III particularly in the low partial pressure range, but a hysteresis is also observed on desopriton [121]. Type VI isotherms represent multilayer adsorptions on highly uniform and nonporous surfaces [122]. Nitrogen (N_2) gas sorption at 77 K is normally performed on activated MOFs in order to obtain physisorption isotherms. As the majority of MOFs are microporous; they tend to demonstrate type I isotherms upon the soprtion of many gases. However, MOFs are also known to demonstrate unusual hybrids of isotherms. For instance, frameworks with large pores have been shown to demonstrate type III isotherms at low pressure and then transition to type I isotherms at higher pressure [122]. The presence of unusual isotherms can help identify interesting structural occurrences in some MOFs such as framework flexibility.

The most common way of obtaining the apparent surface area for a MOF is through the use of Brunauer-Emmett-Teller (BET) theory. The BET equation is given in Equation 2.8 [111, 121].

$$\frac{P/P_o}{n(1-P/P_o)} = \frac{1}{n_m C} + \frac{C-1}{n_m C}(P/P_o) \tag{2.8}$$

where:

n specific amount of water adsorbed at relative pressure (P/P_o)

n_m specific monolayer capacity

C constant related to the enthalpy of adsorption

The monolayer capacity (n_m) can be calculated by plotting $\frac{P/P_o}{n(1-P/P_o)}$ *vs* P/P_o (the ' BET plot') and obtaining the values of the slope (s) and intercept (i) for use in the below equations [121]:

$$s = \frac{C-1}{n_m C} \tag{2.9}$$

$$i = \frac{1}{n_m C} \tag{2.10}$$

$$n_m = \frac{1}{s+i} \tag{2.11}$$

The n_m value (in moles) can then be used to calculate the total BET surface area (A_s) of the adsorbent, providing that the average area (molecular cross-sectional area, σ_m) occupied by an adsorbate molecule in the complete monolayer is known [121]:

$$A_s(BET) = n_m.L.\sigma_m \tag{2.12}$$

L Avogadro constant

σ_m molecular cross-sectional area

The specific BET surface area (a_s) can then be obtained by simply dividing A_s with the mass of the adsorbent (m), giving the surface area for one unit of sorbent. This is the most commonly expressed

value for BET surface area found in the literature and is generally expressed as m^2/g [121].

$$a_s = \frac{A_s}{m} \tag{2.13}$$

TGA is used to determine the thermal stability of an MOF and to evaluate if solvents have been effectively removed from MOF pores during activation [111]. SEM is useful for gaining an insight into MOF crystal size and morphology [111]. NMR can be used to determine MOF purity, linker ratios and evaluate the presence of any left over solvents post-activation [111].

2.6.1.5 *Stability of MOFs*

Whilst MOFs generally demonstrate high thermal stabilities (as aforementioned in Section 2.6.1 around 250 - 500 °C), they have been frequently criticized for their instability in water or to humid conditions. For many years, this has been considered a major challenge for the commercialization of MOFs for a number of applications owing to the omnipresence of water in many environments and settings [122]. However, the number of reported water-stable MOFs is vastly increasing and recent developments in the field have sought to standardise how water stability in MOFs is classified and measured. As such, it is encouraged and becoming commonplace in the published literature that all new MOFs are characterised for their humidity stability and classified as to how stable they are [122, 123].

Characterisation of water stability

The stability of a framework towards moisture is ascertained by evaluated two parameters; the retention of structure and porosity. The former is typically characterised through an assessment of the crys-

tallinity of the material pre- and post- exposure to water using powder X-ray diffraction (PXRD) and the latter by an evaluation of the BET surface area (using probe gases such as N_2, CO_2 or by even water vapour itself). It should be noted that the retention of porosity is the most important of the two parameters, as aforementioned, MOFs do not require crystallinity to maintain their function [123]. However, crystallinity change does give an additional indication as to the extent to which the material is affected by the imparted conditions.

Classification of water stability

When classifying a MOF's water stability two factors are considered; the level of water exposure that the framework has been exposed to and as mentioned above; the effect that this exposure has on the material in terms of structure and function (porosity). Burtch *et al.* [122] used three main categories to classify the stability of MOFs in the presence of water:

- Thermodynamically Stable - MOFs that are stable after long-term exposure to aqueous solutions. For example, immersed in pure water for longer than a week or boiled in acidic/basic conditions for a period of day(s).
- High Kinetic Stability - MOFs that are stable after exposure to high humidity conditions but decompose after short exposure times in liquid water.
- Low Kinetic Stability - These are MOFs that are stable under low humidity conditions.

For example, if a MOF retains it's pristine crystallinity and porosity upon the harshest of conditions (e.g. boiling in water for a month) it can be declared that this MOF has high thermodynamic stability with respect to water according to Burtch *et al.* [122]. Conversely, if

a framework yields a PXRD pattern that is entirely amorphous and the calculated BET value is negligible, the framework is classified as having no stability towards humidity. In reality, most MOFs fall somewhere between these two extremes. Shimizu *et al.* recognised this and proposed more explicit categories for the benchmarking of water stability in MOFs. The group proposed six levels of humidity exposure (1-6 given in Table 2.3) and four metrics for the proof of stability (A-D given in Table 2.4); they suggest the pairing of a value from each (e.g. 3B), gives more specific classifications to be used as guidelines for discussion [123].

Relative humidity (RH) is the ratio of the absolute amount of water vapour present in the atmosphere, to the equilibrium (or saturated) vapour pressure of water at a given temperature.

Table 2.3: Water exposure level as proposed by Shimizu *et al.*[123].

Level	Degree of exposure
1	Near ambient conditions (20 °C at 20% RH)
2	Mild humid conditions (25 °C at 50% RH)
3	Intermediate humid conditions (50 °C at 50% RH)
4	Immersion in water
5	Harsh humid conditions (80 °C at 90% RH)
6	Boiling water

Table 2.4: Metric of water stability as proposed by Shimizu *et al.*[123].

Category	Proof of stability
A	Retention of crystallinity
B	Retention of some porosity but loss of order
C	Retention of some order but loss of porosity
D	Loss of porosity and crystallinity

Both of these classification types are used interchangeably within literature. Therefore, where humidity stability measurements have been performed within this thesis; both ways of classifying a MOFs humidity stability will be used.

2.6.2 *The origin of fluorescence in MOFs*

The origin of the fluorescence in emissive MOFs results from a number of different sources. By virtue of their nature, MOFs have two distinct kinds of potentially emissive components; the metal ions and the organic linkers. In addition, the incorporation of guest molecules encapsulated within frameworks can also induce fluorescence in MOFs. Furthermore, effects such as the antennae effect, charge-transfers and the formation of excimers and exciplexes can all have an influence on the emissions of fluorescent MOFs [65, 67]. An illustrative example of the different modes of fluorescence in MOFs can be seen in Figure 2.14.

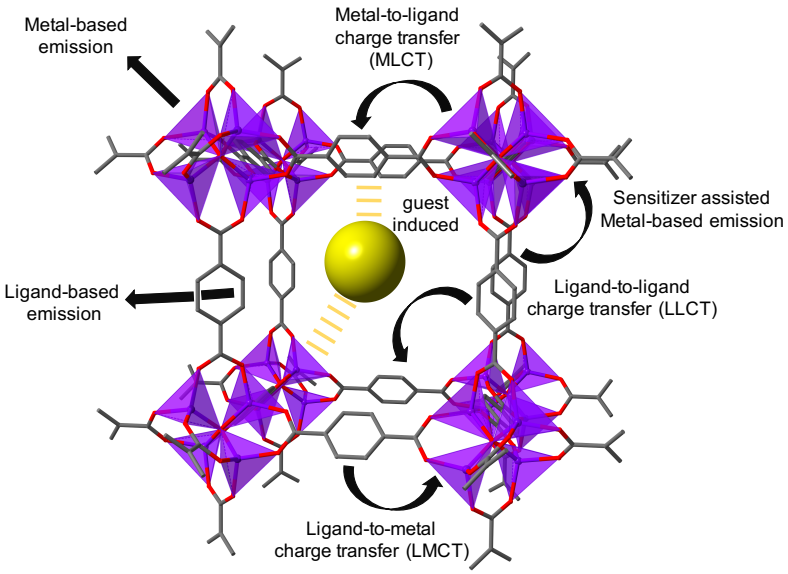

Figure 2.14: Illustrative example of the origin of fluorescence in MOFs. Figure reproduced from [67] with permission from The Royal Society of Chemistry.

The organic ligands are the most prevalent source of fluorescence in MOFs. Organic ligands that are highly conjugated are often strongly absorbing and emissive, they also have very little spin-orbit coupling, and so they are commonly chosen for the construction of fluorescent MOFs [65]. The excitation of the linker usually occurs *via* the

allowed singlet state transition (Figure 2.3) with the emission typically occurring from the lowest singlet excited state as fluorescence. If efficient non-radiative transfer to lower-lying states such as the triplet state, or states localised on the metal unit is achieved, no emission is observed. The triplet states are non-emissive as the spin selection rules are not relaxed *via* organic ligand spin-orbit coupling in MOFs [65]. The emissions can occur directly from the linker themselves or may result from a charge transfer with the coordinated metal ion or aggregate (or other linkers within the framework). If the emission spectra of a particular MOF and the free organic linker with which it is constructed show a similar profile (when excited at the same fixed wavelength); the MOF is said to be demonstrating linker-based emission [65]. For this to occur, generally the MOF must be constructed with transition-metal ions without unpaired electrons, such as d^{10} metal ions. Paramagnetic transition-metal MOF complexes are typically not very emissive due to ligand-field transitions (d–d) which can lead to the quenching of fluorescence (i.e. electron or energy transfer from the organic molecule through the partially filled d-orbitals). The most commonly reported linker-based and highly emissive MOFs are constructed from Cd(II) and Zn(II) metals [65]. The immobilization of organic ligands in ordered orientations within frameworks can lead to perturbations of the Stoke shift; which leads to the broadening of emission peaks for MOFs in comparison to individual ligand molecules. In addition, some organic linkers that are non-fluorescent in solution may become emissive once once incorporated into rigid MOF frameworks, this phenomenon is known as aggregation induced emission (AIE) [124]. Furthermore, owing to the well-defined spatial arrangements of the linkers, other interesting intermolecular communications can occur which result in photoemissions that are different from free linker forms, such as charge-

transfers [65, 95]. Charge transfers include ligand-ligand charge transfers (LLCT), metal-to-ligand (MLCT) or ligand-to-metal (LMCT) charge transfers. LLCT causes the loss of vibronic structure and enhance luminescence lifetimes of MOF emissions [67][65]. LMCTs result in emissions from the metal moiety of the complex. It is the structure of a MOF that depicts whether linker-based emissions, or charge transfers arise, or some combination, as these emission pathways are not mutually exclusive. The orientations of the organic linkers, the HOMO - LUMO gap of the metal and ligand components, as well as the electronic configurations and bonding geometry of the metals, all play a part in the resulting fluorescence emission of a MOF [65].

LLCT arise from the intermolecular stacking between adjacent linkers. LMCTs occur as a result of excited electron migration from the ligand molecular orbitals to those of the metals in the frameworks.

Generally, metal-based fluorescence in MOFs is observed when lanthanide ions are incorporated into frameworks. Lanthanides are luminescent, but their electronic transitions are forbidden by the parity Laporte selection rules. Thus, weak luminescence, low quantum yields, but very long lifetimes are most typically encountered for individual lanthanide compounds. However, when lanthanides and strongly absorbing organic ligands are combined together in a MOF, an increase in the lanthanide fluorescence is observed. This is attributed to the vibronic coupling between the metal and the ligands which facilitates energy transfer from the linker-excited state to the lanthanide ions (LMCT). This process is often referred to as the 'antenna' effect. When the luminescence of lanthanides is sensitized by antenna organic ligands, the long emission lifetimes of the lanthanides further increase; reaching almost a millisecond in duration [65].

Alternate origins of fluorescence in MOFs can arise from the formation of exciplexes and exciplexes; heterodimers and homodimers in the excited state respectively. These complexes originate through either π - π interactions between the organic linkers present within the MOFs or through interactions between the organic linkers of the

MOF and guest molecules. The formation of these complexes generate broad, featureless fluorescence emission spectra that are typically at red shifted wavelengths compared to their corresponding monomer MOF units [65]. Additionally, fluorescent guest molecules that are able to reside in the pores of MOFs sometimes create opportunities for non-emissive MOFs to demonstrate some level of luminescence. This fluorescence turn-on phenomena is increasing in popularity for sensing applications [65].

2.6.3 *Advantages of MOFs as fluorescence-based explosives sensors*

As discussed (Section 2.3), key requirements that are sought when developing explosives detectors for use in a given scenario include their ability to detect explosives sensitively, selectively and rapidly; while still maintaining detector integrity and re-usability of the material. Fluorescent MOFs have many inherent characteristics that can address these requirements and help promote their potential as explosive sensing materials. For example, the sustainable porosity of many MOFs facilitates their sensitive detection of target analytes. Through the encapsulation of analytes into MOF pores, the chances of sensor-analyte interactions are increased. Also, the capture of analytes into pores yields pre-concentration of the guests; increasing the sensitivity of these materials [67, 95]. Further to this, explosives sensors such as fluorescent conjugated polymers have demonstrated the fundamental importance of porosity on the sensitivity of analyte detection, and synthetic methods have been attempted to impart this characteristic in these materials (Section 2.5.3). Thus, MOFs, which are inherently porous, gain an automatic advantage in terms of their sensing potential over such materials [34, 95, 125].

With regards to selectivity, a substantial advantage of MOFs over other fluorescent sensing materials is their diverse and easily modifiable structures and topologies. Through the careful consideration of their building components, MOFs with specific pore sizes and dimensions can be produced, that can allow for the capture of some analytes and not others (the 'size exclusion principle' or 'molecular sieving' effect, as previously discussed in Section 2.5.3). Moreover, the skilful manipulation of organic ligands within the frameworks can introduce functional groups such as Lewis acidic or basic sites, and/or open metal sites; these can help promote a greater affinity of analyte binding with the MOFs; to impart greater selectivity in detection [67, 95]. A further benefit is the systematically tunable electronic properties of fluorescent MOFs. Through alterations of either the metal, organic linker, secondary building unit geometry and/or overall network connectivity; band gaps and atomic compositions of the valence band (HOMO) and conduction band (LUMO) of the MOFs can be altered. This is an important consideration for sensing applications as these properties directly correlate to the facilitation of electron and/or energy transfer between a MOF and an analyte. Thus, the ability to design MOFs to promote these features is highly beneficial [95].

The size, shape and nature of MOF pores are also directly linked to analyte adsorption kinetics and strongly influence the speed in which a response signal is produced. For example, MOFs possess the ability to be synthesised as nanoparticles which facilitate the faster diffusion of analyte molecules into the framework pores [31]. MOFs have the potential for rapid response times as a result of their porosity [67].

Generally analytes are physisorbed in MOF pores and can typically be easily desorbed through the application of appropriate stimuli, such as heat. MOFs are also very structurally stable and are able to retain their fluorescence at elevated temperatures (a phenomenon

not observed for AFCPs). Therefore regeneration of these materials is facile. Whilst stability with respect to heat is generally not an issue for MOFs; the hydrolytic stability of these materials can be a barrier to their use. However, as discussed (Section 2.6.1.5), such issues are being adressed by the MOF community and a number of water stable MOFs, fit for application, are being produced. The following section herein details the contributions made to date in the field of fluorescent MOFs for trace explosives detection. Each of these contributions demonstrate how the above-mentioned characteristics of MOFs promotes their potential as explosives sensors.

2.6.4 *Previous contributions to research on MOFs as explosives sensors*

2.6.4.1 *Pioneering research*

The pioneering research outlining the potential of fluorescent MOFs for explosives detection was reported by Li *et al.*, who solvothermally synthesised mixed ligand MOF $[Zn_2(bpdc)_2(bpee)]\cdot 2DMF$, for the vapour-phase detection of the TNT derivative 2,4-DNT and the plastic explosives taggant DMNB [126].

Metal-organic framework $[Zn_2(bpdc)_2(bpee)]\cdot 2DMF$ is constructed from 4,4'-biphenyl dicarboxylic acid (H_2bpdc) and 1,2-bipyridylethene (bpee). Single crystal X-ray diffraction confirmed the structure of this MOF to be three-dimensional and to contain eight membered-ring type secondary building units (SBUs). In addition, one-dimensional channels were observed to run throughout the structure of this MOF, within which, solvent DMF molecules were found to reside. As discussed (Section 2.6.1.3), solvent free, 'activated' frameworks are desirable for sensing; as the presence of surplus guests within MOF pores can hinder the encapsulation of target analytes. Thus, the guest DMF molecules present within this MOF's cavities were removed through

the use of a solvent exchange procedure. Powder X-ray diffraction (PXRD) confirmed the guest free framework ($[Zn_2(bpdc)_2(bpee)]$) to have retained its crystallinity upon solvent evacuation, although some distortions of the unit cell were apparent as evidenced by shifts in the PXRD peaks, indicative of a slight structural change of the framework. The Langmuir surface area of the active MOF was reported to be 483 m^2g^{-1}. An illustration of guest free MOF $[Zn_2(bpdc)_2(bpee)]$ can be seen in Figure 2.15a.

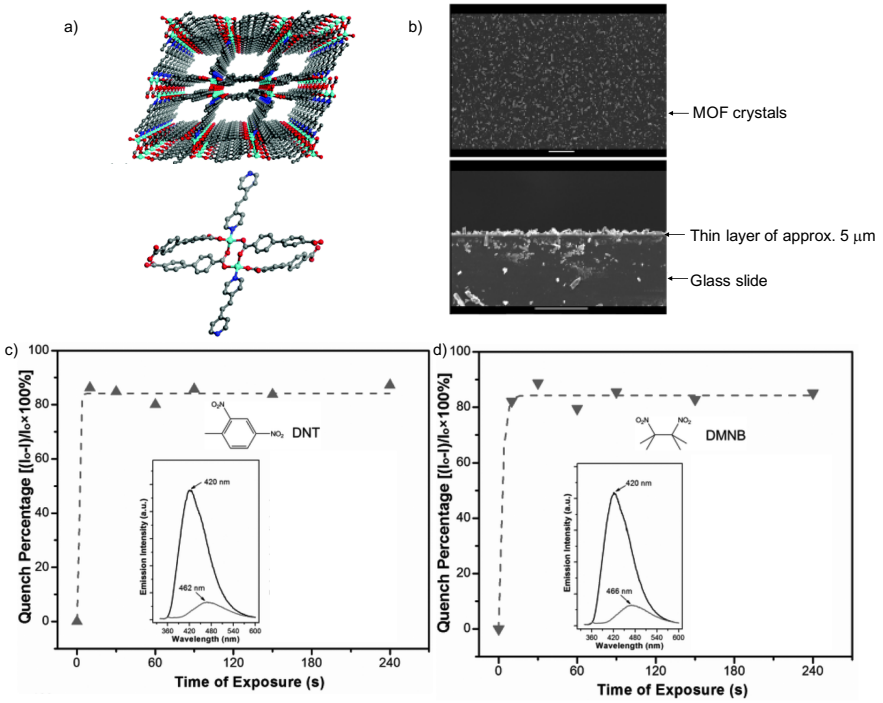

Figure 2.15: a) Representation of the overall three-dimensional structure of active MOF $[Zn_2(bpdc)_2(bpee)]$ and the secondary building units through which this MOF is constructed. Carbon atoms are denoted by the colour grey, oxygen atoms red, nitrogen atoms navy blue and zinc atoms light blue. Hydrogens have been omitted for clarity. b) SEM images of a typical thin film of the MOF; top SEM as viewed from the top of the film and bottom SEM; a side on view. c) and d) Results of the time-dependent sensing reposes of the MOF upon exposure to DNT and DMNB saturated vapours respectively, plotted as quenching percentages. Inset of the graphs show the initial fluorescence emission profile of the MOF and the emission after 10 s exposure to the analytes. Reprinted with permission from [126]. Copyright 2009 Wiley-VCH.

'Thin films' of the activated metal-organic framework, of approximately 5 μm thickness were fabricated using quartz slides. Double sided tape was applied to the slides and subsequently removed to

allow for an adhesive residue to remain, onto which, finely ground crystals of the MOF were scattered (Figure 2.15b). Upon illumination by UV radiation (λ_{ex} 320 nm) this MOF was observed to be highly fluorescent in the solid state, with its emissions attributed to the organic linkers present within the structure (inset of Figure 2.15c and Figure 2.15d).

In the sensing procedure the films were exposed to the saturated vapours of the analytes 2,4-DNT and DMNB (Table 2.1) each for 10 s, 30 s, 60 s, 90 s, 150 s and 240 s, during which, changes in the fluorescence intensity of the films were measured.

The high intensity of the MOF fluorescence emission peak was observed to attenuate upon exposure to each analyte. Quenching percentages (QPs; calculated using Equation 2.14) were reported as 85% and 84% for 2,4-DNT and DMNB respectively, after 10 s of exposure to the MOF, with no additional quenching observed after longer exposure times (Figure 2.15c and Figure 2.15d). It is significant to note that thicker films of the framework (*ca.* 30 μm) produced much slower response times, attributed by Li *et al.* to the restricted diffusion pathways for the analytes to penetrate MOF pores. The same was reported for non-activated, solvent containing MOF films [126].

$$\text{Quenching Percentage (QP)} = \left(\frac{I_o - I}{I_o}\right) \times 100 \tag{2.14}$$

where

I_o Original peak maximum intensity

I Maximum intensity after exposure to the analyte

The magnitude of the quenching response demonstrated by the 'thin films' of this MOF towards 2,4-DNT is comparable to that reported for this analyte using amplified fluorescent conjugated polymer (AFCP) films. Whereas, the reported speed and sensitivity of the

response by this MOF towards DMNB seems to outperform those reported for AFCPs significantly (Section 2.5.3)[126]. Li *et al.* attributed such findings to the microporosity of the MOF and thus, its ability to facilitate strong and rapid host-guest interactions through the encapsulation of the analyte into the framework cavities. The quenching mechanism through which these analytes quenched the MOF was briefly hinted at during this initial proof-of-concept study and attributed to the PIET mechanism (Section 2.5.2.1), similarly to AFCPs. Subsequent research by Li *et al.* sought to clarify this.

Mechanism proposition

In their follow up research, Li *et al.* generated 'thin films' of MOF $[Zn_2(oba)_2(bpy)]\cdot DMA$, where oba = 4,4'-oxybis(benzoic acid), bpy = 4,4'-bipyridine, and DMA = N-N-Dimethylacetamide (Figure 2.16), using the same film fabrication method as previously stated. This MOF was reported to have a porosity of 84 m^2g^{-1}. During sensing, the MOF was exposed to the vapours of two groups of analytes; group A and B [127].

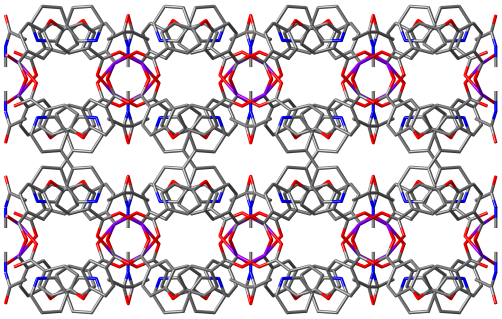

Figure 2.16: Structure of MOF $[Zn_2(oba)_2(bpy)]\cdot DMA$, where oba = 4,4'-oxybis(benzoic acid), bpy = 4,4'-bipyridine, and DMA = N-N-Dimethylacetamide as synthesised by Li *et al.*. Figure reproduced from the crystallographic data available and with permission from [127]. Copyright 2011 American Chemical Society.

Group A consisted of electron-poor nitroaromatic compounds that contained electron-withdrawing moieties (e.g. 2,4-DNT, NB, *p*-NT)

and group B contained electron-rich aromatic compounds on which, electron-donating groups were present (e.g. toluene, benzene, chlorobenzene). Upon exposure of the MOF to these different groups it was seen that group A analytes quenched MOFs fluorescences, where as group B analytes enhanced the fluorescence emissions of the framework.

Based on these results Li *et al.* proposed that the observed quenching and enhancement of the MOF occurred as a result of the photo-induced electron transfer mechanism. The group suggested that although MOFs have extended structures, they can be characterized by narrow energy bands owing to their highly localized electronic states, particularly those containing d^{10} metals. Thus, proposing that MOFs can be regarded as 'giant molecules', and their 'valence' (VB) and 'conduction bands' (CB) can be expressed in an approach similar to that for molecular orbitals (HOMOs and LUMOs) [127]. Li *et al.* suggested that the electron deficient compounds with low lying π^* LUMOs below the conduction band of the MOF (or MOF LUMO containing an excited sate electron), were able to receive excitons from the framework and thus, a quench of the system was observed. The group confirmed the positions of the MOF conduction bands and analyte HOMO - LUMO gaps through computational calculations. This proposed mechanism has been widely accepted by the MOF community as a plausible explanation for the quenching of MOFs in the presence of such analytes [67, 128].

Regarding the electron-rich aromatic compounds enhancing the fluorescence of the MOF, the group attributed such findings as a result of the excited electrons from the high-lying non-bonding orbitals of these electron-rich analytes, which are above the CB of the MOF, being transferred from the analytes to the MOF; thereby leading to fluorescence enhancements. An illustration of these fluorescence quench-

ing and enhancement mechanisms as suggested by Li *et al.*, for MOFs in the presence of these two distinct analyte groups can be seen in Figure 2.17. Additionally, it was proposed that the direction of the electron transfer between the photo-excited states of MOFs and analytes could be determined based on the reduction potential of the analytes. Group A analytes all had reduction potentials more positive than the MOFs and group B analytes had more negative reduction potentials. As such, the MOFs would act as electron donors in the case of group A analytes and electron acceptors of group B compounds [127].

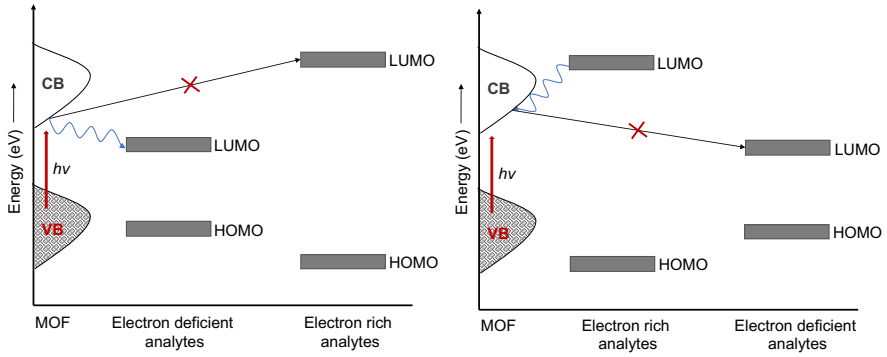

Figure 2.17: Energy diagram representation of the PIET mechanism that occurs for MOFs in the presence of different analytes as proposed by *et al.*. Left: shows the fluorescence quenching process by electron deficient analytes and Right: shows the fluorescence enhancement process in the presence of electron rich analytes. Reprinted from [127]. Copyright 2011 American Chemical Society.

The rationale proposed for the enhancement of MOF emissions (occurring as a result of PIET from analytes to MOFs) has been somewhat criticised by the MOF sensor community. It has been claimed that such explanation is unlikely, as this opposite electron transfer would instead cause the MOF fluorescence to be attenuated owing to non-radiative relaxation of the excited state [128, 129]. An alternate explanation that has been proposed is that the sorbed analytes inhibit linker rotations (vibrations, torsional displacements etc.) that otherwise facilitate the non-radiative decay of the photo-excited state (and therefore enhance fluorescence emissions of the MOF), or, the formation of MOF-analyte exciplexes [128, 129]. Whilst Li *et al.* have

acknowledged these differing explanations, there is still some ambiguity as to which mechanism is the reason for such fluorescent enhancement in these materials [95]. Nevertheless, it is significant to note that these electron-rich analytes cause different changes in the fluorescence emissions of the MOF in comparison to the electron-poor nitroaromatics; potentially allowing for differentiation between some explosive and non-explosive compounds by virtue of the electron deficient nature of most explosives [127].

The importance of MOF structure and porosity on sensing

Another interesting observation gleaned from this secondary study by Li *et al.* was the minimal quenching effect observed by MOF [Zn_2-$(oba)_2(bpy)$](Figure 2.16) in the presence of DMNB (<1 %). This is very different to that observed by the initial MOF [$Zn_2(bpdc)_2(bpee)$] (Figure 2.15) which was quenched by 84% after DMNB exposure. These differences were noted despite the two MOF 'thin films' being made and exposed to the analyte in the same way. These observations were rationalised based upon the differing structures of the two MOFs. Li *et al.* suggested that the reduced sensitivity of MOF [$Zn_2(oba)_2(bpy)$] towards DMNB is attributed to its poor orbital overlap between the MOF conduction band and the LUMO of the analyte, leading to difficulty in electron transfer. This poor orbital overlap was attributed to the pore sizes of the MOF being too small for the non-planar, bulky, DMNB to enter. This size exclusion principle is very useful for imparting selectivity into MOF sensors. In addition, the observed minimal response towards DMNB was also attributed to the similar reduction potentials between the MOF an the analyte, therefore the driving force for the electron transfer was lacking [127]. These results highlight the importance of MOF structure and porosity on sensing capabilities.

Peak shift phenomenon and two dimensional maps

In addition to demonstrating alterations in the intensity of fluorescence emission upon exposure to explosive related analytes; a number of MOFs synthesised by Li *et al.* have also displayed shifts in their fluorescence emission wavelength (frequency), which differ upon contact with various analytes [67, 126, 130–132]. Such shifts typically originate due to strong MOF-analyte interactions during excitation; such as the formation of exciplex structures (Section 2.6.2) [31]. These transformations in wavelength are by in large only observed for flexible framework structures that facilitate pore-based host-guest interactions and structural perturbations. This phenomenon of fluorescence emission peak shift adds great value to these materials as sensors. The detection of explosive analytes with very low vapour pressures based on fluorescence intensity changes alone can be challenging. Additionally, compounds of a similar chemical nature generate almost identical changes in emission intensity. Therefore, through monitoring changes in fluorescence intensity alongside the shifts in emission frequency, better discrimination of analytes is possible. Li *et al.* used these two dimensions of analysis to construct maps that allow for the 'fingerprinting' of explosive related analytes, by representing each analyte as a point on the 2D Cartesian coordinate projection, as shown in Figure 2.18 [133].

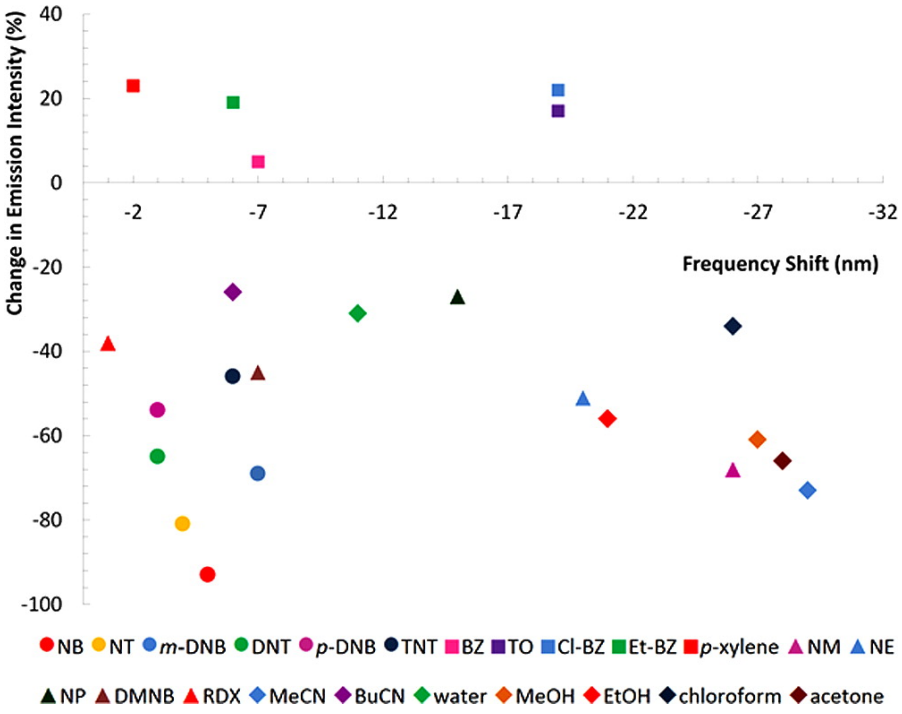

Figure 2.18: An example of a two-dimensional cartesian coordinate projection of the sensing responses of a MOF as synthesis by Li *et al.* after 5 minutes of exposure to varying analytes at room temperature. Electron deficient nitroaromatic compounds are represented by coloured circles, electron rich aromatic compounds are denoted by coloured squares, nitroaliphatics are shown by triangles and solvents as diamonds. Reprinted with permission from [133]. Copyright 2013 American Chemical Society.

Regeneration studies

As discussed, the re-usability of a sensor is desirable for its use within real-world detection scenarios. All of the metal-organic frameworks synthesised by Li *et al.* were subjected to regeneration studies, whereby the reversibility of analytes binding to the MOFs were tested. After the initial sensing experiments, the exposed MOFs would be heated at elevated temperatures, causing the bound analytes to disassociate, leaving fully regenerated and intact guest-free frameworks. Post regeneration, the frameworks were re-tested against the same analytes they were initially exposed to and were noted to still maintain their detection capabilities with very little response variation [126].

2.6.4.2 *Vapour vs solution phase sensing*

Since these initial exploratory studies on the use of fluorescent MOFs for explosives detection, a number of groups have attempted to exploit the beneficial characteristics of these materials (Section 2.6.3), in an attempt to yield MOFs that are best fit for the application in terms of sensitivity, selectivity, regeneration and stability; some of which will be discussed in the following section. Similarly to the research conducted on AFCPs, there are two different ways in which MOFs can be exposed to explosives to test their potential as sensors; exposing the MOFs to analytes in the SOLUTION or VAPOUR-PHASE [95].

Vapour-phase detection

As demonstrated in the work conducted by Li *et al.* vapour phase sensing involves the exposure of metal-organic frameworks in the solid state to vapours of target analytes [95]. Another metal-organic framework that has demonstrated the successful detection of target vapours is $[In_2L][NH_2(CH_3)_2]_2 \cdot (DMF)_4(H_2O)_{16}$ (where L= tetrakis[(3,5-dicarboxyphenoxy)methyl]methane). This anionic framework exhibited significant quenching responses upon exposure to the saturated vapours of nitrobenzene (82% quench with 5 s of exposure). Upon exposure to 1,3-dinitrobutane (1,3-DNB) and 2,4-DNT much slower and less pronounced responses were noted, with around a 10% quench of the MOF upon 5 seconds of interaction with the analytes and a ~ 50% quench after 15 minutes exposure (both analytes yielded similar responses of the MOF). Du *et al.* attributed these differences to the low vapour pressures of 1,3-DNB and 2,4-DNT, meaning in the tested time frame; the MOF and analytes were not able to form adequate interactions, unlike the MOF and NB. In addition the group attributed the difference in responses between analytes to the inability of the bulkier

1,3-DNB and 2,4-DNT molecules to enter into the MOF pores owing to size exclusion [134].

Although sensing in the vapour-phase is highly desired, as it tests the potential of MOFs as stand-off sensors, and despite a collection of MOFs having already demonstrated such potential (each of which have noted the importance of porosity on the successful detection of target analytes) [31, 135–139]; there is a limited amount of research whereby the responses of MOFs in the presence of explosives analytes in the vapour-phase is tested [140]. This is potentially due to the aforementioned difficulty in thin-film fabrication. The majority of vapour-phase research has used 'thin films' that have been fabricated in a simplistic way similar to that reported by Li *et al*. Whilst some work has been done to fabricate thin films for the effective vapour-phase detection of explosives (or related compounds), this area is very much in its infancy [67]. The most notable contribution to date has been from Yang *et al.* who produced a thin film of MOF $[Eu_2(TDC)_3(CH_3OH)_2]\cdot CH_3OH$, using an electrodeposition method, for the vapour-phase detection of saturated nitrobenzene vapours [141]. The films showed an 80% quench upon exposure to the analyte for 240 seconds. This work demonstrates a promising route for the fabrication of fluorescent MOF thin films for explosives detection. However, it remains at proof-of-concept stage and further work is required to better understand the optimum synthetic conditions and thin film morphology that yields the greatest sensitivity in sensing. Additionally, all current research on MOFs for the vapour-phase sensing of explosives is limited to using saturated vapours of explosives-related compounds. This approach makes it difficult to determine the potential sensitivity and selectivity of a MOF towards different analytes, owing to their different saturated vapour concentrations at room temperature. Further to this, the ability of MOFs to detect the vapours of real explo-

sives is very much under reported. Consequently, the majority of research on the use of MOFs for explosives detection has tested the sensors detection capabilities in the solution phase, which allows for MOFs to be exposed to known concentrations of explosive substances as well as related compounds [95]. An additional benefit to sensing in the solution phase with adding known quantities of explosives is that estimates as to the quenching efficiencies of materials, as well as the type of quenching process operating, (static or collisional) can be ascertained; through analysis of Stern-Volmer plots and constants (Section 2.5.2.5). Further to this, knowing the concentration of analytes through titrations in the solution phase can allow for limits of detection to be determined [142] [143].

Solution-phase sensing

The sensing of explosives in the solution phase is typically achieved by suspending the MOF crystals in solvents such as methanol (MeOH), ethanol (EtOH), acetonitrile (MeCN), or N, N-Dimethylformamide (DMF), and subsequently titrating in known quantities of explosive analytes, whilst monitoring any apparent changes in fluorescence emissions. For example, Mukherjee *et al.* dispersed 5 mg of MOF $[Zn_4O(L)_2 \cdot 3DMA \cdot 3EtOH \cdot H_2O$ (where L = 5-(4-carboxyphenylethynyl)-isophthalate) in 2 mL of ethanol using sonocation [144]. The MOF suspension was exposed to 1 mM (1.0×10^{3} M) solutions of NB, *p*-NT, 2,4-DNT and TNT by incremental addition of 20 μL of the analytes, with fluorescence measurements taken after each addition, until 200 μL of each analyte were added. Figure 2.19 denotes the changes observed upon addition of TNT to the framework. The group reported the limit of detection of TNT in ethanol using this MOF to be 10 ppb. Which is comparable to the detection of this analyte by AFCP in

solution [79]. Centrifugation of the dispersed solution after use and washing with ethanol was able to regenerate the MOF [144].

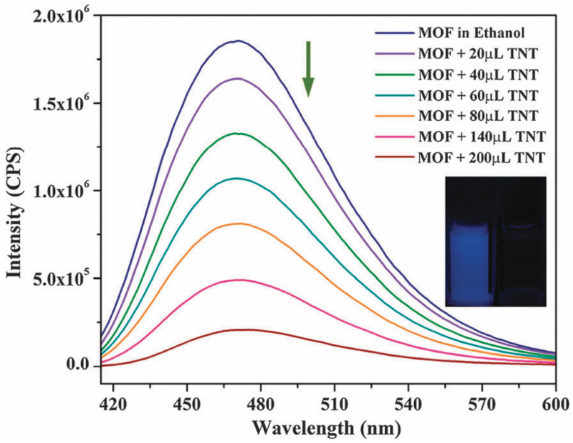

Figure 2.19: Illustration of the fluorescence emission profile of MOF $[Zn_4O(L)_2 \cdot 3DMA \cdot 3EtOH \cdot H_2O]$ suspended in ethanol, upon the gradual addition of a 1mM solution of TNT (in ethanol). The arrow in the figure denotes the loss of fluorescence intensity of the MOF suspension upon addition of the analyte. Inset demonstrates the visual colour change of the MOF before and after titrating with TNT under a UV-light. Reproduced from [144] with permission from The Royal Society of Chemistry.

Mandal *et al.* demonstrated how Stern-Volmer (SV) plots and lifetime measurements can be used to understand the sensing dynamics in MOFs. The group synthesised MOF $[Zn_2(NDC)_2(bpy)]$ (where NDC = 2,6-napthalenedicarboxylic acid and bpy = 4,4'- bipyridine) which was found to contain minimal porosity [136]. The MOF was suspended in ethanol and titrations adding $1-7$ μL of 1,4-Dinitrobenzene (1,4-DNB), NB, TNT, 2,4−DNT, *p*-NT (4.4 mM) solutions were performed. Unexpectedly, it was observed that *p*-NT yielded the greatest quenching of the MOF, with the order of quenching magnitude of the other analytes (at the same concentration) following that of 2,4-DNT > TNT > NB > 1,4-DNB. SV plots were generated for the addition of each of the analytes to the MOF and K_{SV} values obtained. It was concluded that the small *p*-NT molecules yielded the most efficient quenching, evidenced by the greatest K_{SV} value observed for *p*-NT compared to the other tested analytes. The group rationalised the

preferential sensing of *p*-NT due to its higher dipole moment in comparison to the other compounds. Therefore, leading to the strongest MOF-analyte interactions. Mandal *et al.* additionally performed time-resolved measurements to depict which type of quenching process was causing the attenuation of the MOF during sensing. The lifetimes of the MOF decreased upon incremental addition of the analytes and it was observed that the absorption maximum of the MOF remained the same post interaction with the analytes; indicating no MOF-analyte complex formation. Thus, it was determined that collisional quenching dominated the sensing of analytes using this MOF, which coincides with its minimal porosity [136].

2.6.4.3 *Rational design of MOF sensors*

Tuning MOF band gaps for enhanced analyte detection

As discussed (Section 2.6.3), a great merit of MOFs is their tunable nature. Li *et al.* demonstrated how changing MOF framework structures can lead to different electronic properties, such as different band gaps, which can cause the varied sensing of analytes based on the thermodynamics of the PIET mechanism (Section 2.6.4.1). Ghosh *et al.* further built on this by constructing a MOF with a tuned band gap, which was highly selective towards TNP in the presence of other explosives, owing to its emission spectrum overlapping with the absorption spectrum of TNP. Thus, allowing for both PIET and FRET mechanism to cause the quenching of the framework.

MOF [Cd(NDC)0.5(PCA)] (NDC = 2,6- napthalenedicarboxylic acid, PCA = 4-pyridine carboxylic acid) was dispersed in MeCN and titrated against TNP, TNT, 2,3-DNT, 2,6-DNT, DNB, NB, DMNB, NM, and RDX. The MOF showed pronounced fluorescence quenching in the presence of TNP compared to the other nitroaromatic analytes [143]. Subsequent titrations demonstrated that the selectivity towards TNP

by this MOF was still apparent even in the presence of other interfering analytes (which were added first to the MOF suspension) whose chemical compositions were similar to that of TNP. For example, upon addition of a saturated TNT solution to the MOF, there was little effect on the fluorescence intensity of the framework, however, the following addition of aqueous TNP to this same solution resulted in significant quenching of the MOF's fluorescence. Similar results were also observed for the other analytes mentioned above. This selective detection of TNP was attributed to both the photo-induced electron transfer and Förster resonance energy transfer mechanisms causing the quenching of the MOF with this analyte. This was rationalised based on the deviation of linearity of the Stern-Volmer plot as well as the good spectral overlap between the absorption spectrum of TNP and the emission spectrum of [Cd(NDC)0.5(PCA)] (as demonstrated in Figure 2.20). The absorption spectra of the other analytes and the emission spectrum of MOF had negligible overlap, and so any quenching observed of the MOF upon exposure to these analytes was attributed to the PIET mechanism alone. A number of other groups have also successfully reported the amplified detection of TNP/Picric acid over other nitroraromatic explosives and related compounds as a result of FRET quenching mechanisms [145–148].

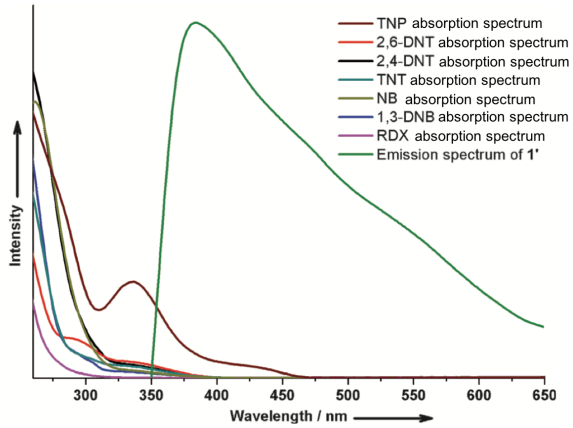

Figure 2.20: Illustrative example of how the fluorescence emission spectrum of MOF [Cd(NDC)0.5(PCA)] (denoted as **1'** in the figure) overlaps with the absorption spectrum of TNP; leading to FRET. The figure also shows the minimal spectral overlap between the emission of the MOF and the absorption spectra of the other analytes. Reproduced with permission from [143]. Copyright 2013 American Chemical Society.

The work in this study also demonstrated the successful detection of TNP by the MOF suspended in an aqueous solution. The ability of MOFs to detect explosives in the aqueous-phase is beneficial as it allows for the detection of threat materials in aquatic systems, waste water, and soil; which is important for both security and environmental monitoring applications [149]. A number of other MOFs have also demonstrated the successful detection of explosives or related analytes in water [150–152].

Optimisation of the organic linker component

An alternate approach that has been sought by researchers to increase the sensitivity of fluorescent MOF explosive sensors has been to engineer highly electron dense and exceedingly fluorescent MOFs; this has been achieved through the design and syntheses of highly conjugated organic linkers. The introduction of such linkers in a framework has been suggested to better attract aromatic or conjugate analytes (such as nitroaromatic explosives) through $\pi - \pi$ interactions. Further to this, the relative orbital energies of the CB (or LUMO) of the

MOFs can be tailored through the manipulation of the organic linkers through which they are constructed (the benefits of which have been aforementioned) [95]. The judicial choice of organic linkers can also allow for MOFs to be designed with various cavity sizes, which as discussed, can impart selectivity through size exclusion (Section 2.6.4.1). Also, functionality can be introduced into ligands which can be used to construct MOFs with additional interaction sites, for the potential targeting of specific analytes or groups of analytes. For example creating MOFs with Lewis basic sites has been shown to facilitate the detection of metal ions and the acidic analyte TNP (or Picric acid) [127, 143]. In addition, the use of unsaturated metal sites (UMS) has been reported to preferentially bind NH_3 groups. Such interactions are significant for the facilitation of detection of non-aromatic compounds [127]. Figure 2.21 illustrates some of these linkers created by various groups, all of which have formed MOFs able to successfully detect explosives and/or explosive related materials [135, 144, 146, 153–158].

UMS are open metal sites in MOFs which are produced upon the removal of weakly bound solvent molecules coordinated to the MOF metals.

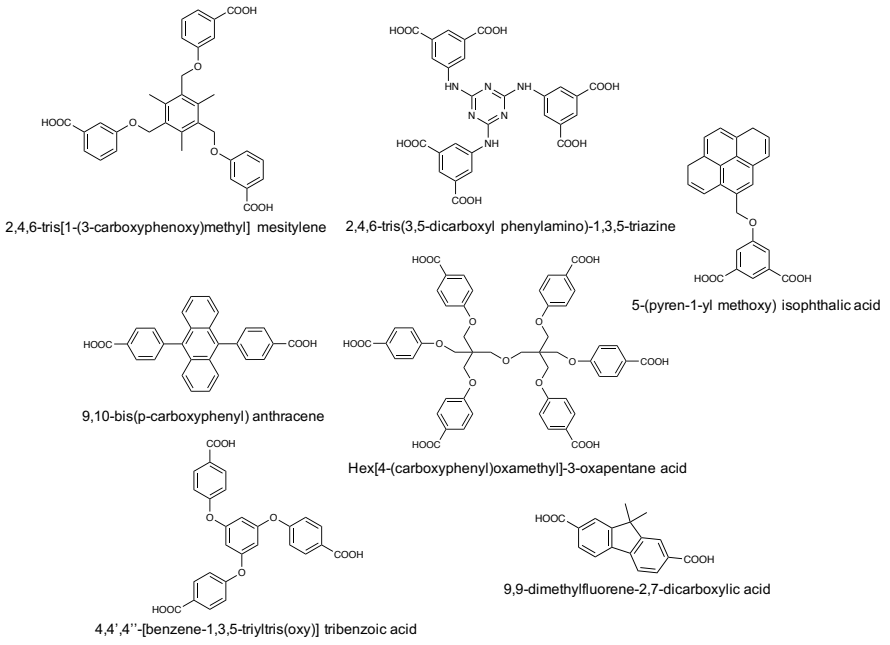

Figure 2.21: Examples of organic linkers that have been designed and used for the construction of highly fluorescent MOFs for explosives detection.

Judicious choice of MOF metal component

The inorganic metal component of an MOF can also be judiciously chosen to yield highly fluorescent frameworks. Transition metals, specifically d^{10} transition metals, have been most frequently used in the construction of fluorescent MOF sensors (due to their non-paramagnetism as discussed in Section 2.6.2). However, other main group metals such as lithium [159] and indium [134] have also been explored.

Other research has reported the use of lanthanides for the construction of fluorescent MOFs, as lanthanides themselves can be good sources of luminescence when used alongside highly absorbing organic linkers (Section 2.6.2). As discussed (Section 2.6.2), the fluorescence of lanthanide containing MOFs arises as a result of the antennae affect. The predominantly reported quenching mechanisms of lanthanide-containing MOFs in the presence of explosives is the PIET mechanism, whereby photo-induced electron transfer from the MOF organic ligands to the explosives causes an interruption of the antennae effect, resulting in the quench of the lanthanide emission in the MOF [31, 67].

In one report by Zhou *et al.* the quenching of a lanthanide MOF was attributed to a number of contributing factors, primarily as a result of the PIET mechanism but also due to the competition for light absorption between the analytes and the organic ligands of the MOF. It was suggested that analytes with high absorbance (a large molar absorption coefficient ε) can efficiently absorb light with which the samples are excited. This prevents the light from being absorbed by the organic linker antennaes and transferred to the lanthanide metals, thus, also causing a quench of the lanthanide emissions; this is termed the antennae screening effect [160]. The group synthesised MOF $Eu_3(MFDA)_4{\cdot}(DMF)_3$ which is constructed from Eu^{3+} ions and the highly-electron rich ligand H_2 MFDA (9,9-dimethylfluorene-2,7-

dicarboxylic acid, Figure 2.21). The MOF demonstrated good quenching responses upon exposure to a number of different explosive related analytes [160], in particular 3,4-DNT was found to be the most effective quencher of the MOF with quenching efficiencies of ~ 45 % (0.5 mM conc. solution in DMF). Due to the quenching magnitudes of the MOF not following those expected based on the electron withdrawing abilities of the analytes; the group attributed the quenching of the MOF in the presence of the nitroaromatics as a combined result of mainly the PIET mechanism but also the competition for absorption of the excited light source between the analytes and organic ligands [160].

Although a number of lanthanide-based MOFs have been reported, this area of research is still very much underdeveloped, as only terbium and europium based frameworks are known [145, 160–162].

The use of NanoMOFs

Substantial efforts are being made to synthesise nanocrystalline fluorescent MOFs for improved detection sensitivities, as sensing kinetics can be enhanced with smaller particle sizes [31]. For example, Mandal *et al*. noted that decreasing the particle size of one of their MOF sensors from 20 μm to 50 nm nearly doubled the quenching efficiency of the MOF towards TNP. The nanoparticles of this MOF were able to be fabricated into test strips which demonstrated visible quenching response upon exposure to TNP in amounts as low as 7.24 nm, or 1.66 ppb [163].

2.7 THESIS AIMS, OUTLINE AND NOVELTY OF RESEARCH

This thesis aims to further expand the knowledge of fluorescent metal-organic frameworks as explosives sensors. The synthesis and characterisation of three novel MOFs will be presented, each of which have different framework architectures, pore environments, and electronic structures; which impact on their sensing capabilities towards explosive substances and related compounds. The sensing performance of these MOFs has been evaluated in both the solution and vapour-phase. As well as contributing to the research field through the generation of new MOF sensors, this thesis explores the use of MOFs in a sensor array (chemical nose) for the discriminative detection of explosives. In addition, the ability of MOFs to be used as standalone pre-concentrator sorbent materials towards explosive vapours (and not as sensors) has also been investigated; with the aim to evaluate whether MOFs can potentially be used to increase the sensitivity of other trace explosives detectors. Both of these aspects add a significant contribution to the field of research on MOFs for trace explosives detection, as such investigations have not been reported in the current literature. In essence, the Ph.D. research presented in this thesis has sought to further interrogate the potential applicability of MOFs within the field of trace explosives detection.

3

A PILOT STUDY INTO TWO NOVEL MOFS FOR VAPOUR-PHASE SENSING

3.1 INTRODUCTION

This chapter details the synthesis and characterisation of two novel fluorescent metal organic frameworks [Zn(dcbpy)(DMF)]·DMF (MOF **1**) and [Dy(dcbpy)$(DMF)_2(NO_3)$] (MOF **2**) (where H_2dcbpy = 2,2′-bipyridine-4,4′-dicarboxylate and DMF = *N*,*N* -Dimethyl formamide), for the vapour-phase detection of explosive related analytes and derivatives [164].

As discussed in Chapter 2, it is believed that one of the greatest attributes of MOFs as potential sensors, is the ease with which they can be tailored (through the judicial choice of organic ligands and metal ions) for their potential targeting of particular analytes (or groups of analytes). The preliminary research presented in this chapter sought to explore what effects altering one building block component may have on the overall structure of an MOF that is formed, and what impact different topologies may have on sensing. The work also investigated how to form MOF 'thin films' and how to undertake sensing on relevant analytes in the gas phase.

Metal-organic frameworks **1** and **2** have been synthesised from the same organic ligand H_2dcbpy (Figure 3.1), but vary in metal composition (zinc and dysprosium).

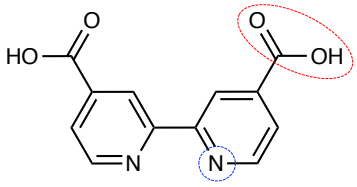

Figure 3.1: Molecular structure of 2,2′-bipyridine-4,4′-dicarboxylate (H_2dcbpy). The dotted circles denote the potential binding sites of this linker.

This organic linker was chosen because of its aromatic and electron rich nature; to allow for linker-based fluorescence emissions of the MOFs. Further to this, the presence of two potential binding sites of this ligand (the carboxylate and pyridine moieties, as highlighted in Figure 3.1) allow it to coordinate with metal ions in different ways; potentially leading to interesting and diverse MOF structures. The use of a lanthanide for the construction of one of the MOFs was employed with the aim to increase the system's fluorescence; resulting in the synthesis of the first dysprosium MOF for the sensing of explosives related analytes and derivatives. The research presented in this chapter also demonstrates how microwave synthesis can be implemented to rapidly generate homogeneous microcrystals of MOF **1**, termed **1M**, and it examines the effect that these uniform crystals had on the MOF's sensing performance.

The metal-organic frameworks synthesised were tested for their abilities to act as fluorescence-based sensing materials towards the TNT derivatives 2,4-dinitrotoluene (2,4-DNT), *para*-nitrotoluene (*p*-NT) and nitrobenzene (NB), as well as the plastic explosives taggant 2,3-dimethyl-2,3-dinitrobutane (DMNB) (Figure 2.2). These analytes were chosen as they are often good markers as to the presence of explosives, they have considerably higher vapour pressures than explosives themselves, and they are readily available for testing in non-specialised explosives research laboratories (Section 2.3.2.2). Furthermore, dinitrotoluenes and nitrobenzene are known toxic, organic pollutants that are often discharged into the environment by industrial

processes, therefore the detection of these compounds is of more general interest [165]. Due to the aforementioned need for new portable, stand-off, vapour-phase detection methods for the trace detection of explosives; the sensing capabilities of the frameworks were assessed with the analytes in the gaseous-phase. The methodology employed for the initial examination of these materials was modelled on that reported by Li *et al.* who conducted the pioneering and state of the art research within this field (Section 2.6.4.1).

3.2 EXPERIMENTAL

3.2.1 *Synthesis of metal-organic frameworks*

3.2.1.1 *Synthesis of [Zn(dcbpy)(DMF)]·DMF (**1**)*

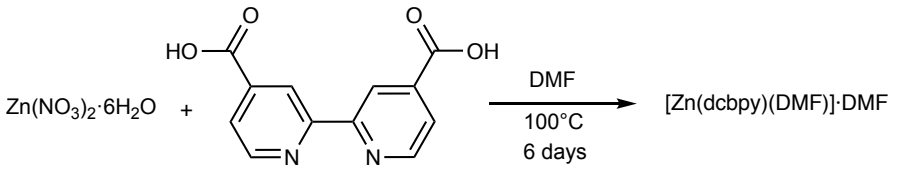

Scheme 3.1: Reaction scheme detailing the synthesis of [Zn(dcbpy)(DMF)]·DMF (**1**)

MOF [Zn(dcbpy)(DMF)]·DMF (**1**) was synthesised *via* a typical solvothermal method (Section 2.6.1.2), the reaction scheme of which is given in Scheme 3.1. Zinc nitrate hexahydrate ($Zn(NO_3)_2 \cdot 6\,H_2O$, 0.4 mmol, 119.0 mg) and 2,2'-bipyridine-4,4'-dicarboxylate (H_2dcbpy, 0.4 mmol, 97.8 mg) were dissolved in 15 mL of *N*,*N*-dimethylformamide (DMF) whilst stirring in a glass vial. The vial was sealed to generate an autogenous pressure and placed inside a conventional heating oven set to 100°C for 6 days; affording colourless rectangular plate-like crystals of **1**, in approximately a 80% yield.

3.2.1.2 *Microwave synthesis of [Zn(dcbpy)(DMF)]·DMF (**1M**)*

$Zn(NO_3)_2 \cdot 6\,H_2O$ (0.2 mmol, 60.0 mg) and H_2dcbpy (0.2 mmol, 48.8 mg) were dissolved in 12 mL of DMF in a glass vial and stirred at 40°C for approximately 10 minutes. After most of the contents had dissolved, 3 mL of the cloudy reactant solution was syringed into a new glass vial, which was subsequently sealed and placed into a 700 W microwave oven operating at a 40% power output*. The sample was irradiated initially for 30 s, followed by three more 30 s cycles. This yielded a clear solution and a microcrystalline MOF precipitate.

* Full details of the microwave used can be found in Chapter 8.

3.2.1.3 *Synthesis of [Dy(dcbpy)(DMF)$_2$(NO$_3$)] (**2**)*

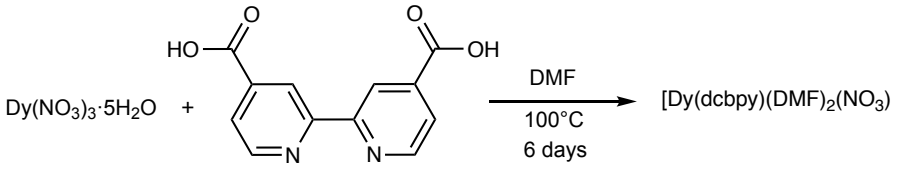

Scheme 3.2: Reaction scheme detailing the synthesis of [Dy(dcbpy)(DMF)$_2$(NO$_3$)] (**2**)

MOF [Dy(dcbpy)(DMF)$_2$(NO$_3$)] (**2**) was also synthesised solvothermally (as per Scheme 3.2). Dy(NO$_3$)$_3$·5 H$_2$O (0.4 mmol, 175.6 mg) and H$_2$dcbpy (0.4 mmol, 97.9 mg) were dissolved in 15 mL of DMF, with stirring in a glass vial. The glass vial was sealed and placed in an oven set to 100°C for 6 days; yielding pale-pink rhomboidal crystals of MOF **2** (~ 60% yield), Scheme 3.2.

3.2.2 *Washing regimes to afford active MOFs*

As active, guest-free frameworks are desirable for vapour-phase sensing (Section 2.6.1.3) MOFs **1**, **1M** and **2** were subjected to washing regimes in order to yield their 'active' counterparts: **1′**, **1M′** and **2′**. The solvent-exchange procedure previously reported by Li *et al.* (used for the activation of the pioneering explosives detection MOF) was implemented on MOFs **1**, **1M** and **2** [126]. The MOF crystals were initially dried under vacuum through use of Buchner filtration. The dry crystals were subsequently immersed in methanol (MeOH) for four days, after which they were re-dried (again using Buchner filtration). This was followed by immersion of the crystals in dichloromethane (DCM) for three days. A final vacuum filtration of the crystals afforded the active materials used in the sensing procedures.

3.2.3 *Fabrication of the MOF 'thin films' used in sensing*

'Thin films' of the metal-organic frameworks (in their active form) were constructed prior to vapour-phase sensing experiments. The films were fabricated by the compaction of the MOF crystals (finely ground†) onto microscopy slides (Thermo scientific, size = 76 x 26 mm, thickness = 0.8 - 1.0 mm). Approximately 5 mg of a MOF sample was compressed down onto each microscope slide using a spatula, until the material was firmly into place‡. Any excess residue was tapped off from the slides prior to their use. A representative MOF **1'** 'thin film' slide (with a side on view) as obtained by scanning electron microscopy (SEM), can be seen in Figure 3.2. This particular 'thin film' has an approximate thickness of 10 μm.

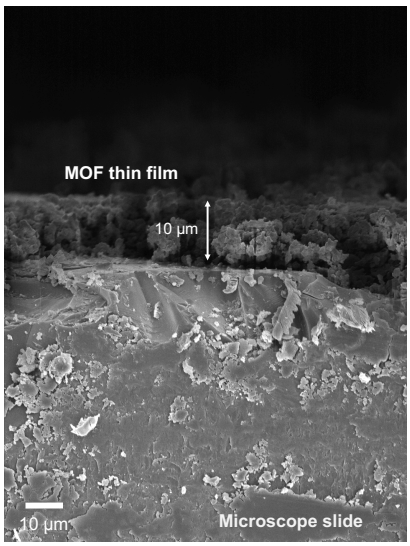

Figure 3.2: Scanning electron microscopy (SEM) image showing the side on view of a representative MOF **1'** 'thin film' used in vapour-phase sensing experiments.

† The crystals of MOF **1M'** were not ground but compacted as-synthesised and activated.

‡ Different MOF synthetic batches were used to generate the various 'thin films' used in repeat experiments. Efforts were made to ensure compaction methods remained consistent.

3.2.4 *Generation of analyte vapours and 'thin film' exposure method*

The vapours of DMNB, 2,4-DNT, *p*-NT and NB were generated by depositing ~ 0.5 g of each of the analytes into individual centrifuge tubes, covered by tissue paper, to ensure there was no direct contact between the analyte and the MOF-containing microscope slide films. The sealed tubes were left for one week to equilibrate prior to their use, generating a static saturated head-space of the analytes. The MOF 'thin films' were quickly placed inside the sealed tubes (and subsequently removed) for fixed amounts of time during the sensing procedure. This methodology employed was modelled on the pioneering work within the field reported by Li *et al.* (Section 2.6.4.1) [126]. Figure 3.3 illustrates how the MOFs were exposed to the vapours.

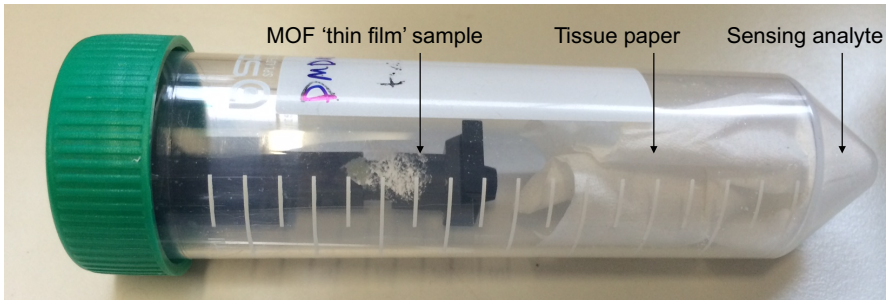

Figure 3.3: Illustration of how a MOF 'thin film' (in this case a 'thin film' of MOF **1'**) was exposed to the static vapour head-space of a particular analyte (in this case DMNB) during its sensing.

3.2.5 *Fluorescence sensing methodology*

Fluorescence measurements on the active MOF 'thin film' were conducted using a time-correlated single photon counter (TCSPC), operating in steady-state mode, with a fixed excitation wavelength of 405 nm. The fluorescence emission spectra were obtained by scanning between 420 - 600 nm. Prior to the exposure of a 'thin film' to any analyte; the initial fluorescence intensity of the film was mea-

sured, after which, the thin film was placed in an empty centrifuge tube for 30 s (which was left open to the environment), and the fluorescence intensity was re-measured. This was repeated three times and the fluorescence emission was averaged to give a stable baseline initial intensity for each thin film (I_0) prior to sensing. This was conducted to ensure that any quenching of the system observed was as a result of MOF-analyte interactions and not due to MOF material loss or interactions with the laboratory air environment. Then, after the exposure of the film to the vapour head-space of a particular analyte for 10 s, the fluorescence intensity was re-measured (I). Subsequently, the film was exposed to an analyte for 30 s, 60 s, 120 s, and 300 s with the fluorescence intensity being re-measured after each time period.

3.3 RESULTS AND DISCUSSION

3.3.1 *Characterisation of metal-organic frameworks*

3.3.1.1 *MOF [Zn(dcbpy)(DMF)]·DMF (**1**) structure determination*

A rectangular plate-like crystal of approximately 0.06 x 0.02 x 0.001 mm dimension that emerged from the reaction detailed by Scheme 3.1, was used for structural analysis using single crystal X-ray diffraction[§]. The data elucidated this metal-organic framework to have the formula [Zn(dcbpy)(DMF)]·DMF (**1**). MOF **1** discloses a three-dimensional framework belonging to the monoclinic space group $P2_1/n$. The asymmetric unit (ASU) for this MOF consists of one zinc metal, a dcbpy ligand and a DMF molecule; all with full occupancy. In addition, one slightly disordered DMF solvent molecule was found to reside in the pores of this MOF per ASU. An ORTEP (Oak Ridge thermal ellipsoid plot) showing the ASU found in MOF **1** can be see in Figure 3.4.

The asymmetric unit is the smallest part of the unit cell which contains all the structural information, so when treated with the symmetry operations of the given space group, will produce the whole contents of the unit cell [166].

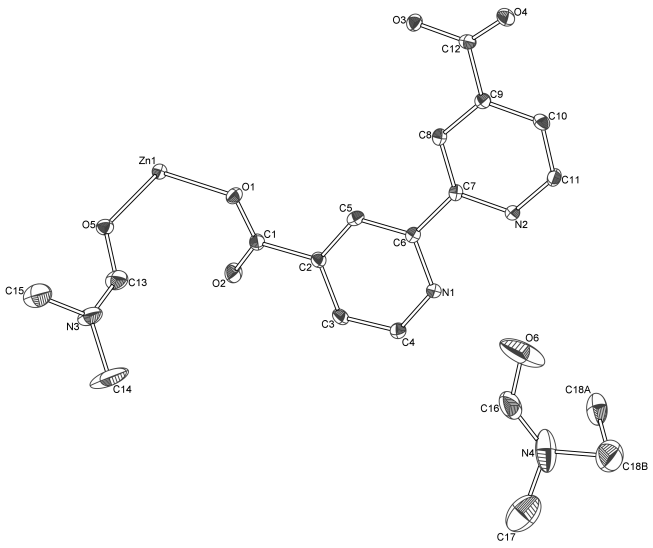

Figure 3.4: ORTEP plot detailing the asymmetric unit (ASU) found in MOF [Zn(dcbpy)(DMF)]·DMF (**1**). Ellipsoids are displayed at the 30% probability level and hydrogen atoms have been omitted for clarity.

§ Full data collection, structure solution and refinement details can be found in Appendix A.

As discussed (Section 2.6.1), SBUs are rigid and defined entities that are found in MOFs, which typically govern their overall structural topology [90].

The overall architecture of MOF **1** is governed by the cyclic secondary building units (SBUs) that are formed. The eight-membered SBUs located in this MOF are constructed from the monodentate carboxylates of two dcbpy ligands, two centrosymmetrically related dcbpy ligands (coordinated to two zinc metals through the N-donor functionalities) and two DMF solvent molecules. Figure 3.5 gives an illustration of the SBUs found in MOF [Zn(dcbpy)(DMF)]·DMF.

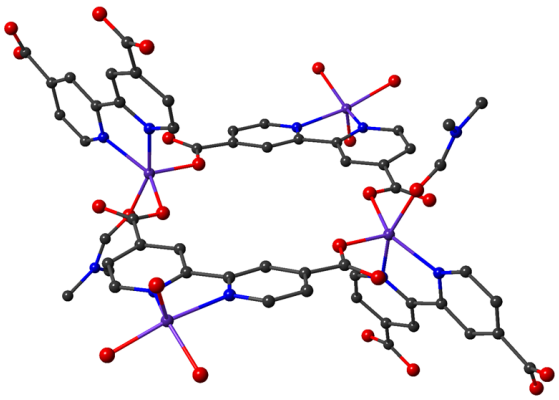

Figure 3.5: Representation of the cyclic 8-membered ring secondary building units (SBUs) found in MOF **1**. Residual DMF solvent molecules and hydrogen atoms have been removed for clarity. The colour grey denotes carbon atoms, purple; zinc atoms, blue; nitrogen atoms, and red; oxygen atoms.

The SBU nodes are further linked to other SBUs through the carboxylate and N-donor moieties of the dcbpy ligands. Thus, the ligands act as structural pillars that form the overall three-dimensional topology of this MOF. The crystallographic data denotes that DMF solvent molecules reside in the pores of this MOF, with two residual DMF present for each SBU. Figure 3.6 illustrates the three-dimensional structure of MOF **1'** with and without solvent guest molecules (presented as both ball and stick and space filling diagrams).

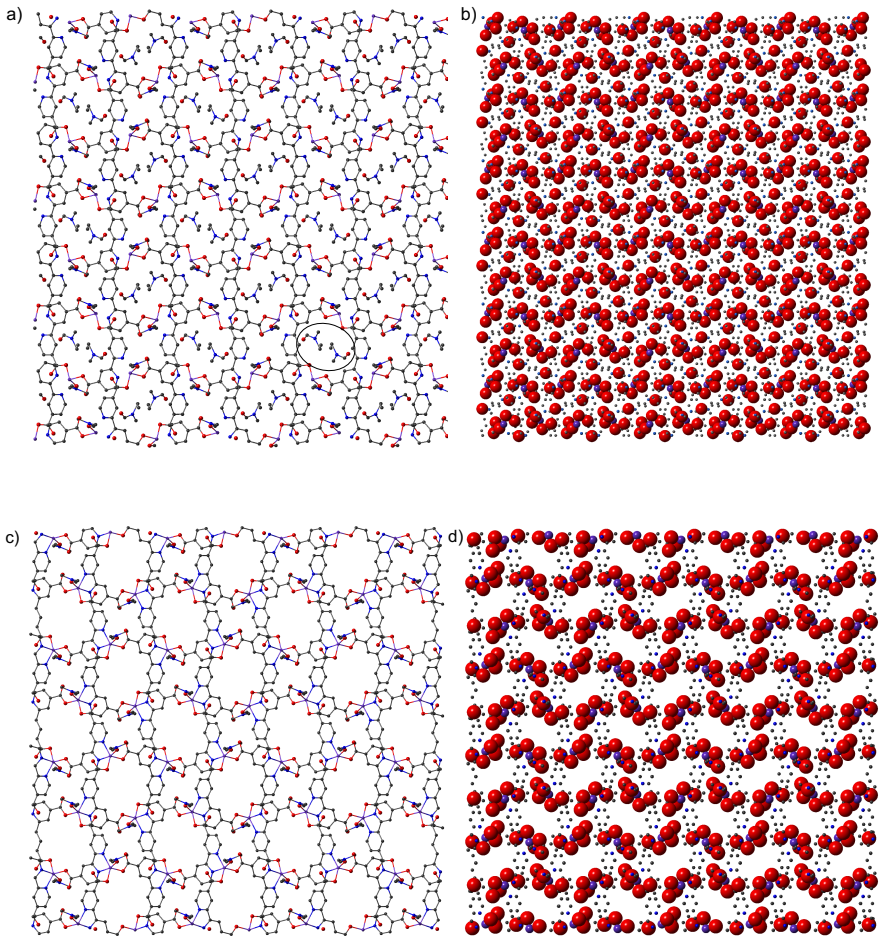

Figure 3.6: a) Representation of the overall three-dimensional structure of MOF **1** with guest solvent molecules present (circled). b) Space filling diagrams of 3D **1** with guest solvent molecules present. c) 3D structure of MOF **1′** without guest solvent molecules present. d) Space filling diagrams of 3D **1′** in the absence of guest solvent molecules. In all figures, hydrogen atoms have been omitted for clarity, and each of the diagrams represent the structure as viewed along the crystallographic *a*-axis.

As can be seen in Figure 3.6, when the solvent molecules are removed from the pores of the MOF (yielding guest-free MOF **1′**), ovaloid one-dimensional channels that are approximately 10.0 Å x 8.8 Å wide can be see to run through the structure of this framework. The space filling diagrams indicate that upon guest removal, solvent accessible voids are present within the MOF **1′** structure. The solvent accessible volume (SAV) for **1′** was calculated to be 15%¶. The framework with the guest DMF present had a SAV of zero.

¶ Solvent accessible volumes were calculated using PLATON software [167] as detailed in Appendix A.

3.3.1.2 *MOF [Dy(dcbpy)(DMF)$_2$(NO$_3$)] (**2**) structure determination*

A pale-pink rhomboidal crystal of approximately 0.14 x 0.11 x 0.04 mm dimension that resulted from the reaction detailed in Scheme 3.2, was used in single crystal X-ray diffraction analysis. It was confirmed that the three-dimensional structure of MOF **2** belongs to the triclinic space group $P\bar{1}$ and has the formula [Dy(dcbpy)(DMF)$_2$(NO$_3$)].

The ASU present within this MOF was significantly different to that of **1**. Contained within the MOF **2** ASU are: two crystallographically independent dcbpy ligands (both with 50% occupancy), two DMF molecules with full occupancy and interestingly; a nitrate group (NO$_3$), as shown by the ORTEP plot in Figure 3.7. The presence of this nitrate group arises from the dysprosium nitrate starting material, whilst unusual, similar observations have previously been reported for lanthanide MOFs [168]. Additionally, there were no residual solvent molecules associated with this ASU, meaning that no solvent guests permanently reside in the pores of this framework.

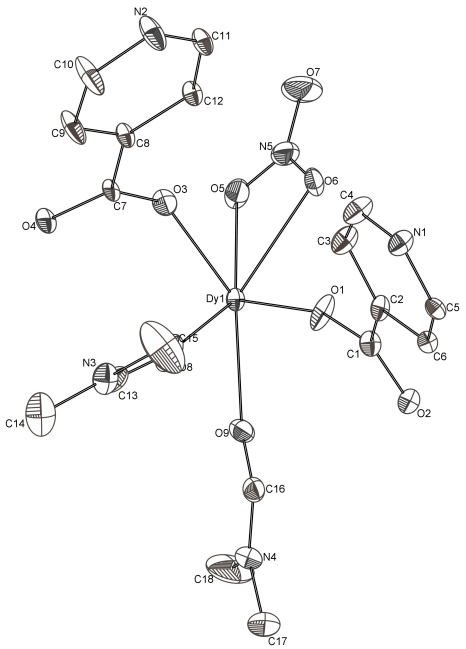

Figure 3.7: MOF [Dy(dcbpy)(DMF)$_2$(NO$_3$)] asymmetric unit (ASU). Ellipsoids are displayed at the 30% probability level and hydrogen atoms have been omitted for clarity.

The SBUs contained within MOF **2** were constructed from three dysprosium metals (each with eight coordinate geometries), the monodentate carboxylates of six dcbpy ligands, six solvent DMF molecules and three nitrates (Figure 3.8).

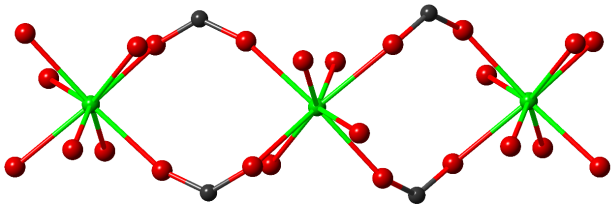

Figure 3.8: Illustration of the secondary building units found in MOF $[Dy(dcbpy)(DMF)_2(NO_3)]$ (**2**). Carbon atom are represented by the colour grey, oxygen atoms; red and dysprosium atoms are green. Hydrogen atoms have been omitted for clarity.

The monodentate caroboxylates of the dcbpy ligands act as pillars to other SBUs, forming one-dimensional chains that run throughout the three-dimensional structure of this MOF, along the crsytallographic *b*-axis. The dcbpy ligands project orthogonally along the crystallographic *a*-axis to link the one-dimensional SBU chains together in order to form the 3D topology observed for this MOF (Figure 3.9). This MOF was found to contain no solvent accessible volume.

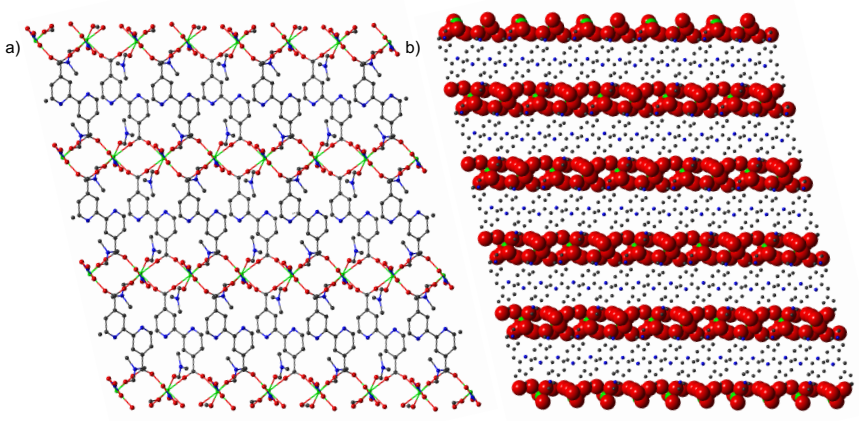

Figure 3.9: 3D structure of MOF **2** given as a ball and stick diagram on the left and a space filling representation on the right (both viewed along the crystallographic *a*-axis). In both representations hydrogen atoms have been omitted for clarity.

A comparison of the crystallographic structure parameters for MOFs **1** and **2** can be seen in Table 3.1[||]. As evident, **1** and **2** demonstrate very different topologies despite being constructed from the same organic linker.

Table 3.1: Crystal and structure refinement data for MOFs **1** and **2**.

	MOF **1**	MOF **2**
Formula	[Zn(dcbpy)(DMF)]·DMF	[Dy(dcbpy)$(DMF)_2(NO_3)$]
Empirical formula	$ZnC_{18}H_{20}N_4O_6$	$DyC_{18}H_{20}N_5O_9$
Formula weight	453.75	612.89
Temperature/K	150	149.9
Crystal system	Monoclinic	Triclinic
Space group	$P2_1/n$	$P\bar{1}$
a/Å	9.3725(2)	9.2414(5)
b/Å	14.7643(3)	10.3040(5)
c/Å	14.7153(3)	12.8291(6)
$\alpha/^\circ$	90	76.338(4)
$\beta/^\circ$	101.058(2)	69.431(4)
$\gamma/^\circ$	90	86.377(10)
Volume/Å^3	1998.47(7)	1111.37(10)
Z	4	2
ρ_{calc} g/cm^3	1.508	1.831
μ/mm^{-1}	2.089	18.524
F(000)	936	602
Crystal size/ mm	0.06 x 0.02 x 0.001	0.2 x 0.15 x 0.05
Radiation	CuKα(λ = 1.54184)	CuKα(λ = 1.54184)
2θ range for data collection/$^\circ$	8.564 to 102.878	8.832 to 149.79
Index ranges	-9$\leqslant$h$\leqslant$9, -14$\leqslant$k$\leqslant$14, -14$\leqslant$l$\leqslant$14	-11$\leqslant$h$\leqslant$11, -12$\leqslant$k$\leqslant$12, -16$\leqslant$l$\leqslant$16
Reflections collected	14313	16503
Independent reflections	2158[R_{int}= 0.0590]	4464[R_{int}= 0.0997]
Data/restraints/parameters	2158/0/282	4464/0/297
Goodness of fit on F^2	1.044	1.109
Final R indexes [I>2σ(I)]	R_1 = 0.0358	R_1 = 0.0576
	wR_2= 0.0875	wR_2= 0.1489
Final R indexes (all data)	R_1 = 0.0459	R_1 = 0.0628
	wR_2= 0.0949	wR_2= 0.1540
Largest diff. peak/hole / eÅ^3	0.37/-0.40	2.71/-1.63

|| The full crystallographic data for both MOFs can be found in Appendix A. The crystallographic information files and structure files have been deposited in the Cambridge Crystallographic Data Centre (CCDC) under 992713 (**1**) and 1026241 (**2**).

3.3.1.3 *Phase purity and 'active' MOF structure evaluations*

Powder X-ray diffraction (PXRD) analysis of the synthesised bulk **1** and **2** samples found them to be in good agreement with their corresponding simulated PXRD patterns (as obtained from single crystal X-ray diffraction data), confirming their phase purity (Figure 3.10). Further to this, the PXRD pattern of the microwave synthesised microcrystals of MOF **1**, termed '**1M**', also demonstrated accordance with the simulated pattern for [Zn(dcbpy)(DMF)]·DMF, verifying that this MOF was successfully yielded using the implemented microwave synthesis procedure (as detailed in Section 3.2.1.2).

As discussed (Section 2.6.1.3), 'active' MOFs are desirable for sensing applications (owing to guest solvent molecules often hampering MOF-analyte interactions), thus, the crystalline materials of **1**, **1M** and **2** were 'activated' using the washing regime described in Section 4.2.3; affording **1'** and **1M'** and **2'**. This activation was particularly significant for MOFs **1** and **1M** as from the crystallographic data it was ascertained that this MOF contains residual DMF solvent molecules present within its pores; obstructing their access. Whilst MOF **2** was shown not to contain any solvent in it's cavities (due to it not having sufficiently sized pores), washing regimes were still implemented on **2** to remove any DMF molecules potentially present on its crystal surfaces from its synthesis. The PXRD patterns of the simulated, as-synthesised and 'active' MOFs can be seen in Figure 3.10.

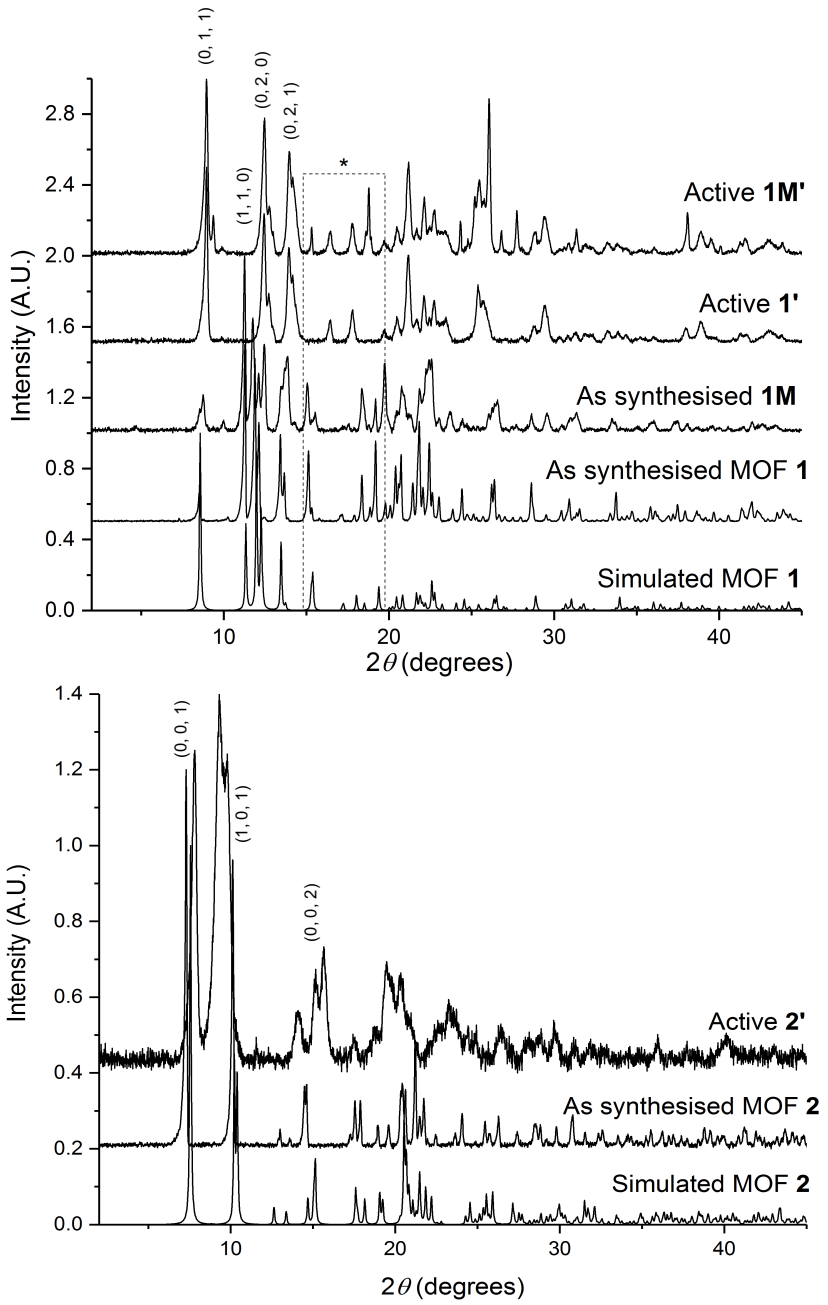

Figure 3.10: Powder X-ray diffraction patterns of: Simulated MOF **1** (produced from crystallographic data), as-synthesised MOFs **1** and **1M**, as well as active MOFs **1′** and **1M′** (top). Simulated MOF **2**, as-synthesised MOF **2** and active MOF **2′**. The h, k, l values of the main MOF peaks as obtained from crystallographic data are given in the figures also. The highlighted box indicates PXRD peak discrepancies.

The PXRD patterns of MOF materials **1′** and **1M′** confirmed that the guest free MOFs retained their overall framework structure post-activation. This is evidenced by the matching of the majority of the main MOF (low angle 2θ) peaks in the PXRD patterns of the active

frameworks with those of their corresponding as-synthesised materials (labelled with their h, k, l values in Figure 3.10). However, both **1'** and **1M'** do demonstrate some distortions in their framework unit cells, indicated by the shifts in the PXRD peaks, the absence of a major peak (h, k, l = 1, 1, 0) as well as the emergence of new peaks (highlighted by the dashed box in Figure 3.10). This is most likely an artefact of DMF loss. Such perturbations in framework structures after guest removal are well documented; as solvents frequently act as templating agents in MOF pores. Thus, their removal may slightly alter the shape of these pores and can lead to structures of lower symmetry [115][126] (as discussed in Section 2.6.1.3 and Section 2.6.1.4).

The PXRD pattern obtained for MOF **2'** shows that the framework does observe some loss of crystallinity post-activation. This can be rationalised by the washing procedure removing some NO_3^- or DMF molecules (or both) coordinated to the dysprosium metal ions; leading to structural defects being created in the framework. This is not uncommon during solvent exchange procedures [113].

3.3.1.4 *MOF crystal morphologies*

The morphologies of the crystalline materials present in MOFs **1**, **2** and **1M** are shown by the scanning electron microscopy (SEM) images in Figure 3.11. The crystals present in the solvothermally synthesised bulk samples of MOFs **1** and **2** demonstrate a wide range of crystal sizes and shapes. In addition they contain crystal cracks, crevices and some smaller nucleation points. Contrastingly, the SEM images of microwave synthesised **1M** show excellent uniformity amongst crystals. The microcrystals are leaf like in structure with dimensions of approximately 25 μm x 10 μm x 2 μm.

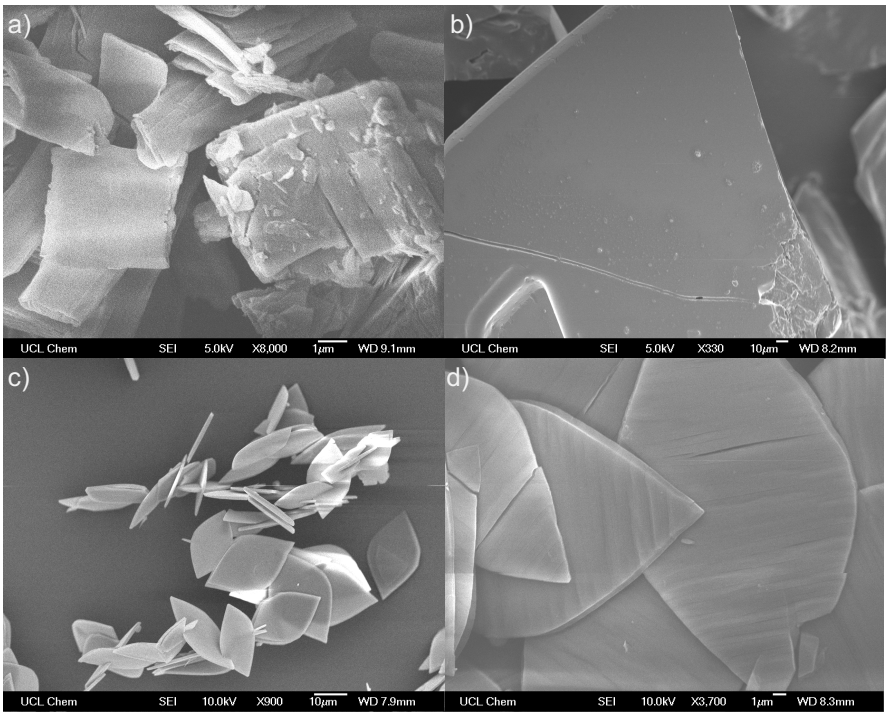

Figure 3.11: Scanning electron microscopy images of: a) the bulk crystals obtained from a sample of solvothermally synthesised MOF **1** crystals. b) solvothermally synthesised MOF **2** crystals; evidencing the crystal cracks and crevices present in the sample. c) the microcrystals of **1M** yielded by microwave synthesis. d) a close up of the surface of the **1M** crystals.

It is important to note that the implemented washing procedure does cause some (further) crystal cracking (for each of the MOF samples including **1M'**), as demonstrated in Figure 3.12, which shows a representative MOF **1'** sample post-activation. Such crystal cracking is common during solvent exchange activation, however, it is not necessarily detrimental to application. The presence of additional analyte vapour binding sites could aid gas-phase sensing [113].

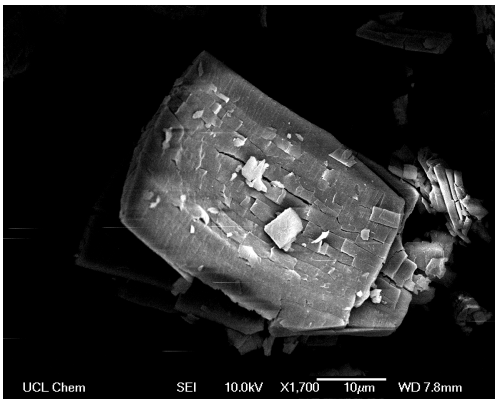

Figure 3.12: SEM image of a representative MOF **1′** crystal after solvent activation.

3.3.1.5 *MOF 1′ porosity characterisation*

In order to confirm the porosity of 'active' MOF **1′**; Brunauer-Emmett-Teller (BET) surface area measurements (with nitrogen as the probe gas) were attempted on this MOF**. MOF **1′** returned a surface area value of 69.3 m^2/g (after degassing at 200 °C). This is a relatively low surface area in comparison to the highest porosity MOFs, but is comparable to one of the first reported MOFs for the vapour-phase detection of explosive related compounds (MOF $[Zn_2(oba)_2(bpy)\cdot DMA]$, surface area = 84 m^2/g) [127]. These results suggest that void space is available in **1′** for analyte encapsulation during sensing. As somewhat predicted, MOF **1** did not return a meaningful BET surface area value (negative), suggesting the non-activated framework to have no residual porosity††.

3.3.1.6 *Thermal stabilities*

The thermal stabilities of activated MOFs **1′** and **2′** were evaluated using thermogravimetric analysis (TGA). The TGA for **1′** indicated it to be stable up to 400 °C and **2′** showed stability up to 460 °C, as shown by Figure 3.13. Both of these decomposition temperatures are

** The BET general experimental procedure details can be found in Chapter 8
†† BET surface area measurements were not attempted on MOF **2′** owing to its lack of pores as indicated by crystallographic data.

comparable to those reported for other MOFs synthesised for the application of explosives detection [126]. Further to this, from analysis of the TGA, it is suggested that the washing procedure implemented on **1′** was able to successfully remove the guest DMF from the pores of this MOF. This is proposed due to the negligible (~ 1%) weight percentage loss in the region of 103 - 156 °C in the TGA of **1′**. Guest molecules are often liberated from the pores of MOFs in the region of their boiling points during thermogravimetric anaysis [111].

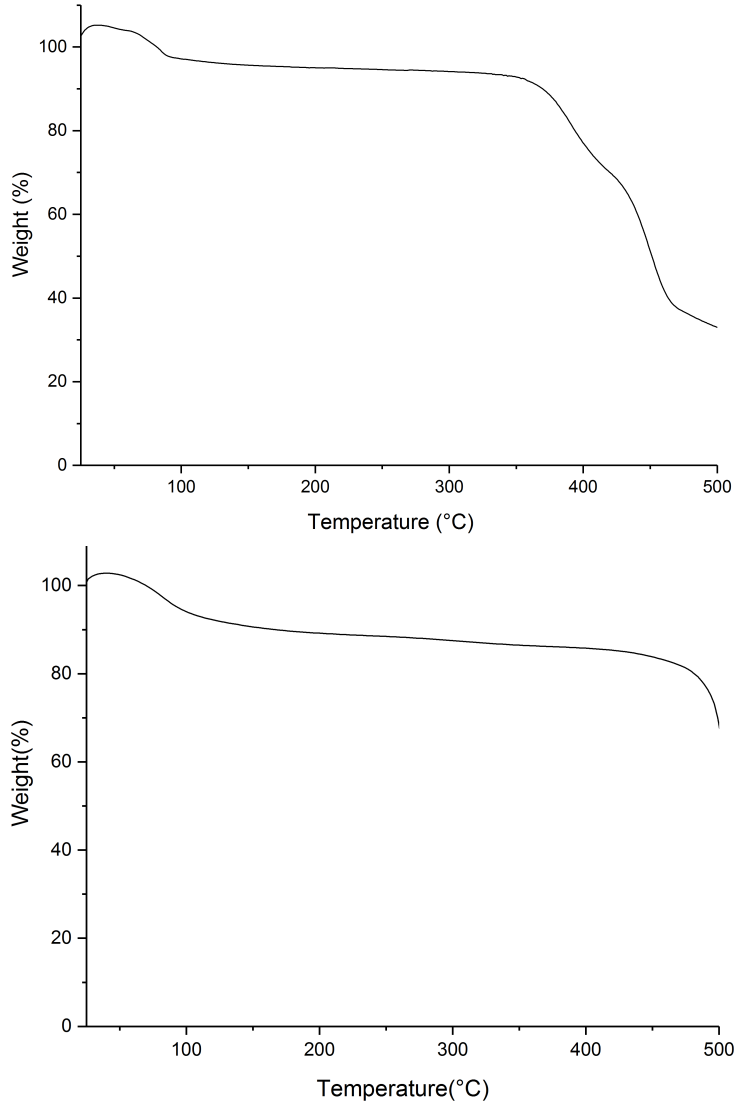

Figure 3.13: Results of the TGA analyses conducted on MOFs **1′** (top) and **2′**(bottom).

3.3.2 *Vapour-phase fluorescence sensing*

Metal-organic frameworks **1′** and **2′** were evaluated for their potential as fluorescence-based sensors of the explosives related analytes DMNB, 2,4-DNT, *p*-NT and NB in the vapour-phase. 'Thin films' of the active MOFs were fabricated (as detailed in Section 3.2.3) and different samples of these were individually exposed to the saturated headspace of the above mentioned analytes for varying amounts of time (as described in Section 3.2.5). The fluorescence emission spectra for each MOF 'thin films' sample, at each analyte exposure, were monitored using a fluoremeter. The different sensing responses of the two MOFs towards the above mentioned analytes were compared; in order to gain insight into how their aforementioned differing topologies impact their vapour-phase sensing capabilities. In addition, 'thin film' samples of the **1M′** microcrystals were also exposed to the same analytes, with the aim to test the effects that these uniform flat, leaf-like crystals have on the sensing capabilities of this MOF.

3.3.2.1 *Sensing of the explosives related compounds using MOF* **1′**

Upon excitation at 405 nm, the fluorescence emission maxima for MOF **1′** 'thin films' (in the solid-state at room temperature) were observed at approximately 465 nm. Minor fluctuations in the fluoresce emission maxima peak positions were observed ($\pm$ 5 nm) and attributed to the non-uniformity of the films. Such findings have also previously been noted for the 'thin films' constructed by Li *et al.* in the aforementioned pioneering work on MOFs for vapour-phase explosives detection (Section 2.5.3)[126]. The observed fluorescence emission maxima of the MOF was significantly blue shifted in comparison to the emission spectrum of the free linker H_2dcbpy (570 nm) upon excitation with the same wavelength (Figure 3.14). Similar observations

have been previously reported and rationalised on the basis of charge-transfers (either metal-to-ligand (MLCT) or ligand-to-metal (LMCT) charge-transfers)[169, 170], which are often present in concurrence with linker-based emissions in fluorescent MOFs (Section 2.6.2)[65].

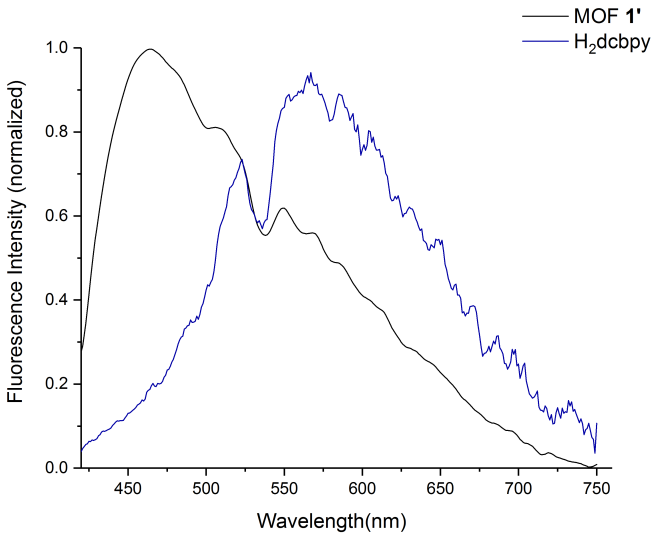

Figure 3.14: An overlay of the fluorescence emission spectra of MOF **1'** and H_2dcbpy (as 'thin films' in the solid-state) upon excitation at 405 nm. The slight dip in the emission spectrum of the free linker (at approximately 525 nm) is the result of an instrumental defect and not an artefact of the molecule.

Figure 3.15 shows an example fluorescence emission profile of a MOF **1'** 'thin film' upon exposure to DMNB for 0 s, 10 s, 30 s, 60 s, 120 s and 300 s‡‡. Figure 3.16, details the results of the time-dependent fluorescence quenching of MOF **1'** 'thin films' upon exposure to each of the four analytes (DMNB, 2,4-DNT, *p*-NT and NB) and includes repeated results. The plot denotes the quenching percentages (QPs) of the MOF upon exposure to these analytes (as calculated by Equation 2.14, Section 2.6.4; $[(I_o - I)/I_o)]$x100; I_o = original peak maximum intensity, I = maximum intensity after analyte exposure)§§.

‡‡ The remaining fluorescence emission profiles of the MOF **1'** 'thin films' upon exposure to the other analytes can be found in Appendix A. As well as this the baseline initial fluorescence intensity measurements that were averaged to give t = 0 in the figure are given in Appendix A. It is important to note these were always stable.

§§ The I_o values used in the QP calculations were obtained from the fluorescence emission data, the wavelengths at which these occurred were the fixed points at which the I values were taken.

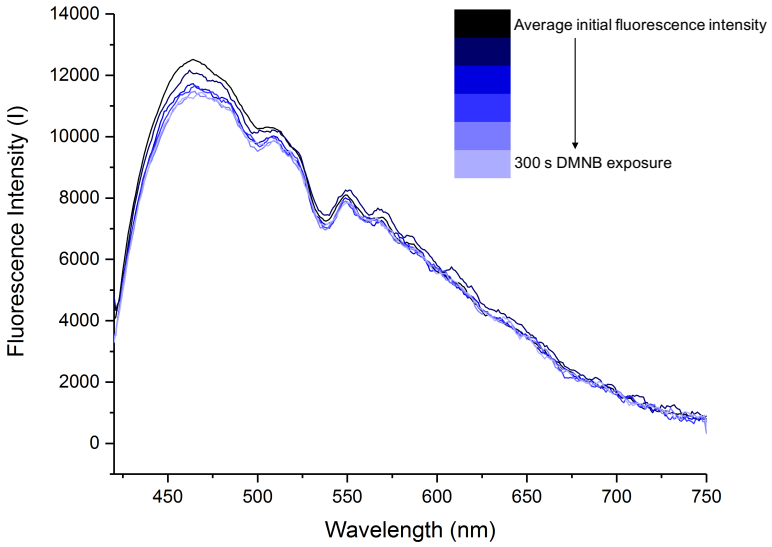

Figure 3.15: Fluorescence emission profile of a representative MOF **1'** 'thin film' sample upon the exposure to the vapours of DMNB for 0, 10 , 30, 60, 120 and 300 seconds. The average initial intensity is the average of three baseline emissions of the MOF prior to analyte exposure (DMNB t= 0 s), which were always very stable.

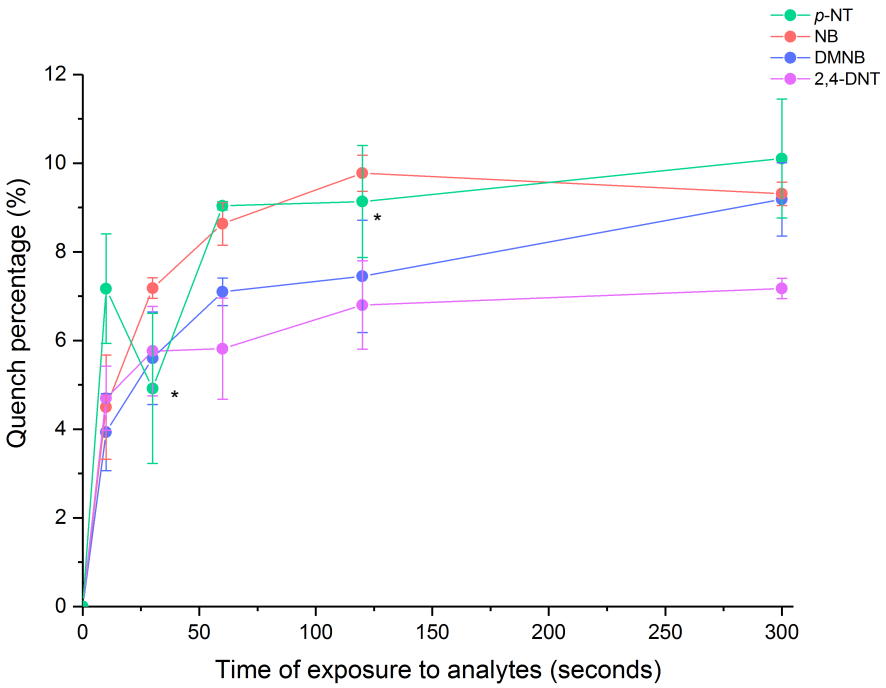

Figure 3.16: Results of the time-dependent fluorescence quenching of MOF **1'** 'thin films' (given as quench percentages) upon exposure to the vapours of each of the four analytes: DMNB, NB, *p*-NT and 2,4-DNT for 0, 10, 30, 60, 120 and 300 s. Repeat results on different MOF **1'** 'thin films' are included; the variance (standard error of the mean) in the results between each sample is represented by the error bars. The asterisks denote points of reference for the discussion in the main text.

Evidently, MOF **1'** responds to each of the tested analytes, with quenching percentages between 6 - 10% observed after only 300 s of exposure. Although the magnitude of the responses yielded by the 'thin films' of MOF **1'** are not as high as some of those reported in previous literature on MOFs for explosives detection (Section 2.6.4), this MOF does demonstrate the ability to detect these explosives related analytes. The variations in the QPs between the repeat measurements can be attributed to the difference in the absolute amount of the MOF that was able to be compacted onto each of the 'thin films' during fabrication. While efforts were made to keep these films as consistent as possible; discrepancies were inevitable and suggested the need for better MOF-film fabrication methods for future work on these materials. Also, the slight dips in the MOF responses upon exposure to the analytes between different time periods (as denoted by the asterisk in Figure 3.16) can be potentially attributed to the depletion of analyte head-spaces during the sequential exposure of the films to the analyte vapours. Similar dips in quenching profiles of the MOFs upon exposure to explosives related analytes can be seen in the studies by Li *et al.* on which this exposure method was modelled on. Nevertheless, these proof-of-concept experiment results serve as a useful initial diagnostic as to the tested analytes detectability using MOF **1'**. It is proposed that the aforementioned and well established photo-induced electron transfer mechanism (PIET) caused the observed quenching responses (Section 2.5.2.1). Interestingly, these results suggest that **1'** has potential as a fluorescence-based sensor of DMNB; which very few other MOFs (and other fluorescence-based detection materials) have been noted to detect [26, 126]. Table 3.2, details the literature reported MOFs to date that have demonstrated the successful detection of this analyte in either the vapour or solution-phase.

Table 3.2: Significant sensing results for DMNB in either solution or vapour phase in the literature. The exposure time or analyte concentration is given where known. For specific MOF details, please see references included.

Group/Reference	Vapour or Solution Phase	Response
Li *et al.* [126]	Saturated vapour	84% quench, 10 s
Li *et al.* [127]	Saturated vapour	8% quench, 15 mins
Li *et al.* [131]	Saturated vapour	< 10%, 10 mins
Li *et al.* [133]	Saturated vapour	47%
Ghosh *et al.* [154]	Saturated vapour	57% , 5 min
Ghosh *et al.* [149]	Solution (H_2O)	<10%
Cao *et al.* [171]	Solution (ethanol)	21% (200 ppm)
Zhou *et al.* [172]	Solution (H_2O)	< 15%

The difficulty in the detection of this analyte arises due to its low electron affinity in comparison to nitroaromatic compounds (as well as its unfavourable reduction potential) which minimises the thermodynamic potential (driving force) for the PIET mechanism. Also, its aliphatic nature prevents it from forming π-π stacking interactions, which typically facilitate strong MOF-analyte interactions and lead to effective PIET [26, 78, 126, 173]. It is therefore suggested that the successful detection of DMNB with MOF **1'** occurred as a result of the encapsulation of the analyte into the cavities of the framework, which potentially allowed for stronger host-guest interactions than surface based interactions, owing to likely better degrees of orbital overlap. This coincides with previous findings by Li *et al.* who also attributed the successful detection of DMNB through its inclusion into MOF $[Zn_2(bpdc)_2(bpee)]$ pores (Section 2.6.4.1) [126]. Further to this, based on the molecular dimensions of the tested analytes reported by Li *et al.* (given in Table 3.3) [127], the pore sizes present in MOF **1'** as calculated from crystallographic data (ovaloid channels which are approximately 10.0 x 8.8 Å wide, as discussed in Section 3.3.1.1), suggest that they are large enough to be able to encapsulate this analyte into its pores, as well as NB and *p*-NT, and potentially 2,4-DNT.

Table 3.3: Molecular dimensions of the tested analytes as reported by Li *et al.*[127].

Analyte	Dimensions (Å)
DMNB	7.1 x 7.3 x 7.7
2,4-DNT	5.6 x 7.7 x 10.1
p-NT	5.6 x 7.7 x 8.1
NB	3.4 x 6.2 x 8.6

Computational band and electronic structure calculations

In order to gain a further insight into the quenching mechanism occurring between these analytes and the MOF; the geometry and electronic structure calculations of **1′** and the analytes were obtained[¶¶]. Figure 3.17, shows the valence band maximum (VBM) and the conduction band minimum (CBM) for MOF **1′** (also known as the MOF HOMO and LUMO respectively), as well as the ionization potentials (IP) and electron affinities (EA) for the analytes (HOMO and LUMO of the analytes respectively).

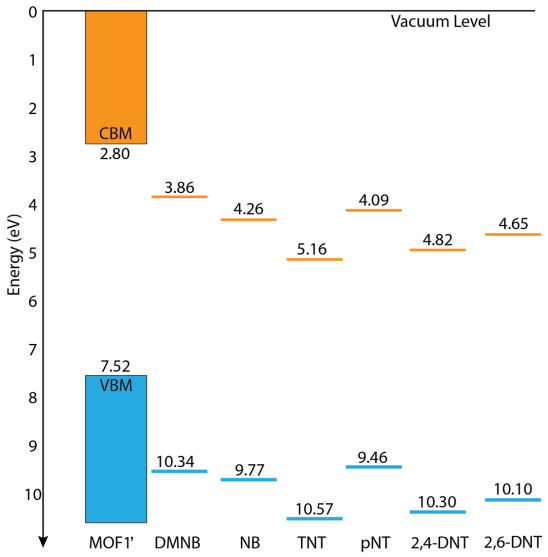

Figure 3.17: Schematic of the calculated valence band maximum (VBM) and conduction band maximum (CBM) positions for **1′**. As well as the ionization potentials (IPs, denoted by the colour bule) and electron affinities (EAs, denoted by the colour orange) for the explosive TNT and 5 explosive related analytes.

¶¶ These calculations were performed by Christopher N. Savory and Dr. David. O. Scanlon, University College London. The calculation experimental details can be found in Appendix A.

As discussed, for photo-induced electron transfer to occur between the excited state electron-rich MOFs and the ground state electron-poor explosive analytes; the LUMO of the analytes (electron affinities) must be below the conduction band maximum of the MOF (Section 2.6.4.1). Figure 3.17 clearly demonstrates that based on the band edge positions of the MOF *versus* the analytes, quenching should occur as electrons in the conduction band of the MOF should drop into the LUMOs (coloured orange) of each of the analytes. This is of course provided that adequate interactions between the host and guest occur to facilitate the electron transfer. These calculations, therefore, support the results that show MOF **1'** to be an effective sensor of DMNB, NB, *p*-NT and 2,4-DNT.

Whilst these theoretical calculations suggest that MOF **1'** should demonstrate the greatest quenching in the presence of 2,4-DNT, followed by NB, *p*-NT and finally DMNB (based on the decreasing electron affinities and so weaker PIET driving force going from 2,4-DNT to DMNB), they cannot account for the effects of interactions between the analytes and the MOFs. In addition, the current vapour sensing method employed exposes the MOF **1'** 'thin films' to the saturated head-spaces of the analytes, which differ in concentration. These facts, coupled with the aforementioned slight variations in the 'thin film' fabrication, could help rationalise some of the discrepancies in the magnitudes of quenching of the MOF observed (Figure 3.16) in the presence of the different analytes compared to those theoretically expected.

*Regeneration studies of MOF **1'***

As a result of the very 'sticky' nature of explosives (Section 2.3.2.2), the ability of a sensing material to be regenerated is a necessary consideration. Whilst previous studies have shown MOFs to be able to be

regenerated back to their initial active form (after saturation by the analytes) through heating at elevated temperatures (>150 °C [126]), the recycling of a MOF sensor under milder conditions had not been investigated. Therefore, a regeneration study on a 'thin film' of MOF **1'** at ambient temperature and laboratory air conditions was attempted for its continued detection of nitrobenzene vapours.

Initially, the 'thin film' was exposed to NB for 300 s and then placed on a bench top at room temperature. The film was left for an hour, after which, sensing was repeated on the same sample; I_0 (initial fluorescence intensity) and I_{300} (fluorescence intensity after 300 s analyte exposure) were measured. Two more sensing cycles were repeated using the same procedure, however, during these subsequent measurements the same 'thin film' was left for 3 hours and 16 hours in-between nitrobenzene sensing. The results of this regeneration study are summarised in Figure 3.18.

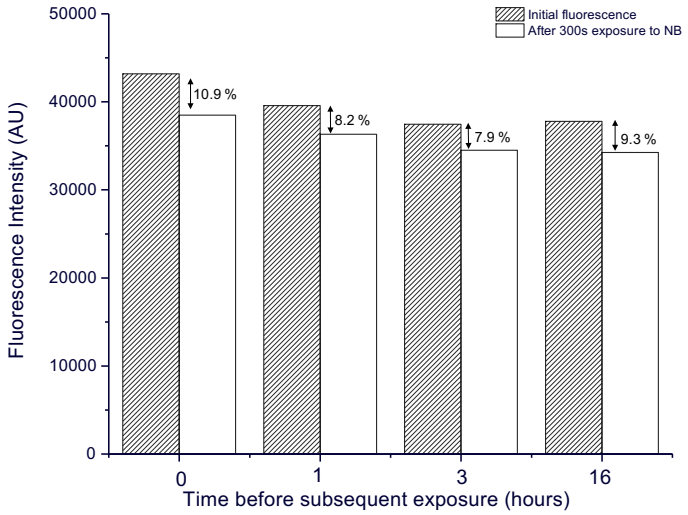

Figure 3.18: Summary of the results from the regeneration of **1'**. The graph indicates the initial sensing response of **1'** towards NB and three cycles of sensing using the same sample after 1, 3 and 16 hours of regeneration at room temperature. At each time point the grey bar shows the initial fluorescence (I_0) and the white bar indicates the fluorescence after 300 s exposure to NB (I_{300}).

As evident (Figure 3.18), this 'thin film' sample of MOF **1'** was still responsive to nitrobenzene after each sensing cycle. Between the initial sensing and those conducted at subsequent cycles, there is a decrease in the initial fluorescence intensity of the sample which suggests that the nitrobenzene molecules that were sorbed (either adsorbed, absorbed, or both) by this MOF were not fully liberated. However, there is some evidence of regeneration occurring as the initial fluorescence intensities (I_0) at these subsequent time periods are observed to be higher than those of the I_{300} intensities from their prior exposure.

In particular, after the 16-hour sensing measurement, the material appears to be regaining its initial fluorescence and the QP of the MOF also begins to approach that of the initial quenching response of this material, at time = 0 h (10.9%). However, the same fluorescence intensity yielded by the pristine MOF **1'** 'thin film' was not realised at t = 16 hours, and suggests the need to leave the films for longer periods of time under these conditions for full MOF regeneration or heating is necessary to overcome the thermodynamic barrier. Still, these results suggest that MOF **1'** could be reused for nitrobenzene detection 1, 3 and 16 hours post-initial sensing. In addition, these results imply that the exposure of the MOF to the interferents present in common laboratory air conditions do not have a significant impact on the ability of **1'** to detect nitrobenzene.

*Preliminary investigation into interferents effects on MOF **1'***

As discussed in Section 2.3.2.3, an important consideration for materials that are to potentially be used in real-world explosives detection applications is the effects of other analytes, interferents, on the sensing system; owing to their potential to cause false alarms. Thus, an exploratory study was conducted which tested the responses of

MOF **1′** against the electron rich analytes toluene and chlorobenzene, nitroaliphatic nitromethane and solvents chloroform, acetone, water and DMF, to investigate the effects of these compounds on the fluorescence of this MOF. Different 'thin films' of MOF **1′** were fabricated in the same way as described in Section 3.2.3, and exposed to these analytes using the same methodology employed for the explosives related analytes (Section 3.2.5, the head-spaces of which were generated using the same methodology outlined in Section 3.2.4). The results of this initial study are summarised in Figure 3.19, which shows the quenching effects demonstrated by the MOF **1′** 'thin films' after 300 s exposure to the above-mentioned interferents.

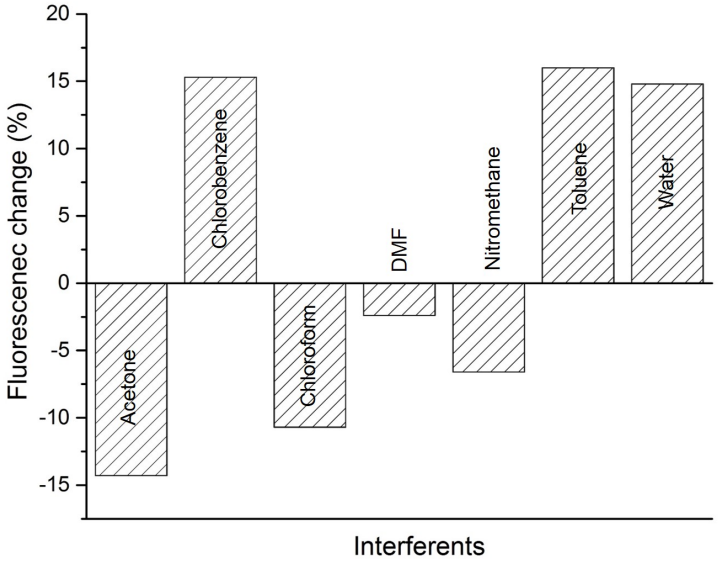

Figure 3.19: Summary of the results from the exploratory study investigating the effects of interferents on 'thin films' of MOF **1′**. The graph shows the change in the fluorescence intensity (quench or enhancement) of different 'thin films' of **1′** after exposure to each of the analytes for 300 s.

As evident, the electron rich analytes (toluene and chlorobenzene) enhanced the fluorescence emission of the MOF **1′** 'thin films', this coincides with previous findings reported by Li *et al.* [127]. The reasons for such enhancement can be rationalised due to the absence of the PIET from the excited state MOF to the ground state analytes (as a result of the electron-rich analytes having higher lying

LUMO orbitals than the conduction band of the MOF), as well as; the sorbed analytes potentially inhibiting linker rotations and vibrations in the MOF that otherwise facilitate non-radiative decay of the photo-excited sate (Section 2.6.4.1). As aforementioned in Section 2.6.4.1, the fact that such electron-rich analytes cause a different change in the fluorescence emissions of the MOF (enhancement *vs.* quench) compared to electron-poor nitroaromatics can potentially aid the differentiation between some explosive and non-explosive compounds, owing to explosives most typically being electron-deficient and thus generally cause a quench in MOF systems. Therefore, being able to differentiate between electron-rich and electron-poor analytes can potentially help minimise the likelihood of some false alarms using MOF sensing systems. The reason for the fluorescence enhancement of **1'** upon exposure to water are unclear, however, a potential explanation could be the inclusion of the analyte into the pores of the MOF inhibiting molecular vibrations and rotations of the framework. Such findings have previously been reported by Zhang *et al.* [202] (and will be discussed further in Section 4.3.3.3). From Figure 3.19 it can be seen that nitromethane gave a decrease in the fluorescence emission of **1'**, rationalised on the basis of being a nitro compound and thus, electron deficient. The solvents acetone, chloroform and DMF were observed to quench the MOF to varying extents. The detection of acetone by this MOF is of relevance as this anlayte is often a constituent of home-made peroxide explosives (Section 2.2.3).

Whilst these initial results of the effects of interferents on MOF **1'** corroborate previous findings and demonstrate that fluorescent MOFs can potentially differentiate between electron poor and rich analytes based on the type of quenching response (increase or decrease), further work is required to fully understand the effects of intereferents on this sensing system.

3.3.2.2 *Sensing using the homogeneous microcrystals of MOF* **1M′**.

In an attempt to yield uniform microcrystals of MOF **1**, an alternative synthetic method was employed whereby the MOF was yielded *via* a microwave assisted method; producing MOF **1M**. Solvent-free 'thin films' of **1M′** (activated as described in Section 4.2.3 and films produced as detailed in Section 3.2.3) were tested for their quenching responses against the same analytes as those exposed to **1′** (employing the same method as described in Section 3.2.5), with the aim to evaluate the impact these differently shaped crystals may have on the sensitivity of analyte detection using this MOF.

The initial sensing results of the **1M′** 'thin films' after exposure to the four explosives related compounds can be seen in Figure 3.20. In addition, the fluorescence emission profile of the **1M′** 'thin film' used for DMNB sensing is given in Figure 3.21 ***.

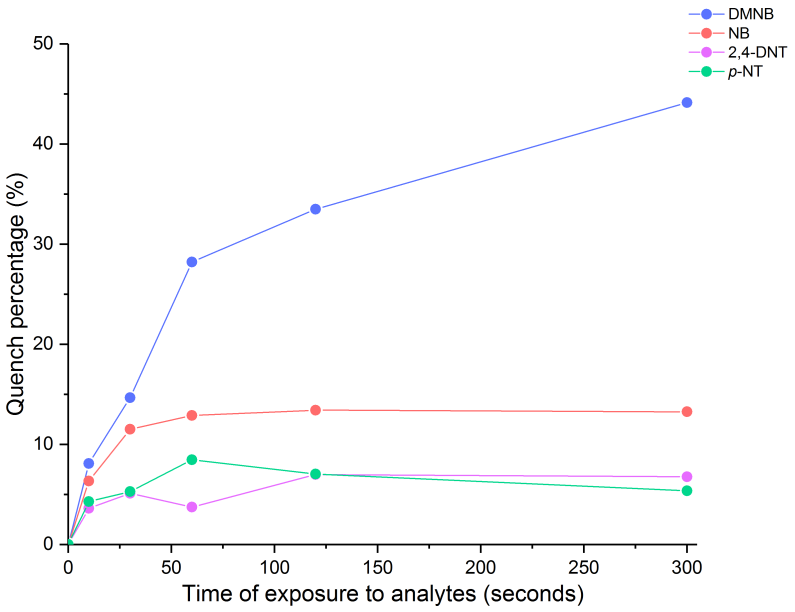

Figure 3.20: Fluorescence quenching percentages demonstrated by 'thin films' of **1M′** upon exposure to explosive related analytes DMNB, NB, *p*-NT and 2,4-DNT for 0, 10, 30, 60, 120 and 300 s.

*** The remaining fluorescence emission profiles of MOF **1M′** upon exposure to the other analytes can be found in Appendix A.

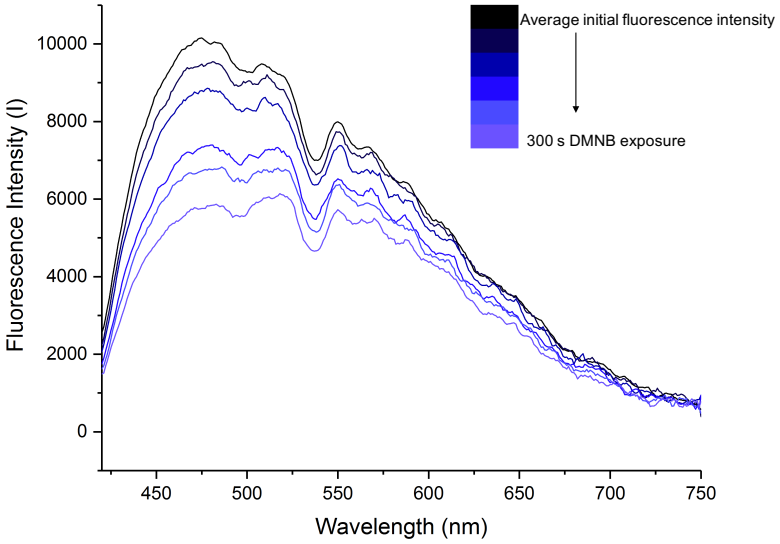

Figure 3.21: Fluorescence emission profile of the **1M′** 'thin film' sample exposed to the vapours of DMNB for 0, 10 , 30, 60, 120 and 300 seconds. The average initial intensity is the average of three baseline emissions of the MOF prior to analyte exposure (DMNB t = 0 s), which were always stable.

As can be seen, the QPs observed for the **1M′** 'thin film' upon exposure to DMNB are significantly greater than those yielded on average by the 'thin films' of **1′**. This is best evidenced by the QPs at t = 300 s DMNB exposure where for the **1M′** 'thin film' a QP of 44.1% was observed compared to an average QP of 9.2% for the films of **1′**. These results suggest that the sensitivity of detection of this analyte by MOF [Zn(dcbpy)(DMF)] was greatly affected by its 'thin film' fabrication.

The QPs for the **1M′** 'thin film' exposed to NB were also slightly higher than those of **1′** (QPs at t = 300 s NB exposure were 13.2% *vs.* an average of 9.3% for **1M′** and **1′** respectively). Interestingly the responses of the **1M′** films in the presence of *p*-NT were lower than with **1′** and within error for 2,4-DNT (QPs at 300 s = 5.4 % *vs.* 10.1% and 6.8% *vs.* 7.2% for films of **1M′** and **1′** upon exposure to *p*-NT and 2,4-DNT respectively). The reasons for such responses are not clear based on these preliminary sensing results and future work is required to better understand the effects of film morphology on the

sensitivity of analyte detection using MOF [Zn(dcbpy)(DMF)], however, they do suggest that optimisation of responses may be possible. It is important to note that previous work by Li *et al.* also alluded to the importance of film fabrication on MOF detection sensitivities. The group reported (as discussed in Section 2.6.4.1) that thicker films of their MOF sensors (30 μm) showed diminished responses in the testing time frame in comparison to their standard test films (of approximately 5 μm), which the group attributed to slower quenching responses of the former as a result of the restricted diffusion of the analytes into the film layers [126]. Thus, yielding weaker responses during the test time. Further to this, similar observations have been found for amplified fluorescent conjugate polymer (AFCP) systems [26]. Therefore, implying that optimised film fabrication is not trivial.

3.3.2.3 *Sensing of explosive related analytes with MOF* **2'**

Upon excitation at 405 nm, 'thin films' of MOF [Dy(dcbpy)$(DMF)_2$-(NO_3)] (**2'**) appeared to demonstrate some form of linker-based emissions and not dysprosium based emissions owing to the absence of the Dy^{3+} peaks in the fluorescence emission spectrum of the MOF, which have been reported to be located at 480 nm, 570 nm and 660 nm and attributed to the ${}^4F_{\frac{9}{2}} \rightarrow {}^6H_{\frac{15}{2}}$, ${}^4F_{\frac{9}{2}} \rightarrow {}^6H_{\frac{13}{2}}$ and ${}^4F_{\frac{9}{2}} \rightarrow {}^6H_{\frac{11}{2}}$ transitions respectively [174].These findings are rationalised as a result of the inefficient ligand-to-metal charge transfer (LMCT) from the dcbpy ligands to the Dy^{3+} metals due to the fast fluorescence emissions of the ligands in comparison to that of the metal. Thus, a poor 'antenna' effect for this lanthanide is observed (Section 2.6.2). A representative fluorescence emission spectrum of a MOF **2'** 'thin film' can be seen in Figure 3.22.

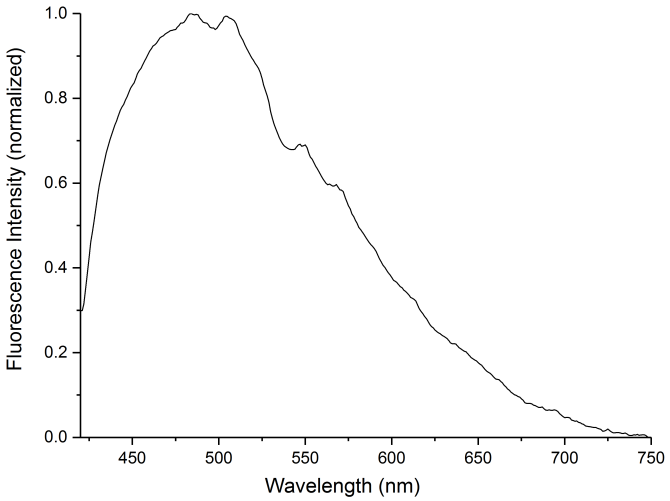

Figure 3.22: Fluorescence emission spectrum of a MOF **2′** 'thin film' (in the solid-state) upon excitation at 405 nm.

When MOF **2′** 'thin films' were exposed to the vapours of the explosives related analytes, quenching responses of the MOF films were only observed in the presence of NB and *p*-NT (demonstrated below in Figure 3.23) and attributed to the PIET quenching mechanism. DMNB and 2,4-DNT yielded negligible change in the fluorescence intensity of the films (< 1%)[†††]. This semi-selectivity of MOF **2′** towards NB and *p*-NT over the other analytes can be attributed to its minimal porosity. Owing to the absence of the pores in this MOF, it is suggested that surface based interactions are the cause of quenching of **2′** by NB and *p*-NT. These two analytes which have the highest vapour pressures of the tested analytes, (Table 2.1), appear to be able to form surface based interactions with the MOF during the testing time; yielding detectable responses. It is suggested that surface based interactions are not of sufficient to yield a quenching of the MOF in the presence of DMNB and 2,4-DNT during the implemented testing time-frame or even at all. Thus, these findings highlight the importance of porosity on a MOF sensing system.

††† The fluorescence emission profiles of MOF **2′** upon exposure to these analytes can be found in Appendix A.

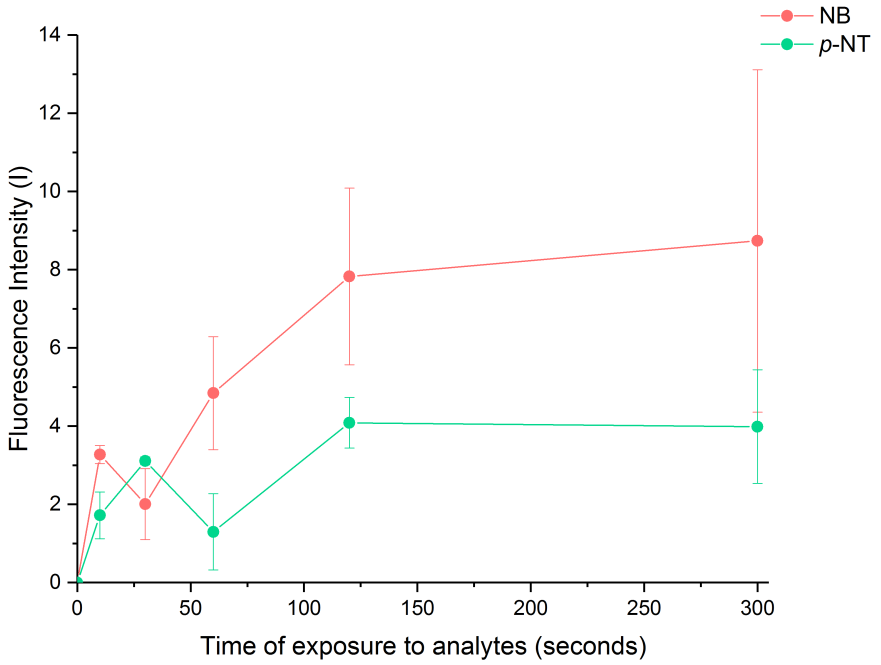

Figure 3.23: Fluorescence quenching percentages demonstrated by 'thin films' of **2'** upon exposure to explosive related analytes NB and *p*-NT for 0, 10, 30, 60, 120 and 300 s. Repeat results on different MOF **2'** 'thin films' are included; the variance (standard error of the mean) in the results between each sample is represented by the error bars.

3.4 CONCLUSIONS AND FUTURE WORK

In summary, during this exploratory pilot study, two novel fluorescent metal-organic frameworks [Zn(dcbpy)(DMF)]·DMF (**1**) and [Dy(dcbpy)$(DMF)_2(NO_3)$] (**2**) were synthesises and characterised for the application of explosives detection. Both MOFs were constructed from the same organic linker ligand but varied in metal composition. As a consequence, the two structures demonstrated very different overall framework topologies. Despite this, both frameworks showed similar linker-based fluorescence emissions, with the possibility of some charge-transfer influences to emissions also. The activated analogues of these frameworks **1'** and **2'** were tested for their vapour phase sensing capabilities against explosives-related compounds DMNB, 2,4-DNT, *p*-NT and NB, and exhibited very different responses.

Porous metal-organic framework **1'** was able to detect the challenging explosives taggant DMNB, as well as NB, *p*-NT and 2,4-DNT *via* the well established photo-induced electron transfer mechanism. The successful detection of the DMNB analyte (as well as potentially the other analytes also) was attributed to the ability of the MOF to be able to encapsulate it in to its framework cavities. Non-porous framework **2'** showed selectivity in sensing towards the nitroaromatic compounds NB and *p*-NT (also *via* the PIET mechanism). The detection of these analytes was determined to be as a result of efficient surface based interactions with the MOF.

The difference in the sensing of the explosive related analytes with these MOFs was rationalised based upon the contrasting nature of their overall framework architectures. Ultimately, this research highlights the importance that the topology of a MOF system plays on its sensing capabilities. More specifically, it underlines the importance of porosity on analyte detection, especially for the detection of unfavourable analytes such as DMNB, that are known to demonstrate weak interactions with MOFs unless encapsulated into frameworks. This coincides with previous research conducted on fluorescent MOFs and amplified fluorescent conjugated polymers [26, 127].

The work presented in this chapter also demonstrated that these frameworks were able to offer timely responses (for analytes with which interactions were favourable, a degree of MOF response was observed even after just 10 s of analyte exposure) and MOF **1'** demonstrated regeneration ability at room temperature; both of these are important considerations for the real-world applicability of these materials.

Additionally, the research presented in this chapter drew attention to the need for uniformity in the 'thin films' used for sensing applications. The initial, exploratory sensing of the explosives related

analytes using the homogeneous shaped and sized crystals of **1M'** demonstrated that the sensitivities of analyte detection are greatly affected by 'thin film' fabrication. Which again coincides with research reported for other fluorescent MOFs for explosives detection, as well as amplified fluorescent conjugate polymers [26, 127]. Therefore, using the film fabrication and sensing methods employed for the research presented in this chapter, only the detectability of the tested anlaytes with the MOFs can be evaluated; an accurate assessment of their sensitivities is not possible. Whilst some efforts were made to fabricate uniform MOF thin films, they were unfortunately unsuccessful. Nevertheless, thin film fabrication should be a priority for future work investigating the vapour-phase detection of analytes using MOFs.

Further to this, the work presented in this chapter eluded to the need for a more robust analyte vapour exposure method. The method proposed by Li *et al.* that was followed for these experiments exposes the MOFs to saturated vapours of the analytes, which doesn't allow for a comparison as to which analytes quench the MOFs to the greatest extent, owing to them being exposed to different concentrations of the analyte vapours. Therefore, future work should aim to construct an accurate and quantifiable vapour delivery flow that exposes MOFs to known concentrations of analytes. While some work on this has been reported by Swager *et al.* for explosives detection using carbon nanotubes [175]; there has been no attempt as of yet to expose MOFs to quantified vapours of explosive analytes in the literature.

Whilst this pilot study gleaned insights into important considerations for future work; namely the importance of porosity for analyte detectability and the need for uniform films for accurate comparisons of MOF sensitivity towards analytes. Further exploratory research on these two MOFs is required prior to their consideration for in-field

detection use. For example, whilst some investigations into interefer-ents effects were attempted on MOF **1′**, these effects should be further probed by exposing the MOFs to more representative levels of in-tereferents that might be found in real-world detection environments (however this does again rely on the use of an accurate vapour de-livery system), as well as this, they should be fully characterised for their humidity stability; as discussed in Section 2.6.1.5 this can be a pitfall of MOFs. Whilst MOF **1′** didn't appear to show instability when exposed to laboratory air (humidity) conditions; this should be further investigated.

With this said, owing to the minimal porosity of MOF **2′** and the pores of MOF **1′** only just potentially being able to encapsulate the analyte 2,4-DNT, these two MOFs were not further tested during the research conducted within the time frame of this doctoral research. Instead, owing to the importance of porosity, a flexible MOF sensor $Zn_4L(H_2O)_4 \cdot (solvent)_n$, MOF **3**, was synthesised, fully characterised and probed in depth for its potential within the domain of explosives detection, and will be the focus of the remainder of this thesis.

4

A FLEXIBLE MOF SENSOR

4.1 INTRODUCTION

This chapter details the synthesis and characterisation of a flexible fluorescent metal-organic framework $[Zn_4L(H_2O)_4 \cdot (solvent)]_n$, MOF **3**, (where L = 5,5′,5″,5‴-[1,2,4,5-benzenetetrayltetrakis(methyleneoxy)tetra-1,3-benzenedicarboxylate) and an evaluation of the differential sensing behaviour exhibited by this MOF, when exposed to explosives and related analytes in both the vapour and solution-phase.

Three structural objectives were sought when rationally designing MOF **3**, these were:

1. To synthesise a framework with sufficiently sized pores to allow for the encapsulation of all common explosive molecules including larger compounds such as Tetryl, TNT and PETN. As discussed in Chapter 3 and in the wider literature, the inclusion of analytes into the cavities of MOFs facilitates stronger MOF-guest interactions [127], which impacts on the level of response (sensitivity) produced by the sensor.

2. To produce a MOF with some degree of flexibility. Dynamic MOFs can yield perturbations in host-guest frameworks which can lead to shifts the fluorescence emission spectra and thus, the possibility to differentiate between target analytes based on both quenching and spectral shift (as discussed in Section 2.6.1.1).

3. To generate a MOF with the potential to contain unsaturated metal sites (UMS). These open metal sites (that are produced upon the removal of the weakly bound solvent molecules coordinated to the MOF metals) have been shown to assist in MOF-guest interactions and have imparted the preferential binding of some analytes (Section 2.6.4.3).

MOF **3** was designed based on a framework pioneered by Eddaoudi *et al.* [176]. The group sought to identify specific building blocks that when combined, would yield MOFs with anticipated topological nets, creating blueprints for the rational design of MOFs with intended architectures that are amenable to isoreticular chemistry. This is a useful synthetic strategy when attempting to design frameworks with specific pore sizes based on topologies that are known to be robust [92, 93, 176]. In doing so Eddaoudi *et al.* synthesised MOF $[Cu_4L(H_2O)_4 \cdot (solvent)]_n$ (L = 5,5′,5″,5‴-[1,2,4,5-benzenetetrayltetrakis-(methyleneoxy)tetra-1, 3-benzenedicarboxylate), which has the same **tbo** net as the prototypical MOF 'HKUST-1' ($[Cu_3(BTC)_2]$, H_2BTC = benzene-1,3,5-tricarboxylic acid). As discussed in Section 2.6.1, MOFs topologies are often characterised by three letter codes (e.g. **pcu** or **tbo**). **Tbo** nets have underlying (3,4)-coordinations; they are constructed from paddle-wheel SBUs with four points of extensions and linkers with three points of extension [177]. HKUST-1 is one of few industrially manufactured metal-organic frameworks [178] and has shown promise for suitability in a number of commercial applications, namely catalysis [179]. The popularity of this MOF arises from it's reported chemical stability coupled with it's high permanent porosity (BET surface areas are typically in the range of 600 - 1600 $m^2\ g^{-1}$ [120]). The structures of both $[Cu_4L(H_2O)_4 \cdot (solvent)]_n$ and HKUST-1 and the linkers by which they are synthesised can be seen in Figure 4.1.

'Isoreticular' defines analogous frameworks that vary in size and nature but their underlying topology ('nets') remains the same (Section 2.6.1).

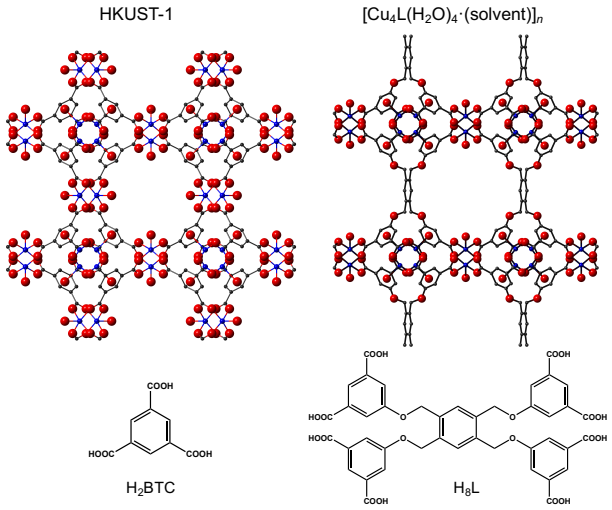

Figure 4.1: Illustration of the overall **tbo** framework topologies of MOFs HKUST-1 (left) and $[Cu_4L(H_2O)_4{\cdot}(solvent)]_n$ (right) as well the linkers by which these two MOFs are synthesised. Figures were reproduced from the crystallographic data obtained from [180] and [176] respectively.

MOF $[Cu_4L(H_2O)_4{\cdot}(solvent)]_n$ contains larger pore apertures than HKUST-1 (Langmuir apparent surface = 2896 $m^2\ g^{-1}$), is synthesised with a flexible fluorescent linker and, similarly to HKUST-1 has the potential through dehydration to contain UMS. Hence, its choice as a blueprint framework for MOF **3** ($[Zn_4L(H_2O)_4{\cdot}(solvent)]_n$), which is isostructural to $[Cu_4L(H_2O)_4{\cdot}(solvent)]_n$, with the only variation between the two being the metal with which they are constructed. MOF **3** is also isoreticular to HKUST-1.

This chapter details the full characterisation of MOF **3** including an in-depth evaluation of its water stability. It also compares how **3** performs as an explosives sensor in both the solution and vapour-phase. This has been seldom reported in the MOF-sensor literature, with many groups focussing on one or the other. This work seeks to compare the two as it may help elucidate which sensing medium is preferential for this MOF, thus, potentially indicating how it may be used within real-world scenarios. For example, as the sensing component of a vapour-phase detector, or, as a solution-phase diagnostic for the detection of particles present on interrogation surfaces.

4.2 EXPERIMENTAL

4.2.1 *Synthesis of linker (H_8L)*

The organic ligand 5,5′,5″,5‴-[1,2,4,5-benzenetetrayltetrakis(methyleneoxy)]tetra-1,3-benzenedicarboxylic acid (H_8L) was synthesised following the previously reported procedure by Eddaoudi *et al.*[176] with some adaptations. The reaction scheme for this synthesis is given in Scheme 4.1.

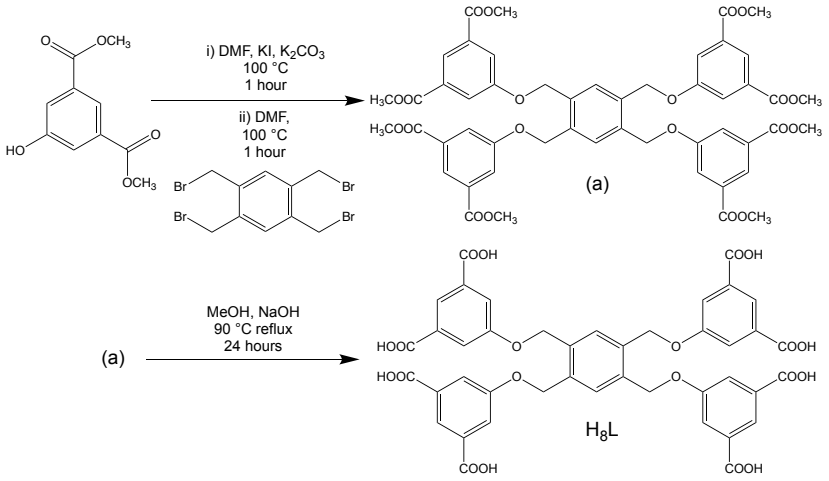

Scheme 4.1: Schematic detailing the synthesis of linker H_8L.

Initially dimethyl 5-hydroxyisopthalate (6 mmol, 1.27 g) was dissolved in DMF (13 mL) in a round bottom flask. A catalytic amount of KI (end of a spatula) was added to the solution whilst stirring, followed by K_2CO_3 (0.026 mol, 2.60 g). This solution heated to 100 °C and left to stir for an hour. After an hour, 1,2,4,5-tetrakis(bromomethyl)-benzene (8 mmol, 0.288 g), which was dissolved in DMF (1 mL), was added to the mixture dropwise (at 100 °C). The solution was further left for an hour at the same temperature whilst still stirring, after which, the reaction was cooled down to ambient temperature. Next, approximately 80 mL of H_2O (deionized) was added to the reaction mixture to produce a white precipitate, which was filtered (using

Buchner filtration), washed with ice cold deionized H_2O and subsequently dried under dynamic vacuum. This afforded the tetramethyl ester (a) as denoted in the reaction Scheme 4.1.

Once dried, the ester was added to a round bottom flask with 20 mL of MeOH. Then, an aqeous solution of NaOH (1.2 g in 12 mL) was added to the solution drop-wise whilst stirring. This final solution was heated to 90 °C and left to reflux for 24 hours (this differs from Eddaoudi *et al.* who only heated the reaction to 50 °C for 12 hours). After this time, the solution (whilst still stirring) was cooled to room temperature. It was then acidified to pH = 1 using concentrated HCl (approx. 37.2 w/w%) and left to stir for an additional half an hour. The final precipitate was separated by filtration, washed with cold H_2O and dried under a dynamic vacuum, giving H_8L (5,5′,5″,5‴-[1,2,4,5-benzenetetrayltetrakis(methyleneoxy)]tetra-1,3-benzenedicarboxylic acid) with a 79.5% yield. (300 MHz, DMSO-d_6) δ 8.07 ppm ($4H_D$, S), 7.82 ppm ($2H_A$, S), 7.78 ppm ($8H_C$, S) and 5.42 ppm ($8H_B$, S).

4.2.2 *Synthesis of MOF $Zn_4L(H_2O)_4\cdot(solvent)]_n$ (3)*

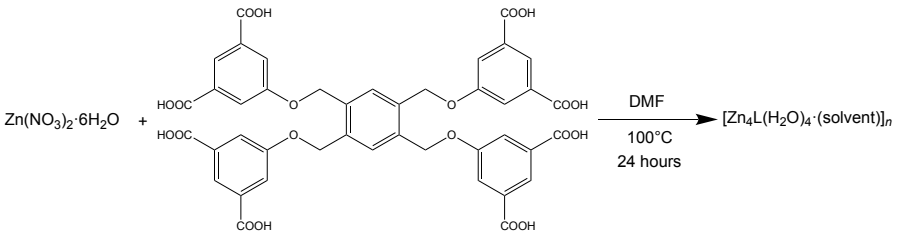

Scheme 4.2: Reaction scheme detailing the synthesis of MOF 3.

Metal-organic framework 3 was synthesised *via* a solvothermal method, the reaction scheme of which is provided in Scheme 4.2. Zinc nitrate hexahydrate ($Zn(NO_3)_2\cdot 6\,H_2O$, 0.1 mmol, 29.8 mg) was combined with synthesised ligand H_8L, Scheme 4.1, (0.1 mmol, 85.5 mg) in 12

mL of DMF in a glass vial. The reaction mixture was stirred until the solution became clear, the vial was then sealed and placed in an oven set to 100 °C for 24 hours, affording clear, block-shaped crystals of metal-organic framework **3**, in approximately a 35% yield.

4.2.3 *Activation of MOF* **3**

A washing (solvent exchange) procedure was implemented on the crystals of the as-synthesised MOF **3** to remove the solvent present within the pores of this framework, generating active MOF **3′**. Initially the DMF mother liqueur in which crystals of MOF **3** were synthesised was decanted off and acetonitrile (MeCN) was added, immersing the crystals in the solvent. The crystals were left to soak in MeCN for 24 hours, after which, the solvent was pipetted off and methanol (MeOH) was added, again immersing the crystals in the new solution. After a further 24 hours, the MeOH was replaced by acetone and the crystals were left (24 hours). After this, the final wash was conducted with the crystals now immersed in dichloromethane (DCM) for a final 24 hours. Post immersion in DCM, the solvent was decanted off and crystals were left to dry under dynamic vacuum, this yielded active MOF **3′**. An active sample of **3′** was re-immersed in MeCN for one month giving a re-solvated structure **3′-MeCN**.

4.2.4 *MOF* **3′** *water and humidity stability tests*

4.2.4.1 *MOF* **3′** *exposure to deionized* H_2O

2 mL of deionized H_2O were added to 5 mg of a MOF **3′** sample and left for 24 hours, after which, the resultant precipitate was filtered under dynamic vacuum using Buchner filtration, ready for powder X-ray diffraction (PXRD) analysis.

4.2.4.2 *MOF 3′ exposure to ambient air conditions*

Samples of **3′** were analysed by PXRD after activation, then placed in open top glass vials and left exposed to regular laboratory conditions for two weeks, after which they were re-analysed using PXRD.

4.2.4.3 *Dynamic Vapour Sorption (DVS) humidity experiments*

Metal-organic framework **3′** was tested for its stability in the presence of water vapour at various temperatures and relative pressures (humidities) using dynamic vapour sorption (DVS).

Relative pressure (RP) is defined as 'the ratio of the analyte vapour pressure to the measured saturation pressure at a given temperature' The RP for water is often termed 'relative humidity' RH. The two are often used interchangeably. [120].

The DVS technique

Water vapour sorption and desorption isotherms were obtained using a vacuum dynamic gravimetric vapor sorption analyser 'DVS Vacuum' manufactured by (and in collaboration with) Surface Measurement System Ltd. London, UK ©.

Dynamic vapour sorption (DVS) exposes a sample to various concentrations (relative pressures, RP, P/P_o) of sorbate vapours and measures the change in mass of the sample that is being monitored, as a function of time. The mass of the sample is left to reach gravimetric equilibrium prior to each incremental increase in the RP (P/P_o) of the system.

'DVS Vacuum' analyser instrument

Figure 4.2 illustrates the 'DVS Vacuum' analyser instrument.

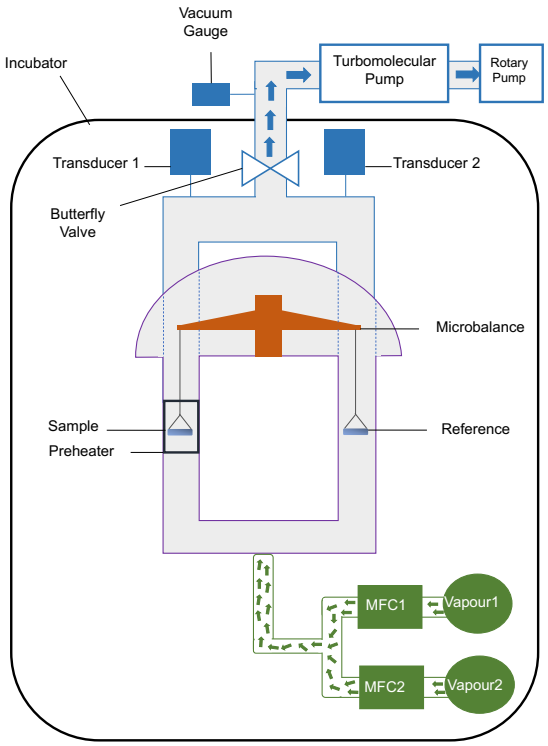

Figure 4.2: 'DVS Vacuum' analyser instrument schematic. This figure has been replicated by the permission of Surface Measurement System Ltd. London, UK ©.

The instrument was enclosed in a temperature controlled unit to allow for a constant temperature (± 0.1 °C) to be maintained by the system. A SMSUltraBalance with a sensitivity of 0.1 μg was used to measure the change in mass of the sample. Sorbate (water vapour) entry rates were controlled by mass flow controllers that ensured the continuous delivery of vapours at constant flow rates. Butterfly valves were used to regulate the sorbate exit rates. The transducers were used to measure the pressure in the system, allowing for communication to the butterfly valves, enabling them to open or close in order to achieve desired RPs (P/P_os).

Specific experimental procedure

Six different synthetic batches of MOF **3** were activated (**3'**) and combined for use in the DVS experiments. Approximately 30 mgs of MOF **3'** were taken from this batch and loaded into the instrument specimen pan during each experiment. Where experiments were completed consecutively on the same MOF sample, they were not removed from the analyser prior to subsequent analysis.

All samples were initially degassed at room temperature, *in-situ*, under high vacuum ($\sim 10^{-5}$ Torr) for two hours. This was followed by degassing of the samples at a temperature of 150 ° C, also under high vacuum, for a further two hours. The samples were subsequently cooled down to the temperature at which the experiments were to be performed. The water vapour sorption isotherms of MOF **3'** were measured at temperatures of 25, 40, 50 and 60 ° C, with RPs ranging from 0-90 % (P/P_0). The saturated vapour pressures of water used (absolute pressure, P_0) at each of the different temperatures are given in Table 4.1.

Table 4.1: Saturated vapour pressures of water used in DVS experiments at different temperatures.

Temperature / °C	Saturated vapour pressure (P_0) /Torr
25	23.8
40	55.3
50	92.5
60	149.4

The experiments were performed in $\delta m/\delta t$ mode. The criterion set to expose the sample to the desired RP (0-90 %) was 0.006 %/min, up to 40% *. A maximum step time of 360 minutes and a minimum step time of 7 minutes were selected. This meant that at each step (from 1-40% P/P_0) mass change measurements were taken every minute, and

* $\delta m/\delta t$ was not available up to 90% RP due to software constraints.

the values measured needed to be below 0.006% for at least 7 minutes. If the mass change went above 0.006%, the step was calculated again, if a mass change of < 0.006% was not achieved in 6 hours; the sample was automatically exposed to the next incremental RP. A time mode criterion was set to collect data above 40% RP (P/P_o) with a dwell time of 120 minutes set for each step. Desorption was recorded in a similar manner with a stage time of 60 minutes for 90-40 % P/P_o and the same $\delta m/\delta t$ for P/P_o 40-1%.

4.2.5 *Solution-phase sensing procedures*

4.2.5.1 *Generation of MOF suspensions in solution*

Solution-phase sensing experiments used stock solutions of MOF **3′** suspended in acetonitrile (MeCN). The suspensions were generated by adding 6 mg of finely ground active MOF **3′** to 6 mL of MeCN. The solutions were ultrasonicated for three hours to generate the ultrafine suspensions of the MOF in solution, Figure 4.3.

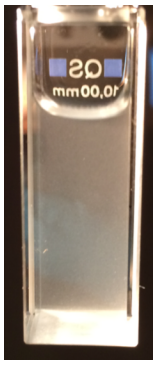

Figure 4.3: Illustrative example of a cuvette containing a MOF **3′** suspension in acetonitrile (MeCN).

4.2.5.2 *Production of explosives stock solutions*

Explosives stock solutions of 1 mM concentration were used for sensing experiments. These were obtained by dilution of commercially purchased explosives standards of 1000 μg/mL in MeOH:MeCN (1:1). The standards were purchased from AccuStandard ® *via* Kinesis Ltd. All stock solutions were kept refrigerated at 4 °C.

4.2.5.3 *Solution-phase sensing methodology*

Prior to the sensing of an explosive substance or related compound with **3'**, 1.5 mL of a freshly ultrasonicated MOF **3'** suspension sample was added to a quartz cuvette. The cuvette was then placed into a Horiba Fluoro-max4 fluorometer and the sample was excited at 315 nm and scanned between 330 - 600 nm, giving a fluorescence emission spectrum for the MOF in suspension. After this, the fluorescence emission was re-measured and a 5 cycle time delay was implemented whereby the sample remained under constant illumination by the source and the fluorescence emission was recorded every 60 s, giving fluorescence emission spectra for t = 0, 60, 120, 180 and 240 s. Next, the sample was held on a vortexer, operating at 400 repetitions per minute (rpm) for 15 s, and the fluorescence intensity was re-measured. This was repeated 5 times in order to ensure a stable base line of the fluorescence emission intensity of the sample prior to analyte sensing.

During a sensing experiment, the MOF suspension was initially vortexed for 15 s to ensure the MOF particulates remained in suspension in the solution. After this, the initial fluorescence emission (I_0) of the suspension was measured, this was repeated another 2 times with mixing between each reading, giving three baseline readings of the initial fluorescence emission of the MOF suspension prior to analyte addition.

Explosive analytes were added in 10 μL aliquots, from 10 -100 μL, from the chosen stock solutions. Upon addition of a 10 μL explosive stock solution to the MOF suspension, the cuvette now containing the MOF and analyte, was replaced onto the vortexer for a further 15 s, and the fluorescence emission was re-measured (I). Two more 15 s vortex and fluorescence re-measurements were repeated, giving three fluorescence emission measurements for the addition of this volume of analyte to the solution. These steps were repeated for each further 10 μL addition of an explosive stock solution until 100 μL were added. In essence, three repeat measurements were taken for each 10 μL addition, with mixing using the vortexer between each measurement.

4.2.5.4 *Stability experiments*

To check the stability of MOF **3′** towards Tetryl and 2,4-DNT, PXRD measurements were taken on samples pre- and post- exposure to 100 μL of 1 mM (62.5 μM) solutions of the two analytes. The PXRD patterns were obtained with the MOF samples in solution. Additionally, a 10 mg sample of **3′** was immersed in a 2 mL solution containing 200 μL of 1 mM (91μM) 2,4-DNT for three months. Single crystal X-ray diffraction was attempted on the crystals of this sample.

4.2.6 *Vapour-phase sensing procedures*

4.2.6.1 *MOF **3′** 'thin film' fabrication*

For vapour-phase sensing 'thin films' of MOF **3′** were fabricated on quartz glass. A 1 cm x 1 cm square of sticky adhesive tape was placed on to the quartz slide, onto which, crystals of the MOF (as activated) were scattered and any excess crystals were tapped off from the slides.

4.2.6.2 *Generation of analyte vapour head-space*

Analyte vapours of 2,4-DNT were generated in the same way as discussed in Section 3.2.4.

4.2.6.3 *Vapour-phase sensing methodology*

The same vapour-phase sensing methodology was used as described in Section 3.2.4. The only discrepancies being that some films were exposed to the analyte for longer periods of time (e.g. for 600 s, 1800 s etc). In addition, four 2,4-DNT tubes containing saturated headspaces of the analyte were used in each sensing experiment, on rotation, in an attempt to mitigate for the depletion of analyte headspaces.

4.2.6.4 *Stability experiments*

The stability of a 'thin film' of MOF **3'** upon exposure to 2,4-DNT was evaluated by measuring the PXRD pattern of the readily made film, then exposing the film to the vapours of 2,4-DNT for 2 weeks, and re-running the PXRD analysis.

An additional stability assessment of MOF **3'** towards the vapours of 2,4-DNT was performed on a freshly activated MOF **3'** sample that was exposed to vapours of the analyte for a prolonged period of time and compared to an atmospherically exposed control sample. 10 mg of a MOF **3'** sample was placed in a glass vial which was inserted into a centrifuge tube containing 2,4-DNT crystals (~ 0.5 g). The centrifuge tube was sealed so that a headspace of the analyte would be generated in the tube, allowing for the MOF crystals to be surrounded by the analyte vapours. At the same time, an additional 10 mgs of the same MOF **3'** sample were also placed in a glass vial and inserted in an empty centrifuge tube, open to the ambient surrounding environment, containing no analyte. The experimental set up can be seen in Figure 4.4. The MOF samples were left exposed to these conditions

for two weeks, after which, PXRD measurements on the two samples were obtained and Le Bail fitting was performed by Dr. Huw Marchbank, University College London.

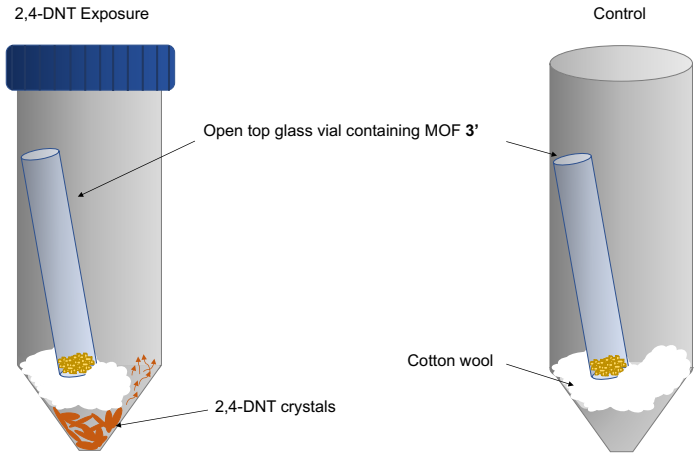

Figure 4.4: Illustration of the experimental set up for the prolonged exposure of MOF **3'** to the saturated headspace vapours of 2,4-DNT and the air exposure control.

A variation of this experiment involved a MOF **3'** sample being initially exposed to atmospheric air conditions as a control sample for two weeks, followed by exposing the same sample to 2,4-DNT vapours for two weeks. Again PXRD measurements after each exposure time were measured and analysed using Le Bail fitting.

4.2.7 *Computational simulations*

Computational simulations were performed by Christopher N. Savory and Dr. David O. Scanlon, the details of which can be found in Appendix B.

4.3 RESULTS AND DISCUSSION

4.3.1 *Characterisation*

4.3.1.1 *Linker characterisation*

^{1}H Nuclear magnetic resonance (NMR) analysis confirmed the successful synthesis of linker ligand H_8L (5,5′,5″,5‴-[1,2,4,5-benzenetetrayltetrakis(methyleneoxy)]tetra-1,3-benzenedicarboxylic acid) after a slight modification to the previously reported synthetic method by Eddaoudi *et al.* [176] (as described in Section 4.2.1). The annotated ^{1}H NMR spectrum can be seen in Figure 4.5.

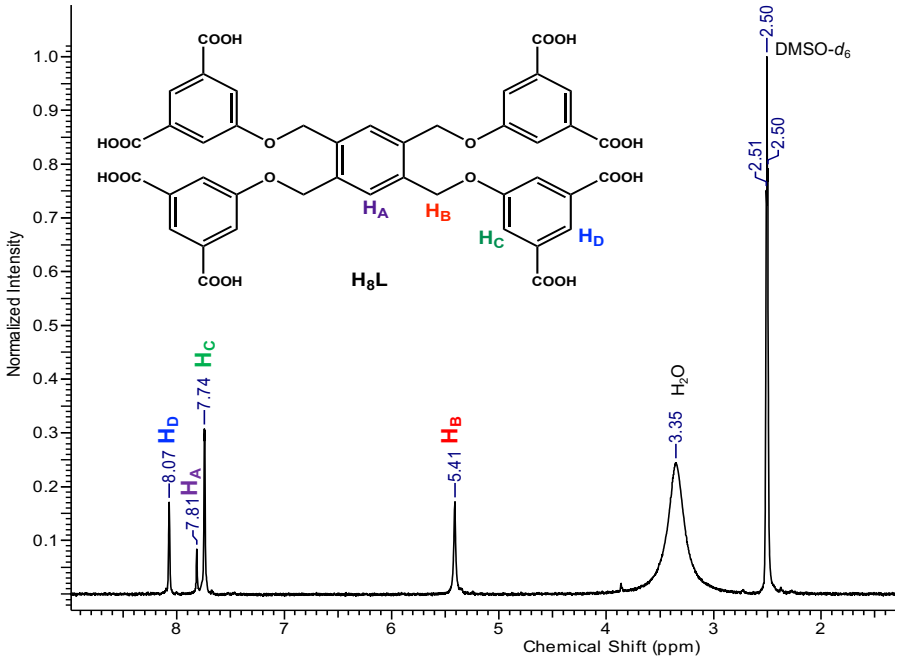

Figure 4.5: Illustration of the proton environments found in linker H_8L.

4.3.1.2 *MOF structure determination*

From the crystalline product that emerged from the reaction detailed by Scheme 4.2, a clear, block-shaped crystal of 0.13 x 0.09 x 0.13 mm size was used for structural analysis using single crystal X-ray diffraction. The data confirmed the structure of this metal-organic framework to be isostructural to that of the copper analogue synthesised by Eddaoudi and co workers [176]; the newly synthesised MOF has the same overall topology as $[Cu_4L(H_2O)_4 \cdot (solvent)]_n$ (L = 5,5′,5″,5‴-[1,2,4,5-benzenetetrayltetrakis(methyleneoxy)tetra-1, 3-benzenedicarboxylate) but is just comprised of a different transition metal. Thus, the formula of this MOF was confirmed to be $[Zn_4L(H_2O)_4 \cdot (solvent)]_n$. A comparison of the crystallographic structural parameters between MOFs $[Cu_4L(H_2O)_4 \cdot (solvent)]_n$ and $[Zn_4L(H_2O)_4 \cdot (solvent)]_n$ is given below.

Table 4.2: Crystal data and structure refinement comparison between $[Cu_4L(H_2O)_4 \cdot (solvent)]_n$ and $[Zn_4L(H_2O)_4 \cdot (solvent)]_n$.[a]

	MOF **3**	Eddaoudi *et al.* MOF
Formula	$[Zn_4L(H_2O)_4 \cdot (solvent)]_n$	$[Cu_4L(H_2O)_4 \cdot (solvent)]_n$
Empirical formula	$C_{42}H_{32}Zn_4O_{24}$	$C_{42}H_{22}Cu_4O_{24}$
Formula weight	1181.52	1164.76
Temperature/K	150	100(2)
Crystal system	Orthorhombic	Orthorhombic
Space group	Fmmm	Fmmm
a/Å	25.0266(5)	25.042(4)
b/Å	28.3181(7)	26.826(4)
c/Å	30.3737(6)	30.848(5)
$\alpha/^\circ$	90	90
$\beta/^\circ$	90	90
$\gamma/^\circ$	90	90
Volume/Å^3	21526.0(8)	20724(6)
Z	32	8
ρ_{calc} g/cm^3	0.737	0.747
μ/mm^{-1}	1.360	0.167
F(000)	4791.0	4656
Crystal size/mm	0.13 x 0.09 x 0.13	0.60 x 0.004 x 0.004
Radiation	CuKα($\lambda = 1.54184$)	$\lambda = 0.40663$ (synchotron)
2θ range for data collection/$^\circ$	6.242 to 134.99	1.15 to 13.06
Index ranges	-29$\leqslant$h$\leqslant$25, -31$\leqslant$k$\leqslant$33, -36$\leqslant$l$\leqslant$36	-25$\leqslant$h$\leqslant$21, -25$\leqslant$k$\leqslant$29, -33$\leqslant$l$\leqslant$25
Reflections collected	21168	16210
Independent reflections	5149[R_{int}= 0.0242]	3497[R_{int}= 0.0432]
Data/restraints/parameters	5633/0/165	3497/21/166
Goodness of fit on F^2	1.102	1.001
Final R indexes [I>2σ(I)]	R_1 = 0.0433	R_1 = 0.0762
	wR_2= 0.1490	wR_2= 0.2391
Final R indexes (all data)	R_1 = 0.0507	R_1 = 0.0986
	wR_2= 0.1584	wR_2= 0.2619
Largest diff. peak/hole / eÅ^3	0.84/-0.53	0.462/-0.491

a The full crystallographic data can be found in Appendix B. Additionally, the crystallographic information file and structure factor files have been deposited in the Cambridge Crystallographic Data Centre (CCDC) number 1552177.

Metal-organic framework $[Zn_4L(H_2O)_4 \cdot (solvent)]_n$ (**3**) discloses a three-dimensional framework belonging to the orthorhombic space group Fmmm. The asymmetric unit (ASU) for the MOF consists of two crystallographically independent zinc metals, an H_8L ligand with 25% occupancy and two crystallographically independent water lig-

ands coordinated to the two zinc metal centres, the ASU is illustrated in Figure 4.6. As evident, one of the coordinated water ligands demonstrates some disorder (atom O1 in Figure 4.6).

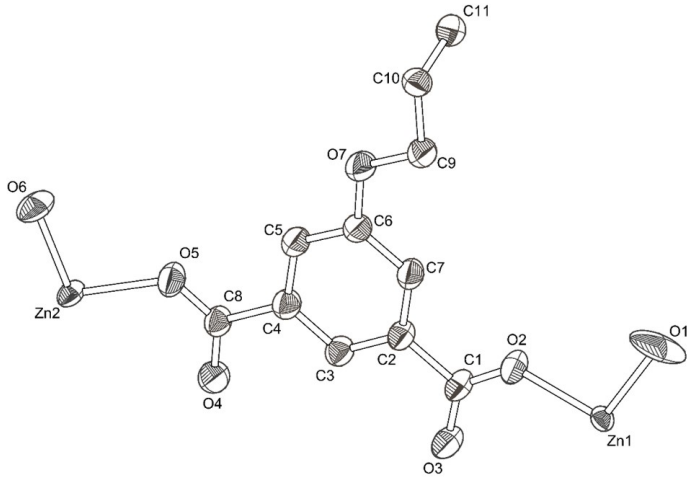

Figure 4.6: Illustration of the asymmetric unit (ASU) found in MOF **3**. Hydrogen atoms have been omitted for clarity and the thermal ellipoids are displayed at the 30% probability level.

It is important to note that solvent guest molecules do reside in the pore of this MOF and are associated with the ASU. However, owing to their high degree of disorder these guests remained unresolved. During the refinement of the MOF crystal structure, a 'solvent mask' was implemented in the structure solution programme Olex2 [181]. This allows for the residual electron density from the disordered solvent to be combined and incorporated as the solvent contribution to the structure factor and refinement calculations [167]. A similar process was implemented by Eddaoudi *et al*. who used SQUEEZE obtained from PLATON [182] to account for the solvent molecules residing in the pores of $[Cu_4L(H_2O)_4 \cdot (\text{solvent})]_n$ [176]. The void electron count for the disordered solvent was found to be 4116.7 electrons for the whole unit cell. As Z is 32, this equates to 128.6 electrons associated with each ASU. This could correlate with the presence of three DMF solvent molecules, however as other solvents could be present, such as water, the total solvent number cannot be fully ascertained using

Z is defined as the total number of asymmetric units per unit cell

this method alone. As will be discussed later, other characterisation methods such as thermogravimetric analysis assist in characterising the nature of the solvents present within MOF **3**'s pores.

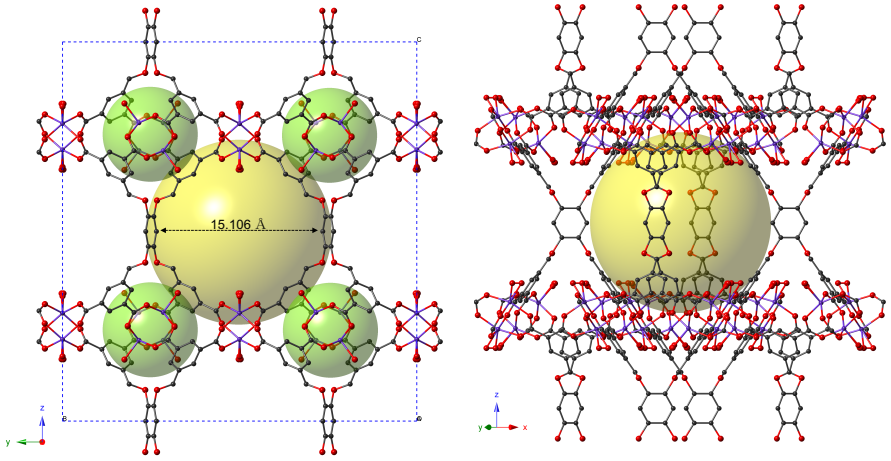

Figure 4.7: Left: MOF **3** unit cell structure showing the two different pore environments found within this MOF (green and yellow spheres). The shortest pore distance found for the largest cavity of the MOF is illustrated by the black arrow (the distance includes Van der Waal's radii and hydrogen atoms). Right: An alternative view of the unit cell, showing clearly the shape of the largest pore found within MOF **3**. In both crystal structure illustrations, hydrogen atoms have been omitted for clarity. Carbon atoms are coloured grey; oxygen atoms red; and zinc atoms are purple.

The ASU of MOF **3** is expanded to give the unit cell shown on the left hand side of Figure 4.7. In this metal-organic framework, each ligand serves as a 4-connected node, each 5-R-isophthalate moeity as a 3-connected node and each Zn2(O2CR)4 paddle-wheel cluster as another 4-connected node, generating an overall **tbo** framework topology for this MOF. Figure 4.7 also gives a representation of the two different pore environments found within the structure of this MOF. The largest pore, expressed as a yellow sphere in Figure 4.7 has a shortest diameter length of 15.106 Å†. The solvent accessible volume (SAV) for this structure was found to be 69.2% using PLATON[182]‡. This is marginally lower than the 72% solvent accessible volume reported for the copper analogue $[Cu_4L(H_2O)_4 \cdot (\text{solvent})]_n$ [176].

† This calculation includes hydrogen atoms and Van der Waal radii. Details of the other pore diameters are given in Appendix B.

‡ The SAV details can be found in Appendix B.

An extended three-dimension representation of MOF **3** is given in Figure 4.8 as well as the space filling diagram for this metal-organic framework.

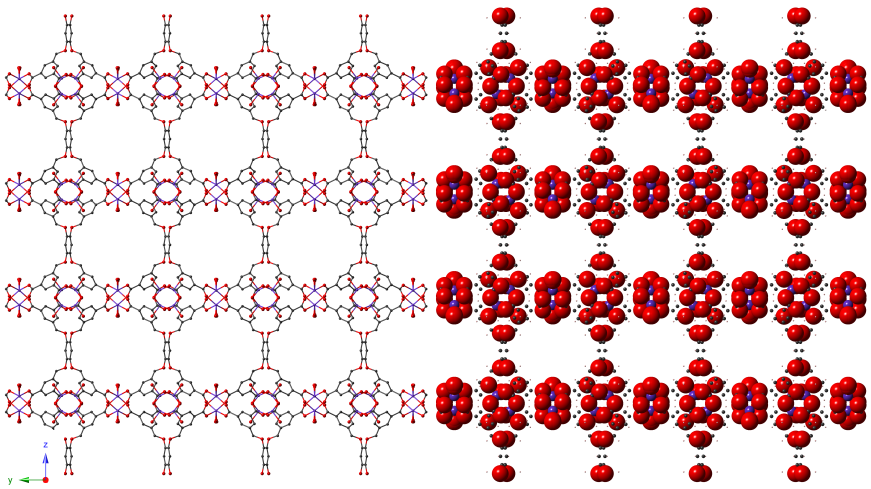

Figure 4.8: Left: Extended three-dimensional representation of MOF **3**. Hydrogens have been omitted for clarity. Right: Space filling diagram of 3D MOF **3**. Hydrogen atoms are included. Both figures are shown with view along the crystallographic *a*-axis.

Molecular dimensions of some common explosives

The molecular dimensions of some common explosives (Section 2.2) have been calculated based on their crystallographic data and are summarised in Table 4.3. The values were calculated by finding the longest distances between the atoms of an explosive molecule within a particular axis, as demonstrated in Figure 4.9 using TNT as an example.

Table 4.3: Explosives molecular dimensions

Explosive	length x Å	length y Å	length z Å	CIF Reference
TNT	6.660	6.984	5.976	[183]
PETN (II/beta[a])	7.979	7.969	7.979	[184]
RDX (I/alpha)	5.033	5.702	5.391	[185]
PA	6.976	6.209	6.970	[186]
Tetryl	6.160	8.206	7.066	[187]
TATP	6.197	5.435	6.397	[188]

a This denotes the polymorph used when calculating the molecular dimensions.

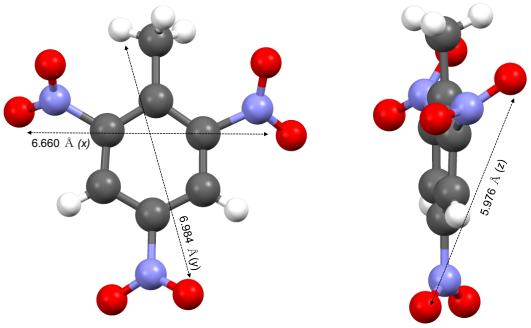

Figure 4.9: TNT molecular dimensions.

Therefore, based on the crystallographic data for both MOF **3** and the named explosives, these analytes should be able to penetrate into this MOF's pores during explosives sensing.

4.3.1.3 *Phase purity and crystal morphology*

Powder X-ray diffraction analysis (PXRD) confirmed phase purity in the synthesised MOF **3** samples owing to good agreement between the simulated PXRD pattern as obtained from single crystal X-ray diffraction data and that of the as-synthesised material. Additionally, the simulated PXRD pattern for MOF **3** is in agreement with the simulated PXRD pattern for $[Cu_4L(H_2O)_4 \cdot (solvent)]_n$; further confirming the two frameworks are isostructural (Figure 4.10).

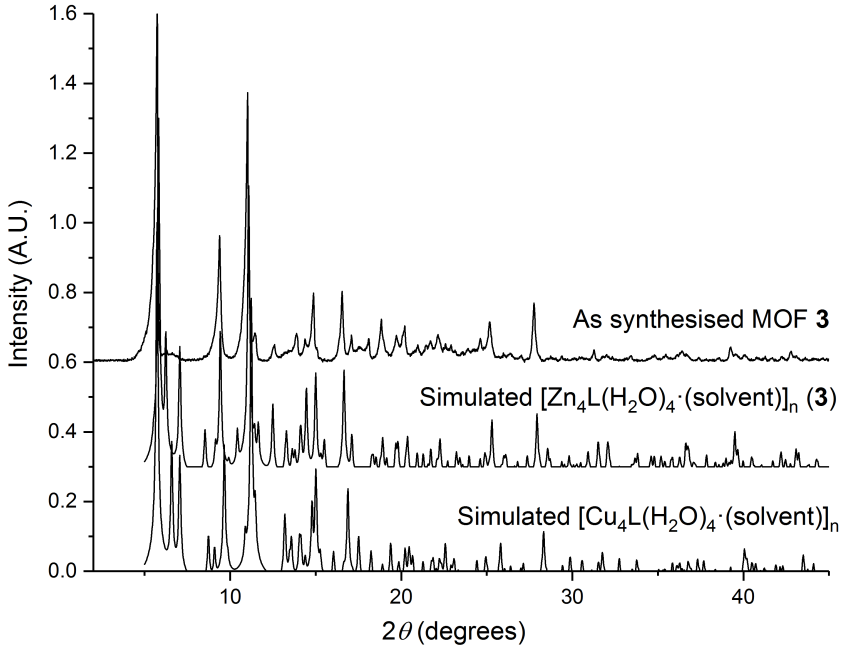

Figure 4.10: Overlay of PXRD patterns of simulated MOFs $[Cu_4L(H_2O)_4\cdot(solvent)]_n$, $[Zn_4L(H_2O)_4\cdot(solvent)]_n$ (**3**) and as synthesised MOF **3**.

The solvothermal method used to synthesis MOF **3** results in clear block-shaped crystals that are clumped together. Scanning electron microscopy (SEM) images of the crystals obtained immediately after synthesis are shown in Figure 4.11.

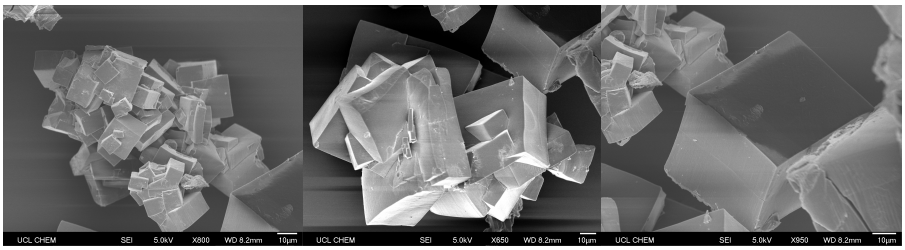

Figure 4.11: Scanning electron microscopy images showing the morphology of the crystals obtained directly from MOF **3** synthesis.

4.3.1.4 *Activation*

As described in Section 4.2.3, a four stage washing (solvent exchange) procedure was implemented for the attempted removal of DMF solvent from the pores of metal-organic framework **3**, in order to yield the active framework **3′** ([Zn4L(H2O)4$_n$). The PXRD patterns of the

crystalline material present after each stage of the washing procedure can be seen in Figure 4.12. The powder X-ray diffraction patterns were obtained with each of the crystals *in-situ*, immersed in the solution they were being washed with. This is true for all of the patterns other than the last, which shows the 'activated' MOF **3'** framework post solvent evacuation at room temperature, under dynamic vacuum.

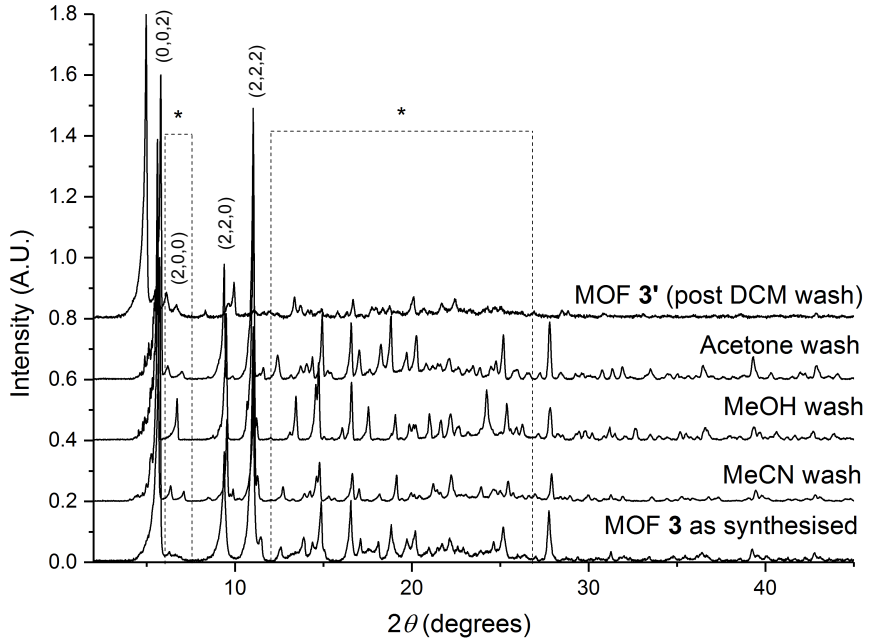

Figure 4.12: PXRD patterns of MOF **3** after each stage of the washing procedure implemented to generate active MOF **3'**. Boxes indicate areas in the PXRD pattern where discrepancies in peak positions arise between the different diffraction patterns.

As can be seen, the overall structure of this metal-organic framework remains intact during the implemented washing procedure owing to the retention of the main MOF peaks (at small 2θ values) in the PXRD pattern (labelled with their h,k,l values in Figure 4.12). However, it is observed there are discrepancies in the peak positions between each of the four washes (see boxes in Figure 4.12), and most noticeably for the activated material **3'**(which also demonstrates some peak splitting in the main MOF peak), indicating some alterations in the MOF's structure (potentially to a lower symmetry structure)

upon solvent exchange and removal. Further to this, the crystals of the metal-organic framework go from clear (MOF **3**) to a pale yellow (MOF **3′**) upon activation. This suggests again, that some structural perturbations are occurring upon activation. These results are not surprising as solvents in MOF pores often act as templating agents keeping the pores shaped, thus, exchanging and removing the solvent present in the cavities of the structure may alter these templating effects, thus, altering the shape of the pores [115] (Section 2.6.1.3). In addition, some of the peaks at higher 2θ angles are less defined, potentially indicating to some loss of local, short-range order upon activation. From PXRD data it is not clear whether the water molecules coordinated to the zinc metal centres in the MOF are being removed during this activation method to leave unsaturated metal sites (UMS, Section 4.1). This is due to the simulated PXRD patterns of the MOF with and without the bound waters being virtually identical (Appendix B).

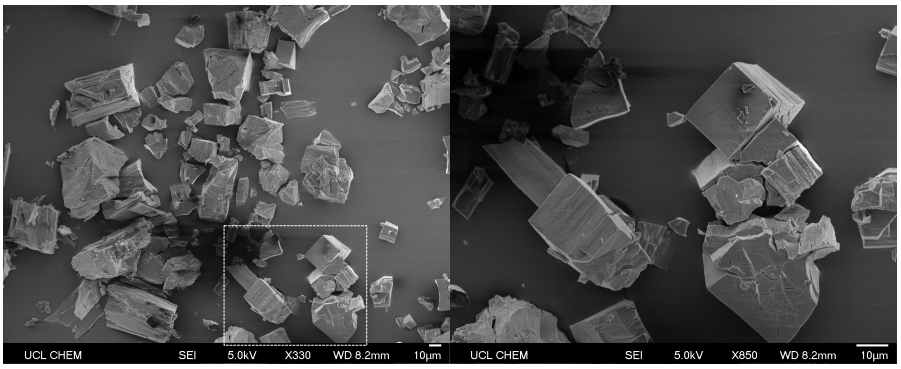

Figure 4.13: Scanning electron microscopy images showing the morphology of the crystals obtained after the activation of MOF **3′**. The image on the right is a zoomed in area of the box highlighted in the left hand image.

The morphology of the washed crystals can be seen in the SEM images of Figure 4.13. The crystals are shown to have been broken apart from the clumpy formation in which they were retrieved from the as-synthesised solution and some also appear cracked. Such crystal cracking is not a detriment to the application of this MOF as the

presence of additional crevices on the crystal surfaces could aid gas absorption and thus vapour-phase sensing.

4.3.1.5 *Flexibility investigation using powder X-ray diffraction*

As a result of the colour change observed and the discrepancies in PXRD peak positions of MOF **3′** upon activation, Le Bail fitting on the powder X-ray diffraction patterns was used to evaluate whether any breathing behaviour (flexibility) was demonstrated by this framework. Breathing (briefly mentioned in Section 2.6.1.1) is defined as transitions (reversible) of a metal-organic framework, where the displacement of atoms of the framework, yield a change in the unit cell volume of the structure ($V \neq 0$) [101]. Le Bail analysis§ was performed on the PXRD data of two as-synthesised MOF **3** samples (**3a** and **3b**) and their corresponding activated frameworks (**3a′** and **3b′**). The as synthesised **3b** sample was halved and two independent activation procedures were performed (**3b′(1)** and **3b′(2)**). The results of the Le Bail fitting are summarised in Table 4.4 which gives the unit cell lengths (*a*, *b* and *c*) and unit cell volume (V) for each sample as well as the agreements of fit from the software model (R_{wp}, R_{exp} and R_p).

Table 4.4: Results of PXRD Le Bail fitting on as-synthesised MOF **3** ($Zn_4L(H_2O)_4 \cdot(solvent)]_n$) and active MOF **3′** ($Zn_4L(H_2O)_4]_n$).

	Agreements of fit			Unit cell lengths			Unit cell volume
	R_{wp}	R_{exp}	R_p	*a* /Å	*b* /Å	*c* /Å	V /Å^3
3a	4.5	1.9	2.8	25.1(0)	28.2(0)	30.9(0)	21859(6)
3a′	2.8	2.1	2.1	25.1(0)	27.5(0)	31.0(0)	21456(10)
3b	8.8	2.1	4.9	25.0(0)	28.0(0)	31.2(0)	21886(24)
3b′(1)	2.9	2.0	2.2	24.9(0)	27.8(0)	31.1(0)	21520(8)
3b′(2)	2.1	1.9	1.6	24.9(0)	28.1(0)	31.2(0)	21782(9)

It can be seen that there is a decrease in the unit cell volumes between the as-synthesised (**3**) and activated (**3′**) samples, suggesting

§ Le Bail fitting analyses were conduced by Dr. Huw Marchbank, University College London.

some pore contraction of the framework post-activation. All of the samples however show differing extents of cell volume decrease, with sample **3b′(2)** yielding the smallest change. This indicates that the interactions between the MOF and the residual solvents present within its pores are complex and their removal does not yield uniform pore structures. In the case of **3b′(2)** it is possible that an ineffective washing procedure was implemented, with some solvent remaining in the pores of this MOF sample, thus rationalising its larger cell volume demonstrated in comparison to the other activated samples. The perturbations in the unit cell parameters show decreases in the *a* cell lengths for all activated samples with changes in the *b* and *c* cell lengths not conforming to a pattern; again, the changes observed are not uniform across all samples.

The results of this analysis suggest that that upon solvent removal breathing effects are existent, however the structural transformations that are occurring appear varied, this is most likely due to the effects of the surface tension and capillary forces that are present during solvent-exchange and evacuation [116]. Based on these results it is hypothesised that the removal of solvent molecules from the pores of MOF **3** yields a flexible **3′** framework that has the same overall topology as the as-synthesised parent framework but some disorder, defects and pore shrinking are present (Section 2.6.1.3), as illustrated in Figure 4.14.

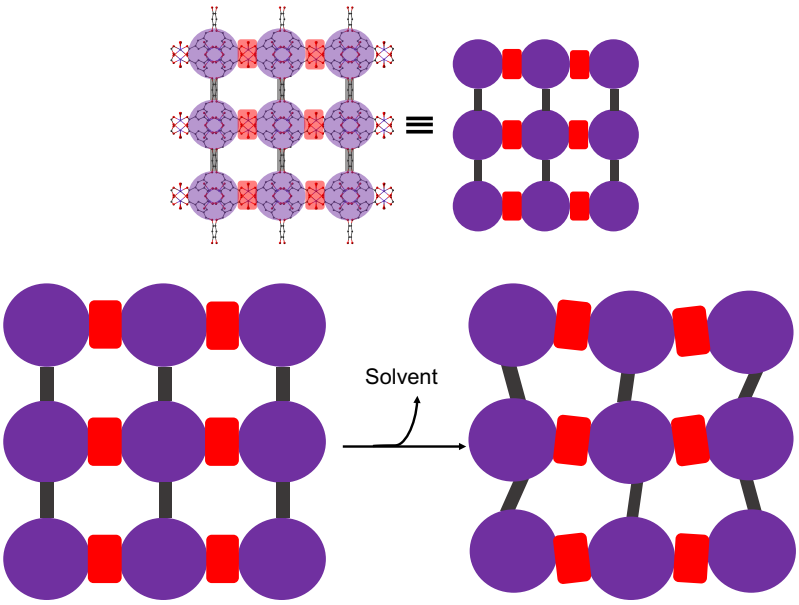

Figure 4.14: An illustration of the proposed nature of the structural alterations occurring in MOF **3′** ($Zn_4L(H_2O)_4]_n$) upon activation.

The powder X-ray diffraction pattern of Figure 4.12 corroborates this hypothesis, as such disorder of the activated framework would yield the loss of short-range order in its PXRD pattern (high angle 2θ). Such transformations upon activation are not uncommon, in-fact recent research has reported the significant interplay between flexibility, disorder and defects in metal-organic frameworks [114]. The presence of such disorder is also not necessarily detrimental to sensing applications [129, 189]. Additionally, the general observation of a large-pore to narrow-pore transition upon activation is common in many flexible MOFs [101, 129].

It is important to note that upon re-immersion of the crystals in solution the short-range order can be restored owing to the solvent molecules re-occupying the pores of the framework, again bringing uniformity to the structure. This is evidenced by Figure 4.15 which shows the PXRD patterns of a MOF **3′** sample as-synthesised, activated and after immersion in MeCN for one month (**3′-MeCN**).

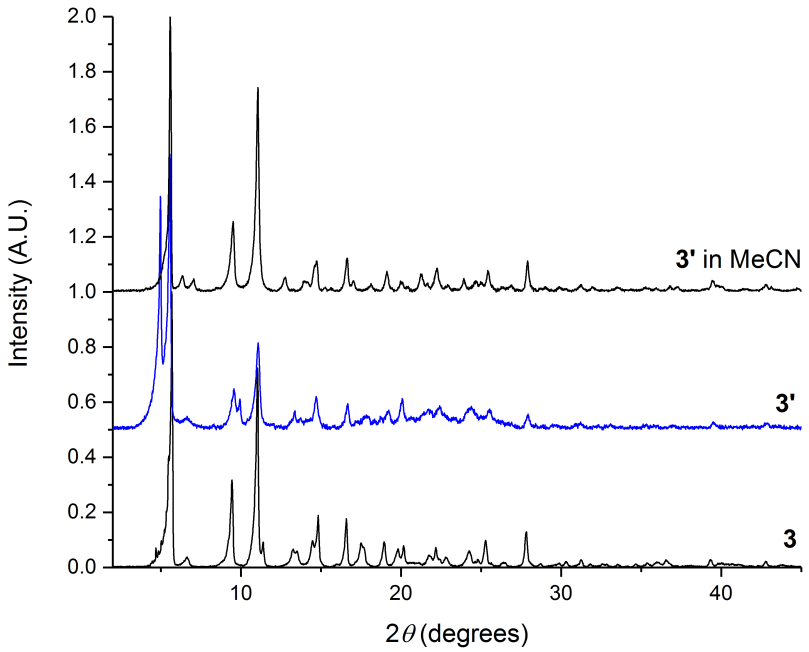

Figure 4.15: PXRD patterns showing the restoration of long-range order in MOF **3′** upon immersion in MeCN.

4.3.1.6 *Porosity of active MOF* **3′**

As discussed in Section 2.6.1.4, sorption and desorption isotherms allow for an evaluation of a MOF's porosity and the calculation of the apparent surface area of a MOF using Brunauer-Emmett-Teller (BET) theory. A standard Nitrogen (N_2) BET gas sorption at 77 K was attempted on active MOF **3′** but unfortunately the surface area was not able to be calculated owing to minimal adsorption of N_2 by the MOF in the typical BET region (0 - 40% P/P_0). However, as will be discussed (Figure 4.3.1.7), BET surface area measurements and sorption and desorption isotherms of the MOF using water as the probe gas were successfully obtained and were indicative of porosity within this MOF.

4.3.1.7 *Stability*

Metal-organic framework **3** was tested for its thermal and humidity stability. This is an important consideration if this MOF is to be used

as an explosives sensor in real-world scenarios where environmental conditions are frequently hot and humid.

Thermal stabilities

Thermogravimetric analysis (TGA) was used to test the thermal robustness of as-synthesised MOF **3** and the active structure **3′**. As can be seen in Figure 4.16 the as-synthesised MOF remains intact until approximately 430 °C and the active structure begins to decompose at around 400 °C.

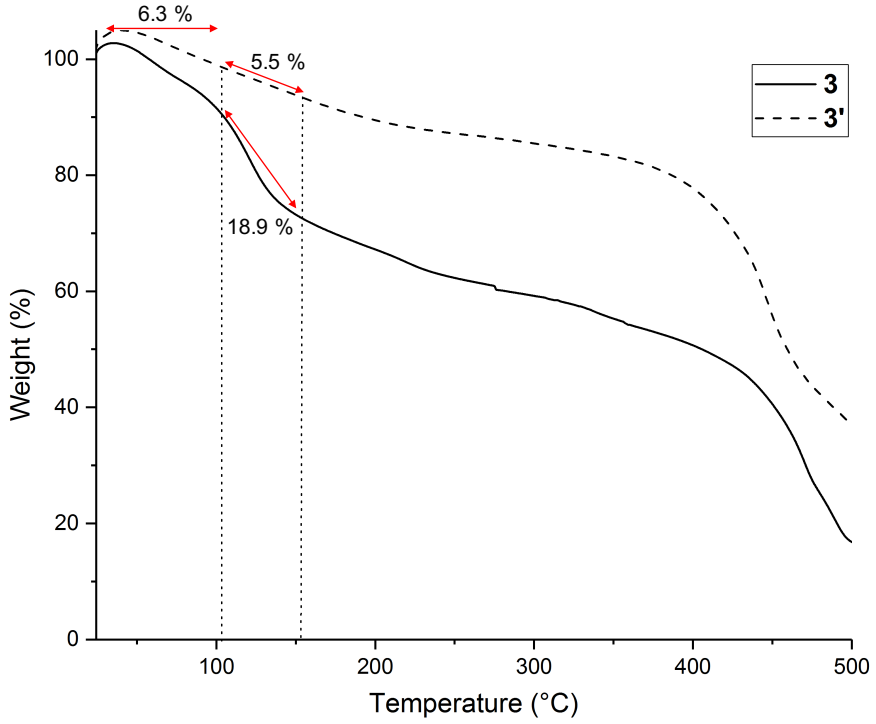

Figure 4.16: Graph illustrating the results of the thermogravimetic analysis of MOFs **3** and **3′**

In addition, the number of solvent molecules that are present in the pores of the as-synthesised MOF can be estimated from the TGA. As denoted in Figure 4.16, there is an 18.9% MOF **3** mass loss between 102 °C and 155 °C. As DMF has a boiling point in the region of 152 - 154 °C (and any water molecules present should have evaporated by 102 °C) the mass loss in this range can be ascribed to the loss of DMF

from the material. An 18.9% mass loss equates to 223.3 g mol^{-1}, this can be attributed to three DMF molecules per $Zn_4L(H_2O)_4 \cdot (solvent)]_n$, which is the MOF empirical formula (this is based on the total mass of the MOF empirical formula being 1181.52 g mol^{-1} and the relative molecular mass of one DMF being 73.1 g mol^{-1}). This corresponds to 1.5 DMFs per asymmetric unit (ASU) and 48 DMFs present within each unit cell. Such findings are an underestimation of those calculated from the single crystal X-ray diffraction data (Section 4.3.1.2) which suggest that 3 DMF molecules are present per ASU, which corresponds to 6 DMF per empirical formulae and thus 96 DMF molecules per MOF unit cell. This helps to rationalise why disorder is evident in the solvent molecules during single crystal structure refinement as each DMF is likely to only be present with a 50% occupancy per ASU.

Structural information about the active MOF **3'** can also be obtained from thermogravimetric analysis. As can be seen, there is a 6.3% MOF **3'** mass loss observed between the start of the experiment (25 °C) and 102 °C. This equates to 74.6 g mol^{-1} and can potentially be attributed to four water molecules per empirical formula unit of the active MOF (Zn4L(H2O)4). This suggests that the zinc-bound water molecules are not removed using the activation procedure implemented. Further to this, there is a 5.5% mass loss observed in the DMF region for active MOF **3'**, indicating that not all solvent molecules have been removed from the pores of the MOF during activation (0.8 DMF molecules per emperical unit remain).

Humidity and water stability

The stability of a MOF towards water is crucial for its consideration as an explosives sensor, particularly for vapour-phase detection. In order to determine which degree of water stability is exhibited by

MOF **3′**, the framework was exposed to three different levels of water 'harshness' conditions; by immersion of the MOF in liquid water, by exposure to ambient air and through dynamic vapour sorption experiments. As discussed (Section 2.6.1.5), PXRD and BET measurements are used to characterize the water stability of MOFs. Both of these methods were used to evaluate the stability of **3′** towards the above-mentioned levels of water exposure. The results of which were used to classify this MOF's stability using the methods proposed by Burtch *et al.* [122] and Shimizu *et al.* [123] as outlined in Section 2.6.1.5.

Powder X-ray diffraction confirmed that metal-organic framework **3′** does not retain its structure when it's crystals are immersed in deionised water for 24 hours. Whilst some peaks in the PXRD pattern (Appendix B) were still distinguishable, these more closely resemble those of the free linker H_8L as opposed to the MOF material, suggesting complete structural collapse. BET measurements were therefore not attempted. Based on these results it can be concluded that MOF **3′** does not have high 'thermodynamic stability' with respect to water as classified by Burtch *et al.* [122].

The PXRD patterns of **3′** pre- and post- exposure to ambient laboratory air conditions (approximately 21 °C[¶]) are given in Figure 4.17.

¶ The relative humidity exposure is unknown. Whilst the average RH for London in May 2016 (during when these experiments were taken) was between 50-80%, the experiments were performed in a heated and well ventilated laboratory, thus, these humidity values are not representative of the air conditions to which the MOF was exposed.

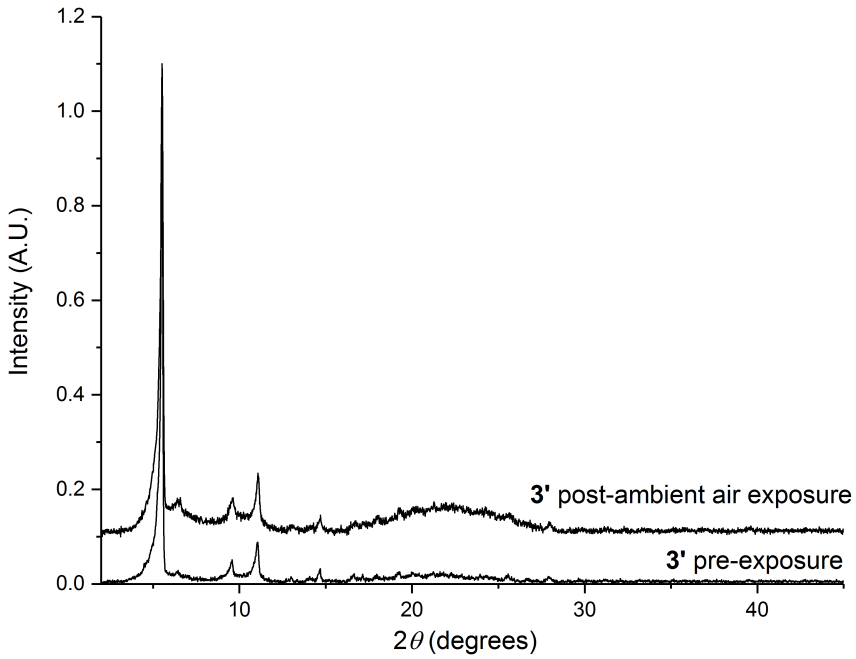

Figure 4.17: PXRD patterns of MOF **3′** pre and post- exposure to ambient air conditions.

The PXRD patterns of both the exposed and un-exposed samples are in good accordance. There is evidence of some loss of local short-range order indicated by the presence of a slight hump in the 2θ region between 20 and 25 degrees. This could be attributed to some structural pore collapse, the uneven inclusion of water vapour into the pores of the MOF causing disorder or the surface hydrolysis of the material yielding some surface amorphicity. As PXRD measurements alone do not yield information about the retention of porosity, BET measurements are required to elucidate as to whether there is structural collapse. Whilst a number of groups have exposed their MOF materials to ambient conditions in this way and subsequently calculated N_2 BET sorption isotherms on the exposed samples, this simplistic method of exposing a MOF to humidity has a major weakness, and that is the absolute control of the relative humidity (RH) present in the air. As RH is calculated based on the external temperature and pressure to produce the concentration of water vapour in

the air, it is highly dependent on local conditions. For example, a well ventilated room that is held at approximately 21°C can have a relative humidity in the range of 20-60% [123]. Therefore, in order to calculate the BET surface area of MOF **3′** after water vapour exposure a more sophisticated and relatively novel technique; dynamic vapour sorption was used.

Dynamic vapour sorption (DVS) is a gravimetric technique that measures how quickly and how much of a sorbate is sorbed (adsorbed and absorbed) by a sample. This is achieved by varying the concentration of sorbate vapours surrounding the sample and measuring the change in mass that this produces as a function of time. DVS allows for BET surface areas to be calculated using water as the probing gas (H_2O BET).

Six different synthetic batches of MOF **3′** were combined and samples were taken from this amalgamated batch during DVS experiments[11]. This was done in order to minimise discrepancies in sorption that may occur as a result of the slight variations in crystallite size between synthetic batches. Prior to exposing a sample to the different RPs (for definition see Section 4.2.4.3) of water (RHs) an *in-situ* degassing procedure was implemented. The samples were heated under high vacuum for two hours at 25 °C followed by 150 °C for a further two hours. This was performed in order to remove any solvent present in the pores of this framework. A MOF crystal colour change from yellow to a very dark brown was observed and indicated that a structural change occurred during degassing. It is hypothesised that this is most likely due to the removal of zinc-coordinated water ligands in the framework and so the dehydration of the MOF. This dehydrated form of the MOF is termed **3″**. This is rationalised due to the similar observations noted for HKUST-1 (the prototypical MOF and isoreticular framework to **3** as described in Section 4.1), which

11 The PXRD patterns of these six synthetic batches can be found in Appendix B

changes colour from pale blue to a very dark blue upon desolvation at 150 °C (not under high vacuum) [190] and to a very dark violet post high vacuum evacuation at room temperature, these colour changes were ascribed to the MOF becoming fully dehydrated [120]. This type of high temperature desolvation does lead to a loss of crystallinity of MOF **3″** as evidenced by the broadening of the peaks in Figure 4.18.

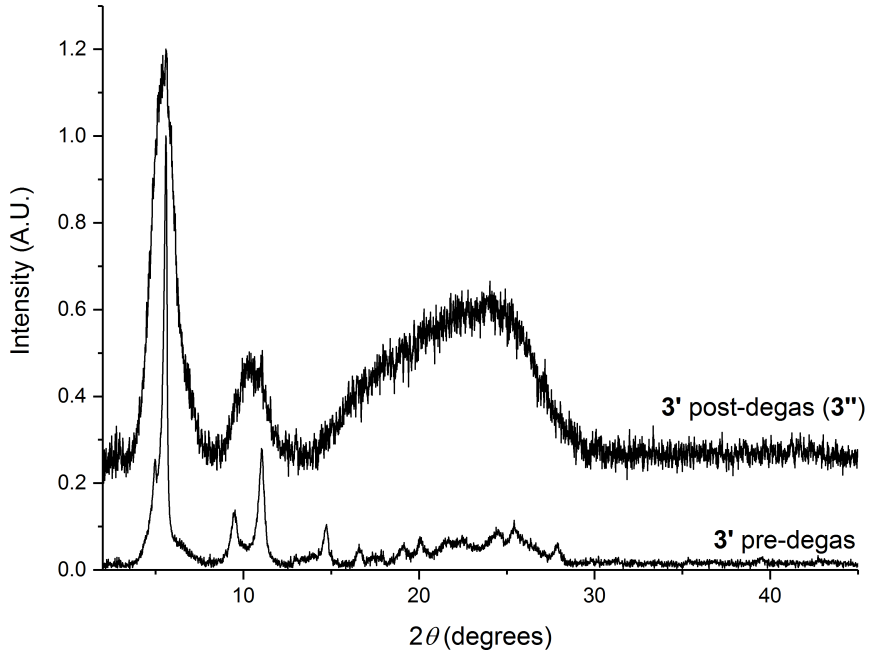

Figure 4.18: PXRD pattern of MOF **3′** pre- and post-degassing to afford MOF **3″**.

Such results are not surprising and are frequently observed [116]. It is suggested that the harsh conditions create disorder in the MOF system as well as some potential pore collapse/shrinking owing to the rapid removal of the zinc bound water ligands. However, owing to the retention of the low angle 2θ it is believe the overall framework structure remains intact.

MOF **3‴** was exposed to incremental, known concentrations (relative pressures, RP, P/P_o) of water, and the mass of the sample was monitored as a function of time. The mass was allowed to reach gravimetric equilibrium at each relative pressure (RP, P/P_o) and so the vapour sorption isotherms express the equilibrium amount of vapour sorbed as a function of steady state relative pressure (at a constant temperature). DVS experiments were completed at different temperatures and H_2O BET surface areas of the MOF were calculated at each of these.

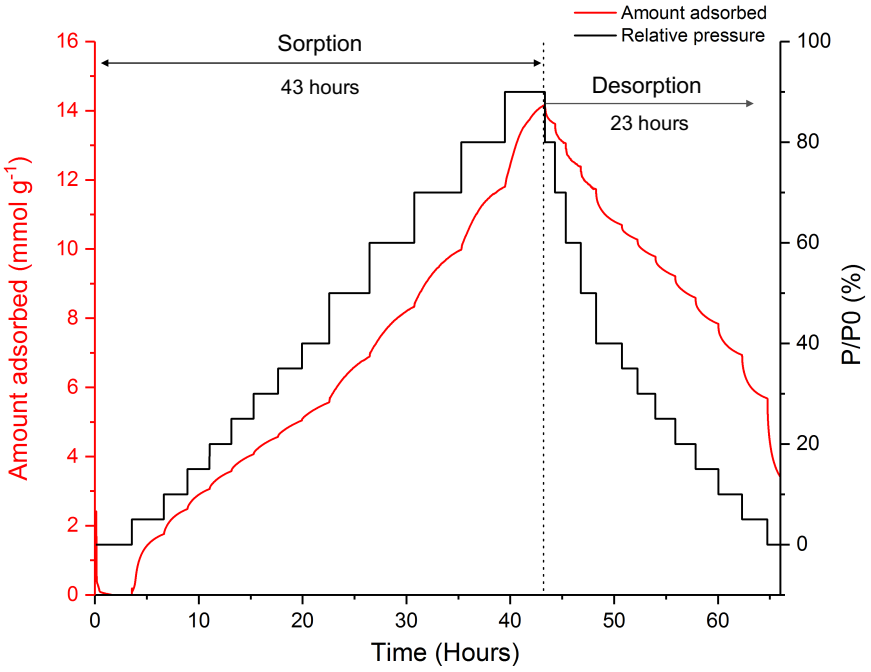

Figure 4.19: Graph illustrating the dynamic vapour uptake of MOF **3″** at 25 °C upon exposure to 0-90% relative pressure of water vapour as a function of time.

Figure 4.19 shows the dynamic water vapour uptake of MOF **3″** at 25 °C when exposed to relative pressures of water ranging from 0-90 %, as a function of time. The graph indicates that it takes a significantly longer time for the sorption of water vapours to reach equilibrium than it does for desorption at the same relative pressures (43 hours and 23 hours respectively). This suggest that whilst the MOF is sorbing water, the interactions between the water molecules and the

framework are weak, owing to their quicker release. This contradicts the findings discovered when the same DVS technique was used to evaluate the water sorption and humidty stability of HKUST-1. It was reported that interactions with this MOF were strong as the desorption process took much longer than sorption (53 hours and 37 hours respectively)[120].

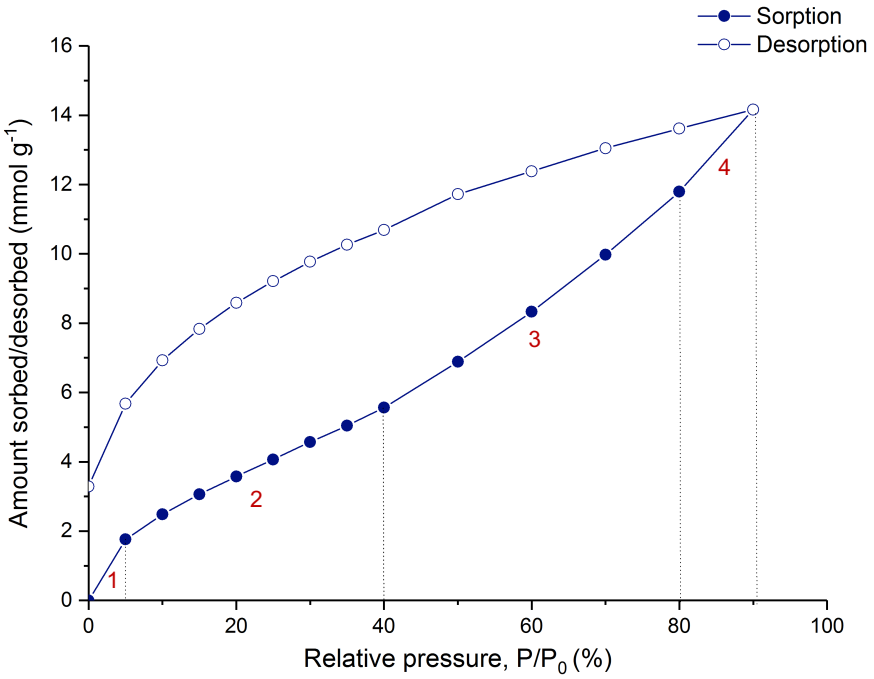

Figure 4.20: MOF **3″** water vapour sorption and desorption isotherms at 25 °C. The numerical labels 1-4 refer to different portions of the isotherm, discussed in detail in the main text.

The water vapour sorption and desorption isotherms for MOF **3″** at 25 °C are given in Figure 4.20. There are four distinct sections to the sorption isotherm which are marked on the graph. The initial sharp increase in the uptake of water vapour (region 1 on the slope, 0 - 5 P/P_0) is rationalised based on the favourable re-coordination of the axially bound water molecules to the zinc metal sites in the MOF. This is suggested based on similar observations made upon the reintroduction of water vapour into the completely dehydrated HKUST-1 MOF structure [120]. These results strengthen the hypothesis that the colour change observed after the degassing of MOF **3′** is a result of

the dehydration of the framework. Section two of the isotherm shows a steadier increase in the soprtion of water. This could be the result of the initial monolayer filling of the large pore located within the MOF. This is followed by the multilayer sorption of water in section 3. However, the fact that there is no obvious step in the isotherm between sections 2 and 3 suggests that there is a degree of overlap between monolayer and multilayer formation [122]. The slightly steeper uptake at the very end of the isotherm, stage 4, is ascribed to the inclusion of water vapour into the secondary and much smaller micropores (pores with widths less than 10 Å or 1 nm) of the framework [120].

The water sorption and desorption isotherms of metal-organic framework **3″** do not conform to any of the IUPAC classical isotherm classifications [121] (Section 2.6.1). The sorption isotherm most closely resembles that of type II, however, the material is neither macroporous (pore sizes > 500 Å) nor as will be ensuingly discussed, nonporous. Additionally, the desorption isotherm and the associated hysteresis are not akin to any of the classically described isotherms. As discussed in Section 2.6.1, it is not uncommon for MOFs to display unusual hybrids of isotherm types, with the most varied shapes being demonstrated by flexible metal-organic frameworks. Thus, rationalising the non-conformity of the MOF **3″** isotherm and further corroborating the flexible nature of this MOF. Similar findings of a non-classical, type II-resembling sorption isotherm were reported for HKUST-1 (Figure 4.21) which is not surprising considering it is isoreticular to MOF **3″** and also shows breathability. A final point to note is the non-closing hysteresis of the isotherms, this is again attributed to the re-coordination of water molecules to zinc metal centres.

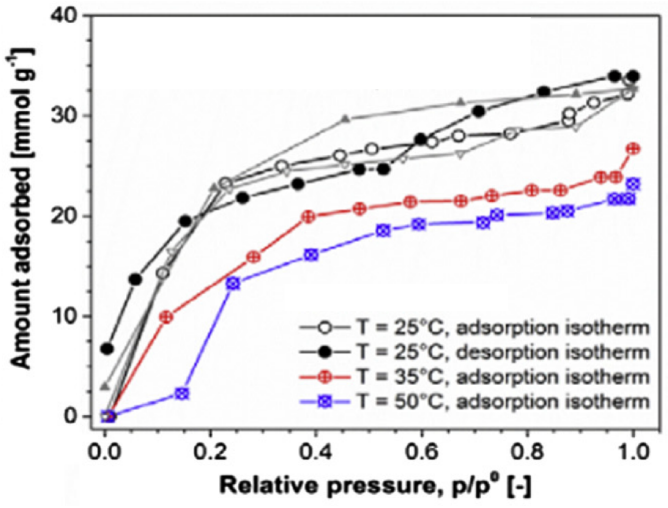

Figure 4.21: The water soprtion and desorption isotherms of metal-organic framework HKUST-1 at 25 °C (up to 90% RH) 35 °C (up to 90% RH) and 50 °C (up to 70% RH) obtained using DVS in collaboration with Surface Measurement Systems Ltd ©. A comparison of another literature reported water sorption isotherm for the same MOF is also given as denoted by the isotherms in grey (traingles). Reprinted from [120] with permission from Elsevier.

A comparison** between the sorption isotherms of MOF **3″** (Figure 4.20) and HKUST-1 (Figure 4.21) suggest **3″** to be less hydrophilic; not only does it demonstrate lower loadings in the low pressure region of its sorption isotherm (0-20 % P/P_o), it also uptakes less absolute loadings of water at 90% P/P_o ($\approx$ 14 mmol g^{-1} *vs.* $\approx$ 35 mmol g^{-1}) despite having a theoretically larger pore volume (as discussed in Section 4.1). A consideration of hydrophilicity is important for a material which is to be used for in-field vapour detection as it is imperative that the material is both stable to water but also does not just absorb water and not the analyte of sensing interest. Therefore implying that metal-organic framework **3″** which has a lower affinity towards water, is potentially better suited for vapour phase sensing applications in real-world scenarios than commercially available HKUST-1.

** These isotherms are comparable as they were generated using the same DVS analyser and by the same collaborators (Surface Measurement Systems Ltd.).

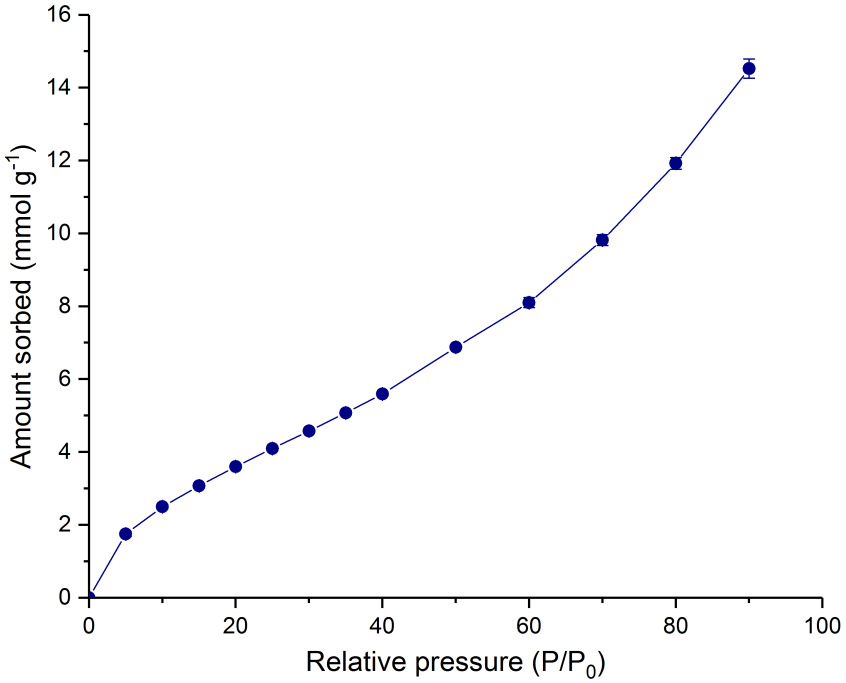

Figure 4.22: Graph illustrating the averaged results of three repeated water sorption isotherms of MOF **3″**. The error bars represent one standard error of the mean.

Figure 4.22 shows the averaged results of three repeat experiments of water sorption on MOF **3″** using two different samples from the amalgamated MOF **3′** batch (at 25 °C). The water sorption on the first sample was repeated immediately after the initial sorption was complete. As is evident, the repeats are in excellent agreement, confirming that the MOF retains its structure and porosity after the exposure (and repeat exposure) to 90% relative humidity (at 25 °C).

Water uptake in **3″** was also measured at different temperatures (25, 40, 50 and 60 °C) to investigate whether the sorption behaviour of the MOF changes. These four different sorptions were performed in succession on the same MOF **3″** sample. A comparison of the isotherms is given in Figure 4.23.

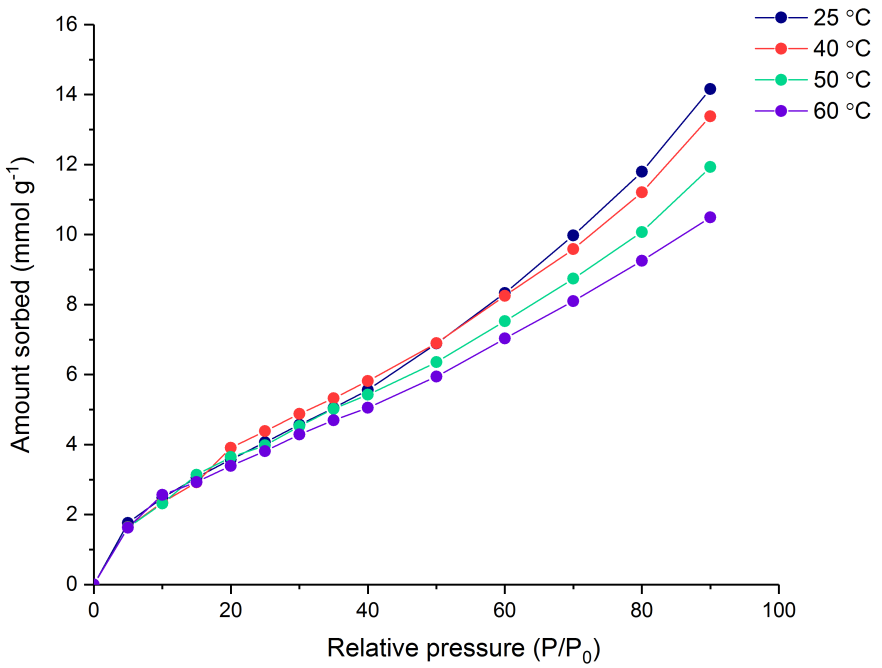

Figure 4.23: Graph comparing the water sorption isotherms of MOF **3″** obtained at different temperatures.

The water vapour soprtion capacity of MOF **3″** diminishes slightly with increasing temperatures between 25 °C - 60 °C. This can be attributed to the gradual degradation of the MOF, and is reflected in the PXRD spectrum of the resultant material from the temperature studies which demonstrates a very broad spectrum indicative of amorphization due to partial degradation (Appendix B). This partial degradation can be attributed to the aggregation of adsorbed water molecules near the zinc metal sites eventually displacing the carboxylate groups of the ligands [120]. Whilst Figure 4.23 indicates that a certain amount of porosity is still retained by the structure it does not give a quantitative amount. Thus, Brunaer Emmett-Teller BET surface areas were calculated (as per the equations detailed in Section 2.6.1.4) for each of the vapour sorption experiments discussed above and can be found in Table 4.5.

Table 4.5: MOF **3′** BET surface area values as obtained from water sorption experiments

Experiment	BET S.A. / $m^2\,g^{-1}$
Sample 1 at 25°C	378
Sample 1 at 25°C repeat	391
Sample 2 at 25°C	380
Sample 2 at 40°C	419
Sample 2 at 50°C	384
Sample 2 at 60°C	352

The BET H_2O surface areas obtained from water sorption experiments are lower than expected. Eddaoudi *et al.* reported a Langmuir surface area for isoreticular MOF $[Cu_4L(H_2O)_4\cdot(solvent)]_n$ to be 2896 $m^2\ g^{-1}$ [176]. Whilst this surface area was calculated using an isotherm produced by exposing the MOF to argon (a much smaller probing gas than H_2O) and at low temperatures, the values reported above are still much lower than expected. This is potentially rationalised based upon the degassing procedure leading to a significant shrinking of the MOF pore upon dehydration. It is unclear based on these results whether a higher porosity could be obtained using a different probing gas and different collection conditions (i.e. at lower temperatures). Further to this Langmuir isotherm calculations are often known to over exaggerate MOF surface areas [111]. However, these experiments were conducted in order to probe the stability of the material and it is evident that the porosity of the degassed framework is retained upon humidity exposure at 25°C and the results are repeatable intra- and inter-sample. Although the porosity is observed to diminish at higher temperatures of water vapour exposure, there is only a 7.4 % loss in porosity observed between the sample initially being exposed to water at 25°C and the final 60°C exposure.

Therefore, under these 'harsh humid conditions' (as outlined in Section 2.6.1.5) MOF **3″** can be said to have a 5B grading for water

stability as classified by Shimizu *et al.* [123], as under 'harsh humid conditions' it retains some porosity but has loss of order. Further, taking all of the humidity tests into account, it can be concluded that MOF **3'** shows 'kinetic stability' towards water, meaning that it is stable to humid conditions but decomposes after short times in liquid water. This is based on the classifications outlined by Burtch *et al.* [122].

4.3.2 *Solution-phase sensing*

As aforementioned (Section 2.6.4.2), the sensing of explosives with metal-organic frameworks in the solution-phase is beneficial as it allows for the facile quantitative analysis of the MOF responses towards real explosive substances. This can help eludicate the efficiency and mechanism of sensing, the sensitivity of the system and it allows performance comparisons to be made with other solution-phase MOF explosives sensors. In addition, a solution-phase sensing system could have the potential to be used as an initial, rapid and cheap diagnostic tool for the infield detection of explosive particles on a surface, prior to their identification using analytical equipment such as liquid chromatography - mass spectrometry (LC-MS). Metal-organic framework **3'** was investigated as a solution-phase sensor for the detection of known quantities of the explosive substances Tetryl, TNT, RDX, PETN and the TNT derivative 2,4-DNT (Figure 4.24).

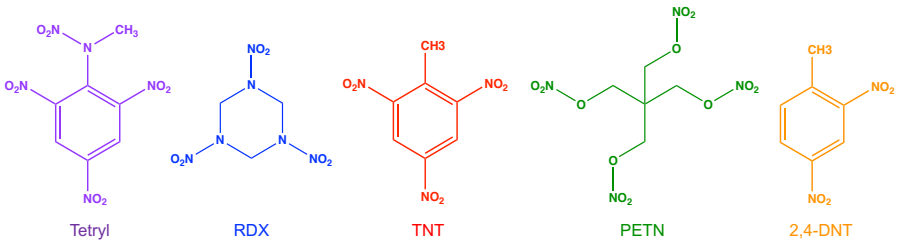

Figure 4.24: Explosive substances and related compounds used in MOF **3'** solution-phase sensing.

4.3.2.1 *Fluorescence characteristics*

Suspensions of MOF **3′** in acetonitrile (MeCN) were used for all solution-phase sensing experiments. Acetonitrile was chosen owing to the stability of the MOF in this solvent, as demonstrated in Figure 4.12, and due to the relative stability of the commercially purchased explosive standards in this medium[††].

The excitation spectrum of the MOF **3′** suspension in MeCN indicated this framework to give strongest emission at an excitation wavelength ($\lambda_{ex.}$) of 315 nm (Figure 4.25), therefore, all sensing experiments were conducted at this wavelength.

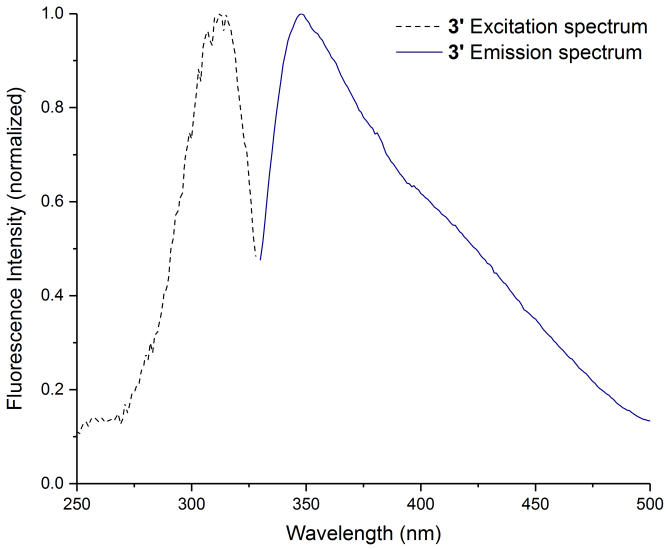

Figure 4.25: Overlay of the fluorescence excitation ($\lambda_{em.350nm}$) and emission ($\lambda_{ex.315nm}$) spectra of MOF **3′** suspended in MeCN.

The fluorescence emission maximum of MOF **3′** in MeCN ($\lambda_{em.}$) was observed to be at 348 nm, whereas that of the linker H_8L (dissolved in DMF) occurred at 335 nm ($\lambda_{ex.}$ 315 nm), as can be seen in Figure 4.26. This observed red-shift in the emission spectrum of the MOF with respect to the free linker and the broadening of the MOF emission peak in comparison to the ligand is very frequently

†† Commercially purchased explosives solution standards are produced from the dilution of 1000 µg of an explosive in a 50:50 mix of MeCN and MeOH. These standards do degrade over time, thus all explosive solutions were kept refrigerated at 4°C and discarded after one-month of opening.

observed when organic ligands are incorporated into MOF structures. Such observations are usually ascribed to the electronic coupling of the neighbouring organic ligands in the framework through the metal ions [144].

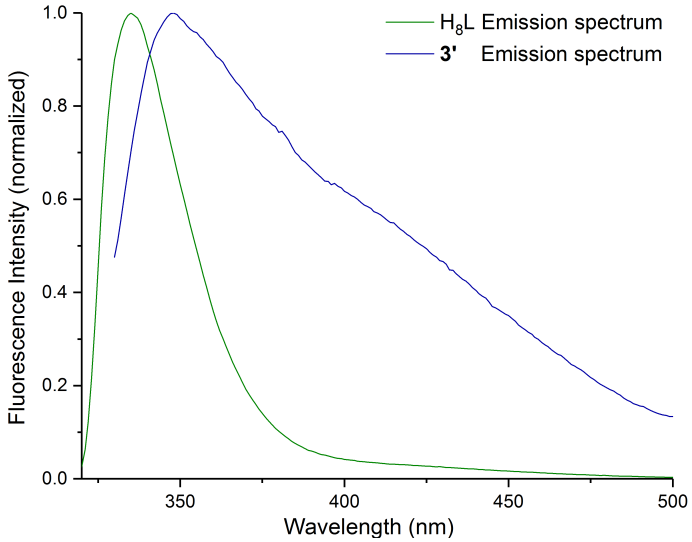

Figure 4.26: Overlay of the fluorescence emission spectra of MOF **3′** suspended in MeCN and that of the Linker H_8L (dissolved in DMF).

4.3.2.2 *Experimental validity testing and variability mitigation*

The effect of particle settling and the implementation of a vortex procedure

As solution-sensing experiments used MOF **3′** suspensions, a study was performed to investigate whether any of the MOF particles were settling out of suspension (as a result of gravity) during sensing. This is an important consideration, as MOFs settling out of suspension cause an attenuation of the system's fluorescence, thus creating ambiguity during sensing whether the fluorescence quenching of a suspension is artifact due to settling or true MOF-analyte interactions.

The study involved measuring the fluorescence emission of a MOF **3′** suspension left under constant illumination ($\lambda_{ex.}$ 315 nm) in the fluoremeter every 60 seconds, from 0 - 240 s. The results of this study are given in Figure 4.27.

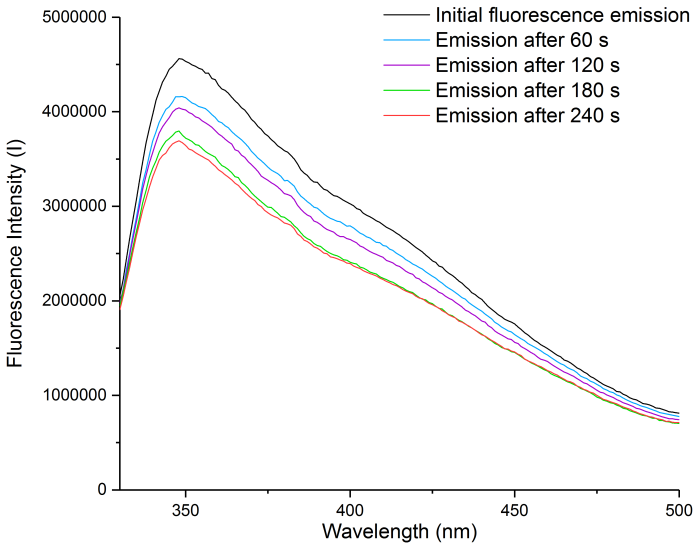

Figure 4.27: Graph illustrating the effects of particle settling in MOF **3′** MeCN suspensions. Fluorescence emission spectra were obtained at 60 s time intervals starting from t = 0 (initial fluorescence emission) to t = 240 s.

It is evident that the settling of MOF **3′** out of the MeCN suspension does occur over the specified timeframe and it does result in the loss of fluorescence intensity, which poses a problem to the validity of sensing in the solution phase. This effect, or measures to prevent such effects, have seldom been reported in MOF explosives sensing literature.

In an attempt to eradicate this effect, a vortexing procedure was implemented (Section 4.2.5.3). The MOF suspensions were subjected to 15 s of mild agitation using a vortexer operating at 400 rpm prior to each fluorescence emission reading. As can be seen in Figure 4.28, with the implementation of this vortexing procedure, repeatable fluorescence emission intensities of MOF **3′** in suspension were obtained. Prior to any sensing experiment, settling and stable-baseline checks were implemented. If a sample did not achieve a stable baseline through vortexing, it would not be used in sensing. In addition, using this step in between each reading during the sensing titrations allowed for a greater degree of certainty that any fluorescence quenching demon-

strated through the addition of explosive analytes to the MOF were as a result of MOF-analyte interactions.

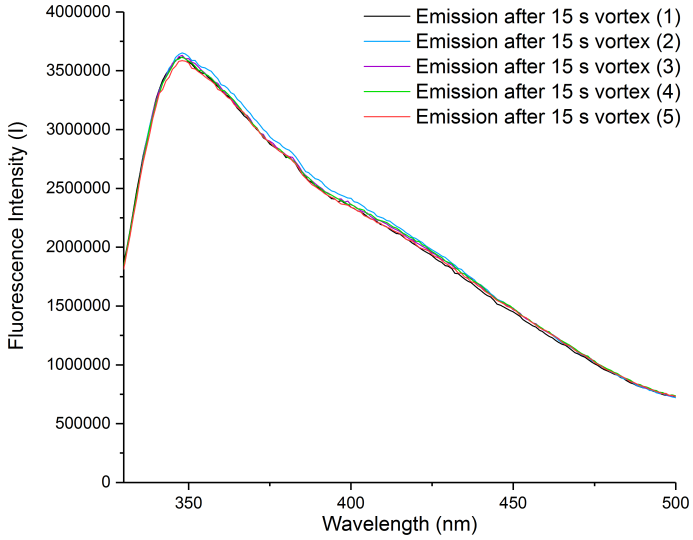

Figure 4.28: Graph demonstrating how the implementation of a vortexing step can yield a stable baseline of the fluorescence emission intensity of MOF **3′** in suspension. Prior to each fluorescence emission reading, the MOF suspension was mildly agitated using a vortexer for 15 s.

MOF sensor concentration in suspension consistency

Another important factor to consider with regard to the validity of this experimental set up is the absolute amount of MOF material that is present within each tested suspension. Whilst the quenching responses calculated for each analyte are relative to the initial fluorescence intensity of a particular suspension sample, the amount of MOF material available to interact with the concentration of analyte added will affect the results obtained. Therefore, suspensions were always generated with the same amount of material and ultrasonicated for the same amount of time. It was observed that a 6 mg sample of finely ground MOF **3′** ultrasonicated for 2 hours gave the most stable suspensions (least amount of settling) and the initial fluorescence intensities (after the implemented settling and vortexing steps mentioned above) would always be between 3.5 - 4.5 million counts. If the count number of a **3′** suspension fell above or below this value,

it would be discarded. In an attempt to mitigate some of the discrepancies in the absolute amount of MOF particles in suspension, each sensing experiment for each analyte was repeated 5 times.

Dilution effects

When sensing in the solution-phase an additional factor that must be acknowledged is that of dilution. The 1 mM explosives stock solutions used for analyte sensing are produced through the further dilution of explosives standards using MeCN (Section 4.2.5.2). Consequently, the effect of adding MeCN to the sensing suspension must be evaluated to make sure that it is not the addition of this analyte (and therefore dilution) that is causing the quenching of the system.

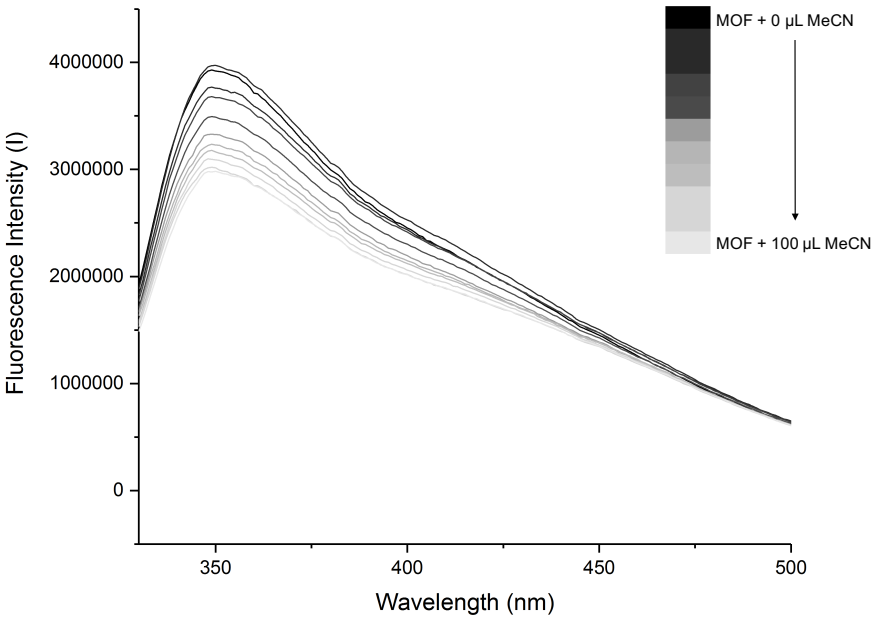

Figure 4.29: The effect of MeCN additions on the fluorescence emission intensity of MOF **3′** in an MeCN suspension.

Figure 4.29 shows how the addition of 10 µL aliquots of acetonitrile (MeCN) does have an effect on the fluorescence intensity of the MOF in suspension, causing some quenching of the system. These effects therefore need to be considered when titrating the explosive substances against MOF **3′**. To date, since the start of the MOF explo-

sive sensors field, there appear to be no reports that explicitly claim to have acknowledged the effects of dilution when expressing a MOF sensors response to a particular analyte. In some instances it can be argued that claimed responses are simply dilution efffects.

4.3.2.3 *Solution-phase sensing using known concentrations of explosives*

Metal-organic framework **3′** (as a suspension in MeCN) was tested for its fluorescence-based sensing responses upon the addition of 1 mM concentrations of the explosives TNT, Tetryl, RDX, PETN and the TNT derivative 2,4-DNT. As detailed in Section 4.2.5.3, prior to the addition of the analyte to the MOF suspension, a steady initial fluorescence intensity baseline was obtained through implementation of three cycles of 15 s agitation of the MOF suspension using a vortexer. After this baseline was achieved, 10 μL of a 1mM solution of a particular analyte was added to the MOF in suspension in an incremental fashion until 100 μL of the explosive (or derivative) was added. After the addition of each 10 μL aliquot of analyte, the vortexing step was repeated three times to ensure no settling of the MOF, generating three fluorescence emissions for each addition of an analyte. The three fluorescence intensities for each addition were averaged and a plot of the responses generated; Figure 4.30 gives the fluorescence emission spectrum of MOF **3′** upon the incremental addition of 1mM Tetryl aliquots, the graph gives the averaged fluorescence response plot as well as some of the raw fluorescence data.

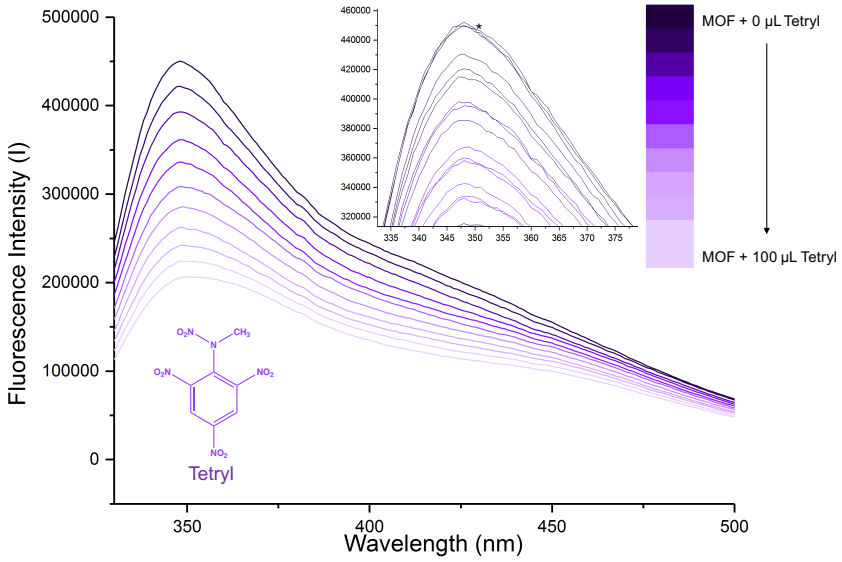

Figure 4.30: Fluorescence emission spectrum of MOF **3′** upon the incremental addition (0 - 100 µL) of 10 µL of a 1 mM solution of the explosive Tetryl. Inset: shows the raw data for each of the fluorescence emission repeats for the first four 10 µL additions (0 - 40 µL) to the average initial fluorescence intensity baseline (I_0 denoted by the asterisk in the graph). This graph has not been corrected for dilution.

As can be seen, MOF **3′** responds effectively to the explosive Tetryl. The averaged fluorescence emission graph shows clear distinctions between each of the added aliquots of Tetryl to the suspension of **3′**. From the inset it can be seen that the initial baseline reading for the experiment is very stable (as denoted by the asterisk in Figure 4.30), and this is representative of all experiments. There are some observed variations in the emission intensities between the measurements taken within an aliquot addition. This could be attributed to the time that it takes for the explosive to diffuse through the solution. The perturbations of the graph shape, namely the broadening and shifting of the peak, at higher Tetryl concentrations suggests that exciplexes between the MOF and the explosive are formed (Section 2.6.2). Spectral shifts are most frequently observed for flexible MOF structures (as discussed in Figure 2.6.4.1), thus, these findings strengthen the hypothesis that MOF **3′** demonstrates framework flexibility. These flu-

orescence emission spectral shifts of MOF **3′** are not observed upon the addition of the other four analytes, Figure 4.31.

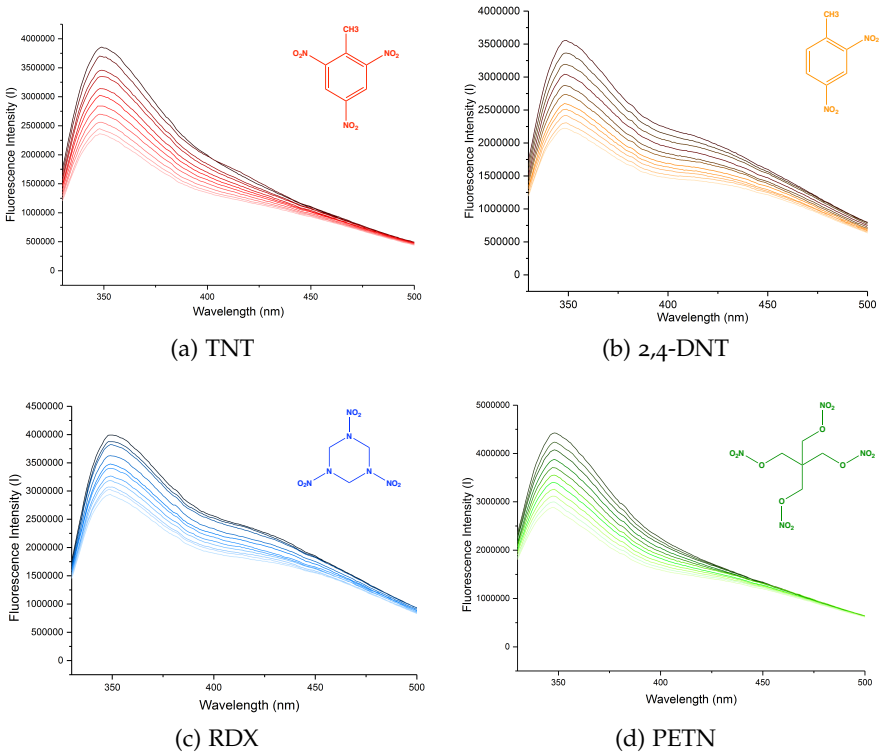

Figure 4.31: Fluorescence emission spectra for MOF **3′** upon the addition of 1mM solutions of TNT, 2,4-DNT, RDX and PETN. The graphs illustrate the averaged graphs for 0 - 100 µL additions. These graphs have not been corrected for dilution.

Magnitudes of quenching

A plot of the quenching percentages (QPs, as calculated using Equation 2.14) of MOF **3′** observed when exposed to each analyte addition can be seen in Figure 4.32. Included in this graph are also the baseline MeCN solvent quenching percentages. The QPs shown are averages of five titration experiments, each completed on different suspension samples, all from different MOF **3′** synthetic batches and have been titrated against at least two independently made 1 mM explosives stock solutions. The error bars (representing one standard error of the mean) of these quenching percentages are expressed by the coloured bands either side of the mean QP values.

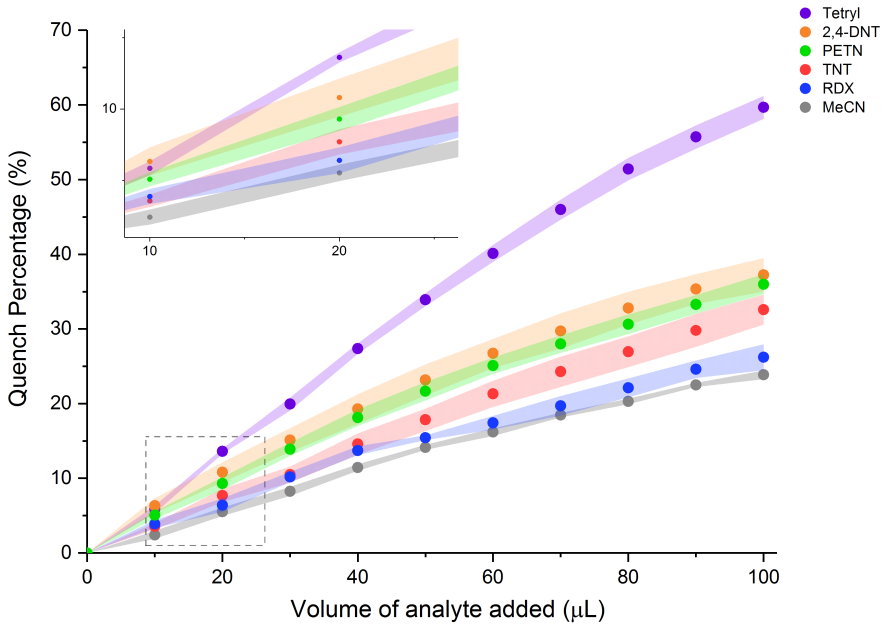

Figure 4.32: Graph denoting the average fluorescence quenching percentages obtained from the addition of Tetryl, TNT, 2,4-DNT, RDX and PETN to MOF **3′** (depicted as circular points on the graph). The coloured bands denote the error bars (one standard error of the mean) that are present for each of the quench percentages. Included in this graph are the quenching percentages obtained from MeCN dilution experiments. The inset of the graph shows a zoomed in region of the graph, focussing on the first two analyte additions.

The order of the greatest quenching of the MOF by the analytes follows Tetryl >> 2,4-DNT > PETN > TNT > RDX with quench percentages at 100 μL of 59.7 %, 37.2 %, 36 %, 32.6 % and 26.2 % respectively. Tetryl is observed to show significantly higher quenching responses in comparison to the other analytes. The quench percentages of 2,4-DNT and PETN are very similar. This is reflected by the overlap in their QP error bars at certain points, suggesting that the two analytes yield similar responses by **3′**. This means that it would be difficult to differentiate which of these compounds were present in an unknown solution, if the same amount of the analytes were added and the quenching results compared (these issues of analyte differentiation will be discussed in greater depth in Chapter 5). Further to this, there is considerable overlap in the QP error bars of explosive RDX and MeCN at certain analyte additions, most notably 20 μL (as

evidence by the inset of Figure 4.32) and 70 μL aliquot additions. This suggests that at these points there is no significant difference between this explosive and the dilution effects yielding a quench response of **3′**.

The molar concentrations of the explosives present in the suspension system after each 10 μL 1 mM explosive solution addition are given in Table 4.6. The table also expresses each concentration in ng/μL (weight/volume) units, which is also the same as the unit of parts per million (ppm). These conversions allow for a facile comparison with other MOF sensing and explosive detection techniques.

Table 4.6: Analyte concentration conversion table

Volume	Molarity	Explosives				
μL	μM	weight/volume (ng/μL) | ppm				
		Tetryl	TNT	2,4-DNT	RDX	PETN
10	6.6	1.9	1.5	1.2	1.5	2.1
20	13.2	3.8	3.0	2.4	2.9	4.2
30	19.6	5.6	4.5	3.6	4.4	6.2
40	26.0	7.5	5.9	4.7	5.8	8.2
50	32.3	9.3	7.3	5.9	7.2	10.2
60	38.5	11.1	8.7	7.0	8.6	12.2
70	44.6	12.8	10.1	8.1	9.9	14.1
80	50.6	14.5	11.5	9.2	11.2	16.0
90	56.6	16.3	12.9	10.3	12.6	17.9
100	62.5	17.9	14.2	11.4	13.9	19.8

4.3.2.4 *Theoretical calculations*

Computational simulations‡‡ of the electronic properties of MOF **3′** and the explosive substances (and related analytes) allow for predictions to be made as to which of the sensing compounds should quench the framework to the greatest extent through the photo-induced electron transfer mechanism (PIET). The alignment of the ionization

‡‡ Computational simulations were calculated by Christopher N. Savory and Dr. David O. Scanlon, Department of Chemistry, University College London. The computational experimental details can be found in Appendix B.

potentials and electron affinities of a range of analyte molecules and the MOF is displayed in Figure 4.33.

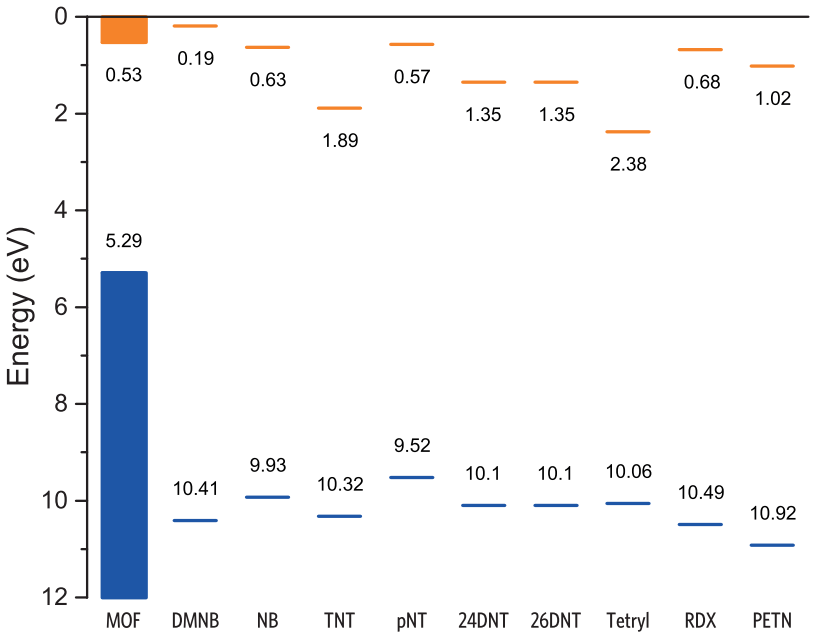

Figure 4.33: Alignment of the valence and conduction band maxima of **3′** (or the LUMO and HOMO, coloured orange and blue respectively) and the ionization potentials (or HOMO, coloured blue) and electron affinities (LUMO, coloured orange) of a range of explosive substances and related analytes. Calculations were performed by Christopher N. Savory and Dr. David O. Scanlon, University College London.

As discussed (Section 2.5.3), the fluorescence of the MOF is quenched through the transfer of an (excited state) electron from the conduction band of the MOF to the LUMO orbitals of the electron deficient analytes. The lower the LUMO energy, the higher the electron accepting ability of the analytes and thus; the highest efficiency and magnitude of quenching of the MOF observed. From the results displayed, it is clear that the calculations predict that the quenching of fluoresence by electron transfer should occur in all analytes except DMNB, which possesses an EA above that of the MOF. However, it was observed that the EAs calculated above were constantly underestimated by 0.3 – 0.4 eV in comparison to literature values [191]. Thus, if these ~0.4 eV underestimation of EAs are included, this brings all the analytes below that of the MOF and so it could be expected that quenching of

the MOF with DMNB can also occur [§§]. The order of quenching magnitude based on these calculations should follow that of Tetryl > TNT > 2,4-DNT > PETN > RDX for the sensing analytes. This somewhat resembles the order observed from experimental titrations, other than the substantial under-performance of TNT in its ability to quench MOF **3′**. Thus, clearly some interactions (or lack of) between the MOF host structure and TNT are occurring to cause such discrepancies, as these are not accounted for in theoretical calculations.

In addition to the above, a further theoretical simulation of the charge density isosurface of the lowest unoccupied state calculated for the MOF with nitrobenzene in its pore (Figure 4.34) gives further evidence of the alignment of the analytes with the MOF.

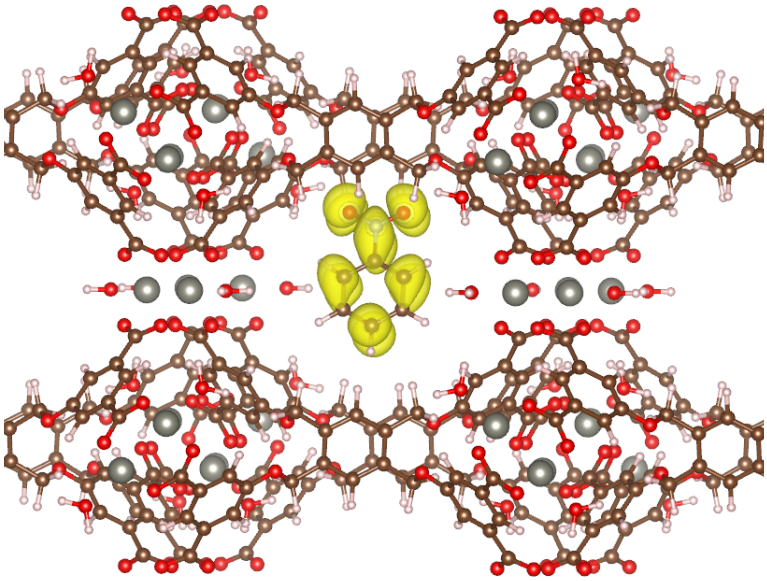

Figure 4.34: Partial charge density of the lowest energy unoccupied state of nitrobenzene in the MOF. Calculations were performed by Christopher N. Savory and Dr. David O. Scanlon, University College London.

The electron density matches that of the LUMO of the nitrobenzene molecule, rather than the charge density of the conduction band of the empty MOF, indicating that electrons may transfer from the MOF to nitrobenzene.

§§ Additionally, some deviation will be expected from the different electrostatic environment within the pore compared to vacuum.

4.3.2.5 *Stern-Volmer quenching constants and processes analysis*

As discussed in Section 2.5.2.5, Stern-Volmer (SV) plots allow for the rate of quenching to be determined, in addition, they indicate how many quenching processes are operative within the sensing system. The SV plots of the five tested analytes are shown in Figure 4.35. These plots have not been corrected for dilution, in order to show the relationship between the analyte and MOF as they appear in this system.

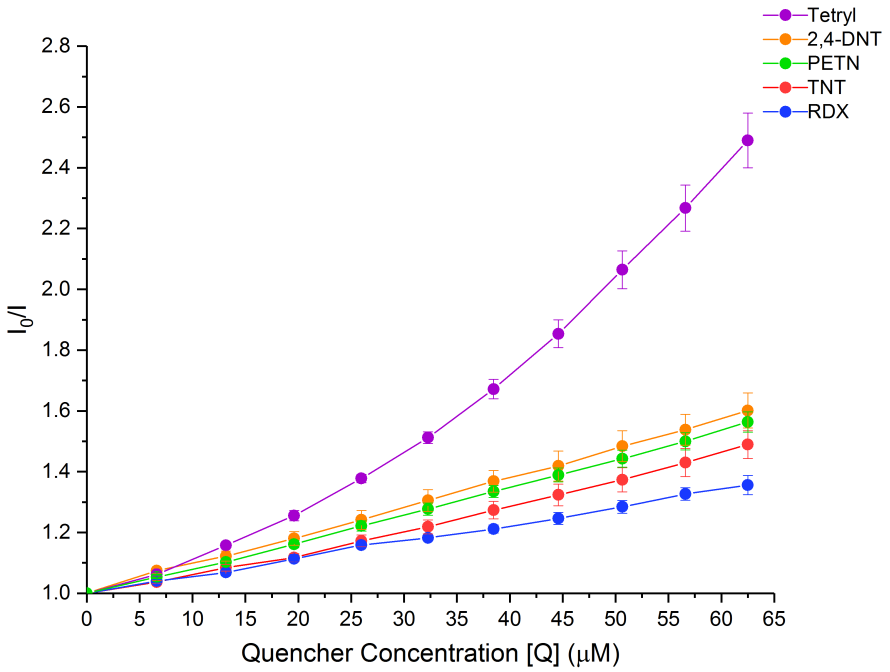

Figure 4.35: Graph showing the Stern-Volmer plots of MOF **3′** after the addition of Tetryl, TNT, 2,4-DNT, PETN and RDX. The error bars represent one standard error of the mean.

The SV plots for MOF **3′** upon exposure to TNT, 2,4-DNT, PETN and RDX are all linear. This implies that only one type of quenching process is operative for MOF **3′** in contact with these four substances. Upon exposure to Tetryl, MOF **3′** demonstrates a near liner SV plot at low concentrations (up to approximately 26 μM) followed by a clear deviation from linearity in the SV plot at higher concentrations. This

suggests that two distinct quenching processes are likely to be causing the quenching of MOF **3′** upon exposure to Tetryl (Section 2.5.2.5).

The rates at which MOF **3′** is quenched by the five substances can be seen in Table 4.7.

Table 4.7: K_{SV} constants of MOF **3′** upon exposure to TNT, 2,4-DNT, RDX, PETN and Tetryl. The R^2 show the goodness of fit for the given SV plot.

Substance	K_{SV} / M^{-1}	R^2
RDX	5.7 x 10^3	0.998
TNT	7.9 x 10^3	0.997
PETN	9.0 x 10^3	0.999
2,4-DNT	9.5 x 10^3	0.999
Tetryl[a]	1.6 x 10^4	0.996

a This K_{SV} was calculated using the first four points of the MOF **3′**-Tetryl SV plot which are in linear agreement. Due to the limited points used in the calculation this value should be viewed as an estimate.

These K_{SV} constants of MOF **3′** upon exposure to these explosives (or related) substances are of the same magnitude as those reported for the solution-phase sensing of explosives using amplifying fluorescent conjugate polymers (AFCP, as pioneered by Swager *et al.*, Section 2.5.3) [79]. For example, one AFCP yielded K_{SV} values of 4.3 x 10^3 M^{-1} and 1.1 x 10^4 M^{-1} upon exposure to TNT and 2,4,6 -trinitrophenol (TNP) in toluene solutions respectively [192]. Another AFCP gave K_{SV} constants of 4.15 x 10^4 M^{-1} and 1.31 x 10^4 M^{-1} for TNP and 2,4-DNT respectively (in tetrahydrofuran solutions) [193]. Whilst the absolute K_{SV} constant values are not comparable owing to discrepancies in the quantities of explosives and sensors used in the experiments; a comparison of the order of magnitude in K_{SV} values is useful, and suggests that MOF **3′** is as efficient at quenching nitroaromatic compounds as amplified fluorescent conjugate polymers. The values are also in accordance with those reported for other MOF explosive sensors [95].

MOF **3′** is observed to be most efficiently quenched by Tetryl; the K_{SV} constant in the presence of this explosive (1.6 x 10^4 M^{-1}) is comparable with that reported for MOF UiO-68@NH_2 in the presence of TNP (K_{SV} 5.8 x 10^4 M^{-1}) [194]. This MOF was shown to have a higher selectivity for TNP over the other nitroaromatic analytes that it was tested against. The SV plots for all the analytes[¶¶] added to UiO-68@NH_2 in water are shown in Figure 4.36.

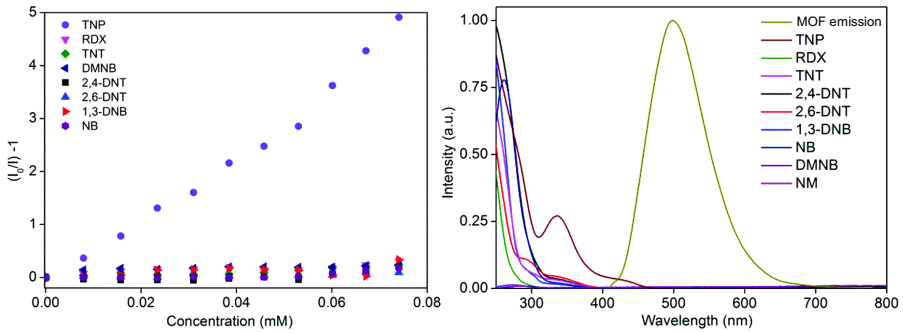

Figure 4.36: Left: Stern-Volmer plots for analytes added to UiO-68@NH_2 in water. Right: Extent of spectral overlap between the absorption spectra of nine explosives or related compounds and the emission spectrum of MOF UiO-68@NH_2 in water. Adapted from [194] - Published by The Royal Society of Chemistry.

The higher selectivity for TNP by UiO-68@NH_2 was attributed to the presence of both collisional and static quenching processes occurring due to both the photo-induced electron transfer (PIET) and Förster-resonance energy transfer (FRET) mechanisms quenching the MOF. This was rationalised based on the higher extent of spectral overlap between the MOF emission and the TNP absorption spectrum than the other analytes (Figure 4.36). Similar findings have previously been reported by the same group (Section 2.6.4.3) [143].

Therefore, to gain an insight into whether such mechanisms could explain the pronounced selectivity of Tetryl over the other analytes by MOF **3′**, the absorption spectra of the sensed compounds and the emission spectrum of **3′** were compared, as illustrated in Figure 4.37.

¶¶ Very similar molar concentrations were used in sensing experiments with UiO-68@NH_2 as with MOF **3′**.

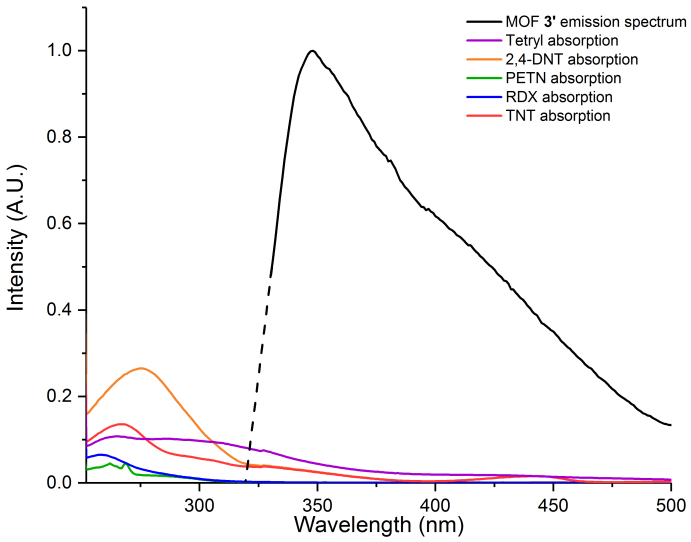

Figure 4.37: Graph illustrating the spectral overlap observed between the emission spectrum of **3′** and the absorption spectra of Tetryl, 2,4-DNT, PETN, RDX and TNT. The dotted black line shows the extrapolation of the emission spectrum of MOF **3′** down to lower wavelengths where measurements were not taken.

Similarly to UiO-68@NH_2 upon exposure to TNP (Figure 4.36), the emission spectrum of MOF **3′** shows the greatest degree of overlap with the absorption spectrum of Tetryl compared to the other analytes. Whilst the difference in the degree of overlap between Tetryl and the other analytes is less pronounced than for TNP and the other nitroaromatics tested by Ghosh *et al.*, there still appears to be better spectral overlap with Tetryl and **3′** than the other compounds. Thus, based on this, the higher quenching efficiency and the shape of the SV plot for MOF **3′** upon exposure to Tetryl, it is hypothesised that both PIET and FRET quenching mechanisms cause the quenching of **3′** with this explosive. It is suggested that the quenching of **3′** in the presence of the other analytes only occurs *via* the PIET mechanism.

Lifetime measurements

As discussed (Section 2.5.2.5), in order to confirm whether both static and collisional processes (as indicated by the SV plot in Figure 4.35) were causing the quenching of **3′** in the presence of Tetryl (and to de-

termine which of the processes were causing the quenching of **3′** with the other analytes); lifetime measurements of **3′** in the presence of the analytes were required. Lifetime measurements were attempted on **3′** in the presence of Tetryl, TNT and 2,4-DNT, however, the results proved inconsistent and therefore inconclusive. Future work is required to understand whether static, collisional, or both quenching processes are causing the attenuation of the MOF in the presence of these analytes.

Limits of Detection

The limits of detection (LOD) for each analyte upon the exposure to **3′** are detailed in Table 4.8.

Table 4.8: Limits of detection

Analyte	LOD	
	μM	ppm
2,4-DNT	3.2	0.6
Tetryl	4.0	1.1
TNT	5.3	1.2
RDX	5.3	1.2
PETN	5.8	1.8

The method used for the LOD calculations was that proposed by Armbruster *et al.* [195], applied to the linear Stern-Volmer plot.

$$\mathrm{LOD} = \frac{\mathrm{I_{o(mean)}}}{\mathrm{I_{o(mean)}} - 2\mathrm{SD}_{(\mathrm{I_o mean})}} \tag{4.1}$$

The mean baseline fluorescence emission intensity (I_o) was divided by the mean I_o, minus two standard deviations (SDs) of I_o, to give an LOD value which was obtained for each analyte repeat experiment (five repeats per analyte) and averaged to give a mean LOD value for each analyte. These LOD values correspond to y values in the SV plots

in Figure 4.35, which were used to find corresponding x values and thus the LOD in μM for each analyte. These values signify the lowest analyte concentrations that are likely to be reliably distinguishable from the baseline measurements. As shown, all LODs fall between 3 - 6 μM for the sensing of these analytes using this methodology.

Stability

To confirm that MOF **3′** was not being degraded during sensing, a PXRD pattern of **3′** in a sensing solution containing Tetryl (62.5 μM) was compared with a PXRD pattern of the MOF in an acetonitrile (MeCN) 'blank' solution. The same analysis was also completed on a 2,4-DNT (62.5 μM) sensed MOF sample, Figure 4.38.

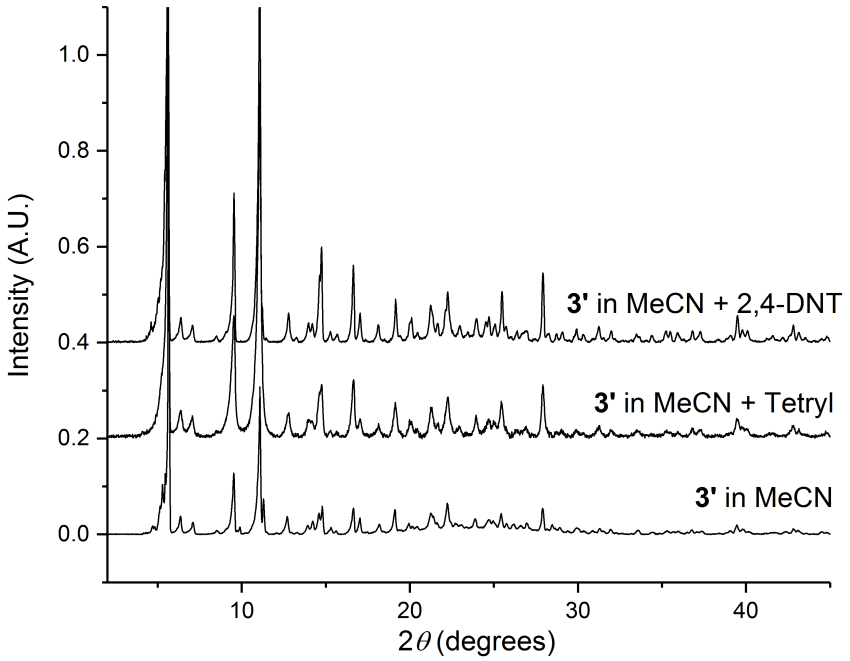

Figure 4.38: PXRD patterns of MOF **3′** in a Tetryl sensing solution (62.5 μM), a 2,4 - DNT sensing solution (62.5 μM) and the PXRD pattern of **3′** in a 'blank' MeCN sensing solution.

As is evident from the PXRD patterns in Figure 4.38 MOF **3′** does not degrade during sensing. It is also apparent that no permanent structural transformations of **3′** occur in the presence of these analytes.

It should also be noted that upon exposure of **3′** to Tetryl and 2,4-DNT there is an observed colour change from pale yellow to orange. Such findings have been previously reported and attributed to some alterations of framework structure upon host-guest interactions [159, 196]. However, as evidenced by the similarity of the PXRD patterns in Figure 4.38 this is not the case for **3′** and so the observed colour change could be a result of the inclusion of the analytes into the MOF pores [197]. Single crystal X-ray diffraction analysis was attempted on MOF **3′** crystals immersed in a 2,4-DNT-containing solution (as detailed in Section 4.2.5.4). However the crystalline quality of the MOF material was not high enough for this analysis, most likely as a result of the non-uniform inclusion of the analyte into the MOF cavities.

4.3.3 *Vapour-phase sensing*

As metal-organic framework **3′** demonstrated the successful and effective detection of explosive substances and related compounds in the solution-phase, it was evaluated for its vapour-phase detection capabilities. MOF **3′** was tested for its ability to detect 2,4-DNT vapours, owing to the facile generation of saturated vapours from readily available, commercially purchased 2,4-DNT solid crystals and to allow for a comparison between the sensing of this analyte in both the solution and vapour phase.

4.3.3.1 *Exposure to 2,4-DNT vapours*

'Thin films' of **3′** were fabricated on quartz slides and tested for their sensing responses towards 2,4-DNT using the methodologies outlined in Section 4.2.6. Figure 4.39 and Figure 4.40 show the fluorescence intensity changes of two different MOF **3′** films when exposed to 2,4-DNT as well as 'empty' centrifuge tubes containing ambient air.

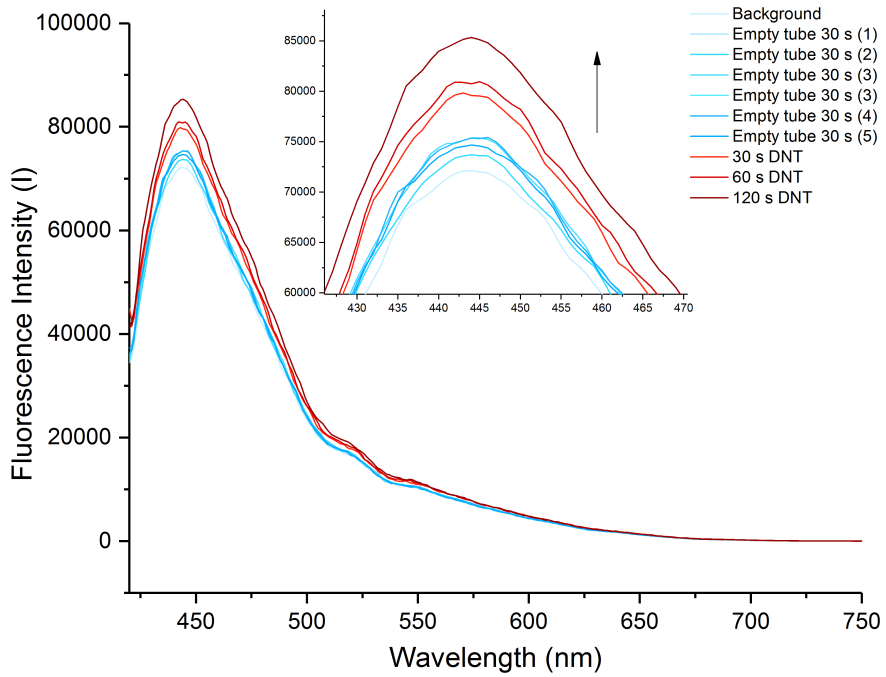

Figure 4.39: Fluorescence emission spectrum of a MOF **3′** lqthin film rq upon exposure to lqempty tubesrq containing only atmospheric air (blue) followed by the saturated headspaces of 2,4-DNT vapours (red).

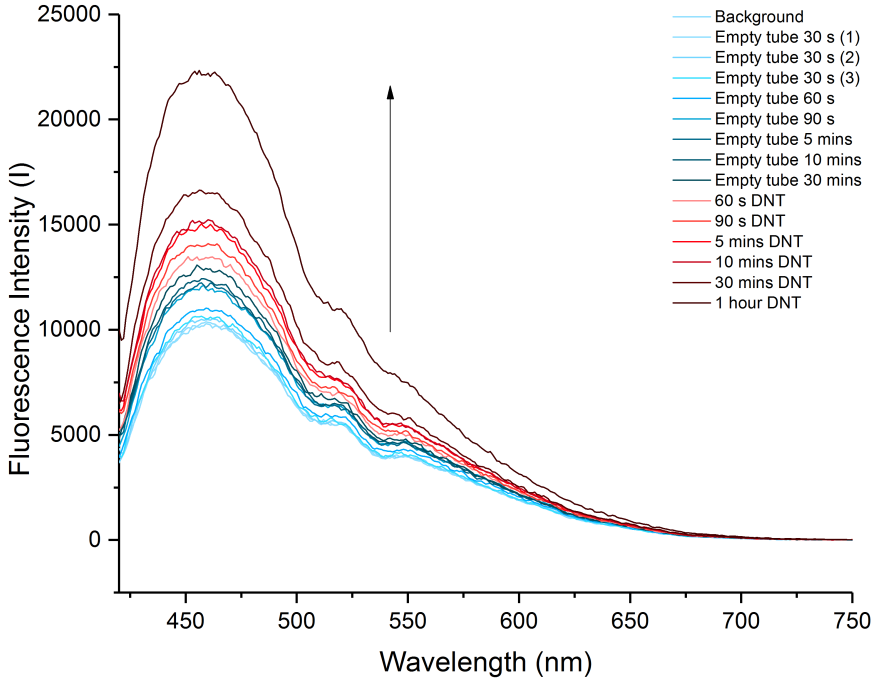

Figure 4.40: Fluorescence emission spectrum of MOF **3′** after the sequential exposure to lqempty tubesrq containing only atmospheric air (blue) followed by the saturated headspaces of 2,4-DNT vapours (red).

As can be seen in Figure 4.39 and Figure 4.40, when **3'** is exposed to 2,4-DNT the fluorescence intensity is observed to increase or 'turn-on'. It can also be seen that there is an increase in the MOF's fluorescence intensity upon exposure to the 'empty tube', ambient air conditions, as most effectively expressed in Figure 4.40.

Whilst such fluorescence increases are surprising, they have previously been noted in the MOF sensing literature. Fluorescence turn-on effects are most typically observed as a result of either guest-induced structural perturbations of the host frameworks ([129]), the coordination of guests to uncoordinated metal centres (UMS) or linkers ([129, 198, 199]), or occasionally as a result of complete framework collapse ([200, 201]). Each of these effects were investigate with aim to explain the turn-on effects observed for MOF **3'**.

4.3.3.2 *Framework stability test*

To ensure the framework was not collapsing as a result of analyte exposure; PXRD patterns of a MOF **3'** thin film pre- and post- 2,4-DNT exposure were obtained and can be see in Figure 4.41. As is evident, the structure of the MOF remains consistent.

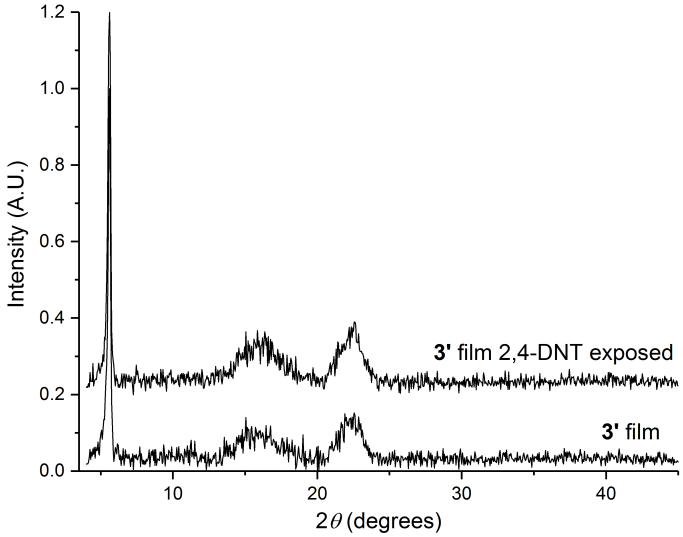

Figure 4.41: Powder X-ray diffraction patterns of a MOF **3'** thin film pre- and post-2,4-DNT exposure.

4.3.3.3 *Investigation of structural perturbations*

MOF fluorescence emission increases due to structural perturbations most typically occur in flexible metal-organic frameworks [129]. PXRD analyses and Le Bail fitting*** were used to evaluate whether any structural transformations occur in **3′** upon exposure to 2,4-DNT. To do this, a sample of MOF **3′** was exposed to the saturated headspace of the analyte for two weeks followed by PXRD analysis and Le Bail fitting. This was compared to the PXRD and Le Bail fitting analysis performed on crystals of the same MOF sample which were exposed to ambient lab air conditions at the same time for two weeks ('control' experiment); the full experimental details of which are given in Section 4.2.6.4. The results of the fitting analysis can be found in Table 4.9.

Table 4.9: Results of PXRD Le Bail fitting on MOF **3′** exposed to 2,4-DNT (**3′**-DNT), atmospheric air (**3′**-cont.) and the as synthesised MOF sample (**3**).

	Agreements of fit			Unit cell lengths			Unit cell volume
	R_{wp}	R_{exp}	R_p	*a* /Å	*b* /Å	*c* /Å	V /Å^3
3	7.0	2.0	4.6	25.4(0)	28.1(0)	30.5(0)	21767(2)
3′-cont.	2.2	2.0	1.7	24.8(0)	28.3(0)	30.9(0)	21722(17)
3′-DNT	2.3	2.0	1.7	24.9(0)	28.3(0)	30.9(0)	21805(16)

As is evident there are discrepancies in the structural parameters between the air exposed (control) and 2,4-DNT exposed **3′** material. However, the relatively small changes in the unit cell *a*, *b* and *c* lengths suggest that there are no substantial framework transformations in the MOF structure induced by analyte interactions.

Thus, a more plausible rationalisation for fluorescence increase is that analyte interactions with the MOF, are rigidifying the flexible MOF structure. It is hypothesised that the sorbed analytes (both 2,4-DNT and analytes present in air, namely water molecules) inhibit

*** Le Bail experiments were performed by Dr. Huw Marchbank, University College London.

linker motions such as vibrations and torsional displacements that otherwise facilitate the non-radiative decay of the MOF photo-excited state [128, 129]. It is suggested that these rigidifying effects are more pronounced upon exposure to 2,4-DNT than to the moisture in air, owing to the larger increase in the fluorescence emission observed for **3′** in the presence of this analyte as opposed to air exposure. Further to this, it is proposed that MOF rigidity is increased from inclusion of the analytes into the MOF pores, leading to a swelling of the activated MOF structure. This is postulated based upon the greater increase in the unit cell volume of the 2,4-DNT exposed MOF sample than the **3′** air exposed sample and the as-synthesised MOF **3** material prior to activation. This is corroborated by an experiment in which the crystals of a MOF **3′** air exposed, control sample, were then exposed to 2,4-DNT for a further two weeks and an additional expansion of the unit cell volume was observed[†††].

This phenomenon of fluorescence enhancement as a result of framework rigidification is typical of MOFs that display breathing behaviour [129]. For example, Zhang *et al.* reported initial attenuation of fluorescence upon the removal of guest molecules from synthesised MOF 'MAF-34' (Figure 4.42a) owing to linker motions, however, upon exposing the active framework to MeOH, EtOH, H_2O and benzene vapours, the fluorescence emission was observed to increase [202]. Additionally, Dong *et al.* reported the luminescence increase of MOF $[Cu_2(bimbpyb)_2I_2]\cdot 4H_2O$ (bimbpyb = 1-benzimidazoyl-3,5-bis(4-pyridyl)benzene) upon the inclusion of atmospheric HCHO into the framework pores [203] (Figure 4.42b). Further, the same group reported the increase in the fluorescence intensity of MOF $[Ln(pyimdc)(ox_{0.5}]\cdot 2H_2O$ (Ln(III) = Eu(III) or Tb(III), H_2pyimdc = pyridyl-4,5-imidazole dicarboxylic acid, H_2ox = oxalic acid) as a result of hydrogen bonding interactions between the OH moieties of H_2O molecules coordinated

††† The full results of this experiment can be found in Appendix B

to its metal centres and the electron lone pair of H_2O analytes from the atmosphere (Figure 4.42c). It was reported that these interactions reduced the O-H vibrational frequency of the coordinated solvents and therefore their quenching effect on the MOF;leading to an enhancement in the MOF fluorescence emission spectrum upon water exposure [204].

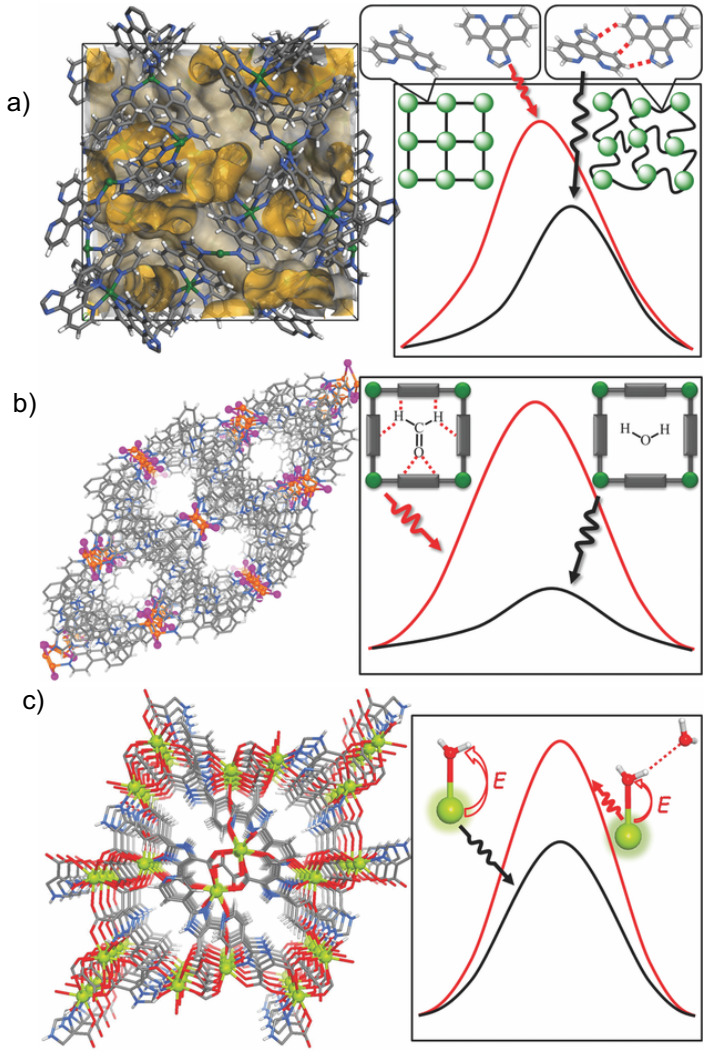

Figure 4.42: Examples of previously reported MOFs that demonstrate fluoresce emission increases due to the rigidification of framework structures upon interaction with guest analytes: a) Illustrates the fluorescence attenuation of MOF 'MAF-34' upon removal of guest solvent molecules due to linker flexibility induced motions. b) Illustration of the increase in luminescence observed in MOF $[Cu_2(bimbpyb)_2I_2]\cdot 4H_2O$ upon exposure to atmospheric HCHO and c) An illustration of the effects of water vapour interactions on the fluorescence emission intensity of MOF$[Ln(pyimdc)(ox_{0.5}]\cdot 2H_2O$. These figures were reproduced with permission from [129].

Each of these examples coincide with the effects that are being observed in MOF **3′**. It should be noted however that fluorescence quenching as a result of the MOF's interaction with the very electron deficient 2,4-DNT molecule is possibly still occurring as a result of PIET mechanism, but its effects are being masked by the rigidifying effect.

4.3.3.4 *Host-guest coordination evaluation*

An alternative means by which the enhancement of fluorescence emission intensity can be observed is through the coordination of guests to unsaturated metal sites (UMS) or to linkers in the framework. As discussed in Section 4.3.1.7, it is suggested that the water molecules bound to the zinc metal centres in MOF **3′** are not removed during the implemented activation procedure (Section 4.2.3) and so UMS are unlikely to be available in this MOF for analyte coordination. However, to check that there are no coordinative effects between the MOF and the analyte, X-ray photoelectron spectroscopy (XPS) measurements were taken on the control and 2,4-DNT exposed MOF **3′** samples discussed above. The XPS analysis confirmed a high degree of similarity between the samples and so it could be concluded that the increase in the emission spectra of the MOF is not as result of analyte-MOF coordination (the results of the XPS analysis can be found in Appendix B).

4.4 CONCLUSIONS

Metal-organic framework $[Zn_4L(H_2O)_4 \cdot (solvent)]_n$, MOF **3**, was synthesised for the purpose of explosives detection.

Single crystal X-ray diffraction confirmed MOF **3** to be isoreticular to the prototypical MOF HKUST-1 and isostructural to $[Cu_4L(H_2O)_4 \cdot (solvent)]_n$ on which the design on the MOF was based. Further to this, crystallographic data determined that there are two pore environments located within this **tbo**-MOF; the larger of which is able to theoretically encapsulate large explosive molecules such as Tetryl, TNT and PETN. This addresses the primary structural objective of the MOF as outlined in Section 4.1.

A number of characterisation techniques, namely power X-ray diffraction, photoluminescence spectroscopy and BET sorption isotherms, elucidated as to the flexibility of active metal-organic framework **3'**. Whilst the observed flexibility is not extensive, the second MOF structural aim was still met.

It was noted that the mild solvent-exchange activation method employed to yield active flexi-MOF **3'** created some disorder and pore shrinking in the MOF, although its overall framework structure was still maintained. However, the original highly ordered and porous structure of the MOF could be re-obtained upon re-immersion of the MOF in a MeCN solution. It was also suggested that this activation method did not remove the zinc-bound water molecules in the framework, and thus, unsaturated metal sites (UMS) in this MOF were likely not realised. Additionally, thermogravimetric analysis indicated that the washing procedure may not have been 100% effective at removing all encapsulated solvent guest molecules from the as-synthesised structure upon activation.

The harsher high vacuum heating activation method of **3** to yield **3″** where UMS were now proposed to be present in the framework, created a greater degree of disorder in the MOF structure. This was evidenced by the loss of crystallinity in the PXRD pattern of the **3″** active material and an underestimation of the H_2O BET values. Thus, a milder method of heating is proposed with aim to induce UMS in the framework without minimising porosity due to disorder.

Nevertheless, **3″** demonstrated very good stability in the presence of varying degrees of relative humidity and even retained much of its H_2O BET porosity even after exposure to high relative humidities at high temperatures, to give an overall water stability grading of 5B for the MOF (as classified by Shimizu *et al.* [123]). Further, humidity testing suggested that whilst the MOF does sorb water, the interactions between the water molecules and framework are weak and it is postulated that it is less hydrophilic than commercially available MOF HKUST-1. Thus, based on humidity testing coupled with thermogravimetric analysis it can be argued that MOF $[Zn_4L(H_2O)_4 \cdot (\text{solvent})]_n$ is well suited in applications where the environmental conditions are hot and humid.

Additionally in this chapter, the validity of the most commonly reported solution-phase sensing methodology in MOF-sensor literature was critiqued. Consequently, new approaches and important considerations were highlighted, which will hopefully be of benefit to the wider MOF community.

The sensing of explosive substances and related analytes in the solution phase using MOF **3′** saw the effective detection of Tetryl, TNT, 2,4-DNT and PETN down to less than 4 ppm based on fluorescence quenching. In addition, there was some evidence of RDX detection using this MOF also. MOF **3′** showed pronounced selectivity towards Tetryl, this was rationalised based on the formation of exciplexes be-

tween the analyte and the MOF, as well as potentially the presence of both PIET and FRET mechanisms causing the attenuation of the MOF in the presence of Tetryl. It was also suggested that two distinct quenching processes (static and collisional) were causing the quenching of the MOF with Tetryl (based on non-linear SV plots with the MOF and this analyte); however lifetime measurements were inconclusive and so this could not be confirmed. The other analytes were observed to quench **3′** through one process, and quenching was attributed to only the PIET mechanism. The order in which these analytes quenched the MOF generally followed that predicted using computational simulations, other than TNT, which gave underestimated quenching of the MOF. The reasons for this are not understood but may be a result of its poor encapsulation into the MOF pores, thus, inhibiting interactions between the MOF and this analyte. The quenching efficiencies of the MOF by the analytes as calculated using Stern-Volmer analysis confirmed **3′** to be as efficient at being quenched in the presence of nitroaromatic compounds as amplified fluorescent conjugate polymers, as well as other MOF sensors. MOF **3′** was also confirmed (using PXRD analysis) to retain its structure during solution-phase sensing.

The vapour-phase detection of the explosive related analyte 2,4-DNT with MOF **3′** yielded interesting results. The increase in the fluorescence emission intensity of the MOF in the presence of this analyte (as well as molecules present in atmospheric air such as water) was attributed to the adsorbed molecules (most likely in the pores of the MOF) rigidifying the flexible MOF structure and inhibiting linker motions.

In conclusion, the results in this chapter suggest that MOF **3′** is a good sensor for the detection of explosives in the solution-phase. Whilst the MOF shows some selectivity towards Tetryl, there is not

much discrimination between the sensing of the other explosives and related analytes tested. Thus, whilst it could potentially be useful as a rapid, cheap, initial diagnostic as to the potential presence of explosives, it would struggle to determine which explosive was present. This is typical of most reported MOF explosives sensors. Thus, in order to induce discrimination into solution-phase MOF-explosives sensing systems, MOF **3′** was combined with two other reported MOF sensors to form a sensory array, which will be presented and discussed in the following chapter (Chapter 5).

Additionally, whilst **3′** was shown to be a poor vapour-phase sensor of 2,4-DNT, there is evidence to suggest that this analyte is being encapsulated into the pores of the framework, potentially even with some selectivity, therefore it could be hypothesised that MOF **3′** is an effective sorbent material. Even with the underestimated porosity of around 380 $m^2\ g^{-1}$ as calculated by H_2O BET, MOF **3′** has greater porosity than some commercially available sorbents, such as Tenax TA, which has a surface area of 35 $m^2\ g^{-1}$. Taking this into consideration, MOF **3′** was tested for its ability to act as a preconcentrator of explosive vapours, which will be discussed in Chapter 6.

5

A MOF SENSOR ARRAY FOR SOLUTION-PHASE EXPLOSIVES DETECTION

5.1 INTRODUCTION

In Chapter 4 it was demonstrated that metal-organic framework [$Zn_4L(H_2O)_4 \cdot (solvent)_n$], MOF **3**, (where L = 5,5′,5″,5‴-[1,2,4,5-benzenetetrayltetrakis(methyleneoxy)tetra-1, 3-benzenedicarboxylate) in its active form (MOF **3′**) was an effective solution-phase sensor of Tetryl, TNT, PETN, 2,4-DNT and arguably RDX, based on the fluorescence quenching of the MOF upon exposure to these analytes. It was found that whilst MOF **3′** was able to demonstrate some degree of semi-selectivity between these analytes when they were added individually to the MOF in the same concentrations (as evidenced by Figure 4.32), the addition of these analytes in different concentrations would likely hamper any of the sensor's inherent selectivity. This is due to the analytes having similar chemical nature and quenching responses. For example, when TNT and Tetryl are added to MOF **3′** samples in the same concentration (62.5 μM addition), Tetryl quenches the MOF by 60%, where as the MOF is quenched by 32% in the presence of TNT. Therefore, at this concentration, if the two explosives were added to different MOF **3′** samples as 'unknowns' they are likely to be able to be discriminated, based on the MOFs higher selectivity towards Tetryl. However, Figure 4.32 shows that a 38.5 μM addition of TNT to MOF **3′** gave, on average, a 21% quench of the system and a 19.6 μM addition of Tetryl; yielded a 20% quench of **3′**. Illustrating the im-

portance of concentration on variable photo-luminescence quenching. In addition, some analytes such as 2,4-DNT and PETN yielded very similar quenching responses when added in the same concentrations; thus no discrimination through the analysis of the quenching percentages would be possible between these two analytes regardless of the concentrations added. As such, in the sensing system discussed in Chapter 4, MOF **3′** is able to detect but not identify explosives.

Previous research by Li *et al.* (Section 2.6.4.1) sought to discriminate between the compounds introduced to a flexible MOF ($[Zn_2(ndc)_2(bpee)\cdot 2.25DMF\cdot 0.5H_2O]$) by monitoring both the changes in fluorescence intensity and emission wavelength (spectral) shift of the MOF upon exposure to saturated vapours of some explosives related analytes [133] (as demonstrated by Figure 2.18 and discussed in Section 2.6.4.1), to create 'fingerprints' of the analytes on a two-dimensional Cartesian map. Although this work effectively demonstrated how using both of these variables in signal transduction can increase the discrimination of analytes using a single MOF system, some analytes still yielded similar responses of the MOF despite being chemically different and having different concentrations. Therefore, the effective discrimination of analytes is still not possible using this 2D-map method and a single MOF sensing system.

A potentially more effective way to introduce discrimination and thus identification of explosive compounds and related analytes using MOFs as sensors is to incorporate them into a sensing array [128], as explored in this chapter.

5.1.1 *Basics of array-based sensing*

The array-based sensing approach is illustrated by the schematic in Figure 5.1 [58, 59].

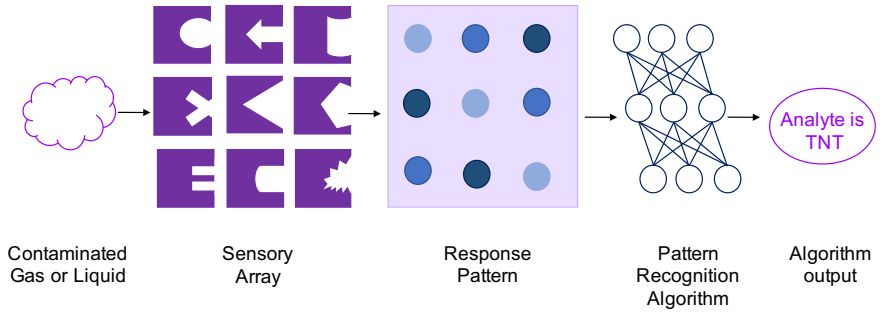

Figure 5.1: General overview of the array-based sensing process. Adapted from [58] with permission from The Royal Society of Chemistry.

In array-based sensing, also known as differential sensing, a known analyte of interest is exposed (through either the vapour or solution-phase) to a collection of semi-selective receptors, that each interact with the analyte in a slightly different way to the other components of the array. This generates a unique collective response pattern for this particular analyte, as well as each known analyte that is introduced to the array. The response patterns of known analytes are subsequently processed and interpreted using pattern recognition algorithms that model the data to generate 'fingerprints' for each analyte that the array is exposed to. These fingerprints are then catalogued for the array to be 'trained-on'. Upon the introduction of an unknown analyte to the array, the cross-reactive sensors again interact differentially to generate a pattern, which is analysed to record the fingerprint for the unknown analyte. This fingerprint is then compared to that of known fingerprints already established for the array, and the "most likely" matching of the fingerprint is then expressed (with some level of confidence) taking into account statistical variation. Therefore, instead of identifying a specific analyte by its affinity for one particular

receptor, it is the combined response that is measured and evaluated for specific patterns [58, 60, 63, 205–207]. As such, an important advantage of this approach is that to identify a molecule, the system is limited by the number of different patterns possible, rather than the number of different receptors. This differential sensing approach is modelled on mammalian olfaction and gustation, and is the reason why such array based systems are often termed as 'chemical noses' or 'electronic noses' (or tongues) [58–60, 208]. It is important to note that the differential sensing approach is not just limited to single-analyte sensing; complex mixtures of analytes may also be identified based on their unique fingerprint generated upon their interactions with the array. In addition, arrays can allow for the identification of new materials, even those that are not fully characterised [58]. Both of these are very important considerations for explosives detection owing to the constantly evolving explosives threat and the complexity of detection environments (Section 2.3.2).

Arrays can be generated through the use of many different signal transducers (sensing materials) [59, 60], and can be analysed using a number of different machine learning tools [63, 205, 207]. The sensing materials typically fall within three broad categories; electrical (e.g. metal oxide semiconductors [209], carbon nanotubes [210], conductive polymers [211]), gravimetric (e.g. quartz crystal microbalance [212], surface acoustic wave [213], microcantilever sensors [214]) and optical (e.g. colourimetric and fluorescent [58, 215]) sensors. The most commonly encountered pattern recognition methods for the multivariate analysis of the array data include (but are not limited to): principle component analysis (PCA), linear discrimination analysis (LDA), hiereachical clustering analysis (HCA), artificial neural networks (ANNs) and support vector machines (SVM) [58, 63, 205, 207]. The main differences in each of these methods are how they

process the sensing data (reduce the dimensionality of the data) to extract the key features that generate the 'fingerprints' of the known and unknown analytes to allow for their reliable classification, and how they compute the similarities/differences between 'fingerprints' [58, 205, 207]. In addition, pattern recognition techniques can be categorised into those that use *supervised* and *unsupervised* learning algorithms [59]. For algorithms that use *supervised* learning, during the model 'training stage', a known set of inputs (analytes) are used to develop a database of descriptors that define the possible output classifications of the sensing system. For example, the identity of an analyte for a particular response pattern is given to the training set so that it knows the exact descriptors that classify that particular analyte. Therefore during identification, an unknown response pattern is analysed and the descriptors identified are compared with those previously learned. As such, the algorithm output is a classification of the similarity of the response to what the algorithm was previously trained on. Examples of such methods include LDA and SVM [59]. For *unsupervised* learning methods, no prior information on how the data should be classified is given to the model. During the training stage, the algorithm itself identifies the classes that define the input and there are no predefined output classes. These methods detect similarities in the response data and typically explore the clustering of data based on class as well as the dispersion of data. Examples of these methods include HCA and PCA [59, 205].

5.1.2 *Previous research on array-based sensing for explosives detection*

Array-based sensing is not a new concept to the explosives detection field, with the effective detection and identification of explosives using arrays having been demonstrated by various groups, using

several array sensor types. Most typically, electrochemical [209, 216], colourimetric [63, 217, 218] and fluorescence-based [58, 219–223] sensor arrays have been reported.

To date, there have been no reports on the use of metal-organic frameworks in a sensor array for explosives detection. In addition, only two reports exist on the use of MOFs in sensor arrays for other applications. Research by Dinca *et al.* demonstrated the effective detection and identification of volatile organic compounds (VOCs) using an array of chemiresistive MOFs [224], and Wilmer *et al.* reported the computational screening of different MOF arrays (based on gas adsorption predictions) with the aim to identify which array combinations were most effective for the sensing of various gases (e.g. CO_2, N_2, C_2H_6) [225]. Therefore, the work presented in this chapter, which investigates whether a MOF sensor array can be used for the detection and identification of explosives, is the pioneering work in this field. It should be noted that this research is a proof-of-concept experiment that seeks to evaluate the added value that the application of the array-based sensing technique can bring to the field of explosives sensing using MOFs. It does not seek to build the most robust or exhaustive MOF array.

5.1.3 *Experimental design*

A metal-organic framework array composed of three different MOFs was constructed in order to investigate whether MOFs can be used to form effective arrays for the fluorescence-based detection and identification of explosives. The array-MOFs were individually exposed to Tetryl, TNT, RDX, PETN and 2,4-DNT through the use of solution-phase titrations (with analyte concentrations ranging from 6.6 μM to 62.5 μM, ~ 1 - 20 ppm), and the fluorescence quenching responses

of the MOFs were monitored and used to yield the response-pattern of the array. The response pattern was subsequently analysed using LDA for the classification of the explosives. This experiment design is illustrated in Figure 5.2 and the rational choice behind each of these elements of the array is discussed below.

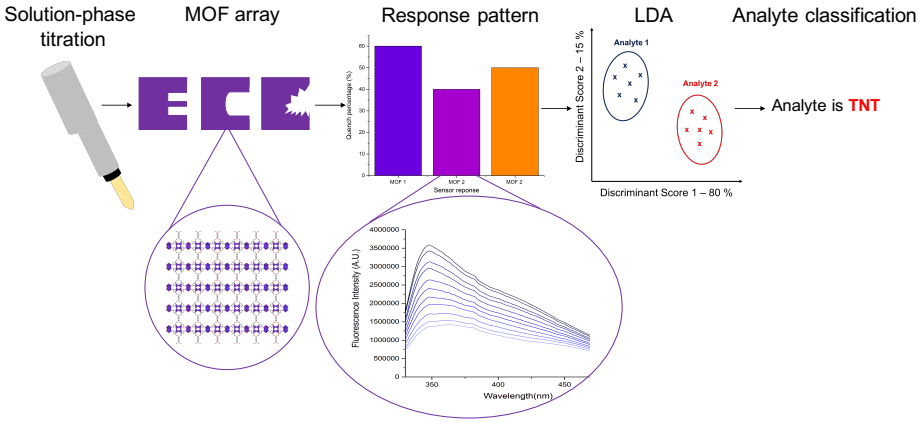

Figure 5.2: Metal-organic framework array experimental design. In essence, the three array-MOFs were exposed to analytes using solution-phase titrations. The fluorescence quenching responses of the MOFs in the presence of the analytes were used as the array response pattern, which was analysed using LDA to give the analyte classifications.

5.1.3.1 *Rational choice of MOF sensor components*

When constructing sensing arrays, the individual sensor elements need not be highly selective towards a given analyte but should respond to a number of analytes with the greatest chemical diversity as possible, so that the array responds to the largest possible cross-section of compounds [60]. MOFs have been reported in the literature to be semi-selective sensors towards a number of analytes including explosives, and they often demonstrate some degree of selectivity as a result of their different framework topologies causing varied host-guest interactions [67, 132, 164] (demonstrated also in Chapter 3). The three MOFs chosen for this array were done so on this basis, and they were:

- Array MOF 1 (**AM1**) - $Zn_4L(H_2O)_4 \cdot (solvent)_n]$ (MOF **3** from Chapter 4), where L = 5,5′,5″,5‴-[1,2,4,5-benzenetetrayltetrakis-(methyleneoxy)tetra-1, 3-benzenedicarboxylate.

- Array MOF 2 (**AM2**) - $[Zn_2(oba)_2(bpy) \cdot DMA]$, where H_2oba = 4,4′-oxybis(benzoate); bpy = 4,4′-bipyridine and DMA = N, N dimethylacetamide. [127].

- Array MOF 3 (**AM3**) - $[Eu(BTC)(H_2O) \cdot 1.5H_2O]$, where BTC is benzene-1,3,5-tricarboxylate.

Each of these MOFs have different framework topologies and demonstrate different fluorescence emission spectrum maxima when excited at appropriate wavelengths. The three-dimensional structures of the MOFs (without guest solvent molecules, as the MOFs were used in their 'active-form' for sensing, Section 2.6.1.3) can be seen in Figure 5.3.

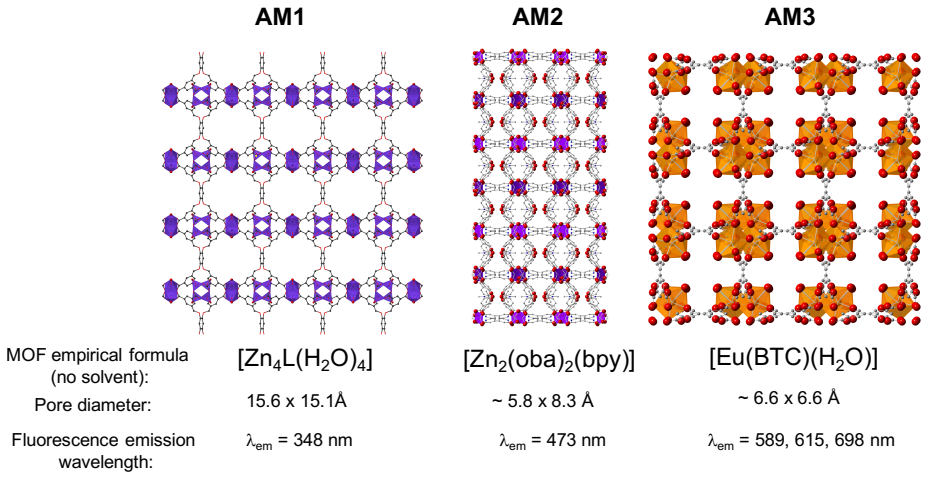

Figure 5.3: Three-dimensional representations of the crystal structures of the three MOFs used in the MOF sensing array in their active form (without guest solvents). Carbon atoms are coloured grey, oxygen = red, nitrogen = blue, zinc = purple and europium = orange. The minimum pore dimensions and the fluorescence emission wavelengths of the MOFs are also given in the figure. The crystal structure, pore sizes and fluorescence emission wavelengths of **AM1** were obtained as discussed in Chapter 4, and those of the other two MOFs are as reported in literature [127, 226].

MOF [$Zn_4L(H_2O)_4 \cdot (solvent)_n$]

The first MOF used in the construction of the array (**AM1**), is metal-organic framework [$Zn_4L(H_2O)_4 \cdot (solvent)_n$] (MOF **3**) as characterised and discussed in Chapter 4. This MOF was chosen by virtue of its large pores (minimum pore diameter of 15.6 x 15.1 Å and a solvent accessible volume of 69%) that allow it to effectively interact with and thus detect the above-mentioned explosives and related compounds (including arguably RDX), as demonstrated in Figure 4.32.

MOF [$Zn_2(oba)_2(bpy) \cdot DMA$]

MOF [$Zn_2(oba)_2(bpy) \cdot DMA$] (**AM2**) was previously reported by Li *et al.* (and is discussed in Section 2.6.4.1) [127]. This MOF is constructed from $Zn_2(oba)_4$ paddle-wheel SBUs, each of which are linked by an oba ligand to form a distorted 4^4 two-dimensional network. Two of these nets are observed to interpenetrate, forming a layered structure. The bpy linkers connect the paddle wheel units from two adjacent layers to form the overall 3D MOF. This MOF is noted to be porous with one-dimensional pores of ~ 5.8 Å x 8.3 Å running through the MOF. The calculated solvent accessible volume for the MOF was 25%. Previous sensing experiments observed [$Zn_2(oba)_2(bpy)$] to be highly fluorescent and effective at detecting explosives-related nitroaromatic compounds (e.g. nitrobenzene, para-nitrotoluene, para-nitrobenzene and 2,4-dinitrotoluene) in the vapour phase. The MOF showed preferential quenching in the presence of smaller nitroaromatics such as NB and demonstrated weak responses towards 2,4-DNT. In addition, the MOF demonstrated selectivity towards nitroaromatic compounds over interferents such as toluene, benzene and chlorobenzene; which were observed to increase the fluorescence of the MOF [127]. This MOF was chosen due to its reported lack of selectivity towards 2,4-DNT which was hypothesised would yield a different sensing re-

Interpenetration is the entwining of multiple lattices and is very common in MOFs [227].

sponse towards this analyte (as well as potentially the other larger explosives tested too) in comparison to **AM1**, thus, potentially aiding the discrimination of the array.

MOF [Eu(BTC)(H_2O)·1.5H_2O]

[Eu(BTC)(H_2O)·1.5H_2O] (**AM3**) is also a previously reported MOF [226]. In this MOF, europium atoms are bridged by BTC linkers to form a 'three-dimensional rod packing structure' as described by Chen *et al.* Each europium metal is coordinated to six oxygen atoms from the BTC linkers and one oxygen from Eu-bound water molecules. The one-dimensional pores within this structure are reported to be of ~ 6.6 Å x 6.6 Å dimension. This MOF demonstrates strong lanthanide fluorescence emissions at 589, 615 and 700 nm (when excited at an appropriate wavelength) which are attributed to the $^5D_0 \rightarrow {}^7F_1$, $^5D_0 \rightarrow {}^7F_2$ and $^5D_0 \rightarrow {}^7F_4$ transitions respectively. Chen *et al.* reported this MOF to be highly fluorescent (in MeCN) and effective at detecting small molecules such as acetone; attributed to the open metal sites present within the active MOF [226]. This MOF was chosen as a component in the MOF sensor array owing to its stability in MeCN (the solvent used for the sensing procedures), as well as due to its strong lanthanide-based fluorescence emissions. As discussed in Section 2.6.4.3, the fluorescence quenching of MOFs containing lanthanides can potentially occur as a result of both the photo-induced electron transfer mechanism and the antennae screening effect. This is where the sensitization of the lanthanides by the organic antennae ligands is prevented due to the competition for light absorption between the analytes and the ligands. Thus, causing a quench of the lanthanide MOF emissions [160]. Therefore, **AM3** is a versitile MOF to introduce into the array.

5.2 EXPERIMENTAL

5.2.1 *Synthesis and activation of array metal-organic frameworks*

5.2.1.1 *$[Zn_4L(H_2O)_4\cdot(solvent)_n]$* (AM1)

MOF $[Zn_4L(H_2O)_4\cdot(solvent)_n]$ (MOF **3**, **AM1**) where L = 5,5′,5″,5‴-[1,2,4,5-benzenetetrayltetrakis(methyleneoxy)tetra-1, 3-benzenedicarboxylate, was synthesised and activated (to afford MOF **AM1′**, **3′**, $[Zn_4L(H_2O)_4]$) using the same procedures as described in Section 4.2.2 and Section 4.2.3.

5.2.1.2 *$[Zn_2(oba)_2(bpy)\cdot DMA]$* (AM2)

Metal-organic framework $[Zn_2(oba)_2(bpy)\cdot DMA]$ (**AM2**), where H_2oba = 4,4′-oxybis(benzoate); bpy = 4,4′-bipyridine and DMA = N,N dimethylacetamide, was synthesised following a solvothermal method previously reported by Li *et al.* [127], the reaction scheme of which is shown in Figure 5.4.

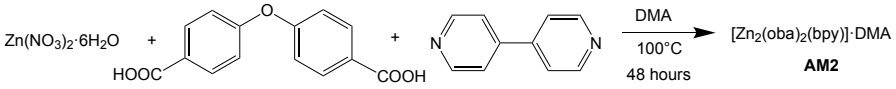

Figure 5.4: Reaction scheme detailing the synthesis of $[Zn_2(oba)_2(bpy)\cdot DMA]$ (**AM2**).

Zinc nitrate hexahydrate ($Zn(NO_3)_2\cdot 6H_2O$, 0.5 mmol, 149.1 mg) was combined with 4,4′-oxybis(benzoicacid) (H_2oba, 0.5 mmol, 129.5 mg) and 4,4′-bipyridine (bpy, 0.5 mmol, 74.5 mg) in 10 mL of N,N -dimethylacetamide (DMA) in a glass vial. The reaction mixture was stirred until all of the contents had dissolved and the solution became clear. The vial was then sealed and placed in an oven set to 100°C for 48 hours. This yielded orange coloured crystals of the MOF.

In order to activate this MOF, to afford **AM2′**, a solvent-exchange procedure was implemented whereby the crystals were submerged

in an acetonitrile (MeCN) solution for three days, after which, the crystals were left to dry under dynamic vacuum. The dried crystals were then placed in an oven at 120 °C for 1 hour.

5.2.1.3 *Eu(BTC)(H_2O)·1.5H_2O (*AM3

MOF Eu(BTC)(H_2O)·1.5H_2O (**AM3**), where BTC is benzene-1,3,5-tricarboxylate, was synthesised according to the method reported by Chen *et al.* [226], the reaction scheme for the solvothermal synthesis of this MOF is given in Figure 5.5.

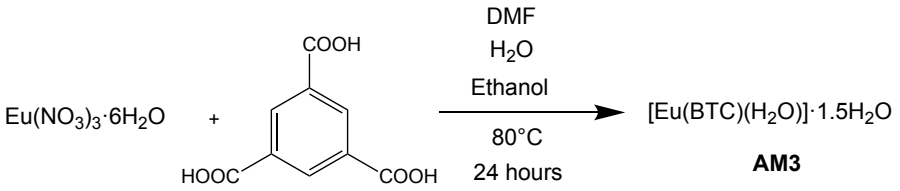

Figure 5.5: Reaction scheme detailing the synthesis of Eu(BTC)(H_2O)·1.5H_2O (**AM3**).

Europium nitrate hexahydrate ($Eu(NO_3)_3·6H_2O$, 0.074 mmol, 33 mg) was added to benzene-1,3,5-tricarboxylic acid (H_3BTC, 0.074 mmol, 16 mg) in 3 mL of N-N-Dimethylformamide (DMF), 3 mL of ethanol and 2 mL of H_2O in a glass vial. The contents of the vial were stirred until the reactants all dissolved. The vial was sealed and placed in an oven set to 80 °C for 24 hours. This resulted in colourless needle crystals of the MOF.

In order to activate this MOF, a solvent-exchange procedure was implemented, whereby the crystals were submerged in an acetonitrile (MeCN) solution for three days, after which the crystals were left to dry under dynamic vacuum at room temperature. The dried crystals were then placed in an oven at 120 °C for 1 hour, yielding **AM3'**.

5.2.2 *Solution-phase sensing methodology*

Each of the above-mentioned active MOFs were suspended in acetonitrile (MeCN) prior to solution-phase sensing experiments. These were produced (as previously described in Section 4.2.5.1) by adding 6 mg of finely ground crystals of the chosen MOF to 6 mL of MeCN. Each of the solutions were then ultrasonicated for three hours to produce the ultrafine suspensions of the MOFs used in the sensing titrations.

The solution-sensing methodology implemented for the exposure of each of the MOFs in the array (suspended in MeCN) to the analytes (Tetryl, TNT, RDX, PETN and 2,4-DNT) was the same as that described in Section 4.2.5.3. The only deviation from the previously specified procedure was the wavelength at which **AM3'** was excited and its emissions scanned (λ_{ex} = 285 nm and λ_{em} = 580 - 750 nm). All sensing titrations were repeated at least three times, for each of the analytes exposed to each of the MOFs.

5.2.3 *Linear discrimination analysis (LDA) on sensing array responses*

5.2.3.1 *LDA overview*

The machine learning technique used for the analysis of the MOF array sensor response was linear discrimination analysis (LDA), which is a classical statistical approach to supervised pattern recognition. LDA is used for both dimensionality reduction and for data classification. The method operates by constructing linear combinations of data features (e.g. the sensor responses) and serves to separate and characterise two or more classes of data (e.g. analytes). LDA seeks to maximise the separation (distance) between classes whilst also minimising the intra-class separation, given a set of defined classes [205, 207]. LDA was chosen as it is one of the simplest pattern recognition

methods to use (therefore the risk of over fitting is minimised), and it has been frequently demonstrated as a very effective tool for the classification of specific analytes such as explosives [205, 223, 228].

Generally, there are two stages to producing a predictive array using LDA; training the model and validating the model (this is true of all supervised pattern recognition techniques). Initially, a mathematical model is developed that relates a series of observations or features in the data, with their defined classification groups. For example, the model will try to identify certain features in the fluorescence quenching responses (response pattern) of a MOF array upon exposure to a particular analyte, in order to classify that response pattern to that specific and known analyte. Such classification models are referred to as *training sets* [205]. Once such a model is developed, it is then tested as to how well it predicts the classification groups from a set of 'unknowns'; this is the validation stage of the process. A simple validation method can be used whereby a set of sensor responses (termed 'trials' or 'validation test set') are left out of the initial model development and are used to probe the effectiveness of the model by evaluating how well it classifies these trial samples. Alternatively, a cross-validation approach (also known as the leave-one-out or jackknife approach) can be implemented. In this approach a single training set is used to generate the model, after this, one sample from this training set is removed and the remaining samples are used to recalculate the model. The removed sample is then used to test the model and the process is repeated until all the samples have been removed and classified [205]. It is important to note that several samples may be removed at once in some jackknife cross-validation tests and not just one. The results of the validation process as well as the results of the classification without validation of the model (in training stage) can be represented in a confusion matrix, which projects the number

of correctly classified samples in each class on the main diagonal and the misclassified samples on the off-diagonal [205]. This concept is demonstrated in Table 5.1, which shows the confusion matrix for an array exposed to ten different samples of each of the analytes a, b and c during a cross-validation process.

Table 5.1: Example confusion matrix for an array exposed to analytes a, b and c.

Analyte	a	b	c	%correct
a	10	0	0	100
b	0	9	1	90
c	0	0	10	100
Total	10	9	11	**97**

As can be seen in the example confusion matrix, the analyte a and c samples are accurately determined to be the correct analytes (therefore accurately classified) by the model 100% of the time. Whereas of the 10 analyte b samples exposed to array, only 9 of the samples were accurately classified as being analyte b, and one of the samples was classified as analyte c when it is infact analyte b; this is called a 'misclassification'. Thus, only a 90% classification accuracy is established for this analyte with the array, and the overall array is said to have a 97% accuracy based on all of the analytes tested.

The results of the clustering and classification of the data itself are most typically represented in a canonical plot, the axes of which are the highest discriminating canonical factors [205]. An illustrative example of a two-dimensional canonical plot for two analytes (1 and 2) can be seen in Figure 5.6. As can be seen, the x-axis in a canonical plot represents the highest discriminating factor of the data and the percentage of its contribution to the classification of the analyte is given in the axis label. The y-axis represents the second highest discriminating factor. The analytes are clustered based on these scores

which determine their class. These are typically circled to represent 95% confidence intervals of the cluster [215].

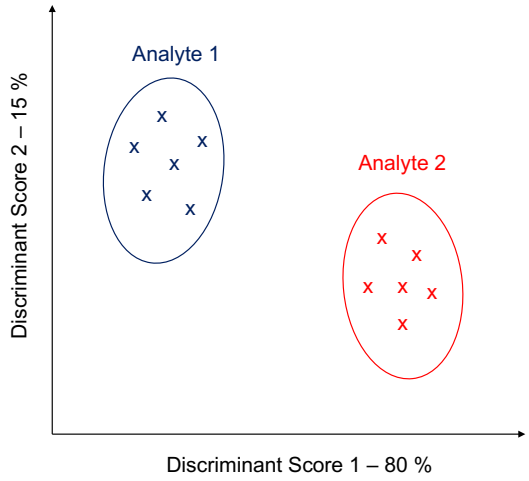

Figure 5.6: Illustrative example of a two-dimensional canonical plot clustering and classifying analytes 1 and 2. The contribution of each discriminating factor (discriminant score) to the overall clustering and classification of the analytes are given in the axis labels. The circle around the cluster represents the 95% confidence intervals of the data. Adapted from [215] with permission from The Royal Society of Chemistry.

5.2.3.2 *LDA method developement for the analyis of the MOF sensing array*

The classification of the array responses using LDA was performed in collaboration with Dr. William Peveler, Department of Chemistry, University College London.

Initially, the raw data from the fluorescence sensing experiments were manually processed to generate quenching percentages (QPs, using Equation 2.14) and $\frac{I_0}{I}$ values (where I_0 is the fluorescence emission of the MOF in the absence of the quencher and I is the fluorescence intensity of the MOF in the presence of the quencher) for each MOF in the presence of each analyte (at each concentration of analyte added and for each repeat experiment). As these values included the contributions of the MeCN dilution components (Section 4.3.2.2), 'QP - blank' and '$\frac{I_0}{I}$ - blank' were also calculated. These were obtained by the subtraction of the average (of 5 experiments) MeCN dilution

contributions (termed as 'blanks') for each MOF at each incremental volumetric addition, from the responses obtained where explosive analytes were present*.

Using SYSTAT (a statistical software package) LDA on the array response data in each of these four forms (QPs, $\frac{I_0}{I}$, QP-blank and $\frac{I_0}{I}$ - blank) at the highest analyte concentration of 62.5 μM was performed. From this initial evaluation, it was observed that the fluorescence sensing data expressed as 'QP-blank' yielded the most discrimination. In addition, this sensing response format is beneficial as it factors in the effects of dilution on the system. Therefore, the array response data was used in 'QP-blank' form for all subsequent LDA.

The LDA on the array sensing data set in QP-blank format was initially explored by running the analysis for each individual explosive concentration, e.g. running an LDA on the array response to a 62 μM addition of TNT. Whilst this yielded 100% classification for each concentration down to 38.5 μM, there were only three data points per explosive at each concentration to run the LDA on, which very much limits the power of the model and increases the risk of misclassifying unknowns. In addition, running LDA at specific concentrations does not resolve the issue of discriminating between unknown analytes at varying concentrations (as discussed in Section 5.1). Therefore, to test the discriminative identification potential of the array, LDA was run on grouped concentration data. For instance, 62.5 μM + 56.6 μM data (yielding six data points per explosive), 62.5 μM + 56.6 μM + 50.6 μM (nine data points per explosive) and so on, the classification rates and details of misclassified points were reported for each analysis. All LDAs were performed using SYSTAT, which was also used to run cross-validation (jackknife) analyses to test the model. For each LDA run; a set of four canonical factors were generated and the first two were used to generate the two-dimensional canonical plots, the

* The raw data spreadsheet file can be found in Appendix C.

axes of which were labelled with the percentage contribution of each linear contribution to the discrimination. The ellipses marked in the canonical plots were included to show one standard deviation of the mean of the cluster. It is important to note that all three of the wavelengths of **AM3'** were used in the sensor array responses that were analysed using LDA, as they each contributed meaningfully to the discrimination of the analytes.

5.3 RESULTS AND DISCUSSION

5.3.1 *MOF structure confirmation*

Powder X-ray diffraction (PXRD) was used to confirm the structures of the three MOFs used in the sensing array; $[Zn_4L(H_2O)_4 \cdot (solvent)]_n$ (**AM1**), $[Zn_2(oba)_2(bpy) \cdot DMA]$ (**AM2**), and $[Eu(BTC)(H_2O) \cdot 1.5H_2O]$ (**AM3**), which were synthesised and activated as described in Section 5.2.1. The PXRD patterns obtained from the synthesised crystals were compared with the simulated patterns for the MOFs as obtained from single crystal X-ray diffraction†. By virtue of the matching of diffraction peaks between the simulated and as-synthesised PXRD patterns for all three of the metal-organic frameworks (Figure 5.7), it was concluded that the synthesised MOFs were of the expected topology. The active frameworks (**AM1'**, **AM2'** and **AM3'**) were also in accordance with the previously reported MOF structures [127][226]. To test the stability of the three MOFs in acetonitrile (the solvent medium used for sensing experiments) the crystals of the activated MOFs were immersed in MeCN for 24 hours, after which they were filtered and

† For MOFs $[Zn_2(oba)_2(bpy) \cdot DMA]$ (**AM2**) and $[Eu(BTC)(H_2O) \cdot 1.5H_2O]$ (**AM3**) the simulated PXRD patterns were generated from the MOF crystallographic information files (CIF) obtained from the Cambridge Crystallographic Data Centre (CCDC).

analysed using PXRD. As shown in Figure 5.7, all three of the MOFs maintain their structural integrity when immersed in MeCN.

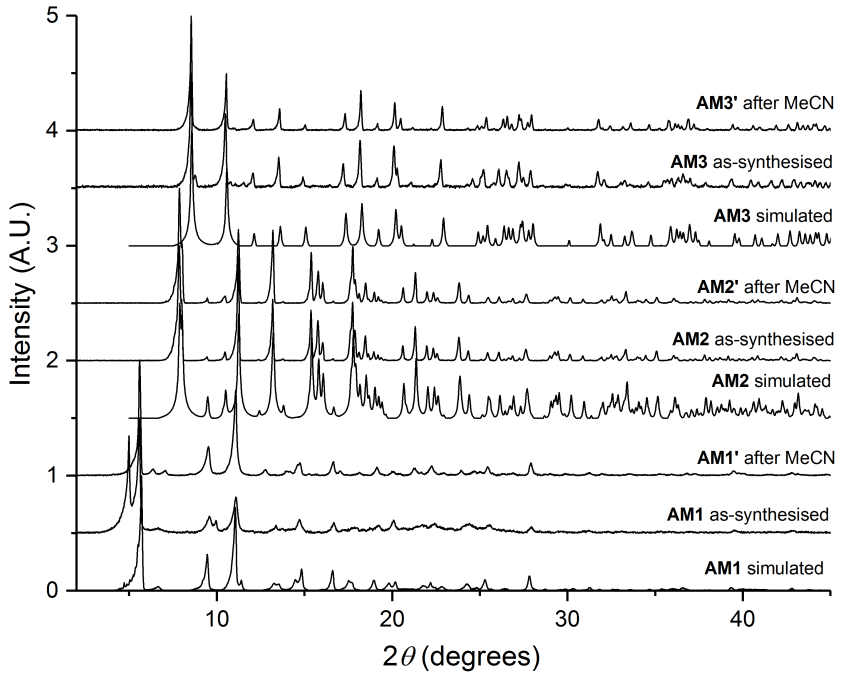

Figure 5.7: Powder X-ray diffraction patterns of the simulated (as obtained from single crystal x-ray diffraction data) and as-sythesised MOFs $[Zn_4L(H_2O)_4{\cdot}(solvent)]_n$ (**AM1**), $[Zn_2(oba)_2(bpy){\cdot}DMA]$ (**AM2**), and $[Eu(BTC)(H_2O){\cdot}1.5H_2O]$ (**AM3**). As well as the PXRD patterns of the active MOFs **AM1′**, **AM2′** and **AM3′** after immersion in acetonitrile (MeCN) for 24 hours. The peak splitting observed for **AM1**-as synthesised in this case is believed to an artefact of the PXRD measurement as opposed to a different synthesised phase.

5.3.2 *Fluorescence sensing results*

Each of the array MOFs demonstrated strong fluorescence emissions while suspended in MeCN (the MOF sensing suspensions were produced as described in Section 5.2.2). MOFs **AM1′** and **AM2′** demonstrated fluorescence emission maxima at 348 nm and 470 nm when excited at 315 nm respectively. The fluorescence emission of **AM2′** was observed to be slightly red-shifted from that reported by Li *et al.* (420 nm) [127]. This could be as a result of a different wavelength of excitation used in these experiments compared to previous (315 *vs*.

280 nm respectively), or due to the previous emission of **AM2'** having been recorded on a solid sample of the MOF and not a suspension (or a combination of these two factors). Upon excitation of **AM3'** at 285 nm three different fluorescence emissions of the MOF were observed; at 589, 615 and 700 nm, and coincide with the fluorescence emissions previously reported for this MOF in acetonitre by Chen *et al.* [226]. Through the implementation of a vortexing step (as described and discussed in Section 4.3.2.2); stable baseline measurements of these MOFs in suspension were obtained prior to sensing experiments, example graphs of which can be found in Appendix C.

Each of the array MOF sensors were titrated against the explosives: Tetryl, TNT, RDX, PETN and the TNT derivative 2,4-DNT, according to the sensing procedure previously outlined in Section 4.2.5.3. The results of these sensing titrations can be seen in the Stern-Volmer plots ($\frac{I_0}{I}$ v [Q]) in Figure 5.8.

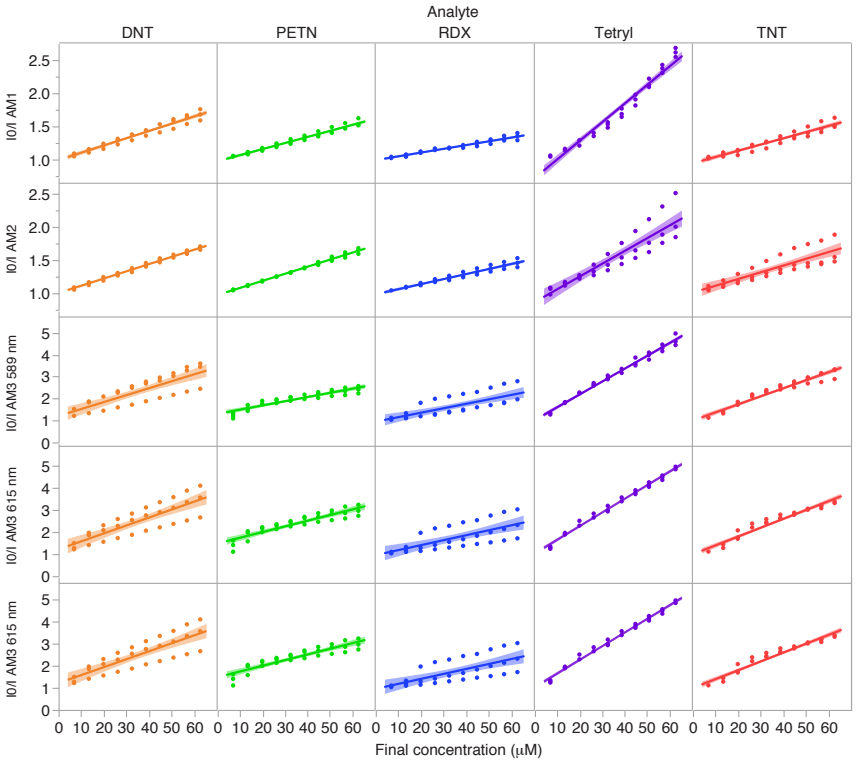

Figure 5.8: The sensing responses of the array MOFs **AM1'**, **AM2'** and **AM3'** ($[Zn_4L(H_2O)_4]$, $[Zn_2(oba)_2(bpy)]$ and $[Eu(BTC)(H_2O)]$ respectively) upon exposure to Tetryl, TNT, RDX, PETN, and 2,4-DNT, given as Stern-Volmer quenching plots. In these plots, the straight line fit is also shown.

The responses from the different MOFs in the array appear varied for the different analytes. For example, all three MOFs demonstrate the greatest quenching responses in the presence of Tetryl and seemingly the weakest (if any) responses upon the addition of RDX. However, based on visual observations alone, the sensing responses of the three MOFs towards the same analytes appear very similar, thus, demonstrating the need to use machine learning approaches for pattern recognition.

The sensing responses were also represented as quenching percentages (QP, as calculated by Equation 2.14), these showed similar responses to the SV plots and again any distinct patterns between the sensors were impossible to visually identify. Nevertheless, whilst these two commonly used formats for the presenting of MOF sens-

ing data are effective for response visualisation, they do not take into consideration the effects of solvent dilution.

As discussed in Figure 4.3.2.2, the addition of MeCN solvent (in which the MOFs are suspended and the explosives diluted) causes a quench of the MOF system owing to the solvent diluting the MOF suspension. Therefore, the dilution factor should be taken into account when trying to identify the true response of the MOFs in the presence of target analytes, as what might seem like a sensor response; could simply be an artifact of dilution. For example, from the data presented in Figure 5.8, it is unclear whether the weak responses of the MOFs in the presence of RDX are real (but poor) responses of the MOFs, or whether they are due to dilution effects. Therefore, the array sensing responses were also computed as '$\frac{I_0}{I}$ - blank' and 'QP-blank', whereby the dilution components ('blanks') were subtracted from the MOF responses in the presence of the explosive analytes (as described in Section 5.2.3.2).

5.3.3 *Results of linear discrimination analysis (LDA)*

As discussed in Section 5.2.3.2, during preliminary LDA testing, it was observed that the array sensing responses expressed in the 'QP-blank' format (as shown in Figure 5.9) gave the greatest discrimination of analytes whilst also accounting for dilution. Therefore, the sensing data presented in this form was used as the array response pattern for all subsequent LDA.

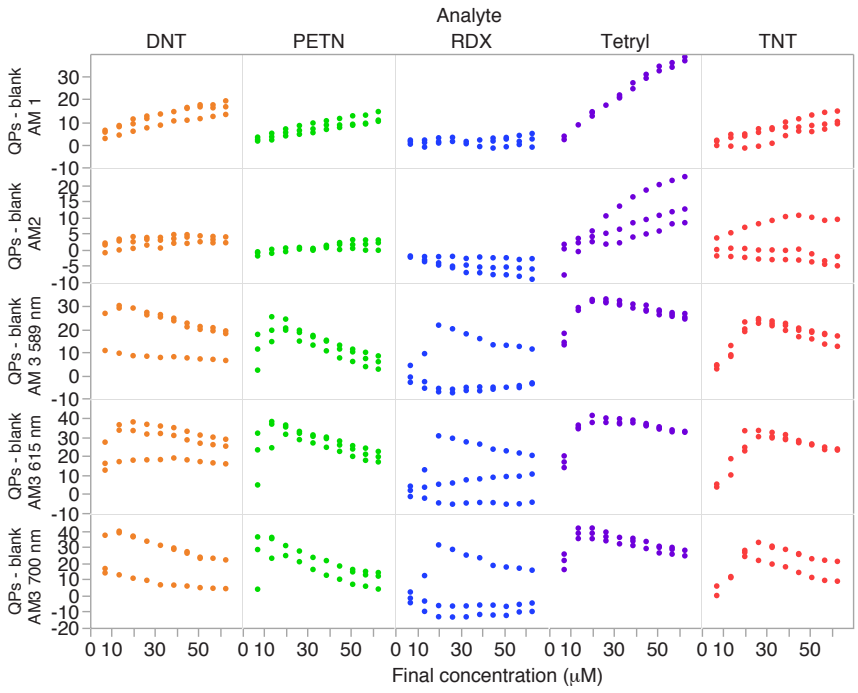

Figure 5.9: MOF array response pattern obtained for the MOFs AM1, AM2 and AM3 ($[Zn_4L(H_2O)_4]$, $[Zn_2(oba)_2(bpy)]$ and $[Eu(BTC)(H_2O)]$ respectively) upon exposure to Tetryl, TNT, RDX, PETN, and 2,4-DNT, presented in quench percentage - solvent contribution ('QP - blank') format, used for LDA.

In order to allow for the identification of the above mentioned explosives (and related compounds) at different concentrations using this proposed MOF array; the responses of the array at the different analyte concentrations were grouped together and linear discrimination analysis was performed on the response pattern generated for these ranges of concentrations (as discussed in Section 5.2.3.2).

An iterative process was implemented to evaluate the lowest concentration level that could be included in the LDA whilst still maintaining good classification rates and examining which data points misclassify. It was hypothesised that the low concentration samples would misclassify first as they would 'look most similar' to the array.

A missclassification of an analyte is where the LDA model identifies an unknown that is exposed to the array as the wrong classification (analyte class) e.g. the array was exposed to TNT but the array identified it as RDX.

Initially, LDA was performed on the array response to the concentration range 62.5 μM - 38.5 μM. The canonical plot, classification matrix and the jackknifed classification matrix are given in Figure 5.10, Table 5.2 and Table 5.3 respectively.

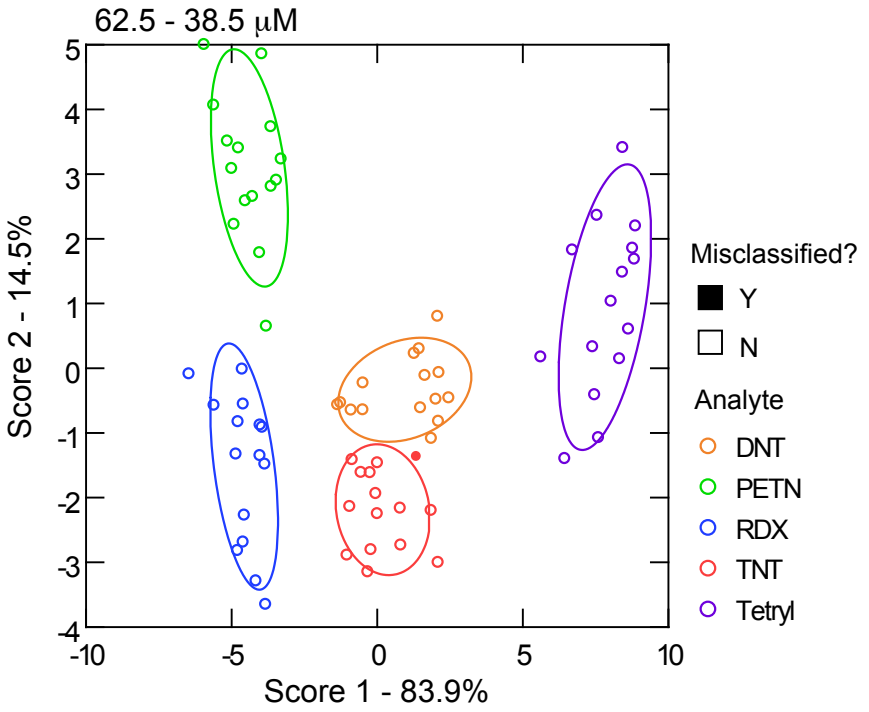

Figure 5.10: A canonical plot showing the classification results of the LDA on the MOF array sensing responses to the explosive (and related) analytes in the 62.5 μM - 38.5 μM concentration range. Accurately classified points are denoted by hollow circles and misclassified points are represented by coloured circles. The ellipses marked on the plot show one standard deviation of the cluster mean.

Table 5.2: LDA classification matrix for the MOF array upon addition of the explosive (and related) analytes in the 62.5 μM - 38.5 μM concentration range.

Analyte	2,4-DNT	PETN	RDX	TNT	Tetryl	%correct
2,4-DNT	15	0	0	0	0	100
PETN	0	15	0	0	0	100
RDX	0	0	15	0	0	100
TNT	1	0	0	14	0	93
Tetryl	0	0	0	0	15	100
Total	16	15	15	14	15	**99**

Table 5.3: LDA cross-validation (jackknifed) classification matrix for the MOF array upon the addition of the analytes in the 62.5 μM - 38.5 μM range.

Analyte	2,4-DNT	PETN	RDX	TNT	Tetryl	%correct
2,4-DNT	14	0	0	1	0	93
PETN	0	15	0	0	0	100
RDX	0	1	14	0	0	93
TNT	3	0	0	12	0	80
Tetryl	0	0	0	0	15	100
Total	17	16	14	13	15	**93**

The results of the LDA on the pattern response yielded by the MOF array upon exposure to the explosives (and related) analytes in the 62.5 μM - 38.5 μM concentration range, show that the array gives a 99% classification accuracy. This means that 99% of the time, this MOF-based sensor array (with LDA) could accurately identify the explosive (or related) analyte to which it was exposed. The one misclassification observed was a TNT analyte being misclassified as 2,4-DNT. Interestingly, this misclassified TNT sample was of the highest concentration (62.5 μM).

Table 5.3 shows the jackknifed classification (the procedure of which is described in Section 5.2.3.2) for this same concentration range of analytes exposed to the array. As can be seen, the jackknife classification process gave a 93% classification. The three misclassifications arose from two TNT analytes being misclassified as 2,4-DNT and one PETN was mistaken for an RDX.

For the concentration range of 62.5 µM - 32.3 µM, LDA yielded a 96% classification accuracy with two TNT analyes being misclassified as 2,4-DNT, and one vice versa. In addition, one RDX was misclassified as PETN. The jackknifed classification gave a 93% classification accuracy with the same aforementioned misclassifications, as well as one more TNT and 2,4-DNT each being misclassified as each other‡.

The canonical plot yielded from the LDA analysis of the MOF array response pattern obtained from the addition of the analytes in the 62.5 µM - 26.0 µM concentration range is given in Figure 5.11. The array was able to classify analytes with a 94% accuracy for this concentration range (as evidenced in Table 5.4). However, the jackknifed classification accuracy dropped to 89% (Table 5.5), indicating an increase in the variance of the responses given by each of the lower concentration samples.

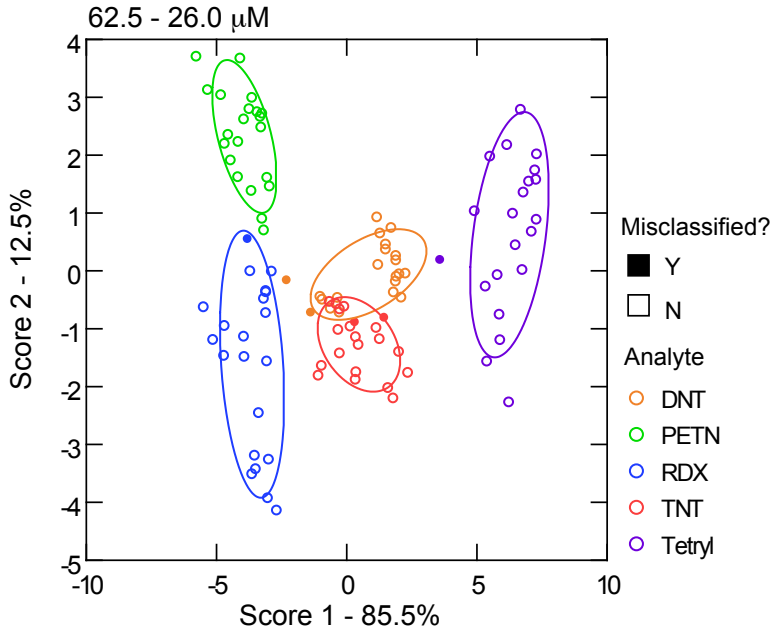

Figure 5.11: Canonical plot showing the classification results of the LDA on the MOF array sensing responses to the tested analytes in the 62.5 µM - 26.0 µM range. Accurately classified points are denoted by hollow circles; misclassified points are represented by coloured circles. The ellipses show one standard deviation of the cluster mean.

‡ The canonical plot, classification matrix and the jackknifed classification matrix can be found in Appendix C.

Table 5.4: LDA classification matrix for the MOF array upon addition of the explosives and related analytes in the 62.5 μM - 26.0 μM concentration range.

Analyte	2,4-DNT	PETN	RDX	TNT	Tetryl	%correct
2,4-DNT	19	0	1	1	0	90
PETN	0	21	0	0	0	100
RDX	0	1	20	0	0	95
TNT	2	0	0	19	0	90
Tetryl	1	0	0	0	20	95
Total	22	22	21	20	21	**94**

Table 5.5: LDA jackknifed classification matrix for the MOF array upon addition of the analytes in the 62.5 μM - 26.0 μM range.

Analyte	2,4-DNT	PETN	RDX	TNT	Tetryl	%correct
2,4-DNT	18	0	1	2	0	86
PETN	0	21	0	0	0	100
RDX	0	2	19	0	0	90
TNT	6	0	0	15	0	71
Tetryl	1	0	0	0	20	95
Total	25	23	20	17	20	**89**

The results of LDA on the array response to the addition of the analytes in the 62.5 μM - 19.6 μM concentration range gave an 84% LDA classification and the jackknife classification accuracy was observed to be 82%, with the canonical plot showing a greater extent of spread in the data (as evidenced in Appendix C). As a result, the concentration levels below this were not investigated further owing to the array becoming less predictive in nature and thus, less useful for the detection and identification of the explosives. It should be noted however, that using the full data set down to the lowest concentration (6.6 μM) yielded an accuracy of 78% which is still a potentially useful amount of discrimination at this low concentration.

The results of the linear discrimination analyses on the MOF array responses to the different grouped analyte concentration ranges suggest that this MOF-array is able to differentiate between most samples at a potentially acceptable accuracy (> 80%) for both the array with-

out validation and with jackknife validation above 20 μM at a range of concentrations. Interestingly, it is also important to note that the array is able to detect and identify PETN and RDX, often without much misclassification (especially for concentration ranges of 62.5 μM - 26 μM and higher). This is significant as these analytes are often difficult to detect and identify using chemical sensors owing to their aliphatic bulky nature, and weak electron withdrawing ability [229].

5.4 CONCLUSIONS AND FUTURE WORK

The aim of the work presented in this chapter was to investigate whether metal-organic frameworks could be used in sensor-arrays for the discriminative identification of explosives and related compounds.

A three-MOF chemical-nose was constructed using one novel MOF ($Zn_4L(H_2O)_4 \cdot (solvent)_n$, as previously characterised and discussed in Chapter 4) and two previously reported MOF structures [127, 226]. Each of which was judicially chosen with aim to impart varied responses to the explosives tested; based on their different topologies. The MOFs in the array were tested for their fluoresce-based quenching responses towards Tetryl, TNT, RDX, PETN and 2,4-DNT *via* solution-phase titrations; exposing the MOFs to a concentration range of 6.6 μM - 62.5 μM of the analytes. The sensing responses of the MOFs were computed as QP-blank (where QP = quenching percentages, and 'blank' = the dilution factor correction) and were analysed using linear discrimination analysis (LDA), chosen by virtue of its simplicity and effectiveness in the classification of specific analytes. The LDA analysis was run on grouped responses of the array upon exposure to different analyte concentrations. This was performed in order to allow for the array to discriminate not only between ana-

lytes of the same concentration (when introduced into the array as unknowns), but also be able to identify unknown analytes of unknown concentration (providing that the concentration of the unknown lies within the range tested). An iterative process was implemented to evaluate the lowest concentrations feasible for inclusions into the model that would still yield good classification rates.

It was observed that the LDA on the MOF array sensing responses to the analytes in the 62.5 μM - 26.0 μM concentration range gave a 94% classification accuracy for the entire array and an 89% accuracy when the model was cross-validated using a jackknife (leave-one-out) approach. It was suggested that below an analyte concentration of 20 μM the array became less useful, based on an increasing number of misclassifications upon the incorporation of the array sensing responses at lower concentrations. However, a 78% classification was still possible when the entire concentration range sensing data was used in the model. These results clearly demonstrate that the discrimination of these tested analytes is possible when they are exposed to this MOF sensing array. In addition, this MOF array was able to detect and identify the challenging explosives RDX and PETN. Therefore, suggesting that constructing chemical-noses could be a useful strategy for imparting discriminative power into MOF-based sensors. However, this work is very much in its infancy and should be viewed as a proof-of-concept experiment; plentiful further work is required in order to confirm (or deny) the potential of MOF-based arrays for the discriminative detection of explosives.

One significant issue not addressed by this work is the effects of interferents on MOF-based arrays. Whilst in theory, array-based sensors operate on the concept on interference, i.e. they work on the basis of the sensors not being specific towards one compound but responsive to groups of similar compounds for discriminative detection based

Interferents are chemicals that may interfere with the detection of target analytes using trace systems [36]

on pattern identification [60]; the effect of intereference should still be evaluated for the system. It is hypothesised that compounds such as nitrobenzene may add confusion to the array if added in large quantities, owing to its similar chemical and electron-poor nature to the other nitroaromatics tested. However, potentially through training of the array using such compounds, the effects of misclassification may be minimised. In addition, nitrobenzene is often associated with the presence of explosives [230, 231] and so its identification could indicate as to their presence.

In essence the work presented in this chapter is a good starting point for future work investigating the use of MOFs in sensing-arrays for explosives detection and identification, some ideas for such future work will be presented in Chapter 7.

6

A MOF AS AN EXPLOSIVES VAPOUR PRE-CONCENTRATOR

6.1 INTRODUCTION

This chapter explores the use of MOF **3**, $Zn_4L(H_2O)_4 \cdot (solvent)_n$, (as synthesised, characterised and discussed in depth in Chapter 4) as a trace explosive vapour pre-concentrator.

As discussed (Section 2.3.2.2), the effective vapour-phase detection of trace explosives in real-world scenarios is a challenging task for any analytical system due to the inherently low vapour pressures of many explosives; this is particularly true when detecting explosives in open air environments such as transportation hubs [232]. Whilst efforts to improve the intrinsic sensitivity of vapour-phase detectors is very important, a simpler and potentially timelier solution to the sensitivity challenge is to interface current detectors with sub-systems for enhanced vapour sampling, such as, pre-concentrators [232].

Vapour-phase pre-concentrators are sorbent materials that effectively behave as chemical sponges. They trap target analytes* from large volumes of air that are drawn over them, where the analytes are present in low and potentially undetectable concentrations. The trapped analytes are then subsequently liberated, generally through the application of heat, to deliver enriched concentrations in smaller air volumes to an interfaced detector. This increases the probability of detection of the target analytes with the concentration-sensitive detec-

* It is important to note that target analytes are not just limited to explosives. Pre-concentrators can be used to trap a wide variety of analytes including volatile organic compounds [233].

tors [36][234]. Such detectors could include some of those discussed in Section 2.4 such as; ion-mobility spectrometers (IMS) or gas chromatography - mass spectrometers (GC-MS). This concept of explosive vapour pre-concentrators is illustrated in Figure 6.1.

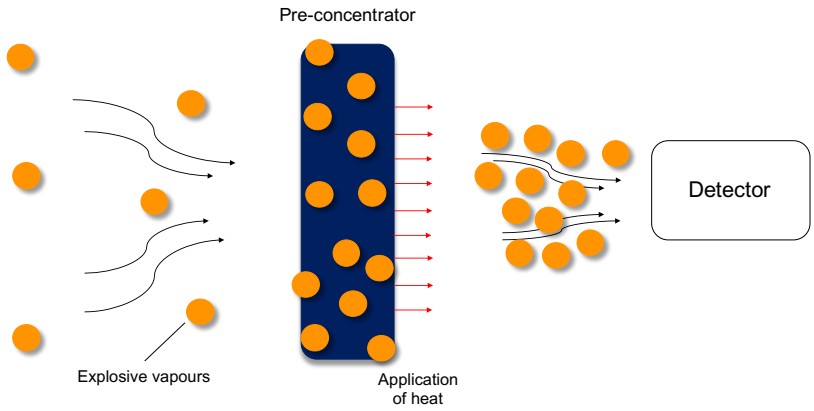

Figure 6.1: Schematic detailing the principles of explosive vapour pre-concentration.

An ideal pre-concentrator sorbent should:

- Have the ability to effectively sorb (adsorb or absorb) target analytes with some degree of selectivity. For example, an explosive vapour pre-concentrator should only capture explosive compounds of interest and not interfering analytes present within the detection environment, such as water molecules (humidity) [235].

- Be able to retain the captured analytes until they are required to be injected or transferred (using a controlled release mechanism) into the chosen detector [236]. Sorbent materials that are able to hold on to captured analytes until they are required to be released (typically through the application of heat) are termed *'low bleeding'* materials.

- Effectively liberate trapped analytes when required to do so. A pre-concentrator material that interacts with target analytes so

strongly that it does not release them, preventing their detection, is detrimental to its purpose [237].

- Have the ability to be re-used. Ideally a pre-concentrator should be able to capture and release target analytes for many cycles of use [44].

A commonly encountered and commercially maufactured pre-concentrator sorbent is the organic polymer poly(2,6-diphenylphenylene oxide), most commonly known as Tenax® TA. The molecular structure of one of the Tenax® TA polymer repeat units is given in Figure 6.2 [238].

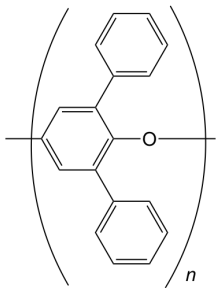

Figure 6.2: Molecular structure of one repeat unit of the organic polymer poly(2,6-diphenylphenylene oxide), more commonly known as Tenax® TA.

Tenax® TA has most frequently been explored for the pre-concentration of volatile organic compounds (VOCs) and is able to pre-concentrate a wide range of analytes [236][239]. It is a hydrophobic, low bleeding, porous sorbent with a reported surface area of 35 m^2/g [238][240]. In addition, Tenax® TA has been shown to be effective at the capture and release of explosive vapours [241][242].

Other explored pre-concentrator sorbent materials (for both VOCs and explosives) include zeolites [232] and graphitized carbon black sorbents such as Carbopack™[243].

More recently, metal-organic frameworks have emerged as promising pre-concentrator materials, most notably for volatile organic compounds. This is due to their characteristic high surface areas and

porosities, as well as the ability to fine tune their chemical compositions and pore environments for targeted MOF-analyte interactions (as discussed in Section 2.6.1). These properties should allow MOFs to be able to capture large amounts of target analytes with some degree of selectivity.

A handful of groups have explored the use of MOFs for the pre-concentration of volatile organic compounds (VOCs) [244–247] and one group reported the use of a MOF for the pre-concentration of dimethyl methylphosphonate (DMMP), a simulant nerve agent [248].

Whilst the good sensitivity (ppb limits of detection) of MOF sensors towards explosives (or related analytes) has frequently been attributed to their pre-concentrator capabilities [67], only two papers to date publish on the use of MOFs as pre-concentrator sorbent materials for explosives (and not as sensors). Keffer *et al.* evaluated the potential of five different MOFs for the pre-concentration of RDX vapours based on computational simulations (classical molecular dynamics and grand canonical Monte Carlo simulations). The group reported that MOFs can be tailored for the effective and selective pre-concentration of RDX [249]. The only experimental evaluation of MOFs as explosives pre-concentrators thus far has been the research presented by Rao *et al*. The group reported how the use of a MOF in combination with an organic semiconductor sensor yielded a sensitive response towards TNT and RDX vapours (ppb and ppm levels of detection for the two analytes respectively), which was attributed to the pre-concentrator capabilities of the MOF [250]. However, the pre-concentration contribution of the MOF to this reported sensitivity was not evaluated, nor did the group report any data to suggest the MOF was behaving as a pre-concentrator and thus increasing the sensitivity of the sensor.

Therefore, the work presented in this chapter is a pioneering contribution to the field that explores the experimental potential of MOFs as standalone explosive vapour pre-concentrator materials. This chapter probes the use of MOF **3**, in its solvent-free form, MOF **3'** (produced as described in Section 4.2.3), as a TNT vapour pre-concentrator. TNT was chosen as the target analyte owing to its relatively low saturated vapour pressure (5.5×10^{6} Torr at 25 °C [30]) which makes it a challenging explosive to detect [23]. The MOF itself was chosen by virtue of its theoretically large pores that are capable of encapsulating TNT molecules (as discussed in Section 4.3.1.2), its good humidity stability (Section 4.3.1.7) and the knowledge that this MOF is a good solution-phase sensor of this anlayte (as demonstrated in Section 4.3.2.3). Figure 6.3 summarises the experimental design implemented in order to evaluate the capability of the MOF (**3'**) to preconcentrate TNT vapours, the results of which will be discussed and evaluated in this chapter.

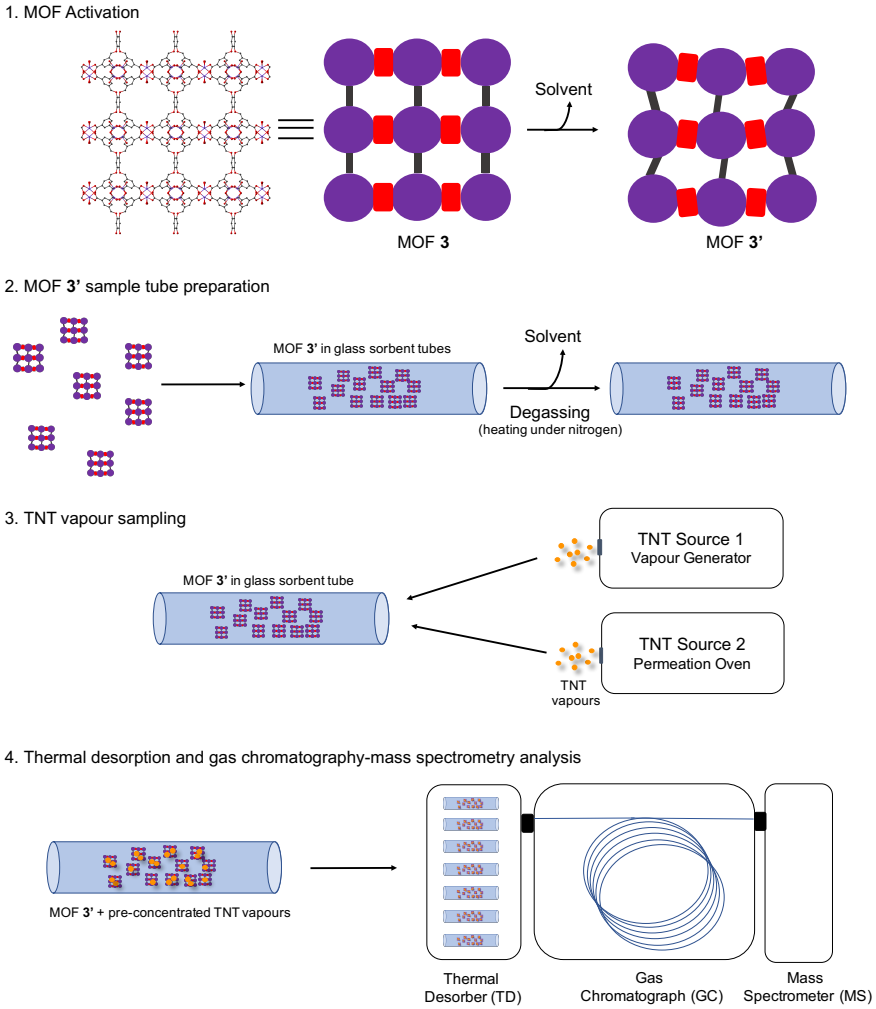

Figure 6.3: Schematic summarising the experimental design implemented in order to probe the capability of MOF **3′** as a TNT explosive vapour pre-concentrator.

1. **MOF activation** - MOF **3** was activated (using the procedure detailed in Section 4.2.3) in an attempt to remove the solvent molecules present within the pores of the MOF originating from its solvothermal synthesis. It is proposed that this activation yields MOF **3′** which has unevenly shaped pores and a slightly contracted unit cell volume in comparison to the as-synthesised MOF (**3**) structure (as discussed in Section 4.3.1.5 and illustrated in Figure 6.3). Nevertheless, MOF **3′** is porous and stable in its active form (Section 4.3.1).

2. **MOF 3′ pre-concentrator sample tube preparation** - The active MOF **3′** crystals (with a fixed mass) were inserted into glass sampling tubes that were used in the pre-concentration experiments. These MOF **3′**-containing tubes were then degassed in an attempt to remove any persistent solvents molecules within the MOF pores remaining from the activation step (we know from Section 4.3.1.7 that the solvent-exchange activation method is not 100% effective). The degassing step involved the heating the of MOF **3′** containing tubes at set temperatures under nitrogen. It is these degassed MOF **3′** tubes that were used in the vapour sampling stage.

3. **TNT vapour sampling** - The degassed MOF-containing tubes were used to sample the TNT vapours of known concentrations produced from one of two sources; either the vapour generator or permeation oven source.

4. **Thermal desorption and GC-MS analysis** - Post-sampling of the TNT vapours, the MOF **3′** tube samples containing the captured TNT analytes were placed in a thermal desorption unit which was interfaced with a gas chromatography-mass spectrometer (GC-MS). Therefore, upon the application of heat, the trapped TNT molecules were liberated from the MOFs and injected into the GC-MS for separation and quantitative analysis.

As will be discussed throughout this chapter, varying the degassing conditions and the sampling from the different TNT sources yielded contrasting pre-concentration capabilities† of the MOF **3′** samples.

† It is important to note that these experiments do not strictly evaluate the capability of MOF **3′** as a pre-concentrator in the definitive sense as the vapours being captured are not present in very large air volumes nor in very low concentrations. However, evaluating the capture and release efficiency - termed pre-concentrator efficiency - of the material in this way gives a good indication as to the sorbent material's pre-concentration capabilities. Thus, these experiments will still be termed as 'pre-concentration evaluation experiments' and the term 'pre-concentration' will refer to the capture and release of the available TNT vapours by the sorbent materials.

The pre-concentration capabilities of the MOF **3′** samples were evaluated by calculating their pre-concentrator efficiency (PE); which is essentially a percentage of the amount of TNT vapours captured and released by the MOFs, compared to the amount of TNT available for capture and release (pre-concentration) as shown in Equation 6.1.

$$\mathrm{PE} = \frac{\text{Amount of vapours pre-concentrated (captured and released)}}{\text{Amount of vapours available for pre-concentration}} \quad (6.1)$$

In addition, the pre-concentration efficiencies of the MOF **3′** samples were compared with those yielded by commercially purchased Tenax® TA samples; in order to benchmark the MOFs' potential for this application.

The work presented in this chapter was completed in collaboration with the Explosives Detection Group, part of the Counter Terrorism and Security Division of the Defence Science and Technology Laboratory (Dstl). The research facilitated by this collaboration allows for the further probing of the potential of MOFs for real-world trace explosives detection applications, and reaches far beyond that possible within a university laboratory.

6.2 EXPERIMENTAL

6.2.1 *Sample tube preparation*

6.2.1.1 *MOF 3′ in glass tubes*

Glass tubes containing samples of MOF **3′** were used for TNT vapour pre-concentration. Initially, empty glass tubes were washed with isopropyl alcohol (IPA) and acetone, then left to dry at 50 °C for an hour. Each glass tube was then filled with 40 mg of MOF **3′** crystals. The MOF **3′** crystals used were obtained from amalgamated synthetic batches, synthesised and activated in the same way as discussed in Section 4.2.2 and Section 4.2.3. Commercially purchased and untreated glass wool was used to block the ends of each glass tube (approximately 75 mg in each end) to ensure the MOF crystals remained contained, as illustrated in Figure 6.4.

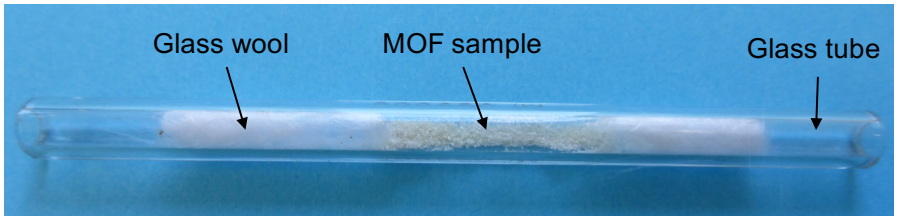

Figure 6.4: A representative MOF **3′**-containing glass sample tube used for TNT pre-concentration experiments.

Prior to their use, each MOF-containing glass tube was degassed (or 'thermally conditioned') using a Markes International Ltd. tube conditioner (Figure 6.5). This instrument heats the glass tubes at specific temperatures for set amounts of time, whilst also passing nitrogen through the tubes. The samples were heated at either 230 °C for 10 - 30 minutes, 100 °C for 1 hour or 150 °C for 1 hour. The nitrogen flow was kept at a constant pressure of 20 psi during all degas experiments.

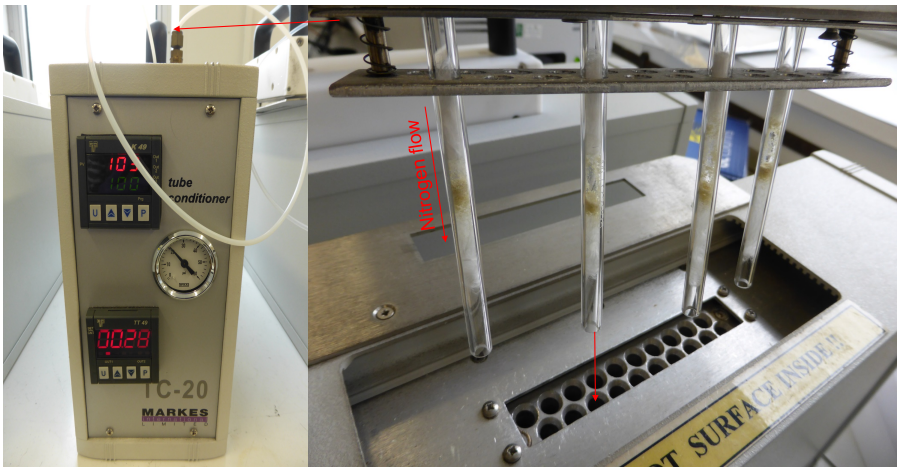

Figure 6.5: Markes International Ltd. tube conditioner used for the degassing of the sorbent sample tubes.

6.2.1.2 *Tenax® TA in glass tubes and stainless steel tubes*

A '60:80 mesh' means that the majority of the Tenax® TA particles are between 177 µm (80 mesh) and 250 µm (60 mesh) in size [251].

Glass tubes containing 40 mg of Tenax® TA (60 : 80 mesh) were fabricated in the same way as detailed above for the MOF-containing glass tubes. These tubes were degassed at 230 °C for 1 hour.

Stainless steel tubes containing 200 mg of Tenax® TA were used for the quantification and variability testing of the TNT vapour sources (discussed in Section 6.2.2). These were also degassed at 230 °C for 1 hour‡.

6.2.1.3 *Glass tubes containing glass wool only*

TNT vapours were also collected on glass tubes containing only 150 mg of glass wool (75 mg in each end with void space in the middle). These tubes were also degassed at 230 °C for 1 hour.

6.2.2 *Vapour generation and sampling*

Two different sources of TNT vapours were used for sampling during the pre-concentration experiments. One method generated TNT

‡ Images of the two types of Tenax® TA sample tubes can be seen in Appendix D.

vapours through the use of a manufactured vapour generator[§] and the other made use of a permeation oven to deliver vapours generated from solid TNT flakes.

6.2.2.1 *Vapour generator method for TNT vapour production*

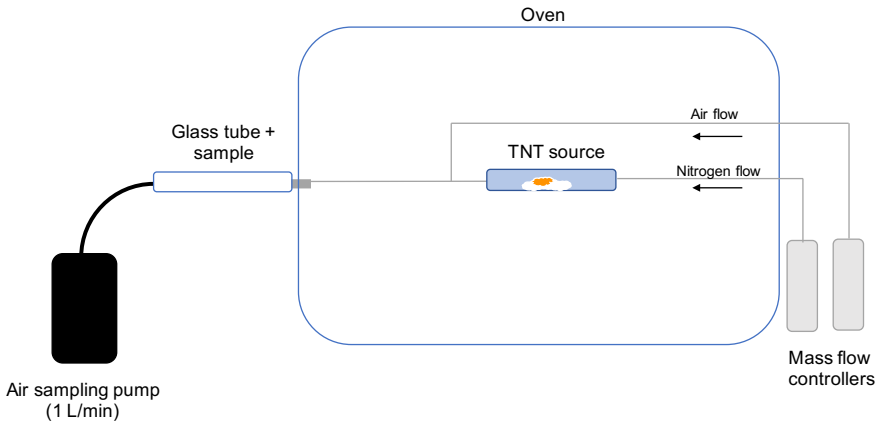

Figure 6.6: A simplistic schematic of the vapour generator instrument used to produce known quantities of TNT vapours. For confidentiality purposes this is not an accurate representation of the instrumental set-up.

Figure 6.6 gives a simplified representation of the vapour generator system used to produce known quantities of TNT vapours. This is not a complete representation of the instrumental set-up due to issues regarding manufacturer confidentiality, but it allows for a general understanding of the vapour generation process. Further to this, the method used to generate the TNT source, which is simply a casing in which glass wool containing solid TNT is enclosed, will also not be detailed for the same reasons.

The Dstl protocol for setting up the vapour generator was used in order to produce the TNT vapours available for sampling from this instrument. The TNT source (prepared following the manufacturer guidelines which are unable to be detailed) was placed into the vapour generator where N_2 gas at a specific flow rate was passed

§ For confidentiality reasons the manufacturer cannot be named and the specific instrumental set-up, including the TNT source preparation, will not be detailed.

through the source (controlled by mass flow controllers), diluting the TNT saturated headspace vapours produced. The N_2 containing TNT vapours were further diluted through the mixing with air flows (of controlled and known flow rates), eventually delivering a known concentration of TNT vapour in a specific flow rate to the output of the vapour generator. The oven in which the vapour generator was contained was kept at 57 °C. The theoretical output concentration for TNT using this oven temperature and including diluent flows was calculated to be approximately 103 ng/ L (11 parts per billion), delivered at a flow rate of 1200 mL/min. However, the pre-concentration experiments did not rely on this theoretical TNT output concentration, the vapours being produced from the generator were quantified using gas chromatography - mass spectrometry (as discussed in Section 6.2.2.3) prior to the pre-concentration experiments.

During sampling, one end of a glass or steel tube containing the sorbent sampling material was placed adjacent to the outlet of the vapour generator, the other end of each tube was attached to an air sampling pump operating at 1 L/min as shown in Figure 6.6 and Figure 6.7. Regardless of the sorbent or sampling tube type, the TNT vapours produced by the vapour generator were actively sampled for 5 minutes.

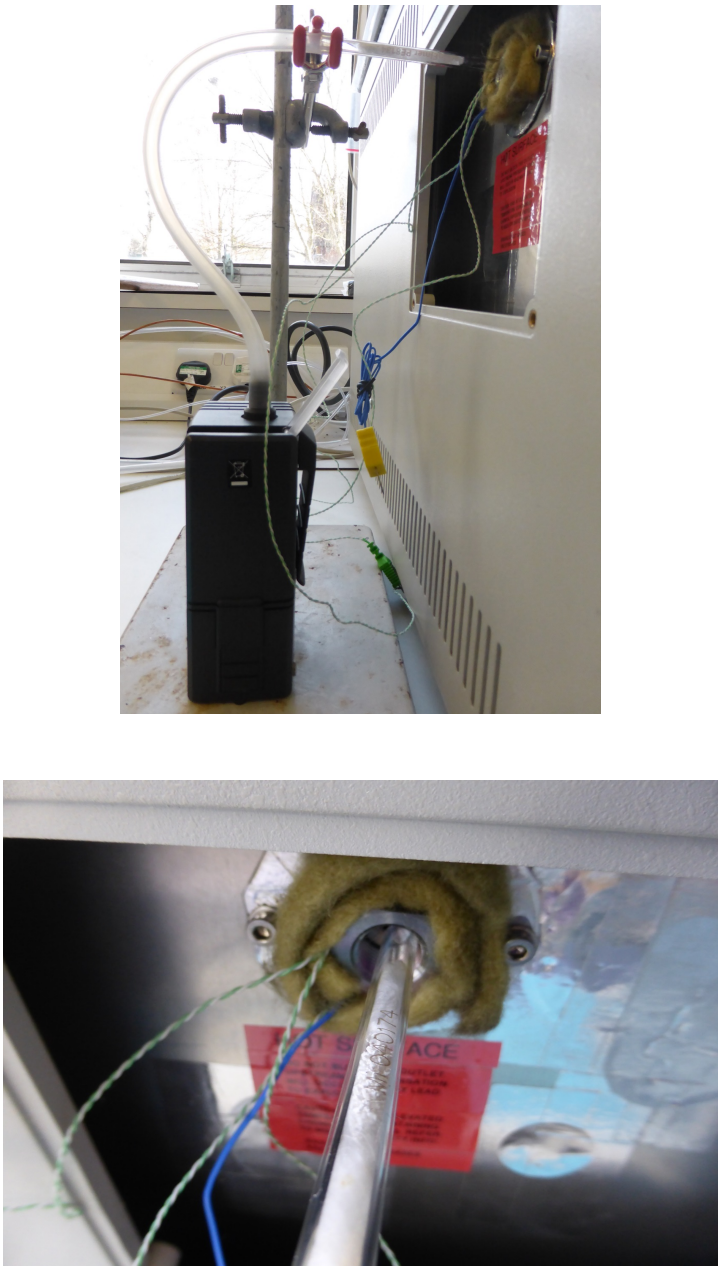

Figure 6.7: The sampling technique employed for the collection of TNT vapours produced from the vapour generator. Top: Representation of how the air sampling pump is attached to the sampling tubes (glass tubes containing Tenax® TA in this specific example) and how they are interfaced with the vapour generator outlet. Bottom: A close up showing how the sampling tubes (in this case glass tubes containing Tenax® TA) are interfaced with the vapour generator outlet by placing the end of the tube adjacent to the outlet hole.

6.2.2.2 *Vapour generation from solid TNT flakes contained within a permeation oven*

The second source of TNT vapours were generated from solid TNT flakes (100 mg) that were contained within a glass tube placed inside a permeation oven (operating at 40 °C), as shown in Figure 6.8. A flow of nitrogen (regulated using a mass flow controller) was passed through the tube delivering vapours of TNT (diluted in nitrogen) to the outlet at a flow rate of 80 mL/min. The theoretically expected TNT output was not calculated owing to the saturated vapour pressure of TNT inside the tube typically not being observed using this set up. The vapours being omitted from this source were quantified using gas-chromatography mass spectrometry prior to each pre-concentration experiment (as described in Section 6.2.2.3).

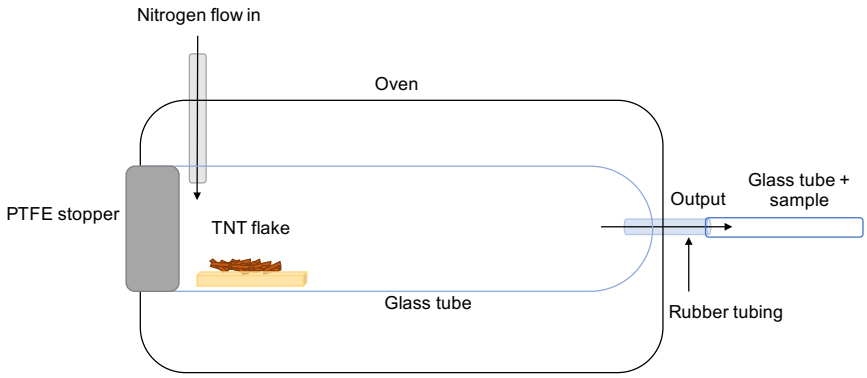

Figure 6.8: A schematic showing how TNT vapours are produced using the permeation oven. The black arrows in the figure show the flow of nitrogen through the system (the nitrogen flow going into the glass tube is regulated by mass flow controllers not shown in the figure) that deliver the vapours to the source outlet where the sampling occurs. The sample tubes are inserted into the rubber tubing at the source outlet, thus holding the tubes into place for passive sampling. The vapours are prevented from leaving the glass tube by the PTFE (polytetrafluoroethylene) stopper in the back.

The TNT vapours produced using this method were sampled for 20 minutes (for all tube and sorbent types). The sample tubes were attached to the permeation oven through insertion into rubber tubing, which served as a connecting point allowing for the sample tubes

to be directly interfaced with the outlet of the source (as shown in Figure 6.8 and Figure 6.9). With the tubes in this fixed position, the nitrogen purge gas allowed for the diluted TNT vapours to be delivered to the sample tubes without any active sampling taking place.

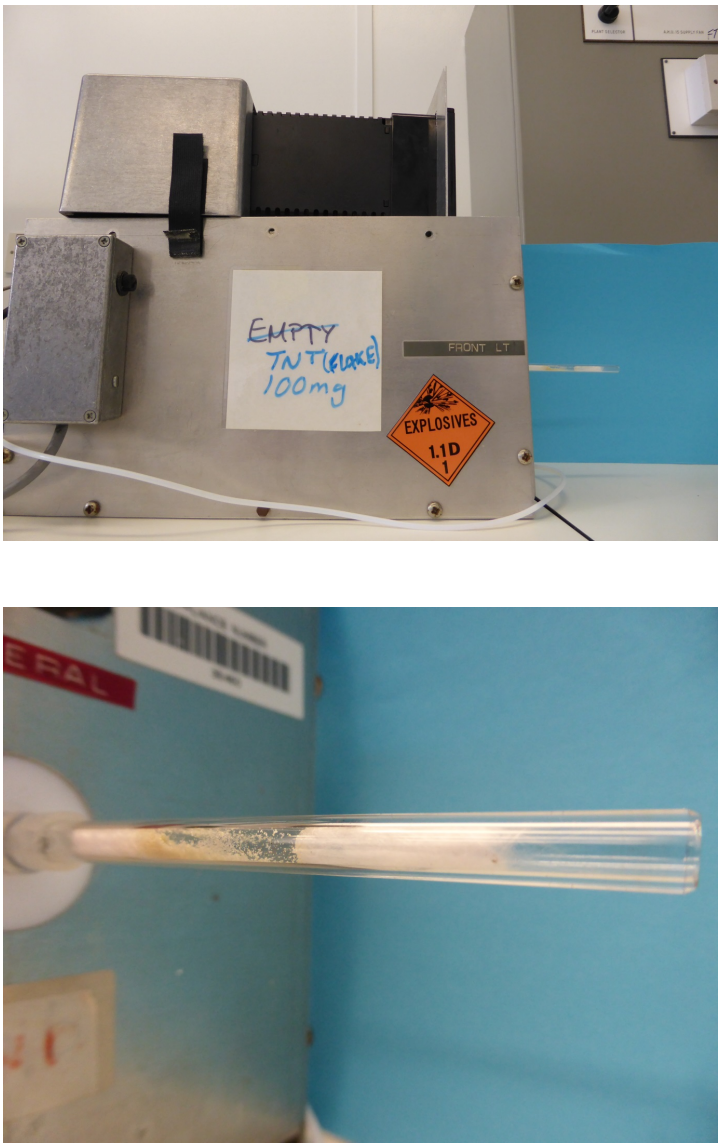

Figure 6.9: Top: A picture of the permeation oven used to generate TNT vapours from solid TNT flakes. The sample tubes were attached to the output through insertion into rubber tubing present on the oven outlet. With the tubes fixed into place, the diluted TNT vapours were delivered to the sample tubes using the outlet flow of 80 mL/ min. Bottom: A close up picture of the permeation oven sampling point, showing how the sampling tubes (in this case glass tubes containing MOF **3'**) were attached to the source outlet.

6.2.2.3 *Quantification of TNT vapours being produced by each source*

The vapours that were produced from each of the two sources were quantified by sampling the vapours onto Tenax® TA (200 mg) in stainless steel tubes, using the sampling procedures detailed above. The tubes were then analysed in the same way as the pre-concentration tubes (Section 6.2.3). It is the quantified vapours collected from these tubes that were used as the vapour source TNT outputs.

6.2.3 *Sample tube analysis*

6.2.3.1 *Instrumentation*

After the collection of TNT vapours (from either source) the sampling tubes were sealed using Markes International ltd. Difflok™ caps; to prevent the loss of trapped analytes or the sorption of any additional (and interfering) compounds. The samples were then inserted into a Markes International ltd. UNITY Ultra Series 2 thermal desorption unit interfaced with an Agilent Technologies gas chromatography - mass spectrometer. The gas chromatographs used were either Agilent 7890A or 6890N instrument models, and the mass spectrometers either Agilent 5977 or 5975C instruments. All of the mass spectrometers used were single quadrupole mass analyzers.

6.2.3.2 *Thermal desorption conditions*

The specific thermal desorption (TD) conditions used for the liberation of trapped TNT vapours from the sorbents are given in Table 6.1¶. The temperatures used were slightly different for the Tenax® TA-containing sampling tubes and the MOF **3′**-containing tubes.

¶ The thermal desorption conditions used were developed and recommended by the Explosives Detection Group in Dstl.

Table 6.1: Details of the specific thermal desorption conditions used on the pre-concentration experiments sample tubes

TD conditions	Sorbent type in sampling tube	
	Tenax® TA	MOF 3′
Desorption temp. (°C)	225[a]	150
Desorption time (mins/tube)	5	5
Desorption flow (mL/min)	50	50
Split (inlet) flow (mL/min)	50	50
Trap low temp. (°C)	-10	-10
Trap high temp (°C)	225	225
Trap hold time (mins)	3	3
Trap split (outlet) flow (mL/min)	13	13
Split ratio (mL/min)	11:1	11:1
Transfer line temp. (°C)	200	200

a All Tenax® TA-containing tubes were desorbed at this temperature other than in the initial proof-of-concept experiment where the glass tubes containing Tenax® TA were desorbed at 150°C.

6.2.3.3 *Gas chromatograph conditions*

In order to separate the TNT from the N_2 gas and other contaminants, a Restek RTX-5MS (15 m in length x 0.25 mm internal diameter x 0.25 μm film thickness) column was used. The GC oven was initially set to 70 °C where it was held for 1 minute, the oven was then programmed to ramp up to 230 °C at a ramp rate of 20 °C/ min. When the oven reached the set temperature of 230 °C it was held at this temperature for a further 2 minutes, giving a total run time of 11 minutes per sample tube analysed. Helium was used as the carrier gas at a flow rate of 1.4 mL/min. The temperature of the transfer line was 230 °C[||].

6.2.3.4 *Mass spectrometry conditions*

An electron ionization (EI) method was used to produce the detected ions. The temperatures of the ionization source and quadrupole were maintained at 230 °C and 150 °C respectively. A solvent delay of 1

|| These gas chromatography conditions used were developed for this analyte and instrument set-up by the Explosive Detection Group at Dstl.

minute was implemented to prevent substantial solvent peaks in the mass spectra. The mass specra were acquired in full scan mode with a scan range of 39 - 250 *m/z* **.

6.2.3.5 *Analysis of GC-MS results*

The results of the GC-MS analysis were rationalised with the assistance of the Explosives Detection Group, Dstl. External calibration standards of TNT were used for both the identification and quantification of the TNT analytes in the pre-concentration samples. External calibration standards are essentially known amounts of known compounds that are introduced into analytical instruments (such as GC-MS) in order to establish what the results of the anlayses should be; in this case through the characterisation of the response in the mass-spectrum. This is so that when unknown samples with unknown concentrations are introduced into the analytical systems, they can be identified through the matching of these responses with those that are known. In addition, through the use of calibration curves (produced from a number of calibration standards) the quantity of the previously unknown (now known) samples can also be determined.

The calibration standards used for the analysis of the pre-concentration samples were made by dilutions of certified reference standards. TNT stock solutions of 50 ng/μL , 100 ng/μL, 300 ng/μL, and 500 ng/μL concentration were produced and used to generate 50 ng, 100 ng, 300 ng, and 500 ng TNT standards on Tenax® TA (200 mg) stainless steel tubes; by spiking 1 μL of a specific concentration onto each tube. At least two independent sets of standards were analysed during each GC-MS analysis. The pre-concentration samples were bracketed between standards to determine the response of the detector across the measurements.

** The mass spectrometer conditions used were those suggested by the Explosives Detection Group at Dstl.

The chromatograms and mass spectra that were produced from the analysis of these calibration standards determined the expected retention times and ratios of the *m/z* ions in the mass spectra for TNT. An example chromatogram obtained for a 500 ng TNT standard is given in Figure 6.10.

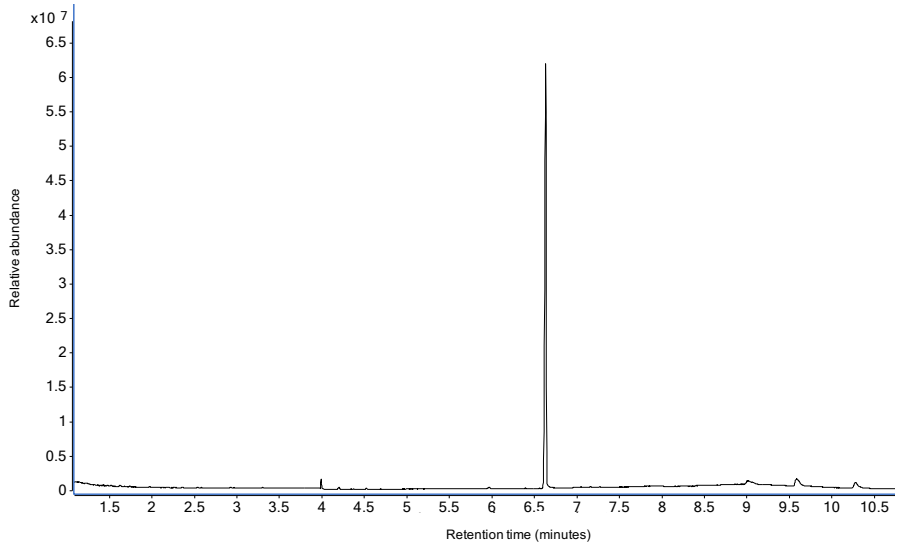

Figure 6.10: An example TNT chromatogram generated from the thermal desorption and GC-MS analysis of a 500 ng standard Tenax® TA stainless steel tube.

In order to confirm that these results were as expected for TNT, the retention times (RT) and *m/z* ratios were compared with the GC-MS instrument's inbuilt libraries (National Institute of Standards and Technology EI MS database) that contain the expected chromatogram and mass spectra details for a number of compounds including TNT. In addition, the mass spectra were manually checked for the presence of the *m/z* ions 210, 89 and 63 which are common fragmentation ions of TNT. The four point calibration curves produced from the analysis of the calibration standards allowed for the quantification of the TNT amounts present on the pre-concentration tubes to be determined. This was achieved through a comparison of the intensity in the instrument response given for the standards and the samples.

6.2.3.6 *Accounting for analysis baseline drift*

To measure the effects of any residual TNT from an analysed sample being left in the GC-MS and thus carrying over to subsequent samples, 'blank' tubes (freshly degassed Tenax® TA , 200 mg, stainless steel tubes) were also thermally desorbed and analysed at the same time as the TNT calibration standards and the pre-concentration experiments sample tubes. These 'blanks' were intermittently analysed in between TNT- containing tubes.

6.2.3.7 *Specific experimental runs*

Files containing the specific analytical sequences ('runs') and the absolute amounts of TNT collected for each sample can be found in Appendix D.

6.2.4 *Chemical analyses on MOF **3'** samples after pre-concentration experiments*

The crystals present in the best and worst performing MOF **3'** TNT pre-concentrator samples were analysed using Powder X-ray diffraction (PXRD), infra-red (IR), X-ray photoelectron spectroscopy (XPS), scanning electron microscopy (SEM), elemental analysis (EA), nuclear magnetic resonance (NMR) and thermogravimetric analysis (TGA). The samples analysed were the two initial proof-of-concept (230 °C degassed) MOF **3'** samples and representative 100 °C degassed MOF **3'** samples. All of the chemical analyses were performed using the experimental methods outlined in Chapter 8.

6.3 RESULTS AND DISCUSSION

6.3.1 *Initial proof-of-concept experiment*

An initial proof-of-concept experiment was performed with aim to investigate whether any TNT vapours were able to be pre-concentrated by metal-organic framework **3′** using the proposed experimental design (Figure 6.3).

For this experiment, the vapour generator method was used to yield the TNT vapours used for sampling. These TNT vapours were sampled by glass tubes containing MOF **3′** crystals, glass tubes containing Tenax® TA and glass tubes containing only glass wool (prepared by the methods discussed in Section 6.2.1). Prior to TNT vapour sampling, the sample tubes were all degassed (as detailed in Section 6.2.1) in order to liberate any unwanted analytes such as residual solvent molecules (particularly for MOF **3′**) on or in the sorbent materials. Glass tubes containing Tenax® TA and glass tubes containing only glass wool were degassed at 230 °C for 1 hour and the glass tubes containing MOF samples were degassed at 230 °C for 30 minutes. Upon the degassing of the MOF **3′**-containing tubes, the majority of the crystals present changed colour from pale yellow to orange (Figure 6.11).

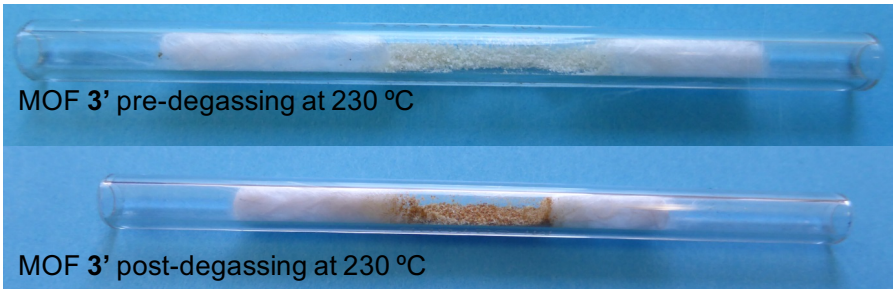

Figure 6.11: Top: A picture of a glass tube containing MOF **3′** crystals that have not been degassed. Bottom: A picture of a glass tube containing MOF **3′** crystals after degassing at 230 °C for 30 minutes.

After sampling the TNT vapours produced from the vapour generator using an active sampling technique (described in Section 6.2.2.1), each of the TNT sampling tubes were thermally desorbed (details of which can be found in Section 6.2.3) at 150 °C, liberating any TNT vapours captured into a gas chromatography - mass spectrometer (GC-MS) for separation and quantitative analysis. Figure 6.12 illustrates the approximate amounts of TNT vapours captured and released, and therefore pre-concentrated, by each sample during this initial proof-of-concept experiment.

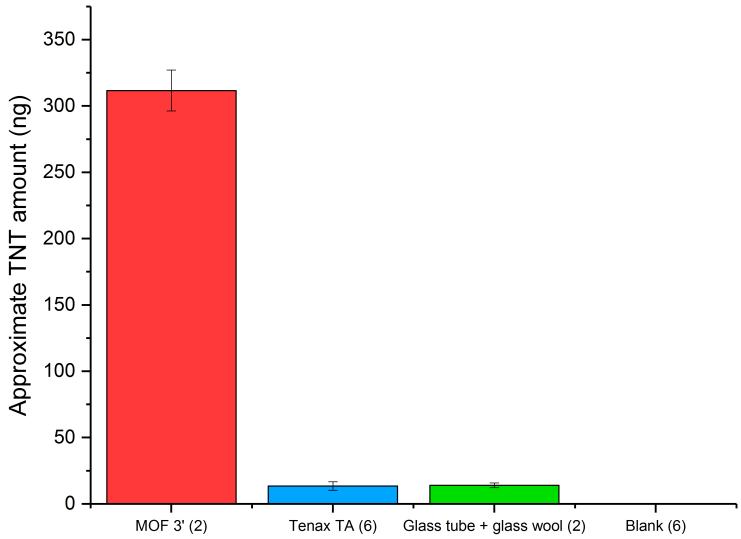

Figure 6.12: Graph showing the approximate concentrations in nanograms (ng) of TNT that were obtained from GC-MS analysis following thermal desorption of the different sorbent samples (MOF **3′**, Tenax® TA and glass wool all in glass tubing) used to collect TNT vapours in the proof-of-concept pre-concentration experiments. The graph also shows the background levels of TNT (expressed as 'blanks') present in the GC-MS instrumentation during the analysis. The numbers in the brackets denote the number of samples that contribute to the approximate mean amounts of TNT retrieved from each sample. The error bars detail the standard error of the mean.

The results in Figure 6.12 show that these samples of metal-organic framework **3′** were able to effectively pre-concentrate TNT vapours. The two MOF **3′** samples collected and released approximately 327 ng and 296 ng of TNT into the GC-MS. In contrast, the glass tubes containing Tenax® TA and glass wool only delivered very approxi-

mately < 15 ng on average of TNT post-desorption into the GC-MS respectively[††]. These substantial discrepancies between the two sorbents (MOF **3′** and Tenax® TA) can potentially be attributed to the temperature of desorption. It is possible that the temperature used to desorb the TNT from these sorbents was adequate for MOF **3′** to release the sorbed TNT molecules but not sufficient for Tenax® TA, which potentially has stronger interactions with the analyte.

The pre-concentrator efficiency (as calculated by Equation 6.1) of the tested samples in this proof-of-concept experiment could not be determined, this is due to the baseline TNT vapour output produced from the vapour generator having not been quantified. Additionally, the quantities of TNT captured by the MOF **3′** samples (in nanograms, ng) obtained from the GC-MS analysis are only approximate concentrations as a result of only a two-point calibration curve (using 100 ng and 500 ng standards, produced as described in Section 6.2.3.5) having been used as a quantification reference, owing to these experiments being an exploratory test.

Based on these initial positive results, additional experiments were attempted to further probe the potential of MOF **3′** as an effective TNT vapour pre-concentrator.

6.3.2 *An attempt to identify optimal MOF 3′ degas conditions*

As a result of the colour change shown by the MOF **3′** samples degassed at 230 °C, and the knowledge that such colour changes are typically ascribed to some structural transformations (as discussed in Section 4.3.1.4) [101], which may or may not be beneficial to application; a milder degassing of the MOF was attempted with aim

†† These values should be viewed as approximations as they are outside the analysis calibration curve owing to being lower than the lowest calibration standard of 100 ng.

to identify the optimal degas conditions that yield the greatest pre-concentration performance.

MOF **3′** samples (that were freshly activated using the procedure detailed in Section 4.2.3) were degassed at 100 °C, (upon which no colour change was observed) and used for the attempted pre-concentration of TNT vapours. In addition, the two MOF samples previously used in the proof-of-concept experiments (POC MOFs) were re-used in order to compare the effects of the two different degassing conditions and to evaluate the re-usability of the POC MOFs. In this instance the POC MOFs were also degassed at at 100 °C. Eight 100 °C degassed MOF **3′** samples were used in two separate experiments, four were used to sample the TNT vapours produced from the vapour generator and the others to sample the TNT yielded from the permeation oven (described in Section 6.2.2.2). The vapours produced by both of these sources were quantified using GC-MS so that pre-concentrator efficiencies could be calculated for these samples.

6.3.2.1 *Vapour generator TNT source sampling*

The calibration curve obtained for the GC-MS analysis of the tubes used to sample the TNT vapours emitted from the vapour generator is shown in Figure 6.13. This calibration curve was produced using four TNT standards (50 ng, 100 ng, 300 ng and 500 ng, as described in Section 6.2.3.5) and as evident, shows good linearity (R^2 = 0.999). Therefore, the quantities of TNT expressed by this analysis are of greater accuracy than those reported in the initial POC experiments.

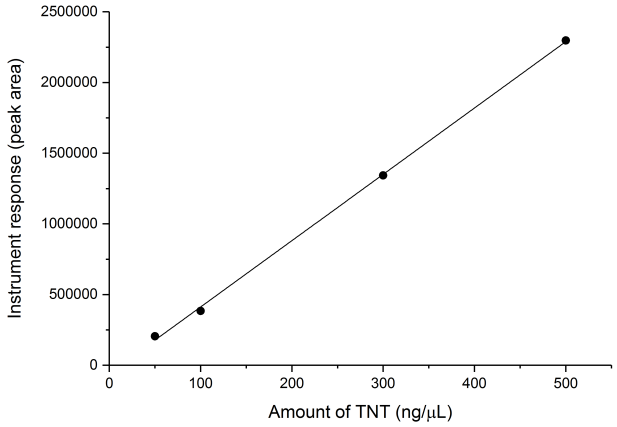

Figure 6.13: Calibration curve for the GC-MS analysis of the sample tubes used to capture TNT vapours produced by the vapour generator, R^2 = 0.999.

Figure 6.14 gives the amount of TNT vapours (produced from the vapour generator) that were pre-concentrated by each of the different sample tube types as analysed by GC-MS.

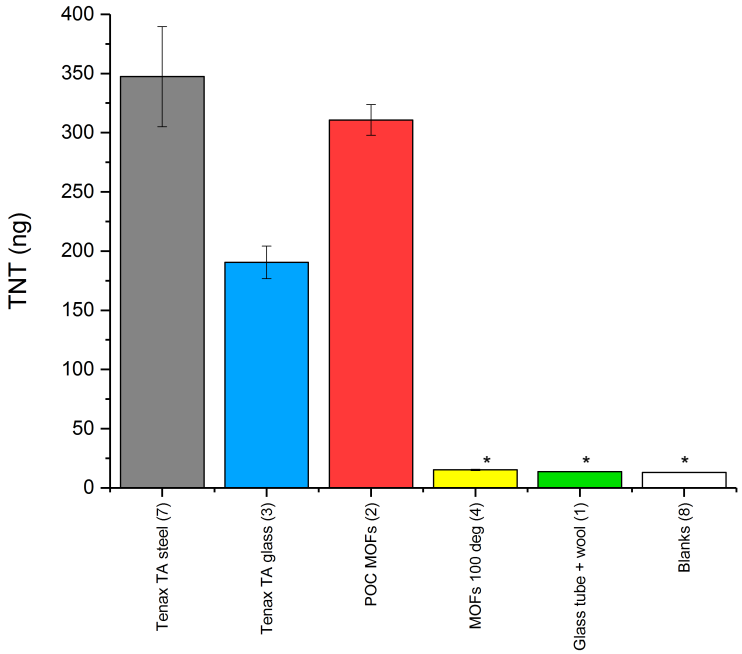

Figure 6.14: Amount of TNT (ng) that was captured by different sample types through the sampling of the vapours produced by the vapour generator and released during thermal desorption, as quantified by GC-MS. The values in brackets detail the number of each sample type that has contributed to the average TNT amount (ng) reported. The error bars detail the standard error of the mean. Blank samples denote those used to check the background levels of TNT in the GC-MS. 'MOF 100 deg' denotes the MOF samples degassed at 100 °C. It is important to note that all values below 50 ng are approximations as they are lower than the lowest standard of the calibration curve (denoted by the asterisk).

The baselining of the TNT vapours being outputted from the vapour generator (obtained through the sampling of vapours using stainless steel tubes containing 200 mg of Tenax® TA as discussed in Section 6.2.2.3) suggested that on average 350 ng of TNT vapours were available for collection by the pre-concentrator sorbents during the sampling time of 5 minutes. As the active sampling method used operated at 1 litre/minute, these results imply that approximately 70 ng/L of TNT vapours were being produced by the vapour generator per minute. However, as evidenced by the error bars for the baselining measurements (standard error was 350 $\pm$ 42.3 ng), there is significant variation in the amount of TNT collected by the Tenax® TA in steel tubes during these baselining measurements. In addition, these TNT vapour output levels quantified by GC-MS are an underestimation of the theoretical vapour generator output of 103 ng/ L. These findings can potentially be attributed to the vapour sampling method; dependent on where the vapour sampling tubes were placed in proximity to the vapour outlet hole, slightly different uptakes of vapours were observed using the stainless steel Tenax® TA (200 mg) tubes.

As evidenced by Figure 6.14, Tenax® TA (in glass tubes) captured and released around 55% less of the available TNT vapours than the Tenax® TA in steel tubes (on average 191 ng *vs.* 350 ng respectively). These results are somewhat to be expected as less of the Tenax® TA sorbent material was contained within the glass tubes than the steel tubes (40 mg *vs.* 200 mg respectively).

A very significant finding from these experiments is that the two MOF **3'** samples used in the proof-of-concept experiments (POC MOFs) demonstrated very good pre-concentration capabilities towards TNT vapours even after a second pre-concentration cycle. The two MOF **3'** samples captured and released very similar quantities of TNT to those observed in the initial experiments (approximately 327 ng and

296 ng of TNT were pre-concentrated by the two MOF **3′** samples in the POC experiments and 324 and 298 ng during second-round sampling). In addition, these results show that the second time degassing at a lower temperature of these samples did not affect their pre-concentrator performance. Furthermore, it is demonstrated that these two MOF **3′** samples showed a greater ability to capture and release TNT vapours than the glass sample tubes containing Tenax® TA; despite the same amount of material used in each of the identical glass tubes that were packed in the same way. This is best evidenced by the significantly higher pre-concentrator efficiencies demonstrated by the two POC MOF **3′** over Tenax® TA as shown in Table 6.2. Such findings are rationalised by the higher surface area of MOF **3′** than Tenax® TA (320 $m^2 g^{-1}$ based on H_2O BET experiments on fully dehydrated MOF **3′** samples and 35 $m^2 g^{-1}$ respectively).

Table 6.2: Pre-concentrator efficiencies for the POC MOF **3′** and glass tube Tenax® TA samples used to pre-concentrate the TNT vapours produced from the vapour generator.

Sample	Pre-concentrator efficiency[a](%)
Glass tube + Tenax® TA	53.1
Glass tube + POC MOF **3′** samples	89.0

a Calculated using the mean amount of TNT collected by the given sample minus the amount (mean) of TNT collected on the 'blank' samples, divided by the mean baseline emission from the vapour generator (as obtained from Tenax® TA steel tube sampling of the vapour generator emissions followed by GC-MS analysis) minus the 'blank' and converted into a percentage.

Interestingly, the metal-organic framework **3′** samples degassed at 100 °C showed the minimal capture and release of TNT vapours. In fact, the amounts of TNT obtained appear virtually indistinguishable from the instrument background TNT levels. The absolute values of which are not reported owing to them lying outside of the calibration curve (being of lower value than the lowest standard, 50 ng, as denoted by the asterisk in Figure 6.14) and so should be viewed as ap-

proximations. The reasons for the poor pre-concentrator capabilities demonstrated by these samples will be evaluated in Section 6.3.5.

The efficacy of the thermal desorption temperature was also investigated during this analysis. To check whether all of the captured TNT was being liberated from the MOF **3′** samples at 150 °C, each MOF-containing tube was thermally desorbed twice during the analysis, with the second desorption and analysis occurring immediately after the first. If a significant amount of TNT was retrieved during the second analysis this would indicate the need for a refinement of the thermal desorption temperature. However, as can be seen in Figure 6.15, this does not appear to be the case. For the POC MOF **3′** samples the initial thermal desorption is very effective, evidenced by the minimal presence of additional TNT (if any) from the second desorption and analysis. As denoted by the asterisks in Figure 6.15, all values below 50 ng should be viewed as approximations owing to them lying outside of the calibration curve.

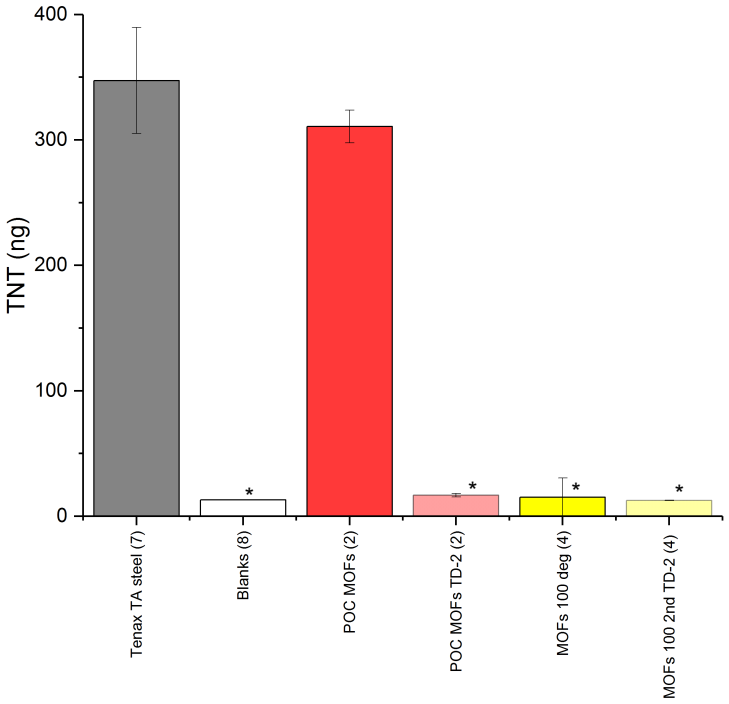

Figure 6.15: The amount of TNT quantified by GC-MS from initial and secondary thermal desorptions on the same MOF **3′** samples (run sequentially) that were used to pre-concentrate the vapours produced from the vapour generator. The label TD-2 refers to the second desorption runs. The values in brackets detail the number of each sample type that has contributed to the average TNT amount (ng) reported. The error bars detail the standard error of the mean. Blank samples detail the background levels of TNT in the GC-MS. The asterisks denote all the samples whose TNT amounts lie outside of the GC-MS calibration curve and thus should be viewed as approximations.

6.3.2.2 *Permeation oven TNT source sampling*

In order to establish whether the vapour generation source sampling method had any effect on the poor performance of the 100 °C degassed MOF **3′** samples to pre-concentrate TNT; MOF **3′**-containing glass tubes (degassed at 100 °C) as well as Tenax® TA-containing glass tubes and glass wool only tubes, were used to sample the vapours produced from the permeation oven using the method described in Section 6.2.2.2. The results of the GC-MS analysis post thermal desorption are given in Figure 6.16‡‡.

‡‡ The calibration curve for this GC-MS analysis again showed good linearity (R^2= 0.999).

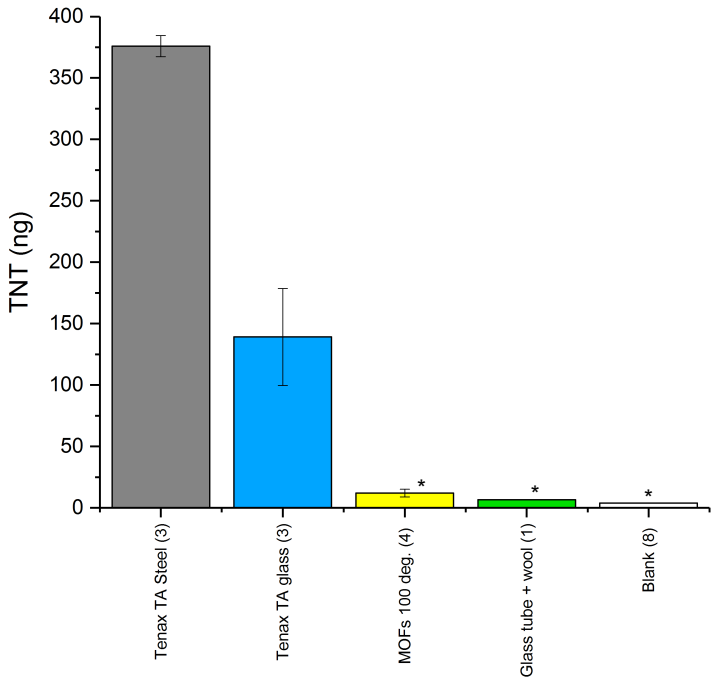

Figure 6.16: The TNT quantities (ng) obtained from GC-MS analysis of four different sample tube types used to sample the TNT vapours produced from the permeation oven. The numbers in brackets details the number of each sample type that has contributed to the average TNT amount reported. The error bars detail the standard error of the mean. 'MOF 100 deg' denotes the MOF samples degassed at 100 °C. The graph also shows the blank samples used to check the background levels of TNT in the GC-MS instrument. The values denoted by the asterisk should be viewed as approximations as they are outside of the analysis calibration curve.

From Figure 6.16 it can be seen that the baseline TNT vapours produced from the permeation oven source showed a lesser extent of variation in the TNT amounts quantified by GC-MS, than the vapour generator source (evidenced by the smaller error bar observed for the amount of TNT captured by the Tenax® TA in steel tubes). This can potentially be attributed to the different sampling methods used. As discussed (Section 6.3.2.1), the quantified amount of TNT produced from the vapour generator was greatly affected by the position and proximity in which the sample tube (Tenax® TA in steel tubes) was interfaced with the vapour outlet during sampling. For the permeation oven source, as described in Section 6.2.2.2, the sample tubes were inserted into rubber tubing which held the tubes into place. Thus,

a more controlled and defined sampling point was possible for this vapour source, therefore rationalising the lesser degree of variation in the amount of TNT captured and released in the baseline measurements.

The amount of TNT pre-concentrated by the Tenax® TA in glass tubes was slightly lower than that observed when these same tubes were used to sample from the vapour generator source. The pre-concentrator efficiencies were 53.1% and 36.4% for the vapour generator and permeation oven sources respectively. These results could be due to the different sampling methods used for the two sources, the former using an active sampling method and the latter using the oven output flow to deliver TNT vapours to the sample. Thus, potentially the Tenax® TA samples in glass tubes more effectively pre-concentrate TNT when actively sampling vapours. However, further testing on this rationale is required.

The MOF **3′** samples degassed at 100 °C again demonstrated poor TNT pre-concentration capabilities. Therefore implying that the different TNT source and sampling methods employed had no effect on the pre-concentration abilities of these MOF samples. Furthermore, from these results it was concluded that the degassing of the MOF **3′** materials once at 100 °C for 1 hour was not sufficient to yield effective TNT pre-concentrators. Thus, the used (100 °C degassed) MOF **3′** materials were degassed again; with aim to investigate whether the secondary degassing of the samples could yield MOFs with pre-concentrator efficiencies approaching those observed for the originally tested POC MOF **3′** samples. The results of these experiments are detailed below.

6.3.3 *Secondary degassing and reuse of MOF* **3′** *samples*

During the secondary degas experiments, the four MOF **3′** sample tubes (initially degassed at 100 °C) used previously to capture the vapours produced from the permeation oven were re-degassed at 100 °C for 1 hour and used to re-sample the same TNT source. It is important to note that a slight colour change of the MOF crystals was observed from the yellow coloured crystals obtained after the initial first time degassing (at 100 °C), prior to vapour sampling and analysis; to darker yellow crystals that were yielded post GC-MS analysis (images of which can be seen in Appendix D). This suggests that the thermal desorption of the MOF **3′** samples at 150 °C had some impact on the metal-organic framework's structure. However, during the secondary 100 °C degassing of these same MOF **3′** samples, no further crystal colour change was observed.

Also during these secondary degas experiments, two MOF **3′**-containing tubes that were used to initially sample the vapours produced from the vapour generator source (initially degassed at 100 °C) were degassed a second time at a temperature of 230 °C for 10 minutes, and used to sample the vapours produced from the permeation oven also. The degassing of these MOF **3′** samples at 230 °C for 10 minutes produced a colour change in some of the crystals present within the sample tubes; the crystals changed colour from yellow to orange. These were similar observations to those noted for the initial proof-of-concept MOF **3′** samples, the only difference was that less of the crystals present within the samples degassed at 230 °C for 10 minutes appeared to have changed colour.

The results of the GC-MS analysis[§§]. after the thermal desorption of each of the above-mentioned samples used for TNT vapour pre-concentration are shown in Figure 6.17.

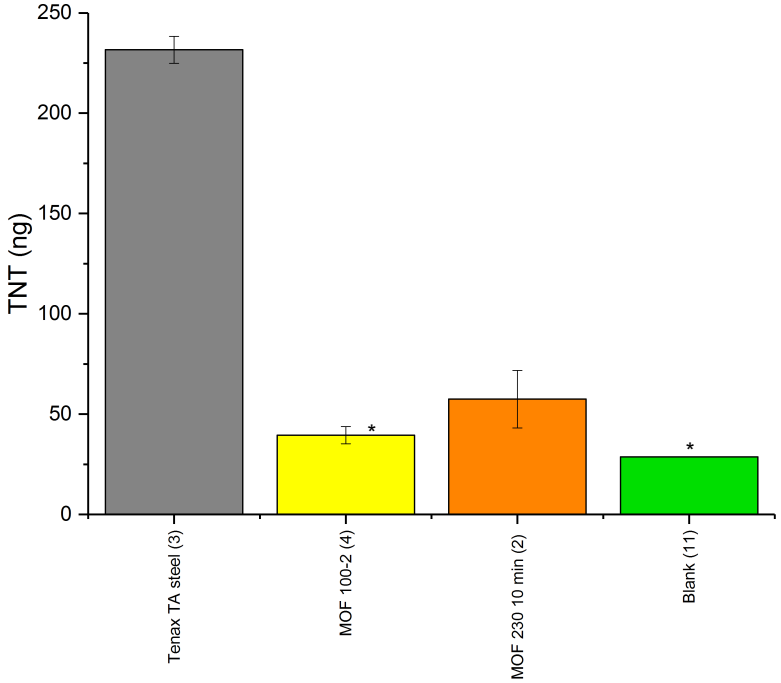

Figure 6.17: TNT amounts (in nanograms) obtained from the thermal desorption and GC-MS analysis of the sample tubes used to capture the vapours produced from the permeation oven TNT source. The two different MOF **3′** sample tube types (represented by the yellow and orange bars) have been re-degassed at different temperatures; 100 °C for 1 hour (labelled MOF 100-2) and 230 °C for ten minutes (labelled 230 10 mins). The number of tubes contributing to each of the average quantities of TNT (ng) reported are detailed by the numbers within the brackets. The error bars denote the standard error of the mean. Included also are the blank samples used to check the background levels of TNT in the GC-MS instrument. The values denoted by the asterisk should be viewed as approximations as they are outside of the analysis calibration curve.

As evidenced by Figure 6.17 the secondary degassing at 100 °C of the MOF **3′** samples (initially degassed at 100 °C) still yielded poor pre-concentration of TNT vapours, with released TNT amounts less than the lowest calibration standard. However, it was observed that the TNT pre-concentrator performance of MOF **3′** samples could be increased with higher temperature degassing, as evidenced by the two MOF **3′** samples that were re-degassed at 230 °C

§§ The calibration curve for this GC-MS analysis showed good linearity (R^2= 0.996)

for 10 minutes. The average pre-concentrator efficiency (PE) for these re-degassed samples was observed to be 14.2%, whereas the approximate PE for these same samples initially degassed at 100 °C (used to pre-concentrate TNT vapours from the vapour generator source) was < 1%.

These results demonstrate how the pre-concentration capability of a MOF **3′** sample was very dependent on the temperature at which that particular sample was degassed. Further to this, it is clear that higher degassing temperatures yielded greater capture and release efficiencies of the MOF. Thus, to further probe this, a final variable temperature degas experiment was attempted using higher degas temperatures, with the aim to identify the optimal degassing procedure for this metal-organic framework.

6.3.4 *High temperature degassing*

Four freshly synthesised and activated MOF **3′** samples were degassed at 230 °C for 30 minutes in an attempt to replicate the TNT pre-concentration abilities demonstrated by the MOFs in the initial proof-of-concept (POC MOFs) experiments (that were degassed in the same way). For comparison, one of the initial POC MOFs was re-degassed at 230 °C for a third TNT pre-concentration cycle. In addition, two just activated MOF **3′** samples were degassed at 150 °C for 1 hour. The TNT vapours used for sampling by these differentially degassed MOF samples were generated using the permeation oven. The results of the thermal desorption and gas chromatography - mass spectrometry analysis[¶¶] are shown in Figure 6.18.

¶¶ The calibration curve for this analysis showed good linearity R_2 = 0.994.

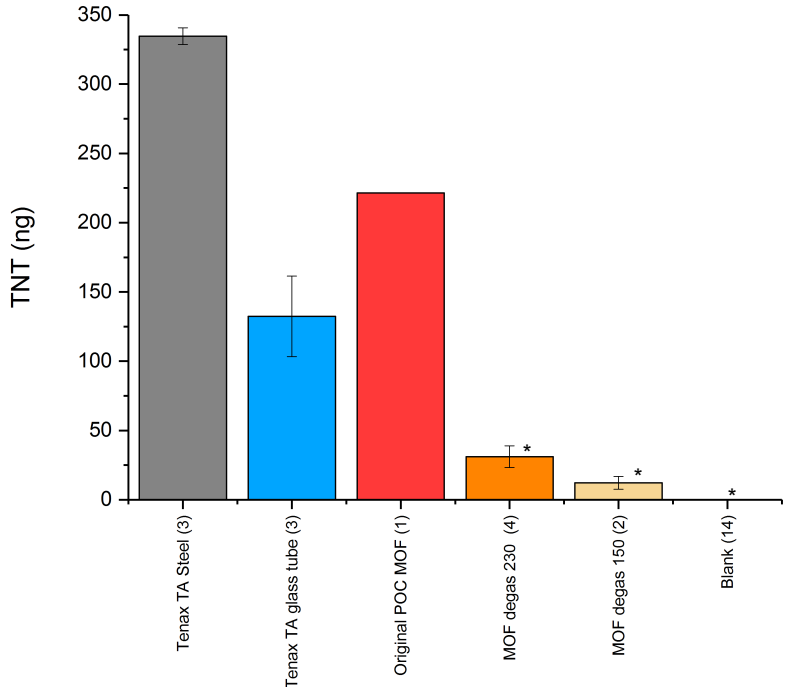

Figure 6.18: TNT amounts (ng) obtained from TD and GC-MS analysis of MOF **3′** samples in glass tubes degassed at different temperatures and Tenax® TA in glass tubes, used to sample TNT vapours from the permeation oven. The labels 'MOF degas 230' and 'MOF degas 150' denoted the temperatures that the MOF **3′** samples were degassed (230 °C and 150 °C) respectively). The number of tubes contributing to each of the average quantities are detailed by the numbers within the brackets. The error bars denote the standard error of the mean. Blank samples detail those used to check the background levels of TNT in the GC-MS. The values denoted by the asterisk should be viewed as approximations as they are outside of the analysis calibration curve.

Table 6.3: Pre-concentrator efficiencies for an original POC MOF (third cycle pre-concentration) and Tenax® TA (in glass tubes) after sampling TNT vapours from the permeation oven.

Sample (glass tubes)	Pre-concentrator efficiency(%)
Tenax® TA (in glass tubes)	39.5
Original POC MOF (230 °C degas)	66.2

From the GC-MS analysis it can be seen that one of the original POC MOFs still demonstrated the effective capture and release of TNT vapours even after a third pre-concentration cycle. This MOF **3′** sample again outperformed the glass tubes containing Tenax® TA as well as the other MOF **3′** samples. It should be noted that this sample demonstrated a lower percentage of pre-concentrator efficiency (the

PEs for the POC MOF sample and the glass tube Tenax® TA samples can be seen in Table 6.3) than when used to sample the vapour generator TNT source, the same was also true for the glass tube Tenax® TA samples. This implies that both the two sorbents (MOF and Tenax® TA) were more effective at pre-concentrating the TNT produced from the vapour generator than the permeation oven. This could be an artefact of the aforementioned different sampling approaches (active and purge-gas controlled) implemented for the two methods. It is therefore suggested that the lower PE observed for the POC MOF is a result of the sampling method and not the diminished performance of the MOF sample with repeat cycles. However, future work is required to confirm this.

The results in Figure 6.18 also show that whilst the fresh batches of MOF **3′** degassed at 230 °C for 30 minutes appear to be able to uptake and release TNT vapours (the TNT amounts obtained were still below the lowest calibration standard), their performance was not comparable to the initial proof-of-concept (POC) MOF **3′** samples, even though the same degassing conditions were used for both. Further to this, in Figure 6.19 below it can be seen there is substantial variation between the pre-concentrator efficiencies that were demonstrated by these four (230 °C degassed) MOF **3′** samples, despite each of the glass tubes being filled by 40 mg of MOF **3′** crystals from the same amalgamated synthetic and activated batch[***]. In addition, as evidenced in Figure 6.18, the MOF **3′** samples degassed at 150 °C yielded very small amounts of TNT captured and released (again TNT amounts obtained from GC-MS were outside the calibration curve and should be viewed as approximations).

*** It is important to note that these TNT values are all approximate, semi-quantitative values, as they are all below the lowest standard in the calibration curve obtained for this analysis.

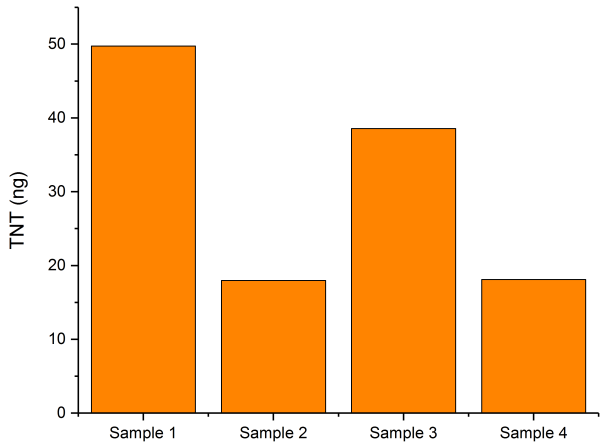

Figure 6.19: The amounts of TNT (ng) obtained from the thermal desorption and GC-MS analysis of four different glass sampling tubes filled with 40 mg of MOF **3′** crystals obtained from the same amalgamated synthetic and activated batch and all degassed at the same temperature of 230 °C for 30 minutes. These values are all approximate, semi-qualitative values as they are each below the lowest standard in the calibration curve obtained for this analysis.

As demonstrated in all of the TNT pre-concentration experiments, the ability of a MOF **3′** sample to capture and release, and therefore pre-concentrate TNT (regardless of the TNT vapour source sampled) was very dependent on the conditions with which the MOF was degassed (temperature and duration of degassing). In addition, the relationship between the degassing conditions and the TNT uptake by MOF **3′** was clearly complex, as evidenced by the different capture and release efficiencies of MOF **3′** samples that were degassed using the same procedures. In order to investigate what factors were causing the varied pre-concentration capabilities of the different MOF **3′** samples, chemical analyses on the best and worst MOF **3′** TNT pre-concentrators were undertaken.

6.3.5 *A chemical investigation into the varied pre-concentration capabilities of differently degassed MOF **3′** samples*

In an attempt to investigate why differently degassed MOF **3′** samples demonstrated varying pre-concentration capabilities towards TNT vapours, chemical analyses were performed on the crystals present in the two 230 °C degassed MOF **3′** samples used in the initial proof-of-concept (and subsequent) experiments that showed very good and repeatable pre-concentrator capabilities, as well as representative 100 °C degassed (and 150 °C thermally desorbed and GC-MS analysed) MOF **3′** samples that showed virtually no capture and release of TNT vapours. The analyses performed on these samples were: powder X-ray diffraction (PXRD), scanning electron microscopy (SEM), thermogravimetric analysis (TGA), X-ray photoelectron spectroscopy[†††] (XPS), infra-red spectroscopy (IR), proton nuclear magnetic resonance (^{1}H NMR) and elemental analysis (EA). The results of which are presented below.

6.3.5.1 *Powder X-ray diffraction analysis*

As discussed, the degassing of MOF **3′** samples at different temperatures yielded different colour changes in the MOF **3′** crystals, which was accompanied by varying TNT pre-concentration capabilities. MOF **3′** 100 °C degassed samples did not appear to change colour post-degassing but a colour change from pale yellow to dark yellow was observed after TNT pre-concentration; attributed to the 150 °C thermal desorption step prior to GC-MS analysis. The 230 °C degassed MOF POC samples observed more dramatic colour changes from pale yellow to orange after degassing. As previously mentioned (Section 4.3.1.4), colour changes in MOFs are generally observed when

††† XPS data were obtained by Dr. Michael Powell, Department of Chemistry, University College London.

structural transformations occur, typically as a result of the removal of solvents from MOF pores or those coordinated to the framework structure (dehydration), or a combination of both [101]. Therefore, in order to investigate whether any obvious structural perturbations occur that could explain the colour changes and thus, the differences in pre-concentration capabilities observed between the best and worst MOF **3′** pre-concentrator samples; powder X-ray diffraction (PXRD) analysis was performed on the orange crystals of the 230 °C degassed POC MOF **3′** samples and the dark yellow crystals of the 100 °C degassed samples, after TNT pre-concentration experiments.

The PXRD pattern of the crystals present in a 100 °C degassed MOF **3′** sample is shown in Figure 6.20, also given in this figure are the PXRD patterns of the same MOF **3′** sample just after synthesis and activation.

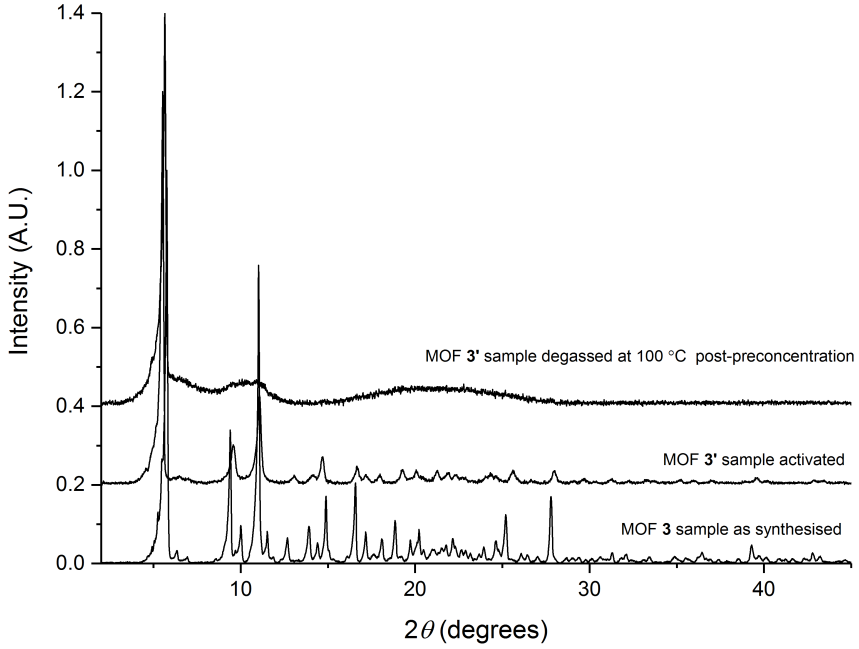

Figure 6.20: Powder X-ray diffraction patterns of a MOF **3′** sample degassed at 100 °C after pre-concentration experiments, the same MOF **3′** sample as-synthesised and just after solvent-exchange activation.

As can be seen, the MOF **3′** sample degassed at 100 °C (and thermally desorbed at 150 °C) was observed to have retained its overall

MOF topology post degassing and TNT vapour pre-concentration, evidenced by the retention of its long-range order and the main MOF peak (2θ= 5.7°). However, there is evidence of additional loss of local, short-range order in the MOF **3'** sample post degassing and its use in the pre-concentration experiment, evidenced by the broadening of the high 2θ angle peaks in its PXRD pattern compared with the PXRD pattern of this sample pre-degassing and thermal desorption (just solvent activation); suggesting that some structural change has occurred. This is also reflected by the aforementioned colour change from pale yellow to darker yellow of the 100 °C degassed MOF **3'** crystals after pre-concentration (TNT sampling, thermal desorption and GC-MS analysis). As discussed in Section 4.3.1.5, when as-synthesised MOF **3** samples are activated by solvent exchange to yield **3'** samples, a colour change in the crystals from clear to pale yellow was observed and there is some loss of short-range order in the PXRD spectra of **3'**, attributed to the removal of solvent molecules from the cavities of the MOF leading to a slight non-uniform contraction of the MOF pores. As also discussed, the washing procedure used to yield **3'** does not appear to remove the water molecules bound to the zinc metal centres in the MOF, nor does it remove all of the residual solvent present in the MOF's pores, owing to a lack of 100% effectiveness of the solvent-exchange process (as evidenced by TGA analysis in Section 4.3.1.7). Therefore, the loss of short-range order (and accompanied slight crystal colour change from pale yellow to darker yellow) between the solvent exchange-activated **3'** sample and the 100 °C degassed **3'** sample used for TNT pre-concentration (including 150 °C thermal desorption), could be a result of further solvent removal from the MOF pores, or, the loss of axially bound water molecules to the zinc metal centres in the MOF. However, from PXRD analysis alone it is impossible to determine which of these two solvent losses, or

if any, or both, are the cause of the apparent slight changes in the framework structure of the 100 °C degassed MOF **3′** samples used in pre-concentration.

Figure 6.21 shows the PXRD patterns of a 230 °C degassed proof-of-concept experiment MOF **3′** sample as well as the same MOF sample when it was just synthesised and activated.

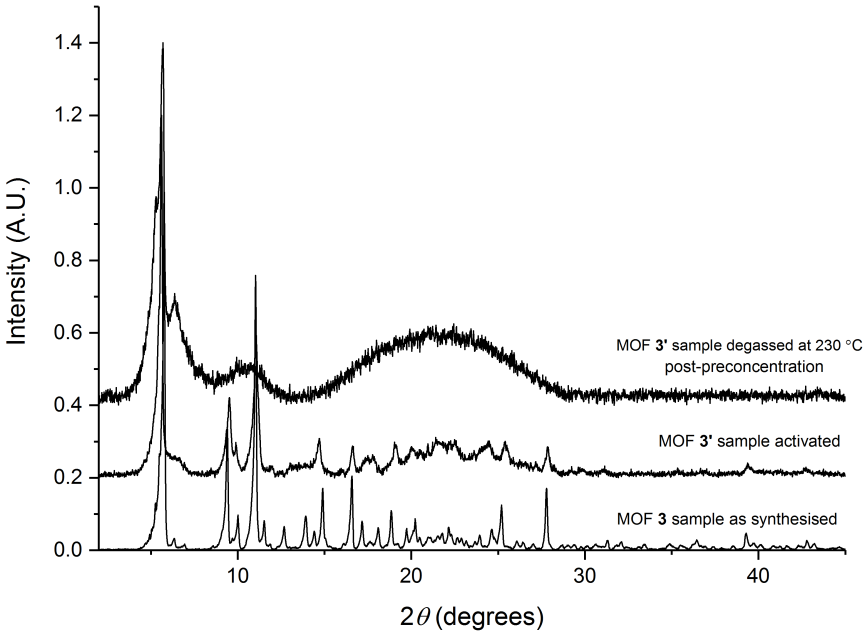

Figure 6.21: Powder X-ray diffraction patterns of one of the MOF **3′** 230 °C degassed proof-of-concept samples, the same MOF **3′** sample as-synthesised and just after solvent-exchange activation.

The PXRD spectrum of the POC MOF **3′** sample degassed at 230 °C indicates that the overall topology of the MOF was retained even after two pre-concentration cycles. This is evidenced again by the presence of the major MOF peak (2θ= 5.7°) and the absence of any additional peaks attributed to the linker as a result of structural collapse. However, a greater degree of short-range order loss and a decrease in the overall crystallinity of this MOF **3′** sample was observed. This suggests that there was more disorder in the framework structure of the MOF **3′** sample post- 230 °C degass and pre-concentration than after only solvent-exchange activation. Again, this reflects the colour

changes observed for the crystals in the sample which are pale yellow prior to degassing and orange after degassing and pre-concentration. These findings can again be rationalised by MOF **3′** solvent loss during degassing, either from the pores of the MOF or the framework structure itself. It is proposed that this 230 °C degassed MOF **3′** is being partially dehydrated during degassing, meaning that some of the zinc bound water molecules are being removed during degassing, but not all. This is suggested based on the results discussed in Section 4.3.1.7 that show a colour change from pale yellow to a very dark brown when MOF **3′** is fully dehydrated (to yield MOF **3″**). Further to this, the PXRD pattern of the fully dehydrated MOF **3″** shows a significant degree of loss of crystallinity of the MOF sample upon dehydration, attributed to pore deformations. However, as the colour change observed for the 230 °C degassed POC MOF **3′** and the degree of amorphisation of this sample did not approach those for the fully dehydrated MOF, it is hypothesised that only a partial dehydration of the MOF **3′** POC sample occurred post-degassing and pre-concentration. However, PXRD analysis alone cannot confirm this hypothesis.

6.3.5.2 *Infra-red analysis*

The IR spectra of the crystals present in the above-mentioned MOF **3′** samples are given in Figure 6.22.

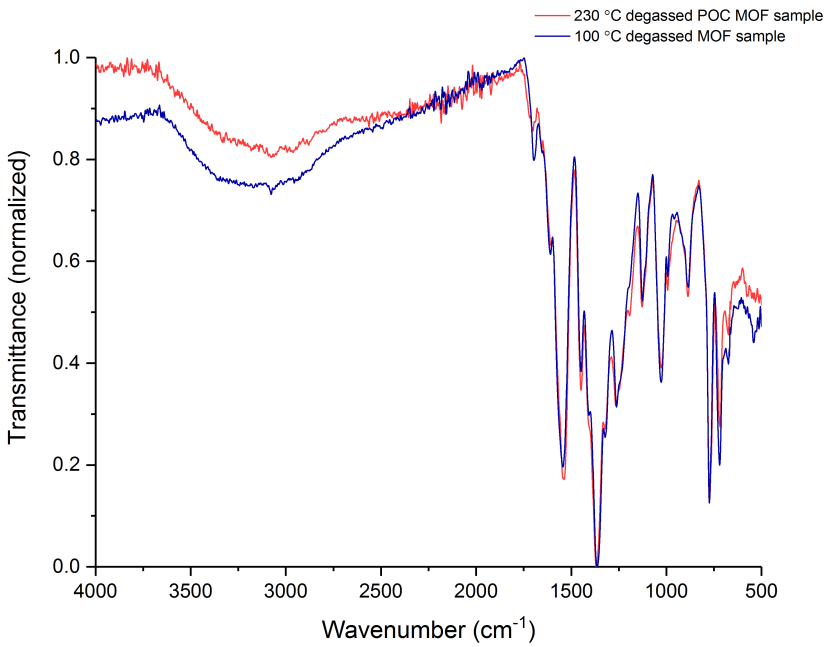

Figure 6.22: IR analysis of the crystals present in the 230 °C degassed POC (red) and 100 °C degassed MOF **3′** pre-concentration samples (navy).

Figure 6.22 shows that the IR fingerprint regions of the two samples are the same. Further to this, the stretches observed are in accordance with those measured for a representative MOF **3′** just activated sample (Appendix D). These results suggest that there is no change to the molecular bonds within the framework of the two samples compared to what is expected for this MOF; suggesting no breakdown of the framework in either sample during pre-concentration. However, there are discrepancies in the ν(O-H) stretch region between the two MOF samples, suggesting that different amounts of water are present within their structures. The broad adsorption peak between 2900 - 3600 cm^{-1}, which can be ascribed to the presence of water molecules, is weaker for the 230 °C POC MOF **3′** sample than the 100 °C de-

gassed MOF **3′** pre-concentrator sample. This suggest less water to be present in the 230 °C POC MOF **3′** sample.

6.3.5.3 *Scanning electron microscopy*

Scanning electron microscopy (SEM) images of the crystals present in the 100 °C degassed and 230 °C degassed POC MOF **3′** samples after TNT pre-concentration can be seen in Figure 6.23.

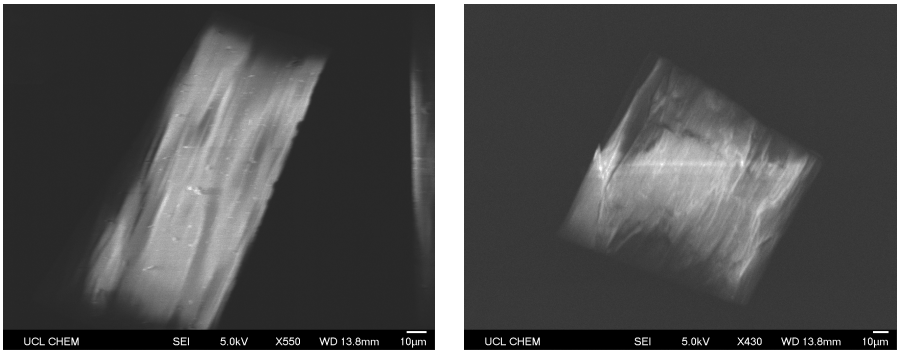

MOF **3'** sample degassed at 100 ℃ used for TNT pre-concentration

MOF **3'** sample degassed at 230 ℃ (POC MOF sample) used for TNT pre-concentration

Figure 6.23: Scanning electron microscopy images of the crystals present in the 230 °C degassed (proof-of-concept) MOF **3′** sample and the 100 °C degassed MOF **3′** sample used in TNT pre-concentration experiments.

As can be seen, there were no obvious differences in the morphologies of the crystals present in the two samples that would yield a greater pre-concentration capability of one over the other, as observed experimentally. In addition, the morphologies were in accordance with those observed in Section 4.3.1.4 for the freshly activated MOF **3′** crystals. It is important to note that the size dimensions of the majority of the crystals present in the two MOF **3′** samples were approximately 100 µm x 200 µm and were therefore similar to the particle sizes of the Tenax® TA used (60:80 mesh, as discussed in Section 6.2.1.2). Thus, the external surface areas of the two materials should have been similar.

6.3.5.4 *X-ray photoelectron spectroscopy*

XPS data on the 100 °C degassed and 230 °C degassed (POC) MOF **3′** TNT pre-concentrator samples were obtained and analysed by Dr. Michael Powell (Department of Chemistry, University College London), the details of which can be found in Appendix D. From the XPS data it was observed that there was no chemical degradation or change to the external surfaces of the two metal-organic framework samples as a result of the degassing (at either temperature) and TNT pre-concentration experiments. This was concluded based upon there being no change in the atomic environments, or relative amounts of the elements evaluated (zinc, carbon and oxygen) by comparison with a MOF **3′** sample that was only air exposed (Appendix B).

6.3.5.5 *Elemental analysis*

CHN elemental analysis was obtained on the two MOF **3′** samples through submission of the materials to an external elemental analysis service at the Science Centre, London Metropolitan University. Each sample was analysed twice and the results are given in Table 6.4. Also included in this table is the theoretical CHN elemental composition of MOF **3′** as calculated from the empirical formulae $[Zn_4L(H_2O)_4]$ (this assumes that no solvent is present in the pores of the MOF and that zinc bound water ligands have not been removed).

Table 6.4: Elemental analysis on 100 °C and 230 °C degassed (POC) MOF **3′** samples used in TNT pre-concentration, and the theoretical CHN elemental composition of MOF **3′** as calculated from the empirical formulae $[Zn_4L(H_2O)_4]$.

Sample	C (%)	H (%)	N (%)
Theoretical MOF **3′**	42.7	2.7	0
MOF **3′** 100 °C degassed sample (1)	41.06	3.57	0.66
MOF **3′**100 °C degassed sample (2)	41.13	3.60	0.66
MOF **3′** 230 °C degassed sample (1)	43.06	3.17	0.69
MOF **3′** 230 °C degassed sample (2)	43.00	3.26	0.67

The results of the CHN analysis are not in full accordance with the theoretically calculated CHN composition of the MOF, most significantly the nitrogen and hydrogen content in the pre-concentration samples was observed to be higher than expected. These results suggest that potentially some residual solvent molecules (from the activation procedure) were retained in both of these MOF samples. The most likely molecules that could cause such increase in nitrogen are acetonitrile (MeCN) and dimethyl formamide (DMF) solvents. In order to further confirm this, ^{1}H NMR analysis on the samples was attempted.

6.3.5.6 *Nuclear magnetic resonance analysis*

As metal-organic frameworks are solid crystalline materials and are generally insoluble in conventional NMR solvents, an acid digestion with a DCl in D_2O system (as desribed in Chapter 8) was performed on the two samples prior to ^{1}H NMR analysis; in order to cleave the carboxylic acid to metal co-ordinations in the MOFs through the re-protonation of the acid linkers to cause a breakdown of the MOFs into their molecular components. The ^{1}H NMR spectra of the two samples each digested and then dissolved in d6 – DMSO[‡‡‡] are shown in Figure 6.24 and Figure 6.25.

‡‡‡ It is important to note that fresh, just purchased, NMR tubes were used for these analyses in order to prevent the cross-contamination of solvents.

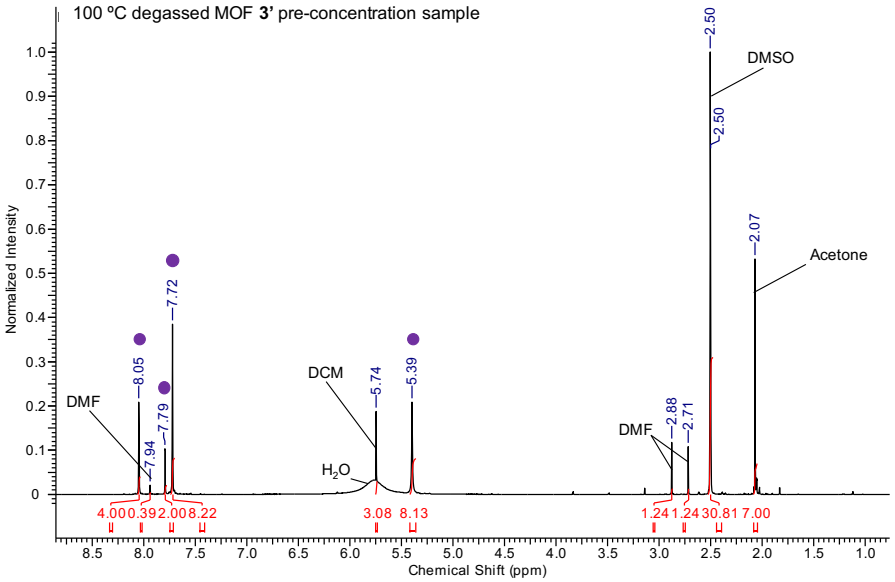

Figure 6.24: ^{1}H NMR analysis of the MOF **3'** degassed at 100 °C TNT pre-concentration sample which has been acid digested in DCl in D_2O and dissolved in d6–DMSO. The purple dots on the spectrum denote the peaks attributed to the H_8L linker where L = 5,5′,5″,5‴-[1,2,4,5-benzenetetrayltetrakis(methyleneoxy)tetra-1, 3-benzenedicarboxylic acid. The peaks were normalised using the peak at 8.1 ppm ,which was set to 4.00. The remaining peaks are ascribed to solvent molecules [252] and are labelled accordingly on the spectrum.

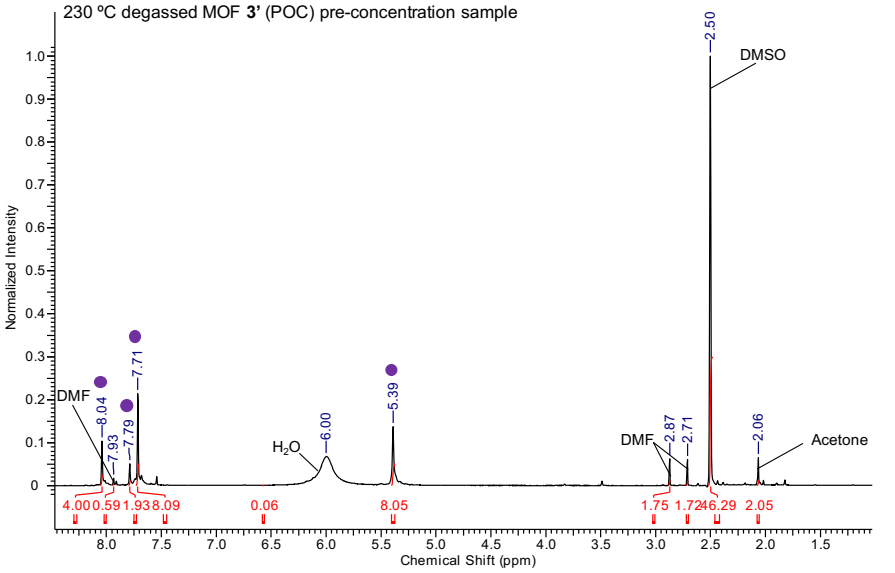

Figure 6.25: ^{1}H NMR analysis of the MOF **3'** degassed at 230 °C proof-of-concept pre-concentration sample which has been acid digested in DCl in D_2O and dissolved in d6–DMSO. The purple dots on the spectrum denote the peaks attributed to the H_8L linker where L = 5,5′,5″,5‴-[1,2,4,5-benzenetetrayltetrakis(methyleneoxy)tetra-1, 3-benzenedicarboxylic acid. The peaks were normalised using the peak at 8.1 ppm, which was set to 4.00. The remaining peaks are due to solvent molecules [252] and are labelled on the spectrum.

From the ^{1}H NMR analysis is can be seen that both of the MOF **3′** samples still contained solvents present within their pores from their solvent-exchange washing procedures. The 100 °C degassed MOF **3′** sample was observed to still contain approximately one and a half dichloromethane (DCM) molecules, just over one acetone molecule, and approximately 0.4 dimethylformamide (DMF) molecules per empirical formula unit of the MOF ($[Zn_4L(H_2O)_4]$). Where as the 230 °C degassed POC MOF **3′** sample contained approximately 0.6 DMF molecules and around 0.3 acetone molecules per $[Zn_4L(H_2O)_4]$. These results demonstrate that both of the degassing (and thermal desorption) procedures used were ineffective at removing all of the persistent solvent molecules that were contained within the pores of these MOF **3′** samples. However, it can be seen that the 230 °C degassed sample contained overall fewer solvent molecules present within its pores than the 100 °C degassed MOF sample. This could help rationalise its greater pre-concentration capabilities owing to potentially bigger void space present within the cavities of this MOF **3′** sample; enabling the greater encapsulation of TNT vapours.

6.3.5.7 *Thermogravimetric analysis*

The results of the thermogravimetric analysis (TGA) on the two differently degassed MOF **3′** samples are given in Figure 6.26.

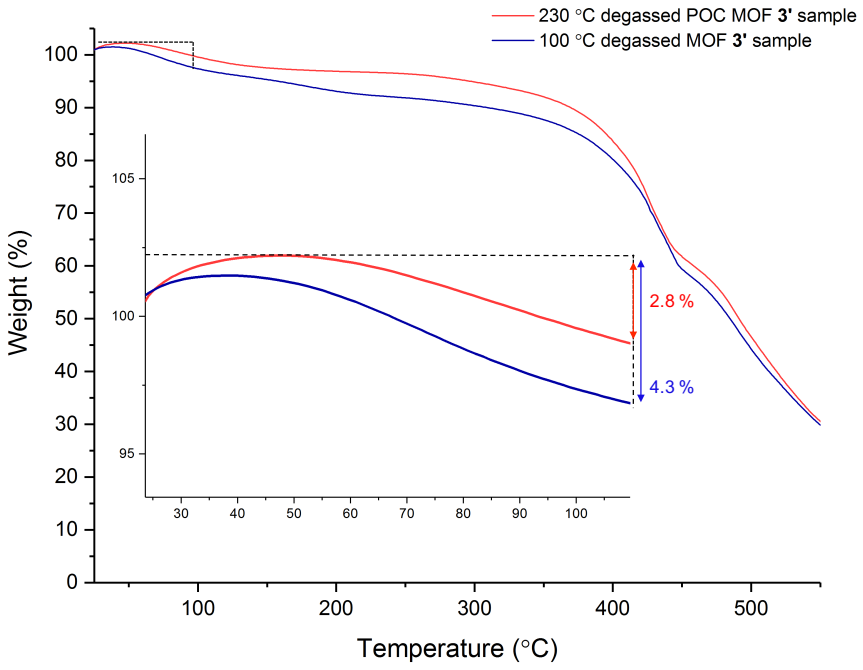

Figure 6.26: Thermogravimetric analysis on the MOF **3′** samples degassed at 100 °C (navy) and 230 °C (red) used in TNT pre-concentration experiments. The inset gives the zoomed in mass loss for the temperature region between 25 and 105 °C.

From the TGA it can be seen that the two MOFs most likely contain different amounts of water present within their structure. This is suggested due to the different mass losses observed for the two samples between the temperature at the start of the analysis (approximately 25 °C) and 102 °C. The MOF **3′** sample degassed at 230 °C looses approximately 2.8% of its mass between these two temperatures, this corresponds to around a 32 g mol^{-1} mass loss (based on the mass of the MOF **3′** empirical formula unit $[Zn_4L(H_2O)_4]$ being 1181.52 mol^{-1}) and is attributed to the potential loss of 1.8 H_2O molecules. For the 100 °C degassed (and 150 °C thermally desorbed) sample, there is an approximate 4.3 % mass loss, which equates to 50.4 g mol^{-1} and is ascribed to the loss of potentially 2.8 H_2O molecules. It is likely

that the water molecules lost are those coordinated to the zinc metal centres, as well as some potentially present within the pores of the MOF. Due to the minimal air exposure of these samples after GC-MS analysis and before TGA analysis, it is suggested that the mass loss is mainly due to the loss of zinc-coordinated water molecules. However, this cannot be definitively determined through TGA analysis alone. Nevertheless, this hypothesis corroborates the colour changes and structural perturbations observed in the PXRD patterns for these two MOFs in comparison to the just activated MOF **3'** samples. It also coincides with the results of the IR analysis.

In addition, the indication that there are fewer coordinated molecules present in the POC MOF **3'** 230 °C degassed sample supports the suggestion that this sample is a partially dehydrated form of the MOF. This means that the framework has fewer water molecules occupying the space within the pores of the structure, thus, allowing TNT vapours to be effectively encapsulated, which could be an explanation for the differences in the pre-concentration efficiencies observed between these two samples. From the TGA analysis it can also be observed that there is mass loss in the region of 102 °C - 154 °C in both of the TGAs and this is attributed to the loss of DMF from the pores of these two MOF **3'** samples. The MOF **3'** sample degassed at 100 °C observes a mass loss of 2.1 % in this temperature region and the POC MOF **3'** degassed at 230 °C shows a 2.0% mass loss. These values correspond to 0.34 and 0.32 DMFs present per sample for the 100 °C and 230 °C degassed (and 150 °C thermally desorbed and GC-MS analysed) pre-concentration MOFs respectively. This again shows the ineffectiveness of the solvent-exchange procedure implemented for guest solvent removal as well as the degassing procedures.

6.4 CONCLUSIONS AND FUTURE WORK

In this chapter metal-organic framework **3** in its active form MOF **3′** (produced through the implementation of a solvent-change exchange procedure) was investigated for its potential as a TNT vapour pre-concentrator.

Sample tubes containing the active MOF **3′** were fabricated and degassed prior to TNT vapour sampling. After sampling the vapours produced from one of two different TNT sources (vapour generator and permeation oven), the TNT-containing MOF sample tubes were inserted into a thermal desorber interfaced with a gas chromatography mass spectrometer; to allow for the liberation, separation and quantification of the TNT vapours using the GC-MS.

As demonstrated throughout this chapter, the conditions (temperature and duration) with which the MOF **3′** samples were degassed prior to vapour sampling, played a significant role in their pre-concentration capabilities. Two MOF **3′** samples that were degassed at 230 °C for 30 minutes were very effective at pre-concentrating TNT vapours; they were able to outperform the commercially manufactured sorbent Tenax® TA under these experimental conditions, and they could be re-used for a number of pre-concentration cycles. However, MOF **3′** samples degassed at lower temperatures (100 °C and 150 °C) as well as some MOF **3′** samples that were degassed using the same conditions as the aforementioned MOF samples; could not replicate the same pre-concentration abilities.

Chemical analyses on the best and worst performing MOF **3′** TNT pre-concentrators eluded to the complexity in the degassing of these materials. Powder X-ray diffraction (PXRD), scanning electron microscopy (SEM), thermogravimetric analysis (TGA), X-ray photoelectron spectroscopy (XPS), proton nuclear magnetic resonance (^{1}H NMR),

elemental analysis (EA), infra-red spectroscopy (IR), as well as visual crystal colour change observations were all performed on the best (230 °C degassed MOF **3′** sample used in the proof-of-concept experiments) and worst (100 °C degassed MOF **3′** sample) MOF **3′** test samples. Collectively these analyses suggested that whilst both of the MOF **3′** TNT pre-concentrator samples retained their overall expected MOF topology; structural transformations in the samples as a result of solvent loss were likely and could explain their varying pre-concentrator capabilities.

It was proposed (through the rationalisation of the results from ^{1}H NMR and EA analyses) that both MOF **3′** samples contained some residual solvent molecules still present in their pores left over from their synthesis and activation. It was also noted that the best TNT pre-concentrator sample (230 °C degassed POC sample) contained less solvent molecules in its pores than the worst performing sample (100 °C degassed sample used for pre-concentration). In addition, it was suggested (based on the interpretation of the IR, TGA, PXRD analyses as well as visual crystal colour change observations) that during degassing and thermal desorption (at 150 °C), some of the water molecules coordinated into the structures of these frameworks (through the zinc metal centres) were being removed. This potentially led to the partial dehydration of the MOF **3′** samples, with a greater degree of dehydration being observed for the best MOF **3′** TNT pre-concentrator (230 °C degassed).

These results help to rationalise the differences in the pre-concentration capabilities reported for these two samples. It is hypothesised that the best performing MOF **3′** pre-concentrator sample had more void space present within its pores than the worst performing MOF **3′** pre-concentrator and so was able to effectively encapsulate more TNT vapours; leading to greater pre-concentration efficiencies.

This initial and pioneering research into the use of MOFs for explosive vapour pre-concentration clearly demonstrates their potential. However, these experiments were very preliminary and a substantial amount of further research is required in order to really test the capabilities of MOFs in this field. In terms of the MOF **3′** system discussed in this chapter, future work should envisage the optimisation of degas conditions for MOF **3′** samples, so that the repeatable production of effective and re-usable MOF **3′** TNT pre-concentrators can be yielded. In addition, studies into breakthrough volumes and captured analyte bleeding should also be sought using MOF **3′**. In general, a wide variety of future studies are required to understand the potential that these materials may have as explosives pre-concentrators, some of which will be discussed in Chapter 7.

7

CONCLUSIONS AND FUTURE WORK

7.1 OVERVIEW OF RESULTS

The ultimate goal of this Ph.D. research was to further probe the potential use of metal-organic frameworks for the application of trace explosives detection. The two main aims that were sought to achieve this were: to build on the knowledge of MOFs as fluorescent-based explosives sensor and to investigate whether these materials could be used as pre-concentrators to enhance the sensitivity of other trace explosives detectors.

In the preliminary, proof-of-concept stages to this project two novel fluorescent MOFs were synthesised from the same organic ligand but varied in metal composition, which led to the frameworks having different overall topologies and porosities; one demonstrated some residual porosity and the other, none. When tested for their sensing capabilities against explosives-related compounds (2,4-DNT, NB, *p*-NT, and DMNB) in the vapour-phase, it was observed that porosity was a significant factor in analyte detectability; especially for the sensing of analytes that are deemed unfavourable to detect (*via* the photo-induced electron transfer mechanism) such as the aliphatic explosive taggant DMNB. Such observations echoed some of the previous findings reported by the pioneers in the fluorescent MOF explosives detection and amplified fluorescent conjugate polymer fields. Further to this, due to their differing overall framework architectures, the MOFs demonstrated different selectivities towards the analytes in the test-

ing time frame; one MOF demonstrated detectability of all four analytes, and the other showed semi-selectivity by only being able to detect half of the analytes in the testing time frame. This semi-selectivity was attributed to the MOF's lack of porosity and thus, its inability to form meaningful interactions with two out of the four analytes. In addition, these two MOF sensors demonstrated timely responses with signals observed in less than 10 s of analyte exposure, and one of the MOFs demonstrated room temperature sensor regeneration. Both of these considerations are significant for the applicability of these materials for in-field use.

Lessons learned from these exploratory experiments were that the sensitivites of analyte detection in the vapour-phase were dramatically affected by 'thin film' fabrication. Also, it was highlighted that a more sophisticate vapour-delivery system which exposes MOFs to known concentrations of analyte vapours is required, to be able to evaluate which analytes quench the MOFs to the greatest extent.

Despite the initially synthesised MOFs demonstrating explosive-related analyte detectability, only one of the MOFs was able to sense the relatively bulky compound 2,4-DNT, and it was not clear if 2,4-DNT was penetrating the pores of this MOF. Therefore, efforts were shifted towards constructing a framework with potentially larger cavities to facilitate the encapsulation and detection of bigger explosive molecules such as TNT, Tetryl, and PETN.

MOF **3** was designed based on a previously reported framework, constructing an analogous, novel MOF structure to that synthesied by Eddaoudi *et al.* [176]. Crystallographically it was determined **3** had theoretically big pores capable of containing large explosive substances. It was also observed that **3** demonstrated a degree of flexibility and pore shape disorder (although still retaining its overall topology) when activated to form MOF **3'**. Nevertheless, this frame-

work demonstrated high thermal (up to 400 °C) and humidity stabilities. The humidity stability of this MOF was probed using dynamic vapour sorption experiments* that allowed for BET surface areas to be calculated using water as a probing gas, at varying temperatures. From these measurements and according to water stability grading guidelines recently introduced into the MOF community, it was proposed that **3′** would be fit for use in hot and humid explosives detection environments. These considerations are of significance as the moisture stability of MOFs has previously limited their practical application in a number of fields.

Sensing experiments probed the ability of MOF **3′** to detect explosive substances and related analytes in both the solution and vapour phase. During the solution-phase sensing experiments, the most commonly used sensing methodology was critiqued and new approaches were suggested, that will hopefully be of benefit to the wider MOF community. In the solution-phase **3′** was able to detect the explosives Tetryl, TNT, and PETN, the explosive related compound 2,4-DNT, as well as arugably RDX, *via* the PIET mechanism. Limits of detection using this approach were noted to be < 4 ppm. Stern-Volmer constants of quenching efficiency were found to be comparable to those reported by Swager *et al.* [79] for fluorescent conjugate polymers; the sensing materials used in commercially available fluorescence-based explosive detectors. Also, **3′** showed preferential sensing towards Tetryl, which was attributed to potentially two types of quenching mechanism being available for this analyte; PIET and FRET. The vapour-phase sensing of the explosive-related compound 2,4-DNT with **3′** produced unexpected but interesting results. Instead of fluorescence quenching, fluorescence enhancements were observed in the presence of this analyte as well as atmospheric air, attributed to the molecules adsorbing onto or into the MOF, rigidifying its flexible

* In collaboration with Surface Measurement System Ltd. London, UK ©.

structure and inhibiting linker motions and vibrations. Whilst these findings eliminated the use of this MOF as a vapour-phase stand-off sensor, they suggested that the MOF was sorbing 2,4-DNT; consequently this framework was probed for its potential as a vapour-phase pre-concentrator.

During the sensing experiments conducted in this thesis, it was noted that typically single MOF sensors can detect explosives, but they are not able to identify which explosives they are detecting, especially when exposed to explosives with varying concentrations. Therefore, a three MOF sensory array (chemical nose) was constructed with the aim to test whether such an approach can induce the discriminative detection of explosive substances and related compounds using MOFs.

The MOF sensor array was constructed from **3′** alongside two previous reported fluorescent MOFs; each of which were judicially chosen to interact with the test analytes in differing ways by virtue of their different topologies. The sensors were exposed to TNT, Tetryl, RDX, PETN, and 2,4-DNT *via* solution-phase titrations. The quenching response pattern obtained from the exposure of the MOFs to these analytes (at varying concentrations) was analysed using the pattern recognition tool linear discrimination analysis (LDA). It was found that when analytes in the concentration range of 26.0 μM – 62.5 μM (approx. 20 – 8 ppm) were exposed to this array as 'unknowns'; a 94% accuracy of classification could be achieved (for total data and 84% accuracy using a cross-validation approach). Therefore, suggesting that when incorporated into chemical noses, MOFs can not only detect but can also identify the explosives to which they are exposed; which may be important for the real-world applicability of these materials depending on the detection scenario in which they may be used. These results were particularly significant as there have been

no other reports to date in the literature that have explored this MOF-array based approach for explosives sensing. However, as these were initial, exploratory experiments, plentiful further research to confirm the applicability of this method in real-world scenarios is required.

Some work exploring the potential of metal-organic frameworks as standalone explosive vapour pre-concentrators was also undertaken; MOF **3′** was investigated for its applicability as a TNT vapour pre-concentrator†. Sample tubes containing **3′** were fabricated and degassed in an attempt to create solvent-free pre-concentrator MOF sorbents. These were then used to sample TNT vapours from one of two sources, after which, the sample tubes were placed into a thermal desorber interfaced with a gas chromatography-mass spectrometer for the liberation, separation and quantitative analysis of trapped ('pre-concentrated') TNT vapours.

The pre-concentration capability of **3′** was evaluated by the pre-concentrator efficiency – a percentage of how many of the vapours available for sampling a particular MOF **3′** sample could uptake and release. These efficiencies were compared to those obtained using a commercially available sorbent material; Tenax® TA, using the same experimental procedure. The results of these proof-of-concept experiments yielded diverse results.

Two different MOF **3′** samples were able to successfully pre-concentrate TNT vapours with efficiencies between 66 – 89 % and for numerous re-use cycles. These samples of **3′** were also able to outperform Tenax® TA under the used test conditions. However, reproducing MOF **3′** pre-concentrators that were as effective as these initial samples was not trivial and the same pre-concentrator efficiencies could not be achieved.

† In collaboration with the Explosives Detection Group, Defence Science Technology Laboratory.

Significant discrepancies in results were observed between different synthetic (and activated) batches which were degassed using different (and sometimes the same) conditions. The worst performing samples were found not to uptake any TNT at all. These extreme variations in the pre-concentrator capabilities of the same MOF structure were attributed to the degassing conditions. From chemical analyses, it was confirmed that the MOF activation procedure was not 100% effective at removing the solvents present within the MOFs pores and the pre-concentrator capability of an **3′** sample was suggested to be directly related to how much solvent was able to be removed during activation and subsequent degassing. Also, the extent of MOF **3′** dehydration (removal of the water ligands bound to the zinc metal centers in the MOF) was also proposed to affect the MOFs pre-concentration efficiency. Essentially, the amount of space available in the framework cavities for TNT encapsulation was deemed crucial for the MOFs pre-concentration capability. Therefore, while these results that explored the first MOF for explosives vapour pre-concentration were promising, plentiful work in the optimisation of this system for the repeatable generation of successful pre-concentrators is required.

In general, the research presented in this thesis has shown that fluorescent MOFs can detect explosive substances and related compounds with a good degree of sensitivity (low ppm levels). They are able to identify which analytes they are exposed to if incorporated into arrays. Also, they demonstrate rapid sensor response times, recyclability, as well as high thermal and humidity stabilities. Furthermore, they can absorb and release analytes when required for pre-concentration applications. These sensing properties of MOFs address some of the requirements outlined in the literature review for an ideal trace explosives detector. However, while this research has further probed aspects of fluorescent MOFs as explosives detectors

not previously reported, and has therefore demonstrated the further potential of these materials; ample future work is still required to realise the true real-world applicability of MOFs for trace explosives detection.

7.2 FUTURE WORK

Regarding future work specific to the novel metal-organic frameworks presented in this thesis, the optimisation of the activation conditions for MOF **3′** is of high priority. Experiments should be attempted whereby different activation procedures are implemented and chemical analyses undertaken in order to analyse their effectiveness. In addition to this, other methods for establishing BET surface areas of the MOF should be investigated, such as using argon as a probe gas, with the aim to gain a greater understanding of the porosity of this material, particularly at different dehydration levels of the MOF.

The optimisation of the activation of MOF **3′** could help generate samples of the MOF that can undergo effective degassing to produce repeatable and re-usable TNT pre-concentrator materials, like those obtained in the proof-of-concept pre-concentrator experiments. Once such degas conditions are optimised for **3′**, the selectivity in the pre-concentration of TNT should be investigated for this framework. MOF **3′** should be tested for its uptake of TNT in the presence of interferents that may be present in a sampling environment, such as petrol or perfume. If the MOF were to prove itself useful after such experiments, then the breakthrough volume and the bleeding of the captured analytes should be evaluated. In addition, whilst the pre-concentrator experiments presented in this thesis evaluated the collection and release of TNT vapours from larger volumes of air than those presented to the detector (GC-MS); they did not really probe how the

materials may capture target analytes when sampling large air volumes containing very small quantities of the targets. Thus, future work should look into the use of optimised MOF **3′** pre-concentrators to sample more challenging environments that may mimic some of those found in real world scenarios. Furthemore, an attempt should be made to interface functioning samples of MOF **3′** to current explosives trace detectors to evaluate the impact they may or may not have on the instruments selectivity. With this said, the work presented in this thesis was an exploratory investigation with one particular MOF and one target analyte. With thousands of metal-organic frameworks having been reported to date and a number of explosives requiring pre-concentration before detection; future work should aim to identify the best MOFs that are fit for pre-concentrating specific explosives. Whilst this is likely to be a challenging feat, as reported by Keffer *et al.*, computational simulations could be a useful tool to assist in this endeavour [249].

As discussed, the 3-MOF sensing array reported in this thesis demonstrated significant success, however, as with the pre-concentrator experiments, this research was also on a proof-of-concept basis. Thus, future work should be undertaken on this topic to gain further insights. It is acknowledged that the MOFs used to construct this array may not be the most effective. Further to this, the ideal number of MOFs to be used in a sensing array is currently not known. Therefore, future work should attempt to construct a refined array that has the optimum number of MOFs that have the most discriminative power. As demonstrated by Wilmer *et al.* computational studies could prove useful for this [225]. Another aspect of future work that should be explored, as briefly mentioned in Chapter 5, is the effect of interferents on the MOF arrays. Furthermore, it is recognised that solution-phase sensing is useful for the testing of MOF-sensor arrays against known

concentrations of real explosives; however, such a sensing approach is not idealistic or very applicable to real-world scenarios. Therefore, the future probing on the applicability of MOF arrays for the discriminative trace detection of explosives should be attempted with the explosive substances and related compounds as gases; owing to the need for effective vapour-phase stand-off detectors. However, as eluded to, in order to be able to evaluate the true sensitivity of MOFs towards gaseous analytes, a method to develop uniform thin films of various metal-organic frameworks should be sought. In addition, as also mentioned, an accurate and variable concentration vapour delivery flow should be produced.

If the future work topics discussed in this chapter were to be addressed, and the knowledge of MOFs in general increases in the same way as it has since their conception, it is hoped that MOF sensors will assist security personnel in the trace detection of explosives and related compounds in years to come.

8

GENERAL EXPERIMENTAL MATERIALS AND INSTRUMENTATION

8.1 CHEMICALS

All of the chemicals used for the research presented in this thesis (unless otherwise stated) were purchased from either Sigma Aldrich, Fischer Scientific, vwr international or Alfa Aesar. All of the solvents used were high-performance liquid chromatography (HPLC) grade, with the exception of DMF which was dried using 4 Å molecular sieves. The water used in all experiments was deionized and room temperature was typically around 20 °C.

All explosives standards (TNT, Tetryl, RDX, 2,4-DNT and PETN) were purchased from Accustandard® *via* Kinesis ltd. Each of the standards were certified as 1 mg/ 1 mL in a 50:50 methanol:acetonitrile (MeOH:MeCN) mix. All dilutions to produce the required stock solutions (as detailed in the relevant chapters) were done so using HPLC grade MeCN. All stock solutions and as-purchased standards were refrigerated at 4 °C and discarded after one month of opening.

8.2 INSTRUMENTATION

The specific instrument details and methods used for chemical analyses not given in the previous chapters (and microwave synthesis) are detailed below *.

* The details of the instruments used in some collaborative analyses namely XPS and computational calculations can be found in the appendices.

Single crystal X-ray diffraction analysis

All single crystal X-ray diffraction data were collected at 150.0 K on a SuperNova, Dual, Cu at zero, Atlas diffractometer with CuKα (λ = 1.54184 Å) radiation. Single crystals were mounted on nylon loops ready for analysis. Using Olex2 [181], the structures were solved with the Superflip [253] structure solution programme using Charge Flipping. The structures were refined with the ShelXL [254] refinement package using Least Squares minimization. The unresolved disordered solvent found in MOF **3** was treated using the 'solvent mask' implemented in Olex 2 [181]. Solvent accessible voids were calculated using the SOLV option within the software package PLATON [167].

Powder X-ray diffraction (PXRD)

For all loose crystalline powder materials; powder X-ray diffraction (PXRD) data were collected on a STOE transmission diffractometer system Stadi-P, with a Cu K alpha, λ = 1.5418 Å, radiation source operating at 40 kilowatts and 30 milliamps. The samples were ground into a fine powder and loaded into capillary tubes of 0.5 mm or 0.7 mm diameter. In some instances, the samples were loaded into 0.7 mm capillaries whilst still immersed in a solvent. Scans were collected between 2θ= 2 - 45°, with 0.5° step intervals, for 20 s per step.

For fabricated 'thin-films' of the MOF **3'** crystals PXRD data were collected on a Lynx-Eye Bruker X-ray diffractometer with a Cu K alpha, λ = 1.5406 Å radiation source, operating at 40 kilowatts and 30 milliamps. Scans were collected between 1.5θ= 4 - 45°, with 0.05° step intervals, counted at 1 s per step.

Thermogravimetric analysis (TGA)

The thermogravimetric analysis of samples were conducted on a Netzsch Jupiter thermal gravimetric analyse using a temperature range of 25 °C to 500 °C and a ramp rate of 10 °C/ min, under a flow of air. Approximately 10 mg of a sample was used for each analysis.

Scanning electron microscopy (SEM)

Scanning electron microscopy images were obtained using a field emission Jeol 6700F SEM, operating at 5kV. All samples were coated with gold using a sputter coater prior to SEM analysis.

Attenuated total reflectance - Fourier transform infra-red (ATR-FT-IR) spectroscopy

Attenuated total reflectance -Fourier transform infra-red (ATR-FT-IR) spectra were collected using a Bruker Alpha Platinum ATR unit, scanning between 400 and 4000 cm^{-1}.

Brunauer-Emmett-Teller (BET) surface area measurements

BET surface area measurements on **1'** were measured with N_2 (77 K) on a Micromeritics Gemini VIII 2390 surface area analyzer instrument ($0.05 < P/P_0 > 0.3$). Approximately 80 mg of the MOF was out-gassed at 200°C for 24 hours prior to analysis.

Proton nuclear magnetic resonance

^{1}H NMR spectra were ran on an Avance 300 MHz or Avance 500 MHz spectrometer in d6–DMSO. The chemical shifts given in the main body of the thesis are in ppm relative to d6–DMSO (2.50 ppm).

All MOF samples were digested prior to ^{1} H NMR analysis. Approximately 5 mg of the crystalline MOF samples were added to 0.4 mL of d6–DMSO and 0.2 mL of a stock solution of 0.1 mL of 35% DCL/D_2O in 3 mL of d6–DMSO. The mixture was sonicated for 15 minutes until all of the crystalline solid had completely dissolved.

Time-correlated single photon counting (TCSPC) spectrometer

Vapour-phase fluorescence measurements were conducted on an Edinburgh Instruments time-correlated single photon counter (TCSPC) with a laser excitation source of 405 nm, and emission measured between 420 nm and 750 nm.

Fluorescence spectrometer

Solution-phase fluorescence spectra were collected on a Horiba FMax 4 instrument running FluorEssence software. Spectra were corrected for lamp and instrument response. Entrance and exit slit widths were typically 5 nm and 2 nm respectively. Emission spectra were measured using a fixed excitation wavelength and the emissions were measured from 15 nm below this wavelength to a maximum of 600 nm. Excitation spectra were obtained by fixing the monochromator at the spectral maxima of the sample, and varying the excitation wavelength from 300 nm to 15 nm above this fixed point.

Microwave synthesis

Mirowave syntheses were undertaken using a conventional microwave oven with a 700 W and 2450 MHz output. The microwave was operating at a 40% power output.

UV-visible absorption spectroscopy (UV-vis)

UV-visible absorption spectra were collected using a Perkin-Elmer Lamda-25 instrument, scanning between 250 - 500 nm. Samples were measured in 10 mm path length quartz cuvettes.

Part I

APPENDIX

A

CHAPTER THREE ADDITIONAL DATA

Additional data from the work presented in chapter three can be found on the attached CD within the folder labelled 'Appendix A'. The additional data from the work presented in chapter two details:

1. Additional crystal structure data for MOF **1** as well as the solvent accessible void parameters
2. Additional crystal structure data for MOF **2** as well as the solvent accessible void parameters
3. Additional sensing graphs
4. Computational simulations experimental details

B

CHAPTER FOUR ADDITIONAL DATA

Additional data from the work presented in chapter four can be found on the attached CD within the folder labelled 'Appendix B'. The additional data from the work presented in chapter three details:

1. Additional crystal structure data for MOF **3** as well as the solvent accessible void parameters
2. Representations of the calculated molecular dimensions of the MOF **3'** pore
3. Simulated PXRD patterns for MOF **3** and **3'**
4. MOF **3'** N_2 BET attempt details
5. PXRD patterns of MOF **3'** after immersion in water and comparison with the H_8L linker
6. PXRD patterns of the MOF **3'** samples used for DVS experiments (just activated, prior to DVS experiments)
7. PXRD pattern of the MOF **3"** crystals after variable temperature DVS experiments
8. PXRD LeBail fitting experimental details and extra data
9. MOF **3** computational simulations experimental
10. XPS results on MOF **3'** air exposed and 2,4-DNT exposed samples

C

CHAPTER FIVE ADDITIONAL DATA

Additional data from the work presented in chapter five can be found on the attached CD within the folder labelled 'Appendix C'. The additional data from the work presented in chapter four details:

1. Raw data file for the array sensing data
2. Example fluorescence emission graphs for the array sensing MOFs stable baseline suspension measurements before sensing experiments
3. Canonical plot, classification matrix and jackknifed classification matrix for the LDA on the MOF sensing array upon exposure to the tested analytes in the 62.5 – 32.3 μM range
4. Canonical plot, classification matrix and jackknifed classification matrix for the LDA on the MOF sensing array upon exposure to the tested analytes in the 62.5 – 19.6 μM range

D

CHAPTER SIX ADDITIONAL DATA

Additional data from the work presented in chapter six can be found on the attached CD within the folder labelled 'Appendix D'. The additional data from the work presented in chapter five details:

1. Picture of Tenax® TA contained within glass and stainless steel tubes
2. Files containing the specific analytical sequences ('runs') and the absolute amounts of TNT collected for each sample.
3. Picture illustrating the colour change of the crystals present in the 100 ° C degassed MOF **3′** sample (from yellow to dark yellow) post GC-MS analysis
4. MOF **3′** (as activated, just air exposed) infra-red spectrum
5. XPS data for the 100 ° C degassed and 230 ° C degassed (proof-of-concept) MOF **3′** samples

BIBLIOGRAPHY

1. HM Government. CONTEST: The United Kingdom's strategy for countering terrorism: annual report 2015 (2016). https://www.gov.uk/government/uploads/system/uploads/attachment_data/file/539683/55469_Cm_9310_Web_Accessible_v0.11.pdf.
2. National Consortium for the Study of Terrorism and Responses to Terrorism. Annex of Statistical Information: Country Reports on Terrorism 2016 (2017). https://www.state.gov/documents/organization/272485.pdf.
3. BBC News. Russian plane crash: What we know (2015). http://www.bbc.com/news/world-middle-east-34687990.
4. BBC News. Paris attacks: What happened on the night (2015). http://www.bbc.co.uk/news/world-europe-34818994.
5. BBC News. Brussels explosions: What we know about airport and metro attacks (2016). http://www.bbc.co.uk/news/world-europe-35869985.
6. BBC News. Baghdad bombing death toll rises to 281. (2016). http://www.bbc.co.uk/news/world-middle-east-36732824.
7. BBC News. Manchester attack: What we know so far (2017). http://www.bbc.co.uk/news/uk-england-manchester-40008389.
8. UK Security Services MI5. UK threat level (Accessed: Nov 2017). https://www.mi5.gov.uk/threat-levels.

9. Marshall, M. & Oxley, J. C. in *Aspects of Explosives Detection* (eds Marshall, M. & Oxley, J. C.) 1–10 (Elsevier, Oxford, 2009).

10. Woodfin, R. L. in *Trace Chemical Sensing of Explosives* (ed Woodfin, R. L.) 13–38 (John Wiley & Sons, Hoboken, 2006).

11. Akhavan, J. in *The Chemistry of Explosives* 27–59 (Royal Society of Chemistry, Cambridge, 2015).

12. Meyer, R., Köhler, J. & Homburg, A. in *Explosives* 118–140 (John Wiley & Sons, Weinheim, 2016).

13. Marshall, M. & Oxley, J. C. in *Aspects of Explosives Detection* (eds Marshall, M. & Oxley, J. C.) 11–26 (Elsevier, Oxford, 2009).

14. Akhavan, J. in *The Chemistry of Explosives* 1–26 (Royal Society of Chemistry, Cambridge, 2015).

15. Oxley, J. C. in *Trace Chemical Sensing of Explosives* (ed Woodfin, R. L.) 35–41 (John Wiley & Sons, Inc., Hoboken, 2006).

16. The Independent. Salman Abedi's explosives same as bombs used in 7/7, Brussels and Paris terror attacks. (2017). `http://www.independent.co.uk/news/uk/home-news/manchester-bombing-latest-salman-abedi-explosives-same-as-7-july-london-brussels-paris-terror-a7755366.html`.

17. Gersbeck, T. in *Practical Military Ordinance Identification* 1–8 (CRS press, Taylor & Francis group, Boca Raton, 2014).

18. Yeager, K. in *Trace Chemical Sensing of Explosives* (ed Woodfin, R. L.) 43–67 (John Wiley & Sons, Inc., Hoboken, 2006).

19. National Research Council. Existing and Potential Standoff Explosives Detection Techniques. `https://www.nap.edu/catalog/10998/existing-and-potential-standoff-explosives-detection-techniques` (The National Academies Press, Washington DC, 2004).

20. Parmeter, J. E. The challenge of standoff explosives detection in *Proceedings of 38th Annual 2004 International Carnahan Conference on Security Technology* (IEEE, 2004).

21. Brown, K. E., Greenfield, M. T., McGrane, S. D. & Moore, D. S. Advances in explosives analysis–part I: animal, chemical, ion, and mechanical methods. *Anal. Bioanal.Chem.* **408,** 35–47 (2016).

22. Steinfeld, J. I. & Wormhoudt, J. Explosives detection: A challenge for physical chemistry. *Annu. Rev. Phys. Chem.* **49,** 203–232 (1998).

23. Lefferts, M. J. & Castell, M. R. Vapour sensing of explosive materials. *Anal. Methods* **7,** 9005–9017 (2015).

24. Gares, K. L., Hufziger, K. T., Bykov, S. V. & Asher, S. A. Review of explosive detection methodologies and the emergence of standoff deep UV resonance Raman. *J. Raman Spectrosc.* **47,** 124–141 (2016).

25. Mostak, P. in *Vapour and Trace Detection of Explosives for Anti-Terrorism Purposes* (eds Krausa, M. & Alekseyvitch Reznev, A.) 23–30 (Kluwer Academic Publishers (Springer), Dordrecht, 2004).

26. Sun, X., Wang, Y. & Lei, Y. Fluorescence based explosive detection: from mechanisms to sensory materials. *Chem. Soc. Rev.* **44,** 8019–8061 (2015).

27. Kolla, P. Detecting hidden explosives. *Anal. Chem.* **67,** 184–189 (1995).

28. UK Health and Safety Executive. Explosives Regulations 2014; security provisions (Accessed: Nov. 2017). `http://www.hse.gov.uk/pUbns/priced/l151.pdf`.

29. National Research Council. Containing the Threat from Illegal Bombings: An Integrated National Strategy for Marking, Tagging, Rendering Inert, and Licensing Explosives and Their Pre-

cursors. https://www.nap.edu/catalog/5966/containing-the-threat-from-illegal-bombings-an-integrated-national-strategy (The National Academies Press, Washington, DC, 1998).

30. Ostmark, H., Wallin, S. & Ang, H. G. Vapor pressure of explosives: a critical review. *Propellants Explos. Pyrotech.* **37,** 12–23 (2012).

31. Banerjee, D., Hu, Z. & Li, J. Luminescent metal-organic frameworks as explosive sensors. *Dalton Trans.* **43,** 10668–10685 (2014).

32. Grundler, P. *Chemical Sensors* 12–13 (Springer, Berlin Heidelberg, 2007).

33. Chaffee-Cipich, M. N., Sturtevant, B. D. & Beaudoin, S. P. Adhesion of explosives. *Anal. Chem.* **85,** 5358–5366 (2013).

34. Senesac, L. & Thundat, T. G. Nanosensors for trace explosive detection. *Mater. Today* **11,** 28–36 (2008).

35. Fisher, D., Zach, R., Matana, Y., Elia, P., Shustack, S., Sharon, Y. & Zeiri, Y. Bomb swab: can trace explosive particle sampling and detection be improved? *Talanta* **174,** 92–99 (2017).

36. Sun, Y. *Field Detection Technologies for Explosives* 45–50 (ILM Publications, St Albans, 2009).

37. Concha, A, Mills, D. S., Feugier, A, Zulch, H, Guest, C, Harris, R & Pike, T. W. Using sniffing behavior to differentiate true negative from false negative responses in trained scent-detection dogs. *Chem. Senses* **39,** 749–754 (2014).

38. Singh, S. & Singh, M. Explosives detection systems (EDS) for aviation security. *Signal Processing* **83,** 31–55 (Jan. 2003).

39. Liscouski, R. & McGann, W. The evolving challenges for explosive detection in the aviation sector and beyond (2016). https://ctc.usma.edu/wp-content/uploads/2016/05/CTC-SENTINEL_Vol9Iss515.pdf.

40. Oxley, J. C. & Waggoner, L. P. in *Aspects of Explosives Detection* (eds Marshall, M. & Oxley, J. C.) 27–40 (Elsevier, Oxford, 2009).

41. Furton, K. G. & Myers, L. J. The scientific foundation and efficacy of the use of canines as chemical detectors for explosives. *Talanta* **53,** 487–500 (2001).

42. Poling, A., Weetjens, B., Cox, C., Beyene, N. W., Bach, H. & Sully, A. Using trained pouched rats to detect land mines: another victory for operant conditioning. *J. Appl. Behav. Anal* **44,** 351–355 (2011).

43. Shaw, J. A., Seldomridge, N. L., Dunkle, D. L., Nugent, P. W., Spangler, L. H., Bromenshenk, J. J., Henderson, C. B., Churnside, J. H. & Wilson, J. J. Polarization lidar measurements of honey bees in flight for locating land mines. *Opt. Express* **13,** 5853–5863 (2005).

44. Linker, K. L. Large-volume sampling and preconcentration for trace explosives detection. (2004). `http://prod.sandia.gov/techlib/access-control.cgi/2004/042117.pdf`.

45. Moore, D. S. Instrumentation for trace detection of high explosives. *Rev. Sci. Instrum.* **75,** 2499–2512 (2004).

46. Collin, O. L., Zimmermann, C. M. & Jackson, G. P. Fast gas chromatography negative chemical ionization tandem mass spectrometry of explosive compounds using dynamic collision-induced dissociation. *Int. J. Mass Spectrom.* **279,** 93–99 (2009).

47. Moore, D. S. Recent advances in trace explosives detection instrumentation. *Sens Imaging* **8,** 9–38 (2007).

48. Sugai, T. *Fundamentals of Mass Spectrometry* (ed Hiraoka, K.) 89–109 (Springer, New York, 2013).

49. Ewing, R. A critical review of ion mobility spectrometry for the detection of explosives and explosive related compounds. *Talanta* **54,** 515–529 (2001).

50. Otiento-Alego, V. & Speers, N. in *Infrared and Raman Spectrocopy in Forensic Science* 207–232 (Wiley, Chichester, 2012).

51. Pacheco-Londoño, L. C., Ortiz-Rivera, W., Primera-Pedrozo, O. M. & Hernández-Rivera, S. P. Vibrational spectroscopy standoff detection of explosives. *Anal. Bioanal.Chem.* **395,** 323–335 (2009).

52. Chalmers, J. M., Edwards, H. G. M. & Hargreaves, M. D. in *Infrared and Raman spectrocopy in forensic science* 10–44 (Wiley, Chichester, 2012).

53. Caygill, J. S., Davis, F. & Higson, S. P. J. Current trends in explosive detection techniques. *Talanta* **88,** 14–29 (2012).

54. Burks, R. M. & Hage, D. S. Current trends in the detection of peroxide-based explosives. *Anal. Bioanal.Chem.* **395,** 301–313 (2009).

55. Brown, K. E., Greenfield, M. T., McGrane, S. D. & Moore, D. S. Advances in explosives analysis–part II: photon and neutron methods. *Anal. Bioanal.Chem.* **408,** 49–65 (2016).

56. Singh, S. Sensors—An effective approach for the detection of explosives. *J. Hazard. Mater.* **144,** 15–28 (2007).

57. Smith, R. G., D'Souza, N. & Nicklin, S. A review of biosensors and biologically-inspired systems for explosives detection. *Analyst* **133,** 571–584 (2008).

58. Diehl, K. L. & Anslyn, E. V. Array sensing using optical methods for detection of chemical and biological hazards. *Chem. Soc. Rev.* **42,** 8596–8611 (2013).

59. Stitzel, S. E., Aernecke, M. J. & Walt, D. R. Artificial noses. *Annu. Rev. Biomed. Eng* **13,** 1–25 (2011).

60. Albert, K. J., Lewis, N. S., Schauer, C. L., Sotzing, G. A., Stitze, S. E., Vaid, T. P. & Walt, D. R. Cross-reactive chemical sensor arrays. *Chem. Rev.* **100,** 2595–2626 (2000).

61. Germain, M. E. & Knapp, M. J. Optical explosives detection: from color changes to fluorescence turn-on. *Chem. Soc. Rev.* **38,** 2543–2555 (2009).

62. Lin, H. & Suslick, K. S. A colorimetric sensor array for detection of triacetone triperoxide vapor. *J. Am. Chem. Soc.* **132,** 15519–15521 (2010).

63. Kangas, M. J., Burks, R. M., Atwater, J., Lukowicz, R. M., Williams, P. & Holmes, A. E. colorimetric sensor arrays for the detection and identification of chemical weapons and explosives. *Crit. Rev. Anal. Chem.* **47,** 138–153 (2016).

64. Lakowicz, J. R. in *Principles of Fluorescence Spectroscopy* 1–23 (Springer US, Boston, 1999).

65. Allendorf, M. D., Bauer, C. A., Bhakta, R. K. & Houk, R. J. T. Luminescent metal–organic frameworks. *Chem. Soc. Rev.* **38,** 1330–1352 (2009).

66. Cui, Y., Yue, Y., Qian, G. & Chen, B. Luminescent functional metal-organic frameworks. *Chem. Rev.* **112,** 1126–1162 (2012).

67. Lustig, W. P., Mukherjee, S., Rudd, N. D., Desai, A. V., Li, J. & Ghosh, S. K. Metal–organic frameworks: functional luminescent and photonic materials for sensing applications. *Chem. Soc. Rev.* **46,** 3242–3285 (2017).

68. Birks, J. B. Excimers. *Rep. Prog. Phys.* **38,** 903–974 (1975).

69. Marcus, R. A. Electron transfer reactions in chemistry. Theory and experiment. *Rev. Mod. Phys.* **65,** 599–610 (1993).

70. He, G., Yan, N., Yang, J., Wang, H., Ding, L., Yin, S. & Fang, Y. Pyrene-containing conjugated polymer-based fluorescent films for highly sensitive and selective sensing of TNT in aqueous medium. *Macromolecules* **44,** 4759–4766 (2011).

71. Selvin, P. R. Fluorescence resonance energy transfer. *Methods Enzymol* **246,** 300–334 (1995).

72. Gole, B., Bar, A. K. & Mukherjee, P. S. Modification of extended open frameworks with fluorescent tags for sensing explosives: competition between size selectivity and electron deficiency. *Chem. Eur. J.* **20,** 2276–2291 (2014).

73. Lakowicz, J. R. in *Principles of Fluorescence Spectroscopy* 277–330 (Springer US, Boston, 1999).

74. Thomas III, S. W. & Swager, T. M. in *Aspects of Explosives Detection* (eds Marshall, M. & Oxley, J. C.) 203–221 (Elsevier, Oxford, 2009).

75. FLIR. Product data sheet - FIDO X3 (Accessed: Nov 2007). `http://www.flir.com/uploadedFiles/flirGS/Threat_Detection/Explosives_Detection/Products/Fido_X3_Explosives_Detector/FLIR-Fidox3-Datasheet-EN.pdf`.

76. Yang, J.-S. & Swager, T. M. Fluorescent porous polymer films as TNT chemosensors: electronic and structural effects. *J. Am. Chem. Soc.* **120,** 11864–11873 (1998).

77. Rochat, S. & Swager, T. M. Conjugated amplifying polymers for optical sensing applications. *ACS Appl. Mater. Interfaces* **5,** 4488–4502 (2013).

78. Thomas, S. W., Amara, J. P., Bjork, R. E. & Swager, T. M. Amplifying fluorescent polymer sensors for the explosives taggant 2,3-dimethyl-2,3-dinitrobutane (DMNB). *Chem. Commun.* **117,** 4572–4574 (2005).

79. Thomas, S. W., Joly, G. D. & Swager, T. M. Chemical sensors based on amplifying fluorescent conjugated polymers. *Chem. Rev.* **107,** 1339–1386 (2007).

80. Focsaneanu, K.-S. & Scaiano, J. C. Potential analytical applications of differential fluorescence quenching: pyrene monomer and excimer emissions as sensors for electron deficient molecules. *Photochem. Photobiol. Sci.* **4,** 817–821 (2005).

81. Ponnu, A. & Anslyn, E. V. A fluorescence-based cyclodextrin sensor to detect nitroaromatic explosives. *Supramol. Chem.* **22,** 65–71 (2009).

82. Costa, A. I. & Prata, J. V. Substituted p-phenylene ethynylene trimers as fluorescent sensors for nitroaromatic explosives. *Sens. Actuators, B* **161,** 251–260 (2012).

83. Barata, P. D. & Prata, J. V. New entities for sensory chemistry based on calix[4]arene-carbazole conjugates: from synthesis to applications. *Supramol. Chem.* **25,** 782–797 (2013).

84. Zhu, W., Li, W., Wang, C., Cui, J., Yang, H., Jiang, Y. & Li, G. CB[8]-based rotaxane as a useful platform for sensitive detection and discrimination of explosives. *Chem. Sci.* **4,** 3583–3590 (2013).

85. Ding, Z., Zhao, Q., Xing, R., Wang, X., Ding, J., Wang, L. & Han, Y. Detection of explosives with porous xerogel film from conjugated carbazole-based dendrimers. *J. Mater. Chem. C* **1,** 786–792 (2012).

86. Shanmugaraju, S., Jadhav, H., Karthik, R. & Mukherjee, P. S. Electron rich supramolecular polymers as fluorescent sensors for nitroaromatics. *RSC Adv.* **3,** 4940–4950 (2013).

87. Batten, S. R., Champness, N. R., Chen, X.-M., Garcia-Martinez, J., Kitagawa, S., Öhrström, L., O'Keeffe, M., Suh, M. P. & Reed-

ijk, J. Coordination polymers, metal–organic frameworks and the need for terminology guidelines. *CrystEngComm* **14,** 3001–3004 (2012).

88. James, S. L. Metal-organic frameworks. *Chem. Soc. Rev.* **32,** 276–288 (2003).

89. Prakash, M. J. & Lah, M. S. Metal–organic macrocycles, metal–organic polyhedra and metal–organic frameworks. *Chem. Commun.* **0,** 3326–3341 (2009).

90. Yaghi, O. M., O'Keeffe, M., Ockwig, N. W., Chae, H. K., Eddaoudi, M. & Kim, J. Reticular synthesis and the design of new materials. *Nature* **423,** 705–714 (2003).

91. Perry, J. J., Perman, J. A. & Zaworotko, M. J. Design and synthesis of metal-organic frameworks using metal-organic polyhedra as supermolecular building blocks. *Chem. Soc. Rev.* **38,** 1400–1417 (2009).

92. Eddaoudi, M, Moler, D. B., Li, H, Chen, B, Reineke, T. M., O'Keeffe, M & Yaghi, O. M. Modular chemistry: secondary building units as a basis for the design of highly porous and robust metal-organic carboxylate frameworks. *Acc. Chem. Res.* **34,** 319–330 (2001).

93. Furukawa, H., Cordova, K. E., O'Keeffe, M. & Yaghi, O. M. The chemistry and applications of metal-organic frameworks. **341,** 1230444–1230444 (Aug. 2013).

94. Rosi, N. L., Eckert, J., Eddaoudi, M., Vodak, D. T., Kim, J., O'Keeffe, M. & Yaghi, O. M. Hydrogen storage in microporous metal-organic frameworks. *Science* **300,** 1127–1129 (2003).

95. Hu, Z., Deibert, B. J. & Li, J. Luminescent metal–organic frameworks for chemical sensing and explosive detection. *Chem. Soc. Rev.* **43,** 5815–5840 (2014).

96. Cui, Y., Li, B., He, H., Zhou, W., Chen, B. & Qian, G. Metal–organic frameworks as platforms for functional materials. *Acc. Chem. Res.* **49,** 483–493 (2016).

97. Zhou, H, Long, J. R. & Yaghi, O. M. Introduction to metal–organic frameworks. *Chem. Rev.* **112,** 673–674 (2012).

98. Horcajada, P. *et al.* Porous metal-organic-framework nanoscale carriers as a potential platform for drug delivery and imaging. *Nat. Mater.* **9,** 172–178 (2010).

99. Seo, J. S., Whang, D., Lee, H., Jun, S. I., Oh, J., Jeon, Y. J. & Kim, K. A homochiral metal-organic porous material for enantioselective separation and catalysis. *Nature* **404,** 982–986 (2000).

100. Li, J.-R., Kuppler, R. J. & Zhou, H.-C. Selective gas adsorption and separation in metal-organic frameworks. *Chem. Soc. Rev.* **38,** 1477–1504 (2009).

101. Schneemann, A, Bon, V, Schwedler, I, Senkovska, I, Kaskel, S & Fischer, R. A. Flexible metal–organic frameworks. *Chem. Soc. Rev.* **43,** 6062–6096 (2014).

102. Lee, Y.-R., Kim, J. & Ahn, W.-S. Synthesis of metal-organic frameworks: A mini review. *Korean J. Chem. Eng.* **30,** 1667–1680 (2013).

103. Rabenau, A. The role of hydrothermal synthesis in preparative chemistry. *Angew. Chem. Int. Ed.* **24,** 1026–1040 (1985).

104. Dey, C, Kundu, T, Biswal, B. P., Mallick, A & Banerjee, R. Crystalline metal-organic frameworks (MOFs): synthesis, structure and function. *Acta Crystallogr., Sect. B: Struct. Sci* **70,** 3–10 (2014).

105. Zhao, D., Timmons, D. J., Yuan, D. & Zhou, H.-C. Tuning the topology and functionality of metal-organic frameworks by ligand design. *Acc. Chem. Res.* **44,** 123–133 (2011).

106. Czaja, A. U., Trukhan, N. & Müller, U. Industrial applications of metal-organic frameworks. *Chem. Soc. Rev.* **38,** 1284–1293 (2009).

107. Park, S.-E., Chang, J.-S., Hwang, Y. K., Kim, D. S., Jhung, S. H. & Hwang, J. S. Supramolecular interactions and morphology control in microwave synthesis of nanoporous materials. *Catal. Surv. Asia* **8,** 91–110 (2004).

108. Son, W.-J., Kim, J., Kim, J., Kim, J & Ahn, W.-S. Sonochemical synthesis of MOF-5. *Chem. Commun.* **0,** 6336–6338 (2008).

109. Zou, J.-P., Peng, Q., Wen, Z., Zeng, G.-S., Xing, Q.-J. & Guo, G.-C. Electrochemical synthesis of some archetypical Zn^{2+}, Cu^{2+}, and Al^{3+} metal-organic frameworks. *Cryst. Growth Des.* **12,** 3489–3498 (2012).

110. Friščić, T. New opportunities for materials synthesis using mechanochemistry. *J. Mater. Chem.* **20,** 7599–7605 (2010).

111. Howarth, A. J., Peters, A. W., Vermeulen, N. A., Wang, T. C., Hupp, J. T. & Farha, O. K. Best practices for the synthesis, activation, and characterization of metal–organic frameworks. *Chem. Mater.* **29,** 26–39 (2017).

112. Bétard, A. & Fischer, R. A. Metal–organic framework thin films: from fundamentals to applications. *Chem. Rev.* **112,** 1055–1083 (2011).

113. Fang, Z., Bueken, B., De Vos, D. E. & Fischer, R. A. Defect-engineered metal-organic frameworks. *Angew. Chem. Int. Ed.* **54,** 7234–7254 (2015).

114. Bennett, T. D., Cheetham, A. K., Fuchs, A. H. & Coudert, F. o.-X. Interplay between defects, disorder and flexibility in metal-organic frameworks. *Nat. Chem.* **9,** 11–16 (2016).

115. Stock, N. & Biswas, S. Synthesis of metal-organic frameworks (MOFs): routes to various MOF topologies, morphologies, and composites. *Chem. Rev.* **112,** 933–969 (2012).

116. Mondloch, J. E., Karagiaridi, O., Farha, O. K. & Hupp, J. T. Activation of metal-organic framework materials. *CrystEngComm* **15,** 9258–9264 (2013).

117. Bennett, T. D. & Cheetham, A. K. Amorphous metal–organic frameworks. *Acc. Chem. Res.* **47,** 1555–1562 (2014).

118. Gándara, F & Bennett, T. D. Crystallography of metal–organic frameworks. *IUCrJ* **1,** 563–570 (2014).

119. Wilmer, C. E., Leaf, M., Lee, C. Y., Farha, O. K., Hauser, B. G., Hupp, J. T. & Snurr, R. Q. Large-scale screening of hypothetical metal–organic frameworks. *Nat. Chem.* **4,** 83–89 (2012).

120. Al-Janabi, N., Hill, P., Torrente-Murciano, L., Garforth, A., Gorgojo, P., Siperstein, F. & Fan, X. Mapping the Cu-BTC metal–organic framework (HKUST-1) stability envelope in the presence of water vapour for CO2 adsorption from flue gases. *Chem. Eng. J.* **281,** 669–677 (2015).

121. Thommes, M., Kaneko, K., Neimark, A. V., Olivier, J. P., Rodriguez Reinoso, F., Rouquerol, J. & Sing, K. S. W. Physisorption of gases, with special reference to the evaluation of surface area and pore size distribution (IUPAC Technical Report). *Pure Appl. Chem.* **87,** 1051–1069 (2015).

122. Burtch, N. C., Jasuja, H. & Walton, K. S. Water stability and adsorption in metal–organic frameworks. *Chem. Rev.* **114,** 10575–10612 (2014).

123. Gelfand, B. S. & Shimizu, G. K. H. Parameterizing and grading hydrolytic stability in metal–organic frameworks. *Dalton Trans.* **45,** 3668–3678 (2016).

124. Li, H., Zhu, Y., Zhang, J., Chi, Z., Chen, L. & Su, C.-Y. Luminescent metal–organic gels with tetraphenylethylene moieties:

porosity and aggregation-induced emission. *RSC Adv.* **3,** 16340–16344 (2013).

125. Ma, Y., Wang, S. & Wang, L. Nanomaterials for luminescence detection of nitroaromatic explosives. *TrAC, Trends Anal. Chem.* **65,** 13–21 (2015).

126. Lan, A., Li, K., Wu, H., Olson, D. H., Emge, T. J., Ki, W., Hong, M. & Li, J. A luminescent microporous metal-organic framework for the fast and reversible detection of high explosives. *Angew. Chem. Int. Ed.* **48,** 2334–2338 (2009).

127. Pramanik, S., Zheng, C., Zhang, X., Emge, T. J. & Li, J. New microporous metal-organic framework demonstrating unique selectivity for detection of high explosives and aromatic compounds. *J. Am. Chem. Soc.* **133,** 4153–4155 (2011).

128. Kreno, L. E., Leong, K., Farha, O. K., Allendorf, M., Van Duyne, R. P. & Hupp, J. T. Metal–organic framework materials as chemical sensors. *Chem. Rev.* **112,** 1105–1125 (2012).

129. Lin, R. B., Liu, S. Y., Ye, J. W., Li, X. Y. & Zhang, J. P. Photoluminescent metal-organic frameworks for gas sensing. *Adv Sci* **3,** 1500434 (2016).

130. Pramanik, S., Hu, Z., Zhang, X., Zheng, C., Kelly, S. & Li, J. A systematic study of fluorescence-based detection of nitroexplosives and other aromatics in the vapor phase by microporous metal-organic frameworks. *Chem. Eur. J.* **19,** 15964–15971 (2013).

131. Banerjee, D., Hu, Z., Pramanik, S., Zhang, X., Wang, H. & Li, J. Vapor phase detection of nitroaromatic and nitroaliphatic explosives by fluorescence active metal–organic frameworks. *CrystEngComm* **15,** 9745–9750 (2013).

132. Hu, Z., Tan, K., Lustig, W. P., Wang, H., Zhao, Y., Zheng, C., Banerjee, D., Emge, T. J., Chabal, Y. J. & Li, J. Effective sensing

of RDX via instant and selective detection of ketone vapors. *Chem. Sci.* **5,** 4873–4877 (2014).

133. Hu, Z., Pramanik, S., Tan, K., Zheng, C., Liu, W., Zhang, X., Chabal, Y. J. & Li, J. Selective, sensitive, and reversible detection of vapor-phase high explosives via two-dimensional mapping: A new strategy for MOF-based sensors. *Cryst. Growth Des.* **13,** 4204–4207 (2013).

134. Xue, Y.-S., He, Y., Zhou, L., Chen, F.-J., Xu, Y., Du, H.-B., You, X.-Z. & Chen, B. A photoluminescent microporous metal-organic anionic framework for nitroaromatic explosive sensing. *J. Mater. Chem. A* **1,** 4525–4530 (2013).

135. Tian, D., Li, Y., Chen, R.-Y., Chang, Z., Wang, G.-Y. & Bu, X.-H. A luminescent metal–organic framework demonstrating ideal detection ability for nitroaromatic explosives. *J. Mater. Chem. A* **2,** 1465–1470 (2013).

136. Asha, K. S., Bhattacharyya, K. & Mandal, S. Discriminative detection of nitro aromatic explosives by a luminescent metal–organic framework. *J. Mater. Chem. C* **2,** 10073–10081 (2014).

137. Qin, J., Ma, B., Liu, X.-F., Lu, H.-L., Dong, X.-Y., Zang, S.-Q. & Hou, H. Aqueous- and vapor-phase detection of nitroaromatic explosives by a water-stable fluorescent microporous MOF directed by an ionic liquid. *J. Mater. Chem. A* **3,** 12690–12697 (2015).

138. Ma, B., Hu, S.-S., Wei, Y.-L. & Zang, S.-Q. Fast and reversible detection of nitrobenzene vapour by a fluorescent metal–organic framework templated by ionic liquid. *J Inorg Organomet Polym Mater* **25,** 1320–1326 (2015).

139. Chen, D.-M., Zhang, N.-N., Liu, C.-S. & Du, M. Template-directed synthesis of a luminescent Tb-MOF material for highly selec-

tive Fe 3^+ and Al 3^+ ion detection and VOC vapor sensing. *J. Mater. Chem. C* **5,** 2311–2317 (2017).

140. Wang, S., Wang, Q., Feng, X., Wang, B. & Yang, L. Explosives in the cage: metal–organic frameworks for high-energy materials sensing and desensitization. *Adv. Mater.* **298,** 1701898 (2017).

141. Zhang, F., Wang, Y., Chu, T., Wang, Z., Li, W. & Yang, Y. A facile fabrication of electrodeposited luminescent MOF thin films for selective and recyclable sensing of nitroaromatic explosives. *Analyst* **141,** 4502–4510 (2016).

142. Bajpai, A., Mukhopadhyay, A., Krishna, M. S., Govardhan, S. & Moorthy, J. N. A fluorescent paramagnetic Mn metal-organic framework based on semi-rigid pyrene tetra-carboxylic acid: sensing of solvent polarity and explosive nitroaromatics. *IUCrJ* **2,** 552–562 (2015).

143. Nagarkar, S. S., Joarder, B., Chaudhari, A. K., Mukherjee, S. & Ghosh, S. K. Highly selective detection of nitro explosives by a luminescent metal–organic framework. *Angew. Chem. Int. Ed.* **52,** 2881–2885 (2013).

144. Gole, B., Bar, A. K. & Mukherjee, P. S. Fluorescent metal–organic framework for selective sensing of nitroaromatic explosives. *Chem. Commun.* **47,** 12137–12139 (2011).

145. Zhou, X.-H., Li, L., Li, H.-H., Li, A., Yang, T. & Huang, W. A flexible Eu(III)-based metal–organic framework: turn-off luminescent sensor for the detection of Fe(III) and picric acid. *Dalton Trans.* **42,** 12403–12409 (2013).

146. Sun, L., Xing, H., Xu, J., Liang, Z., Yu, J. & Xu, R. A novel (3,3,6)-connected luminescent metal–organic framework for sensing of nitroaromatic explosives. *Dalton Trans.* **42,** 5508–5513 (2013).

147. Xiao, J.-D., Qiu, L.-G., Ke, F., Yuan, Y.-P., Xu, G.-S., Wang, Y.-M. & Jiang, X. Rapid synthesis of nanoscale terbium-based metal–organic frameworks by a combined ultrasound-vapour phase diffusion method for highly selective sensing of picric acid. *J. Mater. Chem. A* **1,** 8745–8752 (2013).

148. Shi, Z.-Q., Guo, Z.-J. & Zheng, H.-G. Two luminescent Zn(II) metal-organic frameworks for exceptionally selective detection of picric acid explosives. *Chem. Commun.* **51,** 8300–8303 (2015).

149. Nagarkar, S. S., Desai, A. V. & Ghosh, S. K. A fluorescent metal–organic framework for highly selective detection of nitro explosives in the aqueous phase. *Chem. Commun.* **50,** 8915–8918 (2014).

150. Qin, J.-H., Ma, B., Liu, X.-F., Lu, H.-L., Dong, X.-Y., Zang, S.-Q. & Hou, H. Ionic liquid directed syntheses of water-stable Eu- and Tb-organic-frameworks for aqueous-phase detection of nitroaromatic explosives. *Dalton Trans.* **44,** 14594–14603 (2015).

151. Joarder, B., Desai, A. V., Samanta, P., Mukherjee, S. & Ghosh, S. K. Selective and sensitive aqueous-phase detection of 2,4,6-trinitrophenol (TNP) by an amine-functionalized metal-organic framework. *Chem. Eur. J.* **21,** 965–969 (2015).

152. Yang, J., Wang, Z., Hu, K., Li, Y., Feng, J., Shi, J. & Gu, J. Rapid and specific aqueous-phase detection of nitroaromatic explosives with inherent porphyrin recognition sites in metal–organic frameworks. *ACS Appl. Mater. Interfaces* **7,** 11956–11964 (2015).

153. Zhang, S.-R., Du, D.-Y., Qin, J.-S., Bao, S.-J., Li, S.-L., He, W.-W., Lan, Y.-Q., Shen, P. & Su, Z.-M. A fluorescent sensor for highly selective detection of nitroaromatic explosives based on a 2D, extremely stable, metal-organic framework. *Chem. Eur. J.* **20,** 3589–3594 (2014).

154. Chaudhari, A. K., Nagarkar, S. S., Joarder, B. & Ghosh, S. K. A continuous π-stacked starfish array of two-dimensional luminescent MOF for detection of nitro explosives. *Cryst. Growth Des.* **13,** 3716–3721 (2013).

155. Zhang, C., Che, Y., Zhang, Z., Yang, X. & Zang, L. Fluorescent nanoscale zinc(II)-carboxylate coordination polymers for explosive sensing. *Chem. Commun.* **47,** 2336–2338 (2011).

156. Yi, F.-Y., Yang, W. & Sun, Z.-M. Highly selective acetone fluorescent sensors based on microporous Cd(II) metal–organic frameworks. *J. Mater. Chem.* **22,** 23201–23209 (2012).

157. Wang, G.-Y., Yang, L.-L., Li, Y., Song, H., Ruan, W.-J., Chang, Z. & Bu, X.-H. A luminescent 2D coordination polymer for selective sensing of nitrobenzene. *Dalton Trans.* **42,** 12865–12868 (2013).

158. Lee, J. H., Jaworski, J. & Jung, J. H. Luminescent metal–organic framework-functionalized graphene oxide nanocomposites and the reversible detection of high explosives. *Nanoscale* **5,** 8533–8540 (2013).

159. Kim, T. K., Lee, J. H., Moon, D. & Moon, H. R. Luminescent Li-based metal-organic framework tailored for the selective detection of explosive nitroaromatic compounds: direct observation of interaction sites. *Inorg. Chem.* **52,** 589–595 (2013).

160. Zhou, X., Li, H., Xiao, H., Li, L., Zhao, Q., Yang, T., Zuo, J. & Huang, W. A microporous luminescent europium metal–organic framework for nitro explosive sensing. *Dalton Transactions* **42,** 5718–5723 (2013).

161. Xu, H., Liu, F., Cui, Y., Chen, B. & Qian, G. A luminescent nanoscale metal–organic framework for sensing of nitroaromatic explosives. *Chem. Commun.* **47,** 3153–3155 (2011).

162. Ding, S.-B., Wang, W., Qiu, L.-G., Yuan, Y.-P., Peng, F.-M., Jiang, X., Xie, A.-J., Shen, Y.-H. & Zhu, J. F. Surfactant-assisted synthesis of lanthanide metal-organic framework nanorods and their fluorescence sensing of nitroaromatic explosives. *Mater. Lett.* **65,** 1385–1387 (2011).

163. Asha, K. S., Vaisakhan, G. S. & Mandal, S. Picogram sensing of trinitrophenol in aqueous medium through a water stable nanoscale coordination polymer. *Nanoscale* **8,** 11782–11786 (2016).

164. Jurcic, M., Peveler, W. J., Savory, C. N., Scanlon, D. O., Kenyon, A. J. & Parkin, I. P. The vapour phase detection of explosive markers and derivatives using two fluorescent metal–organic frameworks. *J. Mater. Chem. A* **3,** 6351–6359 (2015).

165. Beauchamp, R. O., Irons, R. D., Rickert, D. E., Couch, D. B., Hamm, T. E. & Lyon, J. P. A critical review of the literature on nitrobenzene toxicity. *CRC Crit. Rev. Toxicol.* **11,** 33–84 (2008).

166. Rissanen, K. in *Analytical Methods in Supramolecular Chemistry* 305–336 (Wiley-VCH, Weinheim, 2006).

167. Van der Sluis, P & Spek, A. L. BYPASS: an effective method for the refinement of crystal structures containing disordered solvent regions. *Acta Crystallogr., Sect. A: Found. Crystallogr.* **46,** 194–201 (1990).

168. Hou, Y.-L., Xu, H., Cheng, R.-R. & Zhao, B. Controlled lanthanide–organic framework nanospheres as reversible and sensitive luminescent sensors for practical applications. *Chem. Commun.* **51,** 6769–6772 (2015).

169. Zou, J.-P., Peng, Q., Wen, Z., Zeng, G.-S., Xing, Q.-J. & Guo, G.-C. Two novel metal−organic frameworks (MOFs) with (3,6)-connected net topologies: syntheses, crystal structures, third-

order nonlinear optical and luminescent properties. *Cryst. Growth Des.* **10,** 2613–2619 (2010).

170. Cui, Y. & Chen, B. in *Metal-Organic Frameworks for Photonics Applications* (eds Chen, B. & Qian, G.) 27–88 (Springer Berlin Heidelberg, Berlin, Heidelberg, 2014).

171. Li, W.-J., Lü, J., Gao, S.-Y., Li, Q.-H. & Cao, R. Electrochemical preparation of metal–organic framework films for fast detection of nitro explosives. *J. Mater. Chem. A* **2,** 19473–19478 (2014).

172. Wang, B., Lv, X.-L., Feng, D., Xie, L.-H., Zhang, J., Li, M., Xie, Y., Li, J.-R. & Zhou, H.-C. Highly stable Zr(IV)-based metal–organic frameworks for the detection and removal of antibiotics and organic explosives in water. *J. Am. Chem. Soc.* **138,** 6204–6216 (2016).

173. Geng, Y., Ali, M. A., Clulow, A. J., Fan, S., Burn, P. L., Gentle, I. R., Meredith, P. & Shaw, P. E. Unambiguous detection of nitrated explosive vapours by fluorescence quenching of dendrimer films. *Nat. Commun.* **6,** 8240 (2015).

174. Pisarska, J., Żur, L. & Pisarski, W. A. Visible luminescence of dysprosium ions in oxyhalide lead borate glasses. *Spectrochim. Acta, Part A* **79,** 705–707 (2011).

175. Schnorr, J. M., van der Zwaag, D., Walish, J. J., Weizmann, Y. & Swager, T. M. Sensory arrays of covalently functionalized single-walled carbon nanotubes for explosive detection. *Adv. Funct. Mater.* **23,** 5285–5291 (2013).

176. Eubank, J. F., Mouttaki, H., Cairns, A. J., Belmabkhout, Y., Wojtas, L., Luebke, R., Alkordi, M. & Eddaoudi, M. The quest for modular nanocages: tbo-MOF as an archetype for mutual substitution, functionalization, and expansion of quadrangular pillar building blocks. *J. Am. Chem. Soc.* **133,** 14204–14207 (2011).

177. Li, M., Li, D., O'Keeffe, M. & Yaghi, O. M. Topological analysis of metal–organic frameworks with polytopic linkers and/or multiple building units and the minimal transitivity principle. *Chem. Rev.* **114,** 1343–1370 (2013).

178. Küsgens, P., Rose, M., Senkovska, I., Fröde, H., Henschel, A., Siegle, S. & Kaskel, S. Characterization of metal-organic frameworks by water adsorption. *Microporous Mesoporous Mater.* **120,** 325–330 (2009).

179. Alaerts, L., Séguin, E., Poelman, H., Thibault Starzyk, F., Jacobs, P. A. & De Vos, D. E. Probing the lewis acidity and catalytic activity of the metal–organic framework $[Cu_3(btc)_2]$ (BTC=Benzene-1,3,5-tricarboxylate). *Chem. Eur. J.* **12,** 7353–7363 (2006).

180. Yakovenko, A. A., Reibenspies, J. H., Bhuvanesh, N. & Zhou, H.-C. Generation and applications of structure envelopes for porous metal–organic frameworks. *J. Appl. Crystallogr.* **46,** 346–353 (2013).

181. Dolomanov, O. V., Bourhis, L. J., Gildea, R. J., Howard, J. A. K., Puschmann, H & IUCr. OLEX2: a complete structure solution, refinement and analysis program. *J. Appl. Crystallogr.* **42,** 339–341 (2009).

182. Spek, A. L. & IUCr. PLATON, An integrated tool for the analysis of the results of a single crystal structure determination. *Acta Crystallogr. Sect. A: Found. Crystallogr.* **46,** 34–34 (1990).

183. Ranko M Vrcelj, John N Sherwood, Alan R Kennedy, Gallagher, H. G., & Gelbrich, T. Polymorphism in 2-4-6 trinitrotoluene. *Cryst. Growth Des.* **3,** 1027–1032 (2003).

184. Cady, H. H., Larson, A. C. & IUCr. Pentaerythritol tetranitrate II: its crystal structure and transformation to PETN I; an algo-

rithm for refinement of crystal structures with poor data. *Acta Crystallogr., Sect. B: Struct. Sci* **31,** 1864–1869 (1975).

185. Choi, C. S. & Prince, E. The crystal structure of cyclotrimethylenetrinitramine. *Acta Crystallogr., Sect. B: Struct. Sci* **28,** 2857–2862 (1972).

186. Bertolasi, V., Gilli, P. & Gilli, G. Hydrogen bonding and electron donor–acceptor (EDA) interactions controlling the crystal packing of picric acid and its adducts with nitrogen bases. their rationalization in terms of the pKa equalization and electron-pair saturation concepts. *Cryst. Growth Des.* **11,** 2724–2735 (2011).

187. Cady, H. H. The crystal structure of N-methyl-N-2,4,6-tetranitroaniline (tetryl). *Acta Crystallogr. A* **23,** 601–609 (1967).

188. Reany, O., Kapon, M., Botoshansky, M. & Keinan, E. Rich polymorphism in triacetone-triperoxide. *Cryst. Growth Des.* **9,** 3661–3670 (2009).

189. Ferrando-Soria, J. *et al.* Highly selective chemical sensing in a luminescent nanoporous magnet. *Adv. Mater.* **24,** 5625–5629 (2012).

190. Schlechte, L, Wehring, B & Klein, N. Metal-organic frameworks as humidity sensor in *Proceedings of Sensors and Measuring Systems 2014;. ITG/GMA Symposium* (IEEE, Nuremberg, 2014).

191. Qasim, M., Kholod, Y., Gorb, L., Magers, D., Honea, P. & Leszczynski, J. Application of quantum-chemical approximations to environmental problems: Prediction of physical and chemical properties of TNT and related species. *Chemosphere* **69,** 1144–1150 (2007).

192. Sohn, H., Sailor, M. J., Magde, D. & Trogler, W. C. Detection of nitroaromatic explosives based on photoluminescent polymers containing metalloles. *J. Am. Chem. Soc.* **125,** 3821–3830 (2003).

193. Saxena, A., Fujiki, M., Rai, R. & Kwak, G. Fluoroalkylated polysilane film as a chemosensor for explosive nitroaromatic compounds. *Chem. Mater.* **17,** 2181–2185 (2005).

194. Nagarkar, S. S., Desai, A. V., Samanta, P. & Ghosh, S. K. Aqueous phase selective detection of 2,4,6-trinitrophenol using a fluorescent metal–organic framework with a pendant recognition site. *Dalton Trans.* **44,** 15175–15180 (2015).

195. Armbruster, D. A. & Pry, T. Limit of blank, limit of detection and limit of quantitation. *Clin. Biochem. Rev.* **29,** 49–52 (2008).

196. Khatua, S., Goswami, S., Biswas, S., Tomar, K., Jena, H. S. & Konar, S. Stable multiresponsive luminescent MOF for colorimetric detection of small molecules in selective and reversible manner. *Chem. Mater.* **27,** 5349–5360 (2015).

197. Yu, Y., Ma, J.-P., Zhao, C.-W., Yang, J., Zhang, X.-M., Liu, Q.-K. & Dong, Y.-B. Copper(I) metal-organic framework: visual sensor for detecting small polar aliphatic volatile organic compounds. *Inorg. Chem.* **54,** 11590–11592 (2015).

198. Lim, K. S., Jeong, S. Y., Kang, D. W., Song, J. H., Jo, H., Lee, W. R., Phang, W. J., Moon, D. & Hong, C. S. Luminescent metal–organic framework sensor: exceptional Cd^{2+} turn-on detection and first in situ visualization of Cd^{2+} ion diffusion into a crystal. *Chem. Eur. J.* **23,** 4803–4809 (2017).

199. Nagarkar, S. S., Saha, T., Desai, A. V., Talukdar, P. & Ghosh, S. K. Metal-organic framework based highly selective fluorescence turn-on probe for hydrogen sulphide. *Sci. Rep.* **4,** 7053 (2014).

200. Dang, S., Ma, E., Sun, Z.-M. & Zhang, H. A layer-structured Eu-MOF as a highly selective fluorescent probe for Fe^{3+} detection through a cation-exchange approach. *J. Mater. Chem.* **22,** 16920–16926 (2012).

201. Yang, Y., Chen, L., Jiang, F., Wan, X., Yu, M., Cao, Z., Jing, T. & Hong, M. Fabricating a super stable luminescent chemosensor with multi-stimuli-response to metal ions and small organic molecules by turn-on and turn-off effects. *J. Mater. Chem. C.* **5,** 4511–4519 (2017).

202. Qi, X.-L., Lin, R. B., Chen, Q., Lin, J.-B., Zhang, J. P. & Chen, X.-M. A flexible metal azolate framework with drastic luminescence response toward solvent vapors and carbon dioxide. *Chem. Sci.* **2,** 2214–2218 (2011).

203. Yu, Y., Zhang, X.-M., Ma, J.-P., Liu, Q.-K., Wang, P. & Dong, Y.-B. Cu(I)-MOF: naked-eye colorimetric sensor for humidity and formaldehyde in single-crystal-to-single-crystal fashion. *Chem. Commun.* **50,** 1444–1446 (2014).

204. Yu, Y., Ma, J.-P. & Dong, Y.-B. Luminescent humidity sensors based on porous Ln^{3+}-MOFs. *CrysEngComm* **14,** 7157–7160 (2012).

205. Anzenbacher, P. & Palacios, M. A. in *Chemosensors Principles, Strategies, and Applications* (eds Wang, B & Anslyn, E. V.) 345–368 (John Wiley & Sons, Inc., Hoboken, 2011).

206. Le, N. D., Yazdani, M. & Rotello, V. M. Array-based sensing using nanoparticles: an alternative approach for cancer diagnostics. *Nanomedicine* **9,** 1487–1498 (2014).

207. Scott, S. M., James, D. & Ali, Z. Data analysis for electronic nose systems. *Microchim. Acta* **156,** 183–207 (2006).

208. Lavigne, J. J. & Anslyn, E. V. Sensing a paradigm shift in the field of molecular recognition: from selective to differential receptors. *Angew. Chem. Int. Ed.* **40,** 3118–3130 (2001).

209. Peveler, W. J., Binions, R., Hailes, S. M. V. & Parkin, I. P. Detection of explosive markers using zeolite modified gas sensors. *J. Mater. Chem. A* **1,** 2613–2620 (2013).

210. Hannon, A., Lu, Y., Li, J. & Meyyappan, M. A sensor array for the detection and discrimination of methane and other environmental pollutant gases. *IEEE Sens. J.* **16,** 1163 (2016).

211. Miranda, O., You, C.-C., Phillips, R., Kim, I.-B., Ghosh, P., Bunz, U. & Rotello, V. Array-based sensing of proteins using conjugated polymers. *J. Am. Chem. Soc.* **129,** 9856–9857 (2007).

212. Jin, X., Huang, Y., Mason, A. & Zeng, X. Multichannel monolithic quartz crystal microbalance gas sensor array. *Anal. Chem.* **81,** 595–603 (2008).

213. Grate, J. W. Acoustic wave microsensor arrays for vapor sensing. *Chem. Rev.* **100,** 2627–2648 (2000).

214. Kim, B. H., Prins, F. E., Kern, D. P., Raible, S & Weimar, U. Multicomponent analysis and prediction with a cantilever array based gas sensor. *Sens. Actuators, B* **78,** 12–18 (2001).

215. Askim, J. R., Mahmoudi, M. & Suslick, K. S. Optical sensor arrays for chemical sensing: the optoelectronic nose. *Chem. Soc. Rev.* **42,** 8649–8682 (2013).

216. Lichtenstein, A, Havivi, E & Shacham, R. Supersensitive fingerprinting of explosives by chemically modified nanosensors arrays. *Nature* **5,** 4195 (2014).

217. Askim, J. R., Li, Z., LaGasse, M. K., Rankin, J. M. & Suslick, K. S. An optoelectronic nose for identification of explosives. *Chem. Sci.* **7,** 199–206 (2016).

218. Li, Z., Bassett, W. P., Askim, J. R. & Suslick, K. S. Differentiation among peroxide explosives with an optoelectronic nose. *Chem. Commun.* **51,** 15312–15315 (2015).

219. Hughes, A. D., Glenn, I. C., Patrick, A. D., Ellington, A. & Anslyn, E. V. A pattern recognition based fluorescence quench-

ing assay for the detection and identification of nitrated explosive analytes. *Chem. Eur. J.* **14,** 1822–1827 (2008).

220. Ivy, M. A., Gallagher, L. T., Ellington, A. D. & Anslyn, E. V. Exploration of plasticizer and plastic explosive detection and differentiation with serum albumin cross-reactive arrays. *Chem. Sci.* **3,** 1773–1779 (2012).

221. Latendresse, C. A., Fernandes, S. C., You, S., Zhang, H. Q. & Euler, W. B. A fluorometric sensing array for the detection of military explosives and IED materials. *Anal. Methods* **5,** 5457–5463 (2013).

222. Germain, M. E. & Knapp, M. J. Discrimination of nitroaromatics and explosives mimics by a fluorescent Zn(salicylaldimine) sensor array. *J. Am. Chem. Soc.* **130,** 5422–5423 (2008).

223. Peveler, W. J., Roldan, A., Hollingsworth, N., Porter, M. J. & Parkin, I. P. Multichannel detection and differentiation of explosives with a quantum dot array. *ACS Nano* **10,** 1139–1146 (2015).

224. Campbell, M. G., Liu, S. F., Swager, T. M. & Dincă, M. Chemiresistive sensor arrays from conductive 2D metal–organic frameworks. *J. Am. Chem. Soc.* **137,** 13780–13783 (2015).

225. Gustafson, J. A. & Wilmer, C. E. Computational design of metal–organic framework arrays for gas sensing: influence of array size and composition on sensor performance. *J. Phys. Chem. C* **121,** 6033–6038 (2017).

226. Chen, B, Yang, Y, Zapata, F, Lin, G, Qian, G & Lobkovsky, E. B. Luminescent open metal sites within a metal–organic framework for sensing small molecules. *Adv. Mater.* **19,** 1693–1696 (2007).

227. Ferguson, A., Liu, L., Tapperwijn, S. J., Perl, D., Coudert, F.-X., Van Cleuvenbergen, S., Verbiest, T., van der Veen, M. A. & Telfer, S. G. Controlled partial interpenetration in metal-organic frameworks. *Nat. Chem.* **8,** 250–257 (2016).

228. Woodka, M. D., Schnee, V. P. & Polcha, M. P. Fluorescent polymer sensor array for detection and discrimination of explosives in water. *Anal. Chem.* **82,** 9917–9924 (2010).

229. Wang, C., Huang, H., Bunes, B. R., Wu, N., Xu, M., Yang, X., Yu, L. & Zang, L. Trace detection of RDX, HMX and PETN explosives using a fluorescence spot sensor. *Sci. Rep.* **6,** 25015 (2016).

230. Mullen, C., Irwin, A., Pond, B., Huestis, D., Coggiola, M. & Herald, O. Detection of explosives and explosives-related compounds by single photon laser ionization time-of-flight mass spectrometry. *Anal. Chem.* **78,** 3807–3814 (2006).

231. Garcia-Reyes, J. F., Harper, J. D., Salazar, G. A., Charipar, N. A., Ouyang, Z. & Cooks, R. G. Detection of explosives and related compounds by low-temperature plasma ambient ionization mass spectrometry. *Anal. Chem.* **83,** 1084–1092 (2010).

232. Zhao, J., Luo, T., Zhang, X., Lei, Y., Gong, K. & Yan, Y. Highly selective zeolite membranes as explosive preconcentrators. *Anal. Chem.* **84,** 6303–6307 (2012).

233. Baya, M. P. & Siskos, P. A. Evaluation of Anasorb CMS and comparison with Tenax TA for the sampling of volatile organic compounds in indoor and outdoor air by breakthrough measurements. *Analyst* **121,** 303–307 (1996).

234. Hannum, D. W., Linker, K. L., Parmeter, J. E., Rhykerd, C. L. & Varley, N. R. Miniaturized explosive preconcentrator for use in a man-portable field detection system in *IEEE 34th Annual*

International Carnahan Conference on Security Technology (IEEE, Ottawa, 2000).

235. Lahlou, H, Vilanova, X & Correig, X. Gas phase micro-preconcentrators for benzene monitoring: A review. *Sens. Actuators, B* **176,** 198–210 (2013).

236. Alfeeli, B., Taylor, L. T. & Agah, M. Evaluation of Tenax TA thin films as adsorbent material for micro preconcentration applications. *Microchem. J.* **95,** 259–267 (2010).

237. Blanco, F, Ivanov, P, Vinaixa, M, Vilanova, X, Gracia, I, Cane, C & Correig, X. Development and optimization of pre-concentrator for enhanced benzene detection in *Spanish Conference on Electron Devices* (IEEE, 2007), 216–218.

238. Alfeeli, B., Jain, V., Johnson, R. K., Beyer, F. L., Heflin, J. R. & Agah, M. Characterization of poly(2,6-diphenyl-p-phenylene oxide) films as adsorbent for microfabricated preconcentrators. *Microchem. J.* **98,** 240–245 (2011).

239. Harshman, S. W. *et al.* Storage stability of exhaled breath on Tenax TA. *J. Breath Res.* **10,** 046008 (2016).

240. Maier, I & Fieber, M. Retention characteristics of volatile compounds on tenax TA. *J. Sep. Sci.* **11,** 566–576 (1988).

241. Giordano, B. C., Field, C. R., Andrews, B., Lubrano, A., Woytowitz, M., Rogers, D. & Collins, G. E. Trace explosives vapor generation and quantitation at parts per quadrillion concentrations. *Anal. Chem.* **88,** 3747–3753 (2016).

242. Sigman, M. E., Cheng-Yu, M. & Ilgner, R. H. Performance evaluation of an in-injection port thermal desorption/gas chromatographic/negative ion chemical ionization mass spectrometric method for trace explosive vapor analysis. *Anal. Chem.* **73,** 792–798 (2001).

243. Camara, M, James, F, Breuil, P, Pijolat, C, Briand, D & de Rooij, N. F. MEMS-based porous silicon preconcentrators filled with Carbopack-B for cxplosives detection. *Procedia Eng.* **87,** 84–87 (2014).

244. Wilhelm, I., Rieger, M., H rttlen, J. r., Wittek, M., Al p e, C., Leidinger, M. & Sauerwald, T. Novel low-cost selective preconcentrators based on metal-organic frameworks. *Procedia Eng.* **168,** 151–154 (2016).

245. Leidinger, M., Rieger, M., Sauerwald, T., Al p e, C. & Sch tze, A. Integrated pre-concentrator gas sensor microsystem for ppb level benzene detection. *Sens. Actuators, B* **236,** 988–996 (2016).

246. Schutze, A., Leidinger, M., Schmitt, B., Sauerwald, T., Rieger, M. & Alepee, C. A novel low-cost pre-concentrator concept to boost sensitivity and selectivity of gas sensor systems in *2015 IEEE Sensors* (IEEE, 2015), 1–4.

247. Gu, Z.-Y., Wang, G. & Yan, X.-P. MOF-5 metal–organic framework as sorbent for in-field sampling and preconcentration in combination with thermal desorption GC/MS for determination of atmospheric formaldehyde. *Anal. Chem.* **82,** 1365–1370 (2010).

248. Zheng Ni, John P Jerrell, Cadwallader, K. R., & Richard I Masel. Metal–organic frameworks as adsorbents for trapping and preconcentration of organic phosphonates. *Anal. Chem.* **79,** 1290–1293 (2007).

249. Xiong, R., Odbadrakh, K., Michalkova, A., Luna, J. P., Petrova, T., Keffer, D. J., Nicholson, D. M., Fuentes-Cabrera, M. A., Lewis, J. P. & Leszczynski, J. Evaluation of functionalized isoreticular metal organic frameworks (IRMOFs) as smart nanoporous preconcentrators of RDX. *Sens. Actuators, B* **148,** 459–468 (2010).

250. Surya, S. G., Nagarkar, S. S., Ghosh, S. K., Sonar, P. & Ramgopal Rao, V. OFET based explosive sensors using diketopyrrolopyrrole and metal organic framework composite active channel material. *Sens. Actuators, B* **223,** 114–122 (2016).

251. Sigma-Aldrich. Particle Size Conversion `http://www.sigmaaldrich.com/chemistry/stockroom-reagents/learning-center/technical-library/particle-size-conversion.html`.

252. Gottlieb, H. E., Kotlyar, V. & Nudelman, A. NMR chemical shifts of common laboratory solvents as trace impurities. *J. Org. Chem.* **62,** 7512–7515 (1997).

253. Palatinus, L, Chapuis, G & IUCr. SUPERFLIP – a computer program for the solution of crystal structures by charge flipping in arbitrary dimensions. *J. Appl. Crystallogr.* **40,** 786–790 (2007).

254. Spek, A. L. & IUCr. Structure validation in chemical crystallography. *Acta. Crystallogr. Sect. D. Biol. Crystallogr.* **65,** 148–155 (2009).